Models and Mechanics of Eruptive Processes

Empirical data from seismology, geophysics, field geology, and petrology give us the precursory signals and ongoing history of the eruption. However, to understand how volcanoes work—and, consequently, to have a volcano-monitoring program with predictive value—requires deeper insight into an eruption's physical mechanisms. A "sticky piston" model of solid-state extrusion was suggested by the drumbeat aspect of the 2004–6 eruption's seismicity. Geologists made a renewed effort to catch the stick-slip process in action, using fixed-camera photography to monitor its visual manifestation and borehole tiltmeters to measure the associated inflation-deflation cycles expected in local ground deformation.

Laboratory testing of the gouge that encases the extruding dome indicates material properties suitable for the sticky-piston model to predict episodic, seismogenic slip, namely plug stiffness that exceeds that of the rising fluid magma and rate-weakening gouge friction at low slip rates. Textural evidence indicates that crystallization and solidification of the ascending magma preceded gouge formation. Comparison of groundmass textures from dome lavas and fault gouge suggests that brittle fracture was confined to the upper 1 km of the conduit. Textural similarity between gouge and the ash emitted by explosions from spine margins in January and March 2005 suggests that fragmentation preceded rather than accompanied these explosions.

Eruption rates and modeling of the magma reservoir allow reasonable fits to either exponential or logarithmic decay curves. For each of these, however, the history of reservoir decompression forms an imperfect match to the rapid, radially inward motion of the ground surface during the first month of the eruption, as deduced from displacement data from the continually transmitting GPS station located 9 km from the vent. That movement suggests that erupted magma was replaced by recharge, but that the recharge rate remained less than the eruption's characteristic effusion rate.

Spine 4 on February 22, 2005. View to east-southeast. Shoestring notch is low point on east crater rim. USGS photo by S.P. Schilling.

A Volcano Rekindled: The Renewed Eruption of Mount St. Helens, 2004–2006
Edited by David R. Sherrod, William E. Scott, and Peter H. Stauffer
U.S. Geological Survey Professional Paper 1750, 2008

Chapter 19

From Dome to Dust: Shallow Crystallization and Fragmentation of Conduit Magma During the 2004–2006 Dome Extrusion of Mount St. Helens, Washington

By Katharine V. Cashman[1], Carl R. Thornber[2], and John S. Pallister[2]

Abstract

An unusual feature of the 2004–6 eruptive activity of Mount St. Helens has been the continuous growth of successive spines that are mantled by thick fault gouge. Fault gouge formation requires, first, solidification of ascending magma within the conduit, then brittle fragmentation and cataclastic flow. We document these processes through field relations, hand samples, and thin-section textures. Field observations show that the gouge zone is typically 1–3 m thick and that it includes cataclasite and, locally, breccia in addition to unconsolidated (true) gouge. The gouge contains multiple slickenside sets oriented subparallel to each other and to the striation direction, as well as surface striations parallel to extrusion direction. Hand specimens show the cataclasite and gouge to be composed of a wide size range of broken dome and wall-rock fragments. This grain-size heterogeneity is even more pronounced in thin section, where individual samples contain fragments that span more than four orders of magnitude in size (from more than 10 to less than 10^{-3} mm).

Textures preserved within the gouge zone provide evidence of different processes operating in time and space. Most individual fragments are holocrystalline, suggesting that crystallization of the ascending magma preceded gouge formation. Cataclasite samples preserve a wide range of clast sizes; pronounced rounding of many clasts indicates extensive abrasion during transport. Within the gouge, crystals and lava fragments adjacent to finely comminuted shear zones (slickensides) are shattered into small, angular fragments that are either preserved in place, with little disruption, or incorporated into shear trains, creating a well-developed foliation. Together, evidence of initial grain shattering, followed by shear, grinding, and wear, suggests extensive transport distances (large strains). Textural transitions are often abrupt, indicating extreme shear localization during transport. Comparison of groundmass textures from dome lavas and fault gouge further suggests that brittle fracture was confined to the upper 400–500 m of the conduit. Observed magma extrusion (ascent) rates of ~7 m/d (8×10^{-5} m/s) permit several weeks for magma ascent from ~1,000 m (where groundmass crystallization becomes important) to ~500 m (where solidification nears completion). Brittle fracture, cataclastic flow, and shear localization (slickenside formation) probably dominated in the upper 500 m of the conduit.

Comparison of eruptive conditions during the 2004–6 activity at Mount St. Helens with those of other spine-forming eruptions suggests that magma ascent rates of about 10^{-4} m/s or less allow sufficient degassing and crystallization within the conduit to form large volcanic spines of intermediate composition (andesite to dacite). Solidification deep within the conduit, in turn, requires transport of the solid plug over long distances (hundreds of meters); resultant large strains are responsible for extensive brittle breakage and development of thick gouge zones. Moreover, similarities between gouge textures and those of ash emitted by explosions from spine margins indicate that fault gouge is the origin for the ash. As the comminution and generation of ash-sized particles was clearly a multistep process, this observation suggests that fragmentation preceded, rather than accompanied, these explosions.

Introduction

The 2004–6 eruption of Mount St. Helens has been characterized by steady lava effusion in the form of a succession of smooth-surfaced dacitic spines (Scott and others, this volume,

---

[1] Department of Geological Sciences, 1272 University of Oregon, Eugene, OR 97403

[2] U.S. Geological Survey, 1300 SE Cardinal Court, Vancouver, WA 98683

chap. 1) that are remarkable for the striated fault gouge that forms a carapace on each of the seven spines erupted between October 2004 and February 2006. This fault gouge is unusually well preserved and well sampled, thanks to helicopter dredging operations (see Pallister and others, this volume, chap. 30). Additional geophysical constraints on dome extrusion include photogrammetry (Schilling and others, this volume, chap. 8), thermal observations (Schneider and others, this volume, chap. 17), and seismic observations (Moran and others, this volume, chap. 2). Notable in these observations is the remarkable steadiness of both the extrusion and accompanying "drumbeat" earthquakes, all of which appear to originate at depths <1 km directly below the growing dome (Moran and others, this volume, chap. 2) and are interpreted to record steady stick-slip behavior of the ascending magma plug (Iverson and others, 2006; Iverson, this volume, chap. 21).

Individual outcrops document an abrupt transition from competent flow-banded dacite to a zone of breccia and cataclasite to finely comminuted and variably consolidated gouge. In this paper we use field, hand-specimen, and thin-section observations of these cataclastic dome facies to constrain some of the physical processes related to dome extrusion and gouge formation. Analysis of observations over this range in scale allows us to (1) describe progressive fragmentation of the solid dome rock to fine-grained fault gouge, (2) trace decompression/crystallization paths within the conduit, and (3) provide depth constraints on both solidification and onset of brittle deformation. We then link processes of fragmentation and gouge formation to relative rates of ascent (shear), degassing, and crystallization. This linkage is important both for recognizing conditions that may lead to changes in the emplacement conditions of the current dome at Mount St. Helens and for generalizing observations at Mount St. Helens to other recent effusive eruptions of intermediate composition magma. In addition, the spectacular preservation of fault textures allows us to extend analysis of tectonic gouge formation to volcanic environments and to compare brittle deformation processes in highly crystalline dacite with those of tuffisites in obsidian flows. Finally, the similarity of clasts preserved within the gouge to those found within ash from dome explosions (Rowe and others, this volume, chap. 29) allows us to speculate on the nature of explosions that have accompanied dome formation.

Background

As detailed descriptions of lava dome emplacement are provided in other papers in this volume (Scott and others, chap. 1; Schilling and others, chap. 8; Vallance and others, chap. 9), we briefly review only the elements of the dome's emplacement history that are directly relevant to the conditions of gouge formation. We then provide an overview of spine formation at other volcanoes, with a particular emphasis on both observations of spine emplacement and eruption conditions that produced these features. Finally, we discuss observational and experimental constraints on decompression-driven crystallization required to form spines.

2004–2006 Activity at Mount St. Helens

After about three weeks of precursory seismic unrest and phreatic explosions in late September and early October of 2004, a dacite lava spine emerged within the central crater of Mount St. Helens, to the south of the 1980–86 lava dome. Extrusion has been continuous since mid-October 2004, with emplacement and partial to complete disintegration of seven individual spines. Extrusion rates were highest, about 6 m^3/s, during the first month of the eruption, after which they dropped to 1–2 m^3/s. Linear rates of spine emergence from the vent have also been constant at 3–6 m/day ($3.5–7\times10^{-5}$ m/s), except during the early stages of extrusion when rates were about twice as fast. Extrusion has been accompanied by only two major explosions—one on January 16, 2005, and another on March 8, 2005. Ash produced by those explosions is described by Rowe and others (this volume, chap. 29).

Lava Dome Emplacement and Morphology

Howel Williams (1932) presented the first comprehensive description of volcanic dome emplacement. He used the term "dome" to describe viscous lava protrusions that could be subdivided into (1) "plug domes" (spines), (2) "endogenous domes" that grow by expansion from within and (3) "exogenous domes" built by surface effusion, usually from a central summit crater. He noted that effusion rate (Q) provided the strongest control on growth style, with the lowest effusion rate leading to plug dome (spine) formation. As a type example for plug-dome behavior he used the famous spine extruded from Mont Pelée, Martinique, in 1903. This massive spine reached a maximum height of >300 m, grew as rapidly as 25 meters in a day (2.9×10^{-4} m/s), and was disrupted continually by both collapse and explosions. The spine was described by Jaggar (1904) as " * * * a most extraordinary monolith, shaped like the dorsal fin of a shark, with a steep and almost overhanging escarpment on the east, while the western aspect of the spine was curved and smooth in profile. The field glass showed jagged surfaces on the steeper eastern side, and long smooth striated slopes on the western" (fig. 1). These smooth, striated slopes also preserved slickensides and breccias produced by differential movement of already solid lava. Lacroix (1904) noted both vertical striations parallel to the extrusion direction and horizontal ridges indicating "successive stages in its upheaval" (Williams, 1932).

Recent eruptions at Mount St. Helens, Washington; Unzen, Japan; and Soufrière Hills, Montserrat, confirm and extend these early concepts. Dome growth at Mount St. Helens from 1980 to 1986 had both exogenous and endogenous phases and erupted a total volume of 0.077 km^3 of dacite magma (62.5–63.5 weight percent SiO_2; Swanson and Holcomb 1990).

Exogenous growth of individual flow lobes was the dominant dome growth mechanism through 1981, with lobes emplaced at rates of 9–24 m^3/s during time periods of less than a week. Exogenous dome lobes were also emplaced from March 1984 until October 1986, although accompanying endogenous growth became increasingly important during this time period (Fink and others, 1990). Times of anomalous activity included (1) March 1982, when a protracted effusive event (24 days at an average rate of 1.6 m^3/s) was preceded by deep seismicity and a vulcanian explosion; (2) February 1983–February 1984, when effusion was continuous at a rate of 0.7 m^3/s (approximately equivalent to the long-term magma supply rate from October 1980 to October 1981) and dome growth was primarily endogenous; and (3) May 1985, when effusion lasted 17 days (at an average rate of 2.9 m^3/s). Only two spines were emplaced during the 1980–86 effusive activity, one in February 1983, during the period of continuous endogenous growth, and one in May 1985, at the end of a protracted (and largely endogenous) dome growth episode. Magma batches feeding individual exogenous dome lobes ascended at 0.1–1 m/s (Chadwick and others, 1988; Endo and others, 1990; Geschwind and Rutherford, 1995), corresponding to decompression rates of ~0.0025–0.025 MPa/s. Because effusion rates were 10–20 times lower during 1983, we infer that ascent rates during periods of continuous dome growth were correspondingly lower (at least by a factor of 2–5), with magma ascent rates for spine production even lower (probably <10^{-3} m/s).

Links between eruption rate and dome morphology can be further constrained by examining two other eruptions of slightly different bulk composition. Unzen volcano, Japan, active from 1990 to 1995, constructed a 0.2-km^3 dome of dacitic composition (64.5–66 wt. percent SiO$_2$). Initial effusion (Q) at ~1 m^3/s produced a spine. Shortly thereafter a rapid increase in Q to ~5 m^3/s triggered a succession of pyroclastic flows accompanied by tremor spurts and two vulcanian eruptions (Nakada and Fujii, 1993; Nakada and others, 1995b, 1999; Nakada and Motomura, 1999). After this time the dome grew nearly continuously, with exogenous growth dominating during periods of higher effusion rates (>4 m^3/s) and endogenous growth dominant when effusion rates were low (<1 m^3/s). Magma ascent rates were estimated to be 13–40 m/d (1–5×10^{-4} m/s; Nakada and others, 1995b), more than an order of magnitude lower than during the time period of continuous magma ascent at Mount St. Helens in 1983. Effusion rates declined gradually until the end of the eruption, which was marked by the emergence of a spine from the endogenous dome (Nakada and others, 1995a).

Soufrière Hills volcano, Montserrat, intermittently active since 1995, has also shown a close correspondence between the rate of lava effusion and dome morphology. By 1999 the volcano had produced almost 0.3 km^3 of silicic andesite (57–61.5 wt. percent SiO$_2$), about two-thirds of which traveled as pumiceous and dense pyroclastic flows into valleys around the volcano. Low effusion rates (Q ~0.5–2 m^3/s) produced a range of spine and whaleback features, most of which grew in a matter of days. Moderate effusion rates (Q ~2–7 m^3/s) produced shear lobes that were active for days to weeks to months. High effusion rates (Q ~7–9 m^3/s) produced pancake-shaped lava lobes with flat tops and scoriaceous surfaces. Very high effusion rates (Q >9 m^3/s) resulted in vulcanian explosions (Watts and others, 2002). Of particular interest are features that bear close similarity to current activity at Mount St. Helens, specifically vertical spines and megaspines that characterized magma emplacement at low volumetric effusion rates (<2 m^3/s; Watts and others, 2002).

Together these case studies present a consistent story of spine growth under conditions of slow magma effusion (typically <1–2 m^3/s). Descriptions of both smooth and striated spine surfaces are common; Watts and others (2002) inferred that these characteristic curved surfaces were controlled by shear faults (for example, Donnadieu and Merle, 1998) in magma made highly viscous by late-stage decompression-driven crystallization. As noted above, spine morphology generally has been interpreted to reflect extrusion of a solid lava plug, which probably solidified more as a consequence of decompression-induced crystallization than of cooling on the way to the surface. However, there has been no detailed characterization of these bounding-fault surfaces or comparison of striated surfaces with tectonic fault textures, and no attempt has been made to use either fault-surface characteristics or crystallization textures to constrain the conditions of magma ascent and decompression that create these volcanic spine features.

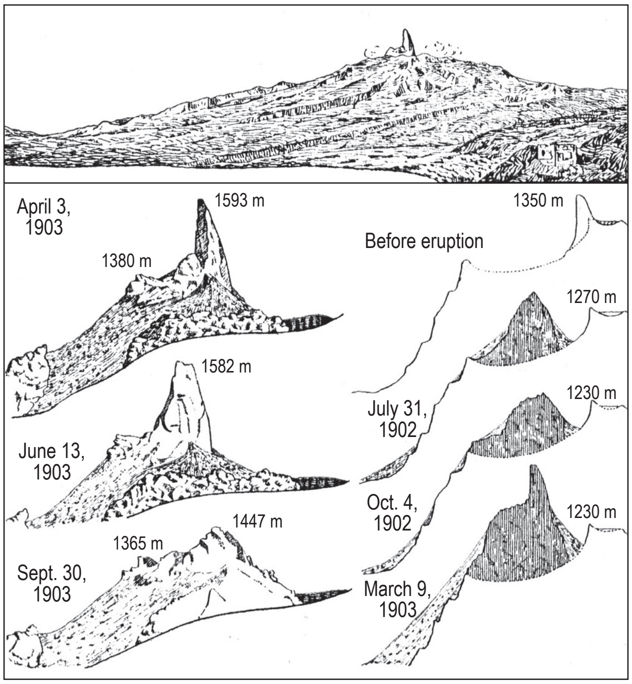

Figure 1. Sketches showing evolution of the great spine of Mont Pelée, Martinique, erupted in 1903. Note the difference between smooth, curved fault surface and rough, near-vertical face. From Williams (1932).

The Importance of Decompression-Driven Crystallization

During the early part of the 20th century, there was great debate about the solidification mechanism that could generate the large Mont Pelée spine. Lacroix (1904) favored rapid cooling of lava on exit from the vent. Gilbert (1904) suggested that solidification of the spine might result from "escape of gases and formation of bubbles" rather than loss of heat by conduction. Gilbert's concept was extended by Shepherd and Merwin (1927), who argued that gas pressures required to support the spine (~10 MPa) resulted from crystallization; they went on to suggest that these high gas pressures also caused the explosive generation of nuées ardentes that accompanied spine extrusion. Williams (1932) extended the concept of crystallization-induced gas pressurization to explain late-stage explosions at several other domes, an association that Newhall and Melson (1983) find in most historical eruptions.

Dome growth during the 1980–86 eruption of Mount St. Helens provided the first quantitative documentation of decompression-driven crystallization in silicic magmas (Cashman, 1992). Decompression-driven crystallization has since been documented during effusive and intermittent explosive phases of numerous recent eruptions (for example, Nakada and others, 1995b; Wolf and Eichelberger, 1997; Gardner and others, 1998; Nakada and Motomura, 1999; Hammer and others, 1999, 2000; Cashman and Blundy, 2000; Martel and others, 2000; Sparks and others, 2000; Metrich and others, 2001; Blundy and Cashman, 2005; Cashman and McConnell, 2005) and is generally considered to be the dominant solidification mechanism in slowly ascending hydrous magma of intermediate composition. Petrographic observations show that plagioclase is the most abundant shallow-crystallizing phase, a consequence of the profound effect of dissolved H_2O on its stability. Quartz (or some other silica phase) joins the crystallizing assemblage when the quartz-feldspar cotectic is intersected, which typically occurs at low pressures, and rapidly increases the total crystal abundance. Both the number and mode of plagioclase crystals vary with decompression path (effective undercooling; ΔT_{eff}).

Decompression experiments on H_2O-saturated melts (Geschwind and Rutherford, 1995; Hammer and Rutherford, 2002; Martel and Schmidt, 2003; Couch and others, 2003) show that plagioclase number density, size, and morphology are controlled by the rate of decompression and the final pressure of equilibration. The extent of crystallization is dependent on both equilibration pressure and experiment duration (Hammer and Rutherford, 2002; fig. 2). Crystallinity increases as equilibration pressure decreases and with increasing time at a given pressure. At low pressure (≤25 MPa), extensive crystallization requires time scales of several weeks. Crystal nucleation rates also are highest at pressures between 25 and 10 MPa, although nucleation diminishes in importance at very low pressure (≤5 MPa) owing to the high viscosity of silicic melts with low H_2O (Hess and Dingwell, 1996). Extensive co-precipitation of quartz and feldspar appears to require equilibration at very low pressure (5–10 MPa).

An additional consequence of extensive late-stage decompression-driven crystallization is the release of latent heat. Evidence of late-stage heating in slowly erupted dome lavas includes both Ti-zoning of magnetite, which increases calculated Fe-Ti oxide temperatures, and reverse zoning of orthopyroxene (Devine and others, 2003; Pallister and others, 2005). These signs of heating have been interpreted as evidence of basaltic input at depth (for example, Devine and others, 2003). However, a recent study of samples erupted from Mount St. Helens in the early 1980s shows a strong correlation between late-stage heating and shallow crystallization, suggesting instead that this is a signature of shallow release of latent heat (Blundy and others, 2006). Because numerical models of conduit-flow dynamics show that even small changes in magma temperature have a large effect on magma discharge rate and eruptive behavior (Melnik and Sparks, 2005), localized crystallization-related heating may be an important component of shallow eruption dynamics.

In summary, the morphology of extruded spines—their asymmetric shape, smooth fault-bounded surfaces, and often imposing height—is controlled by effusion conditions. Formation of these spine features requires that magma ascent is sufficiently slow to allow near-complete volatile exsolution, degassing, and groundmass crystallization within the conduit. Outstanding questions include the relative timing of groundmass crystallization and fault formation, the potential role of latent heating in shear localization, the strain accommodated along these fault surfaces, the deformation mechanisms by which

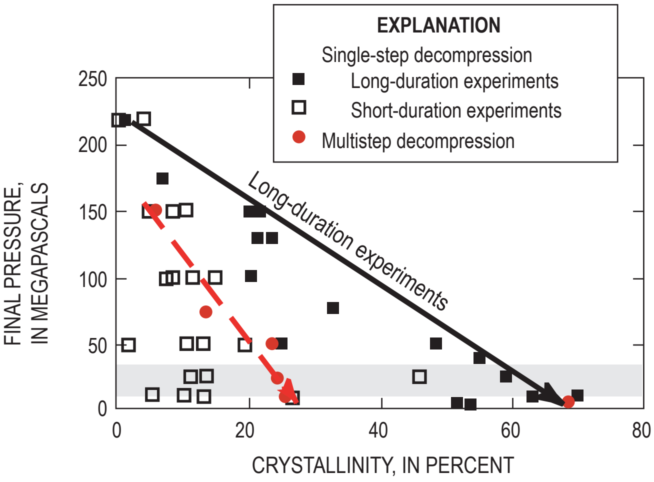

Figure 2. Relative effects of decompression time and equilibration pressure on crystallization of hydrous silicic melts. Single-step decompressions are followed by annealing at the final pressure; short-duration experiments, <30 hours; long-duration experiments, 168–931 hours. Multistep decompressions occur at constant rate of 1.2 MPa/hr. Data from Hammer and Rutherford (2002). Arrow shows equilibrium decompression-crystallization trend.

resulting fault gouge may affect plug extrusion, and the relation between observed seismic signals and spine emplacement.

Methods

Field observations and digital photography of the 2004–6 Mount St. Helens dome, made during two short ground-based sampling missions and numerous close-in helicopter flights, provide an outcrop-scale context for describing the character and origin of the gouge. Because of safety concerns, sampling of the dome and the dome carapace were accomplished primarily by helicopter dredging (Pallister and others, this volume, chap. 30). Although this remote technique did not allow detailed mapping of field relations, it did allow access to steep and unstable parts of the spines that could not have been reached on foot. The source areas for debris and talus samples are, in most cases, well constrained by field documentation. Moreover, both photographic and seismic records document the locations and timing of the specific rockfall events sampled. Finally, data collected during two days of field work in the summer of 2006 confirmed field relations inferred from remote techniques (Pallister and others, this volume, chap. 30). Distinct differences in sample lithology can be correlated with dome rock facies observed in the scree slopes on the dome flanks. A complete catalogue of sample information, including locations, brief descriptions, and bulk chemistry, is provided by Thornber and others (2008b).

All dome samples have been described and curated at the Cascades Volcano Observatory (Thornber and others, 2008b). Samples of unconsolidated fault gouge (SH303 and SH307) were processed in the Cascades Volcano Observatory Sediment Laboratory. Samples were dry sieved to 63 μm; size fractions <63 μm were analyzed using a Micrometrics Sedigraph III particle size analyzer. Additionally, both dome lava and fault gouge were characterized by petrographic analysis. Whole thin sections were scanned at high resolution for general textural characterization and quantitative analysis of plagioclase phenocryst and microphenocryst textures (that is, crystals >30 μm in diameter). Microscopic evaluation of sample textures was accomplished using a JSM-6300V scanning electron microscope at the University of Oregon. Thin sections were imaged in backscattered electron (BSE) mode using 10-kV accelerating voltage and 5-nA beam current. Both scanned and BSE digital images were processed and analyzed using Adobe Photoshop and ImageJ 1.34s (NIH Image for Mac OS X) software. Most techniques that were used are similar to those described elsewhere (for example, Cashman and McConnell, 2005); however, we also experimented with ways of analyzing the size distribution of clasts in the cataclasite for comparison with sieve data. Analysis of larger (>30 μm) dome fragments was performed on low magnification (20×) BSE images. Gray-scale thresholding of individual clasts provided binary images that could be easily processed to allow clast size analysis (fig. 3). All image-analysis data were then analyzed using Microsoft Excel.

Results

In this section we document processes related to spine extrusion. Because the observational record of spine extrusion is unique in the level of detail permitted by the sampling techniques, our primary goal is to provide comprehensive descriptions of textures produced as competent dacite lava is transformed into ultracataclastic fault gouge. We begin by reviewing details of field observations, followed by hand-specimen descriptions and thin-section observations. To describe the textural characteristics of fault rock samples, we follow Snoke and others (1998) in using the nomenclature conven-

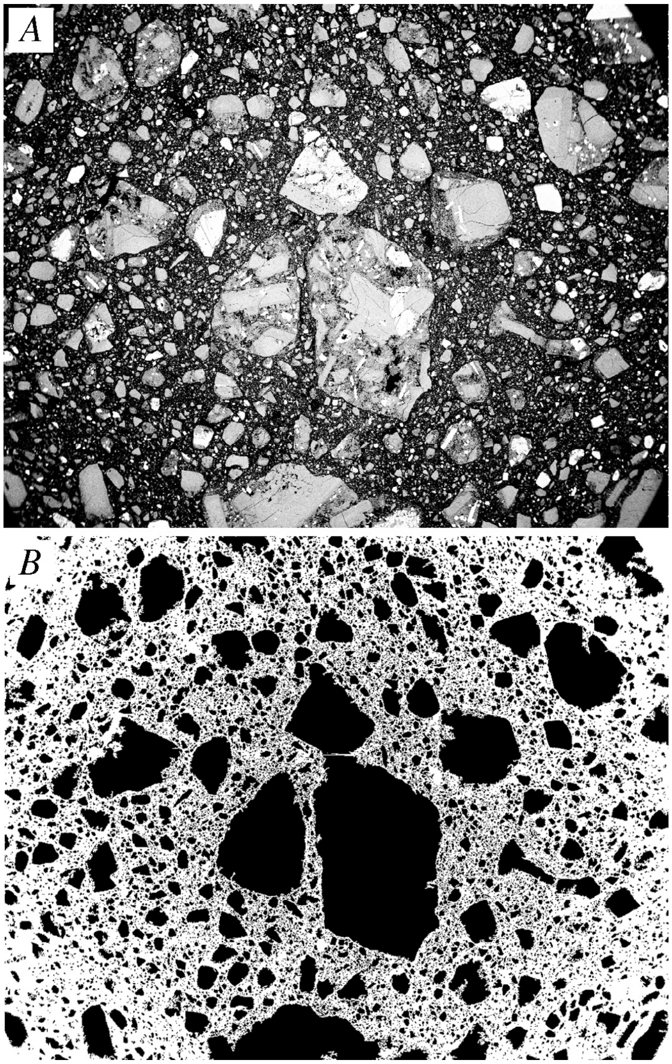

Figure 3. Examples from gouge sample SH326-2A illustrating the image-processing technique used to acquire grain-size data on cataclastic samples. Apparent circular concentration of very fine particles is an artifact of the image-acquisition technique; for this reason, only larger particles are used in final analysis. Images are 6.1 mm across. *A*, Backscattered electron image. *B*, Processed binary image.

tion of Sibson (1977), as modified by Scholz (1990), where "gouge" refers to noncohesive material with visible fragments constituting <30 percent (by volume) of the rock mass, in contrast to fault "breccia" that has >30 percent visible fragments. Although this naming convention would apply the term "cataclasite" to all cohesive brittle fault rocks, we distinguish cohesive breccia from cataclasite on the basis of apparent clast versus matrix support. Moreover, for simplicity we refer to the "gouge zone" when discussing the entire suite of cataclastic material that overlies massive dome dacite.

The View from the Field

The gouge carapace was first observed on November 7, 2004, on the surface of spine 3. At that time a large lava spine (300–400 m north-south by 50–150 m east-west) had been thrust to ~100 m above the surface of the already-uplifted glacier in the southeastern quadrant of the crater (figs. 4*A*, 4*B*). On the east face of the spine, a slope of gouge was exposed above a basal apron of wet, sandy debris containing angular lava blocks. The lower 10–20 m of the slope's exposed east face was composed of gouge that displayed prominent striations that plunged steeply east (parallel to the 45º slope of the spine) in exposures along the southeast face and more northerly along the northeast face. Along both faces a resistant surface layer was underlain by ≤1 m of white, powdery gouge (sample SH303) that was slightly warm to the touch (~30°C), dry, and friable. Sparse rock fragments within the gouge accumulated fine-grained material on their downslope sides, producing features akin to pressure shadows (Pabst, 1931) with a preserved sense of shear that was consistent with uplift of the spine core relative to marginal rocks (fig. 4*B*). Several curvilinear bands of discolored gouge and trails of embedded lithic fragments ("bathtub rings"; figs. 4*A*, 4*B*) paralleled the contact between the gouge and the debris apron at the base of the spine, recording earlier positions of this basal contact that shifted upward with growth. Disintegration of the south face of spine 3 (figs. 4*C*, 4*D*) allowed sampling of the (still hot) spine interior by helicopter dredging. The dominant rock type is dense hornblende-hypersthene-plagioclase-phyric dacite with a microcrystalline groundmass (SH304; Pallister and others, this volume, chap. 30).

The detailed descriptions of spine 3 provided above can be generalized to all other spines. A narrow band of mantling gouge typically forms an intact annulus at the vent margin (fig. 5*A*). Thermal data from a Forward-Looking Infrared Radiometer (FLIR) indicate temperatures of 100–200°C at this margin but show that the gouge surface cools to near ambient temperatures after about 10 m of uplift. A FLIR temperature maxima of 730°C (Schneider and others, this volume, chap. 17) indicates that temperatures remain high in the spine interior (within a few meters of the surface). Throughout the 2004–6 eruption, the thickness of the gouge zone has ranged from 1 to 3 m, always with surface striations oriented parallel to transport (fig. 5*B*). Most commonly, dense flow-banded dacite is abruptly overlain by 1–2 m of reddish cataclasite, which is overlain by poorly consolidated white to tan powdery gouge (fig. 5*C*). Occurring less frequently are examples of foliated gouge with parallel striations on the surface that form a penetrative shear foliation (fig. 5*D*). Samples of foliated gouge show multiple subparallel slickensides that indicate slight variations in slip direction at different depths. In some outcrops, a capping resistant (and striated) surface layer protects the unconsolidated gouge that, at times, posed challenges to sampling efforts. On one occasion, a 75-kg dredge was dragged along the surface of spine 4 without penetrating this surface layer. Bulk chemical analyses of gouge samples show that early gouge included a substantial fraction of older material from the conduit margin, whereas later gouge samples are mostly juvenile dacite (Rowe and others, this volume, chap. 29).

An unusual, well-exposed section of the lava-to-gouge boundary within a graben that formed in spine 4 was photographed in December 2005, more than a year after spine extrusion (fig. 6). Exposed cross sections of the gouge-lava contact showed both breccia and pink (altered) cataclasite separating massive flow-banded dacite from overlying powdery gouge. The abrupt contact between massive dacite and the overlying cataclasite indicates that this is an important mechanical boundary. The progression from breccia to gouge was well displayed, with blocks of intact dacite sheared from the underlying lava and progressively fragmented to produce breccia, cataclasite, and gouge. The sense of brittle shear derived from the inclination of shear surfaces within the breccia is consistent with upward transport from the vent. Photographic interpretations were confirmed by field observations made in the summer of 2006. The observations showed that the gouge formed over a vertical distance of 1–2 m by shear between the upward-thrusting dacite within the conduit and the conduit margins. Reidel shears within the cataclasite provide further evidence of brittle shear failure (Pallister and others, 2006).

Hand Samples

Rock samples collected from the talus of the growing 2004–6 Mount St. Helens dacite dome include both competent dacite (igneous rock) and a variety of fault rocks (cataclasite). Detailed descriptions of all samples can be found in Thornber and others (2008b). Here we briefly describe the varieties of pristine dome dacite before describing the range of fault rocks. Dacite samples vary in color from light gray to reddish or pink (a term used in deference to the first unequivocally juvenile samples of "hot pink" dacite SH304). The reddish alteration results from oxidation that is localized around hornblende, oxide, and hypersthene phenocrysts and does not noticeably affect the otherwise igneous fabric of the rocks.

In hand sample, the igneous facies of dome rocks may be broadly classified as (1) dense, light-gray (to pink) dacite, (2) flow-banded gray (to pink) dacite, or (3) vesicular dark-gray (to pink) dacite. Most samples also contain 1–5 volume percent of coarse-grained hornblende-gabbronorite xenoliths that are similar in abundance and character to those in 1980 to 1986 eruption products (Heliker, 1995). Lithic inclusions of dacite, andesite, and amphibolite are less abundant and typically of smaller size.

Dense light-gray dacite samples dominate the dome talus suite. Because these samples are both angular and dense (porosities <10 percent), and because several of these samples were dredged from collapsed faces of the spines, we infer that they are derived primarily from the dome interior. Flow fabric within the dome facies is not well developed and is indicated only by (1) alignment of acicular hornblende phenocrysts in some samples and (2) entrainment patterns of xenolithic fragments and vesicular pockets around them. Rare flow-banded dacite samples have distinctly light-colored or reddish bands (ranging from less than 10 to 20 mm in width) that are subparallel to foliation evident in dense, dacite host rock. Bands lack evidence of granular flow or other forms of brittle deformation and instead are characterized by high vesicularity relative to the host rock.

Vesicular dacite samples have 25–40 percent porosity and range in color from dark gray to red. In some vesicular samples, igneous flow is evidenced by fanned vesicle-distribution patterns and corresponding flow alignment of xenolith fragments and feldspar megacrysts. Proximity of the most

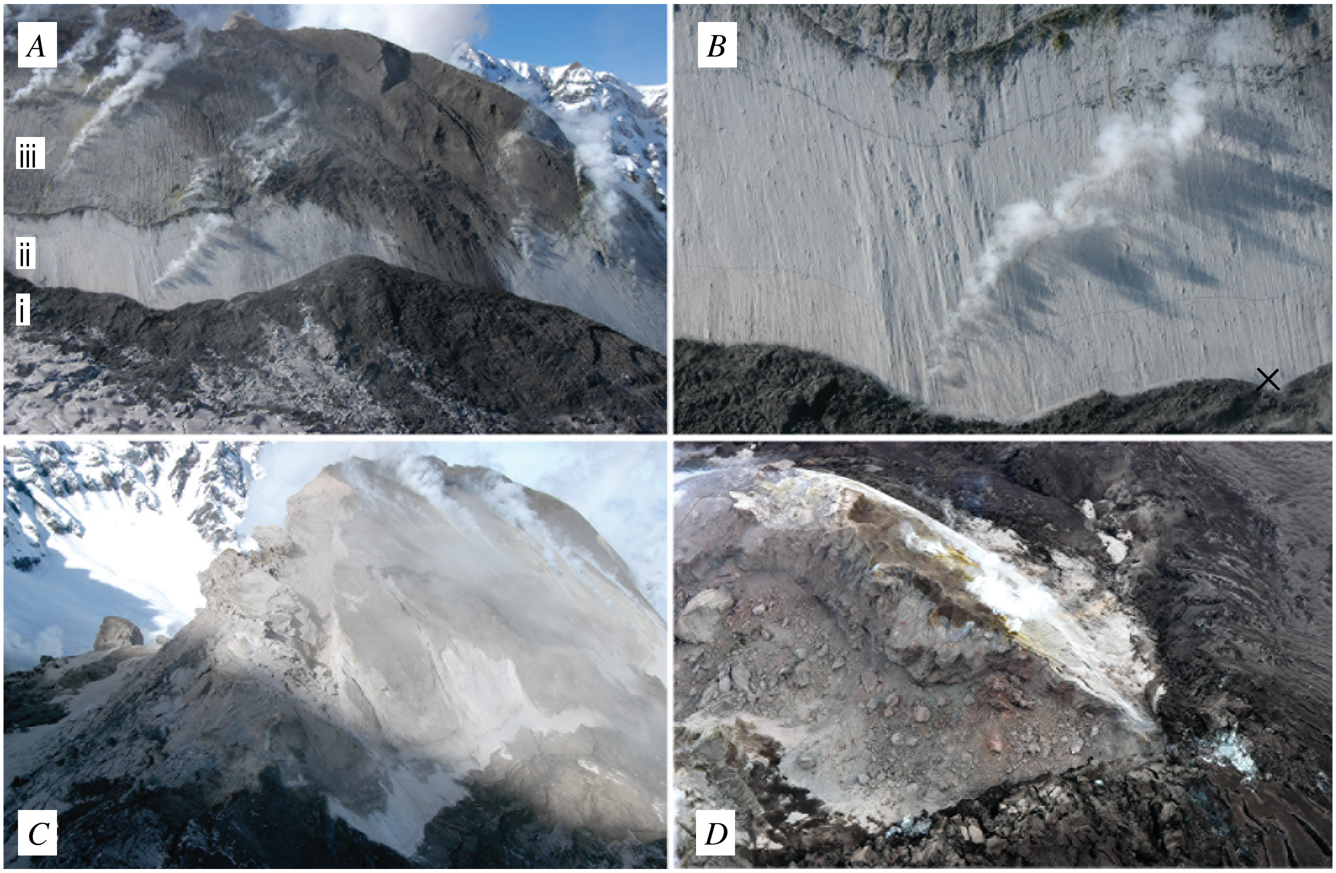

Figure 4. Spine 3 in early to mid-November 2004. USGS photographs by J.S. Pallister. *A*, West-looking view on November 4 showing, from the base upward: (i) an apron of sandy debris, snow, and glacial ice; (ii) 10–15-m-high wall of white slickenside-bearing gouge with "bathtub rings" that mark former contact levels between gouge surface and debris apron; (iii) dark tan (weathered) gouge or cataclasite with steeply dipping erosional furrows. Blocky outcrops (uppermost spine rough-weathering area near center-frame) are uplifted material from the debris apron. Steam is venting from fractures in gouge carapace. *B*, Close-up photograph on November 4 of gouge outcrop showing slickensides and "bathtub" rings that parallel contact between the gouge and the debris apron. Note shadows on the downslope sides of rock fragments within the gouge that suggest upward and westward movement of the spine relative to the debris fan. Sample SH303-1 was collected from the white powdery gouge at site marked by X, about 1 m above the debris apron 10 m north (right) of the prominent steam vent. *C*, Oblique aerial photograph on November 4 of the southeast collapsed terminus of spine 3 showing blocky outcrops of dense dacite of the spine interior. View to the north-northwest. *D*, Photograph on November 10 of the southwest face and south terminus of spine 3 with a dark (ash covered) "bulldozed" glacier on right. White gouge carapace is visible above the blocky interior of the collapsing southwest face; powdery gouge eroded from the carapace has been deposited on the debris apron on the east flank of the spine. View is to the northeast.

vesicular, glassy, and reddish dacite to the outer dome margins is inferred from in-place sampling (SH305-1; fig. 7) and is documented in the exposed cross sections of collapsed spines. Helium-pycnometer measurements of SH305-1 yield a He-accessible porosity of 30.4 percent, nearly identical to the 30.3 percent porosity determined from the measured bulk density of 1,829 kg/m^3 and measured solid density of 2,627 kg/m^3. The similarity of the connected and bulk porosity indicates that the pores are fully connected and, therefore, might allow permeable flow of gas upward along the margin of the conduit. Preliminary permeability measurements of the same samples yield permeabilities of 8–9×10^{-13} m^2, confirming the possible ease of gas flow through the more vesicular dome lavas.

Both abrupt and gradational changes from competent dacite to finely powdered gouge are found within the sample suite. Some fractured and foliated dacite samples reveal a subtle gradation between vesicular dacite and marginal granular gouge. For example, samples from 2–5 m below surface gouge collected in the SH309 dredge along the southern end of spine 4 are somewhat altered and show moderate crushing and compaction associated with postsolidification shearing. Cataclastic rocks are distinguished by visible frag-

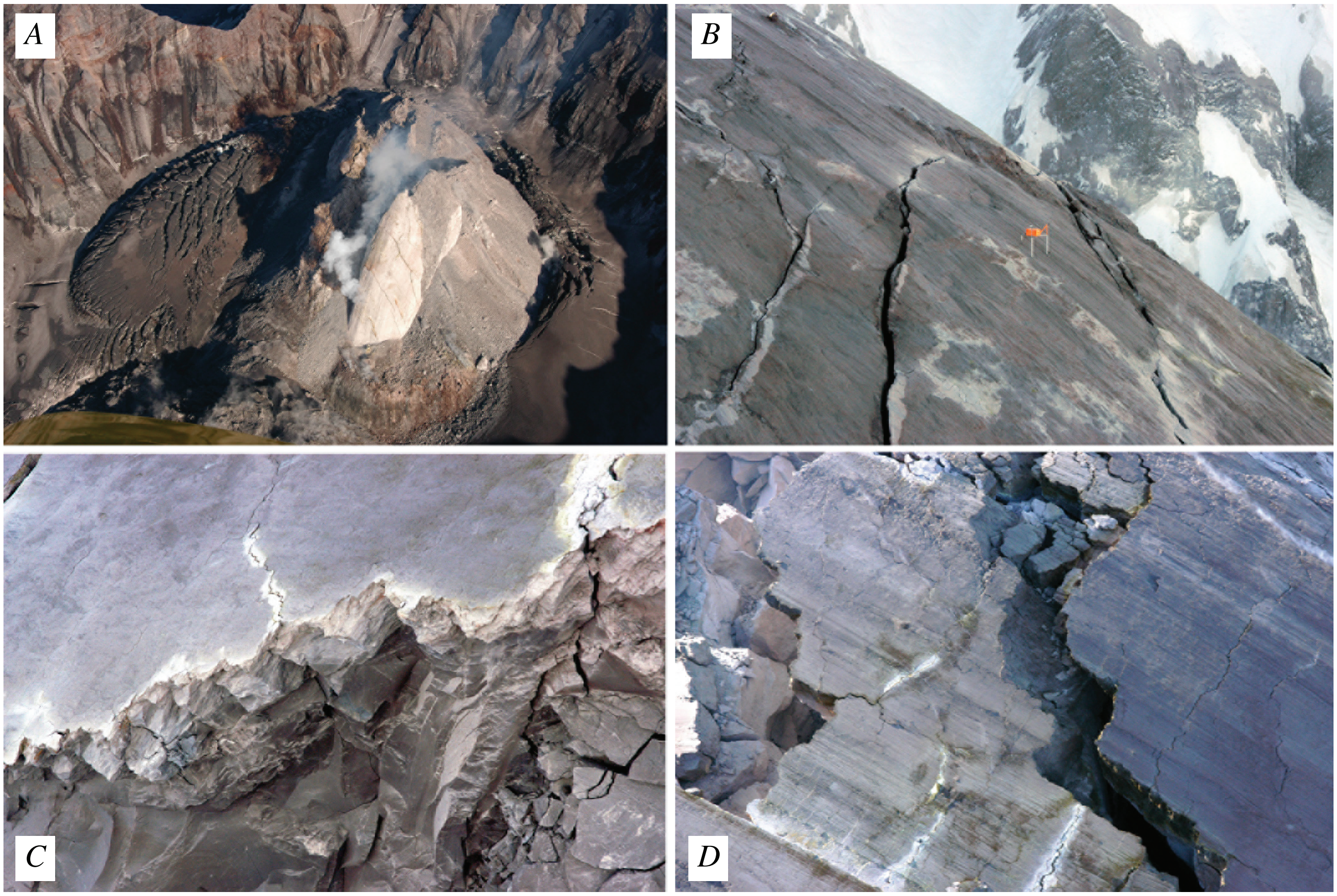

Figure 5. Features of the new lava dome. USGS photos by J.S. Pallister. *A*, Oblique aerial photograph of crater and 2004–2005 lava dome taken from the northwest on June 29, 2005. Spine 3 is in a shadow on left; spine 4 is in the center (highly fractured and altered); and spine 5 is on the right, with white, striated gouge carapace on the north and west flanks, collapse scar on northwest face, and sharp, arcuate contact between hot, powdery gouge and talus marking the periphery of the vent. Crevassed and brown, ash-covered Crater Glacier surrounds the dome. The following three photos were taken on January 14, 2005. *B*, Striated surface of spine 4; direction of transport is from lower right to upper left. Orange box on instrument package at center of frame is 1 m long. *C*, Contacts between gouge (gray, weathered surface lacking distinct striations), underlying cataclastic breccia, and dense dacite exposed on the collapsed south face of spine 4. Note flow foliation in lower right of photograph and in some outcrops immediately below the gouge. Dacite lava is overlain abruptly by pink to yellow consolidated gouge, which in turn is mantled by powdery white to gray gouge. Preserved thickness of gouge zone above contact is 1–2 m, although original thickness was greater. *D*, Parallel striations on surface of spine 4; transport direction from lower right to upper left. Surface striations mark penetrative fabric that creates planar shear lamination of the cataclasite. Block of dacite collected from the interior of nearby spine 4 is flow foliated and displays a strong lineation of elongate amphiboles.

ments of dome lava suspended within a finer grained matrix (figs. 8*A*, 8*B*) and range from well consolidated to friable and from coarse to fine grained. Both the size and abundance of macroscopic lava fragments decrease toward the outer surface of fine-grained noncohesive gouge. Friable and foliated gouge from spine 4 (SH313-1) shows pronounced slickensides forming subparallel striations that permeate the loosely consolidated sample (fig. 8*C*). Powdery fault gouge is light in color and unconsolidated.

Samples in Thin Section

The petrography and petrology of dacite lava dome samples are described by Pallister and others (this volume, chap. 30) and will be reviewed only briefly here. The dacite lava has a uniform bulk composition (65 wt. percent SiO_2) and is highly crystalline, having 41–45 percent phenocrysts and microphenocrysts of plagioclase, hypersthene, amphiboles, and Fe-Ti oxides set in a microcrystalline matrix (fig. 9*A*). Iron-titanium oxide temperatures in early samples are 840–850°C; apparent temperatures increase in later samples in response to latent heat produced by extensive shallow crystallization (for example, Blundy and others, 2006).

Thin sections provide important insight into fine-scale cataclasis of competent dome lava. An unusual sample (SH324-4A) preserves an abrupt boundary between coherent dome lava and highly fragmented fault gouge. In thin section, the boundary between gouge and coherent lava is marked by thin, oxidized bands that are subparallel to the boundary (fig. 9*B*). Approximately parallel to these bands, more subtle variations in matrix density mark a throughgoing shear fabric within the boundary zone. More common are samples of cataclasite that are characterized by rounded fragments of dome lava within a finer grained matrix (SH326; fig. 9*C*). In thin section, dome fragments typically range in size from greater than 10 mm to less than 0.1 mm. The matrix comprises primarily shattered phenocrysts, although pieces of holocrystalline groundmass can also be identified. In friable, foliated gouge samples with obvious slickensides, the grain-size reduction vis-

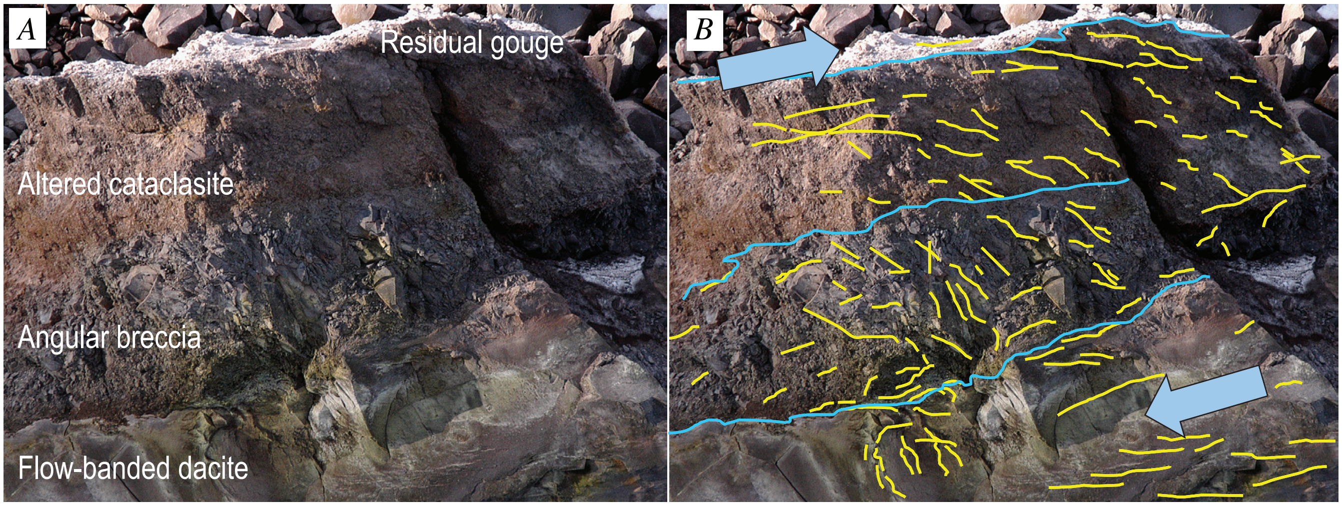

Figure 6. Dome-breccia relations. USGS photo by J.S. Pallister, December 15, 2005. *A*, Erosional remnant atop spine 4 preserves a breccia interval between massive to flow-banded dacite lava at base of outcrop and a thin surface layer of white powdery gouge. Brittle fractures (Reidel shears) are present in breccia and cataclasite. *B*, Trend lines indicate shear couple with basal dacite moving left (away from vent) relative to the upper (external) part of outcrop, consistent with shear between the dacite and the conduit wall during extrusion. Height of outcrop is approximately 3 m.

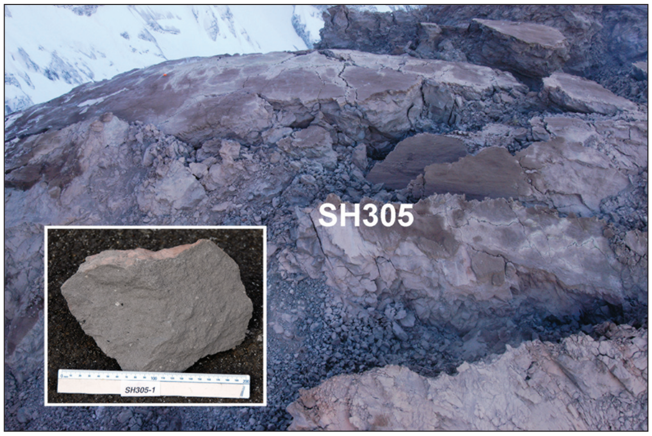

Figure 7. Outcrop and hand-specimen photographs of sample SH305, collected January 3, 2005, from spine 3.

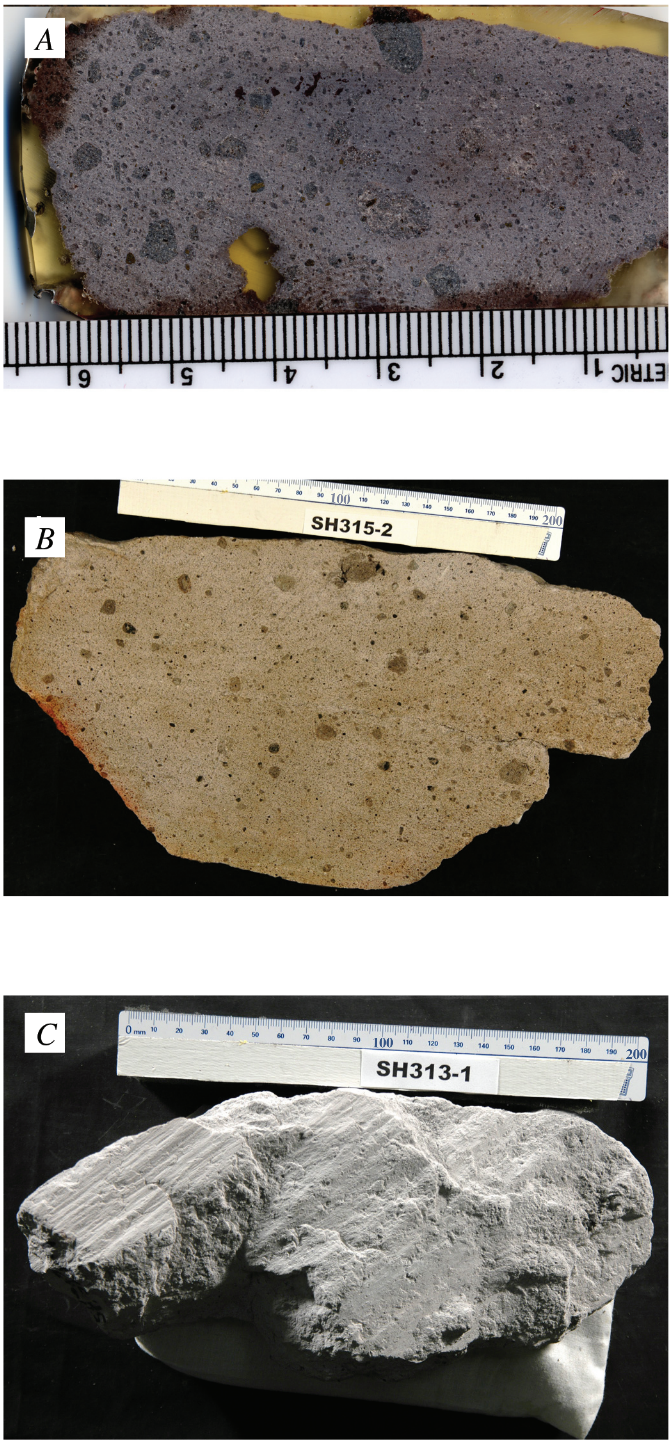

Figure 8. Hand specimen and cut chips showing textural gradation from cataclasite to intensely comminuted fault gouge. *A*, Lithified breccia sample SH326-2A (spine 7); Scale in centimeters. *B*, cataclasite sample SH315-2 (spine 4); Scale in millimeters. *C*, striated gouge sample SH313-1 (spine 4). Scale in millimeters.

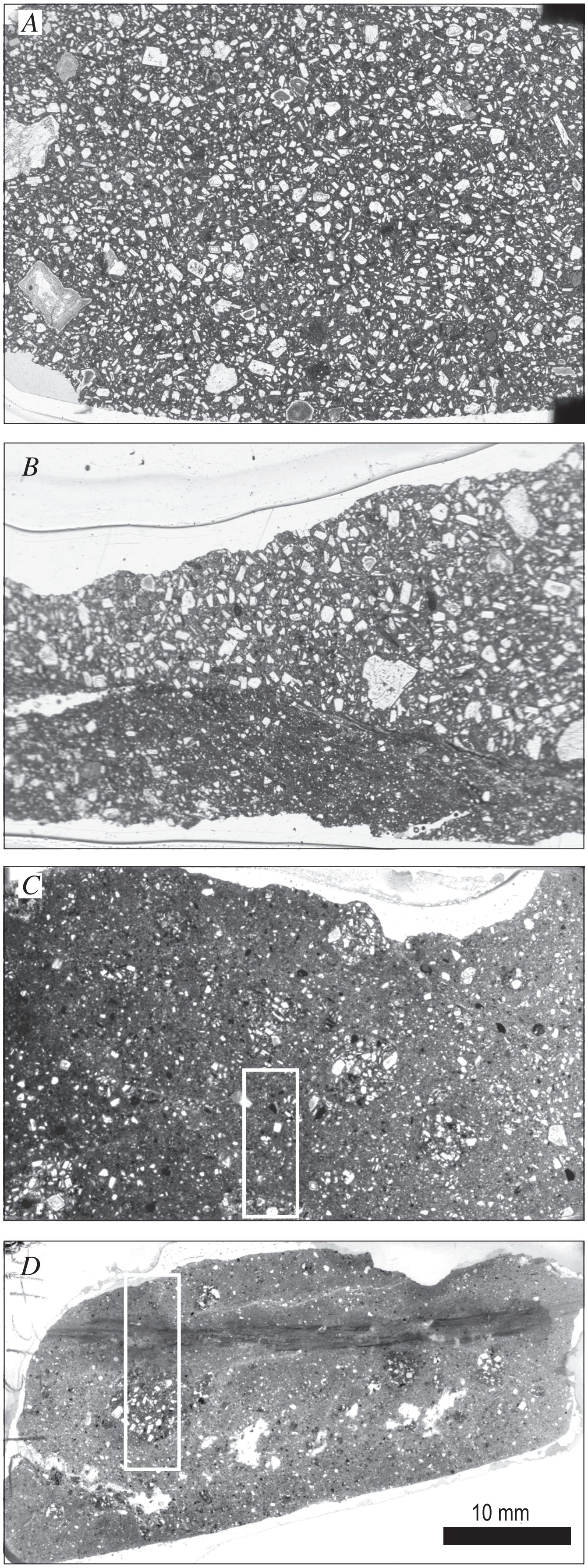

ible in thin section is extreme (SH313-1; fig. 9*D*), with typical cataclasite (fig. 9*C*) cut by an extraordinarily fine-grained, foliated shear zone (an ultracataclasite, with grain size <1 µm). Other thin sections of the same gouge sample show anastomosing branches of foliated ultracataclasite that isolate areas of coarser cataclasite.

Backscattered Electron Imaging Observations

Field, hand-specimen, and thin-section observations of dome and gouge samples indicate that competent (and flow-banded) dome lava achieved threshold conditions for wholesale fragmentation, cataclastic flow, and strain localization to accommodate the large strains achieved during spine emplacement. Backscattered electron (BSE) imaging provides additional textural evidence for (1) the crystallization history of the dome magma that may have led to fragmentation, (2) fragmentation mechanisms, and (3) cataclastic flow.

Detailed characterization of phenocryst textures and composition is provided elsewhere in this volume (Pallister and others, chap. 30; Rutherford and Devine, chap. 31; Streck and others, chap. 34), so we limit our descriptions of phenocrysts to characteristics that may help to constrain shallow conduit processes. A striking feature of virtually all samples we have imaged is the presence of some plagioclase phenocrysts (>100 µm) with irregular margins on one or more growth faces that indicate rapid late-stage rim growth (fig. 10). In contrast, microphenocrysts (30–100 µm) typically are euhedral and prismatic. Phenocryst rim-growth irregularities range from a few to several tens of microns in width (fig. 10*A*) and include either multiple (fig. 10*B*) or single (fig. 10*C*) growth zones. In some samples, irregular growth protrusions partially entrap small pockets of groundmass glass that are substantially less crystalline and less vesicular than adjacent matrix (fig. 10*C*). The combined observations of rapid rim growth in both early-erupted (fast) and late-erupted (slow) dome lavas and clean glass preserved within the growth irregularities suggest that these features reflect relatively fast magma ascent (and overstepping of the plagioclase liquidus) at deeper levels in the conduit system. The prevalence of growth irregularities in large (and often outsized) phenocrysts further suggests that these crystals may have a unique decompression history.

Although the groundmass of all samples is highly crystalline, groundmass textures are variable. At one extreme are juvenile samples, collected by dredge in early November 2004 (SH304), that include several unusually glassy clasts. One such clast has only pyroxene and oxides as groundmass phases

◀ **Figure 9.** Full thin-section scans of samples showing transition from competent dome lava to highly comminuted fault gouge. Scale bar in *D* applies to all four panels. *A*, Sample SH316, from spine 5. *B*, Sample SH324-4A, from spine 7. *C*, Sample SH326-2A, from spine 7; box shows transect illustrated in figure 14*A*. *D*, Sample SH313-1C, from spine 4; box shows transect illustrated in figure 16*A*.

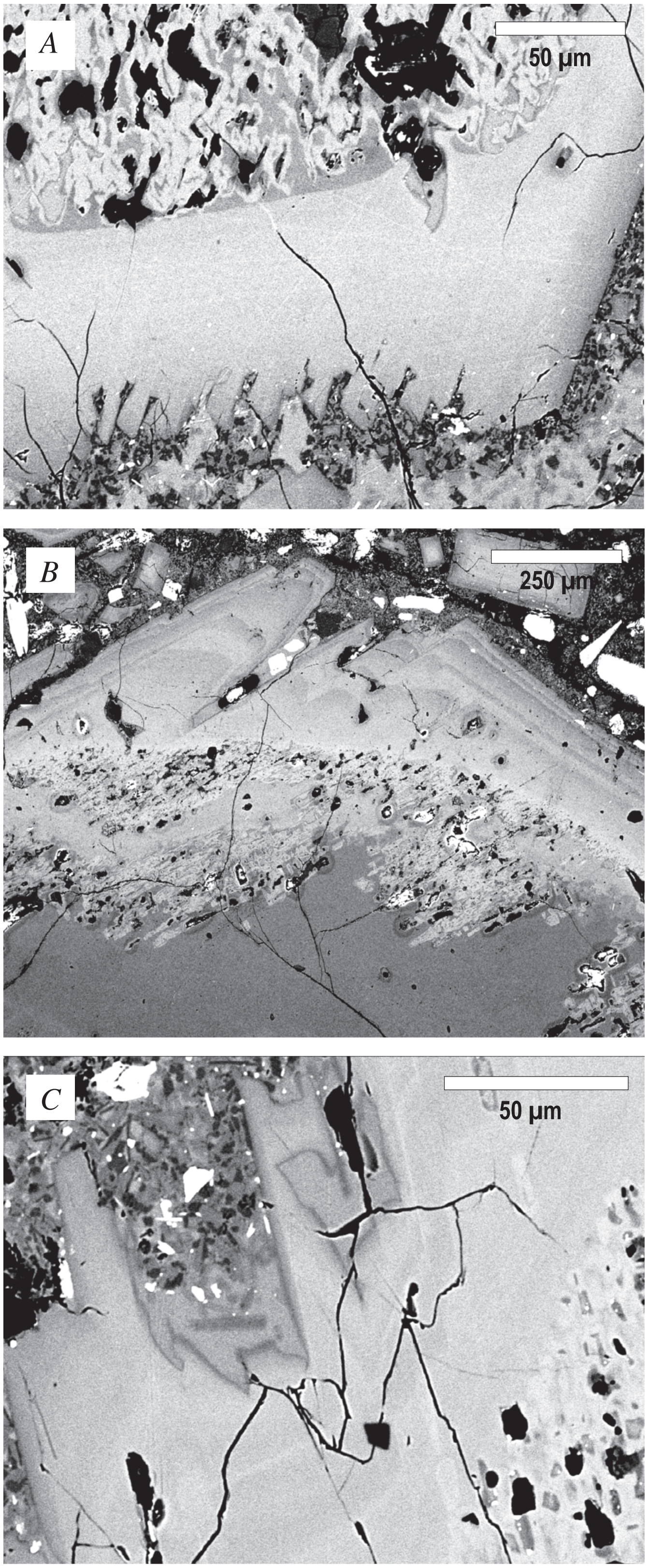

Figure 10. Plagioclase phenocryst textures indicative of rapid growth. *A*, Sample SH316. *B*, Sample SH315-2. *C*, Sample SH309-1.

and preserves ~ 2 weight percent H_2O in the groundmass glass (Pallister and others, this volume, chap. 30). Another sample (SH304-2G3; figs. 11*A*, 11*B*) has a groundmass composed primarily of feldspar microlites (<20 µm in length) with only minor pyroxene, oxides, and quartz. This sample is unusual in having abundant clean glass (~25 percent) and only minimal precipitation of silica phases. Many of the larger plagioclase microlites in this sample have swallowtail terminations that suggest rapid growth (for example, Hammer and Rutherford, 2002). High crystal number densities (~10^7/mm^3) preserved in this sample would suggest that most of the growth was both shallow (<25 MPa; see compilation in Cashman and McConnell, 2005) and rapid. These pressure estimates are roughly consistent with the ~30 MPa indicated by preserved H_2O contents of some other SH304 clasts, confirming that glassy SH304 samples appear to have been quenched at depths of ~1 km (for example, Pallister and others, this volume, chap. 30). More typical of early-erupted samples is SH305-1, from spine 3, emplaced in late November 2004 (for example, fig. 7). Sample SH305-1 is distinct from SH304-2G3 because it has less-numerous, but somewhat more-euhedral, plagioclase microlites in a groundmass mottled with 30–40-µm patches of cotectic feldspar and quartz crystallization, intergrowths that commonly nucleate along plagioclase phenocryst and microphenocryst boundaries and then grow into the melt (figs. 11*C*, 11*D*). Disequilibrium crystallization is a common feature of natural and experimental melts decompressed slowly to shallow levels (Hammer and Rutherford, 2002; Martel and Schmidt, 2003), the result of delayed quartz nucleation in these highly silicic melts (Cashman and Blundy, 2000; Blundy and Cashman, 2001). Quartz may have nucleated more easily along euhedral crystal margins if a thin, slightly SiO_2-enriched, boundary layer helped to overcome the activation energy required for quartz nucleation in the rhyolitic liquid.

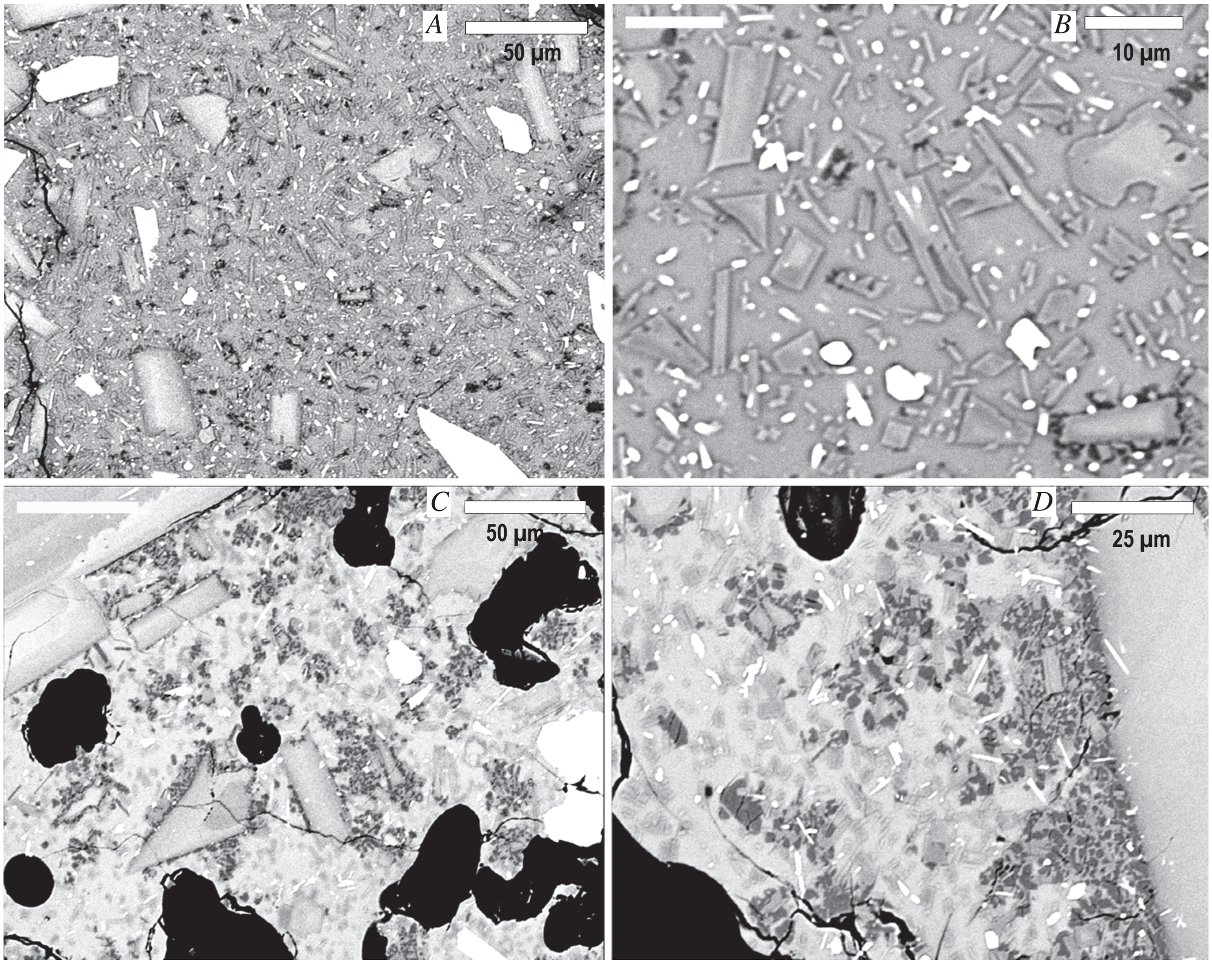

Figure 11. Backscattered electron images of groundmass textures from early-erupted samples (spine 3). *A*, Sample SH304-2G3 showing relatively high glass content and dominance of plagioclase microlites (medium- to light-gray crystals). *B*, Highly magnified view. *C*, Sample SH305-1 showing patchy development of cotectic quartz-feldspar intergrowths (blotchy dark-gray regions) with apparent nucleation on phenocryst margins. *D*, Highly magnified view.

By April 2005, the rate of dome extrusion had diminished and groundmass textures were correspondingly more crystalline. Dome dacite sample SH316 (from spine 5; fig. 9*A*) has a highly crystalline groundmass with abundant plagioclase crystals and patchy cotectic intergrowths of plagioclase and quartz (fig. 12*A*). Also apparent in the groundmass of SH316 are larger (~50 µm in length) acicular (platy in three dimensions) silica-phase crystals that appear to be a form of cristobalite (fig. 12*A*). Other samples, such as SH309, show abundant tridymite as a groundmass phase (figs. 12*B*, 12*C*), a feature that was also observed by Blundy and Cashman (2001) in some samples from the continuous growth phase of the 1983 Mount St. Helens dome. The long axes of tridymite crystals (fig. 12*B*) are aligned locally, recording late-stage deformation.

Backscattered electron imaging also provides a spectacular record of gouge development. As described above, dome dacite samples (fig. 13*A*) show little sign of deformation associated with magma ascent and extrusion, except for some samples with pronounced flow banding. Brittle breakage associated with flow is manifested first as throughgoing fractures, particularly along phenocryst boundaries (fig. 13*B*). Cataclasite sample SH326-2A shows more extensive evidence of crushing. Thin sections illustrate the textural heterogeneity of SH326-2A, with small (≤10 mm in diameter) dome lava clasts distributed randomly in a matrix of smaller clasts, individual crystals, and pulverized matrix (fig. 9*C*). Backscattered electron images show that the matrix itself contains a continuous range of fragment sizes, from intact lava clasts greater than 1 mm to tiny fragments smaller than 1 µm (fig. 14*A*), where

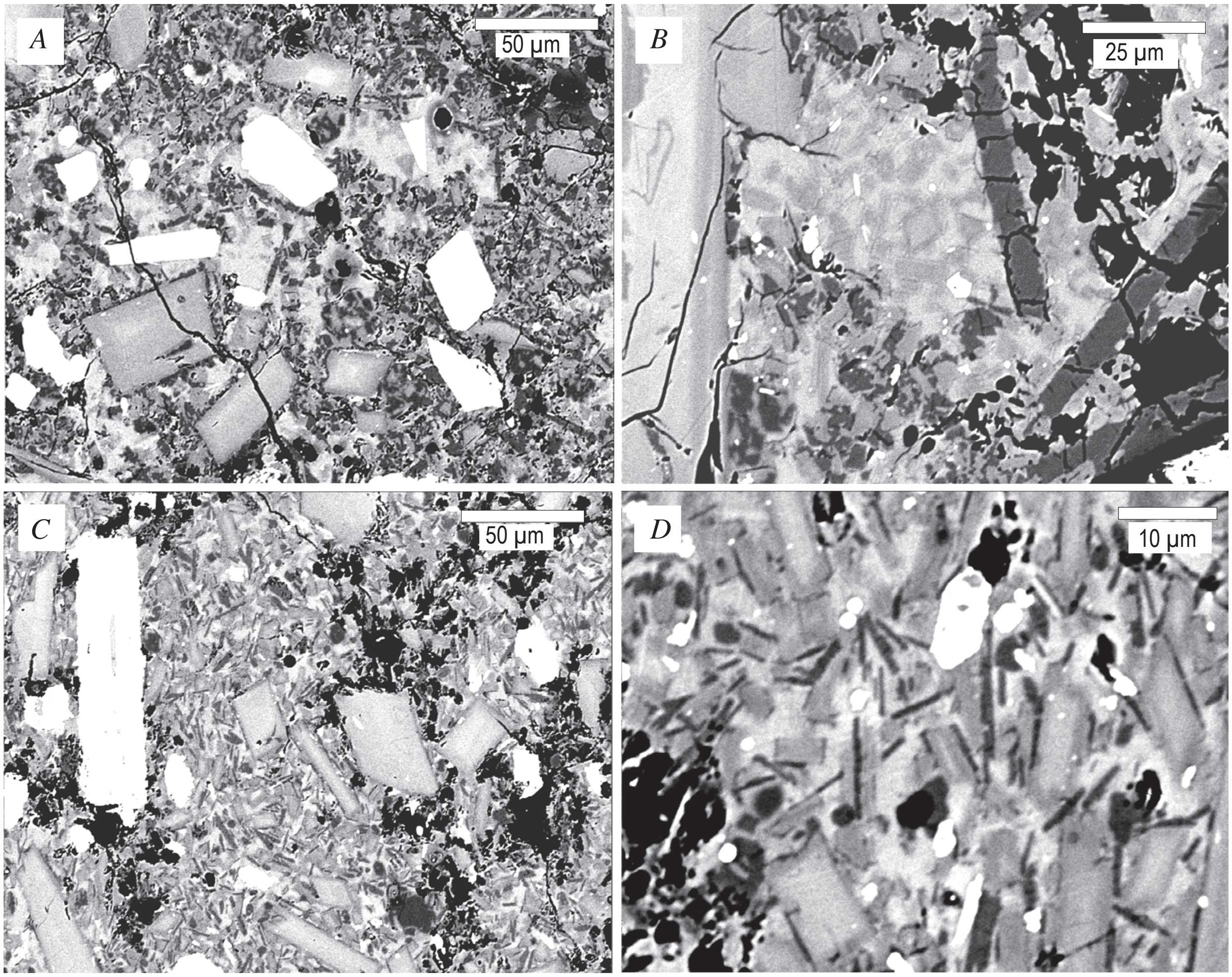

Figure 12. BSE images of groundmass textures from later-erupted samples. *A*, SH316 (spine 5) showing near-holocrystalline nature of groundmass. Dark-gray phase is quartz, medium-gray phase is plagioclase, light-gray phase is quenched glass, and white phases are mafic minerals. *B*, High-magnification view of SH316 groundmass showing high number density of plagioclase microlites in remnant, clean glass patches. *C*, SH309 (spine 4) showing unusual abundance of acicular aligned tridymite crystals in the groundmass. *D*, high magnification view of SH309 groundmass showing the intergrowths of plagioclase and tridymite (dark gray) and remnant patches of clean glass.

crude banding is suggested by regions of higher and lower fragment concentrations.

All samples of cataclasite and gouge show nearly complete groundmass crystallization; groundmass textures preserved within individual clasts are similar to the more crystalline parts of dome-lava groundmass. Larger fragments within the gouge typically are cored by plagioclase phenocrysts enclosed in holocrystalline (and microvesicular) groundmass (figs. 14*B*, 14*C*), although clasts composed entirely of microphenocrysts and microvesicular, holocrystalline groundmass are not uncommon. Commonly, the outer margin of clasts is distinctly rounded and is surrounded by very fine grained fragments, features that suggest extensive grinding, abrasion, and even rolling during transport.

Textural transitions from dome lava to gouge to ultracataclasite can be observed in more detail in samples SH324-4A (fig. 9*B*) and SH313-1 (fig. 9*D*). In SH324-4A (fig. 15), the pronounced boundary between dome lava and gouge seen in thin section marks an abrupt change from intact, holocrystalline, igneous groundmass to fragmented and disseminated matrix plus crystals and crystal fragments (fig. 15*A*). In detail, the boundary is composed of thin (~100 μm) slivers of intact holocrystalline groundmass separated by bands of loose crystal and groundmass fragments (fig. 15*B*). In figure 15*B*, the shear-zone margin shows a single plagioclase crystal in the process of being shattered, providing the source of the aligned crystal fragments seen in figure 15*D*. Patterns of fracture may provide a sense of shear, as in figure 15*C*, where conjugate fracture sets propagate through a dome lava fragment containing both crystals and holocrystalline groundmass.

A traverse across foliated gouge sample SH313-1 (figs. 8*C*, 9*D*) shows more spectacular grain-size variation (fig. 16*A*). Much of the thin section is similar to cataclasite sample SH326 (fig. 14), with intact clasts of dome lava suspended in a fine-grained matrix. However, as shown in BSE imagery, the narrow (≤1 mm) fault zone visible in thin section (fig. 9*D*) is composed of alternating bands (~100 μm wide) of fine-grained (tens of micrometers) and extremely fine grained (<1 μm) material (figs. 16*B*, 16*C*). By analogy with features observed in SH324-4A (fig. 15), we infer that banding develops by incorporation of shattered crystals (fig. 15*B*) and dome fragments

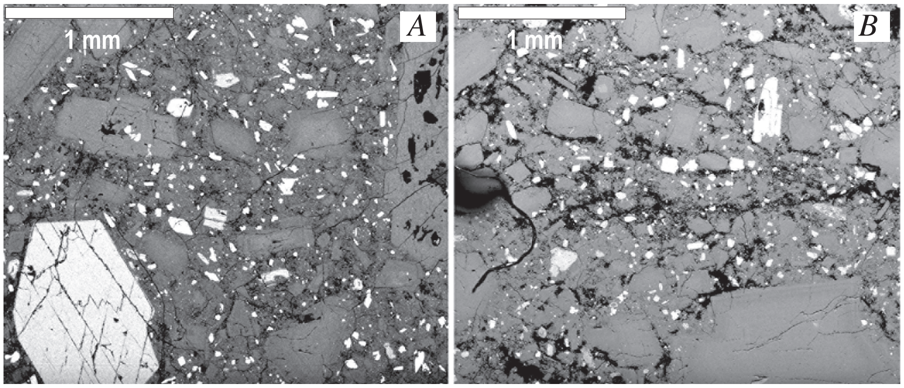

Figure 13. Low-magnification BSE images of two spine 4 samples. *A*, Competent dacite sample SH308-3A. *B*, partially fragmented sample SH309-1C. Note extensive fracturing (black areas indicate void space).

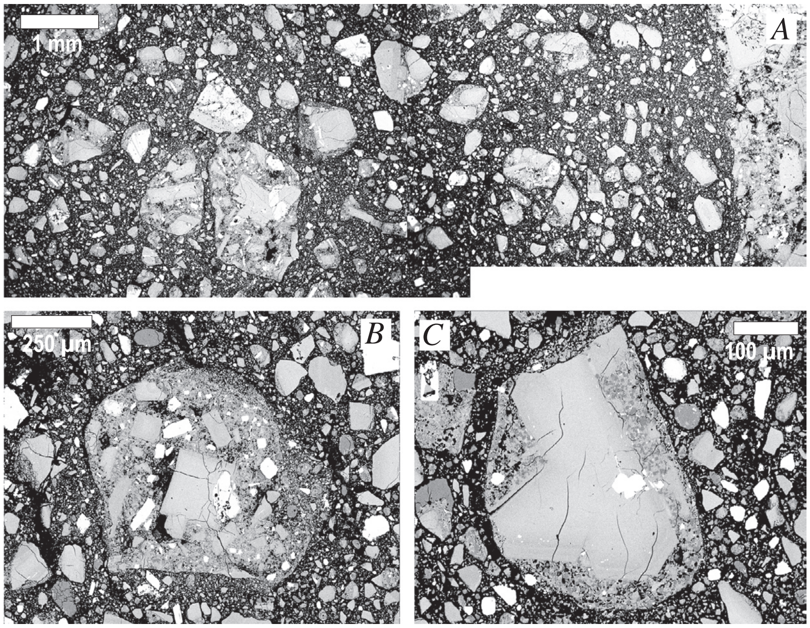

Figure 14. Backscattered electron images of fault gouge textures preserved in sample SH326-2A (spine 7; see fig. 9*C* for smaller-scale view). *A*, Composite transect illustrating textures characteristic of cataclasite samples. *B*, *C*, Typical gouge fragments composed of individual phenocrysts or broken dome matrix surrounded by holocrystalline matrix. Typically clasts are rounded and are surrounded by a halo of finely pulverized material.

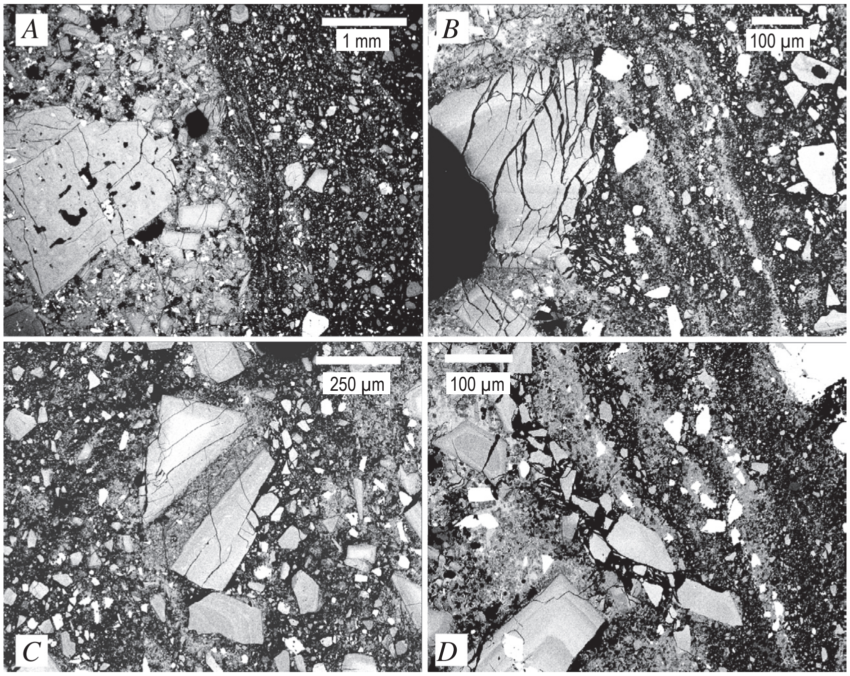

Figure 15. Backscattered electron images showing details of the lava-cataclasite boundary preserved in sample SH324-4A, from spine 7 (see fig. 9*B* for smaller-scale view of boundary). *A*, Low-magnification image across the boundary showing coherent dacite on left and cataclasite on right. *B*, Highly magnified view of boundary (from upper center of *A*) showing extensive fragmentation of a crystal next to the boundary and thin slivers of intact holocrystalline matrix parallel to the boundary. *C*, Lava fragment showing (Reidel?) fractures through plagioclase microphenocrysts and holocrystalline matrix within gouge. *D*, Broken slivers of holocrystalline matrix just below image of *B* that show lateral entrainment of broken crystal fragments into boundary zone.

(fig. 16*D*) into adjacent shear zones. Foliation orientations are both parallel and subparallel to the shear-zone orientation, consistent with macroscopic evidence for slight orientation variations among slickensides (fig. 8*C*). Moreover, in some locations along the shear zone, individual fragments of foliated gouge have been broken and rotated (figs. 16*C*, 16*D*). In other locations, the shear zone itself is anastomosing, forming an ultracataclastic zone that varies in width and complexity (fig. 16*E*). Here too, the orientation of individual foliated layers within the gouge is subparallel to the shear zone.

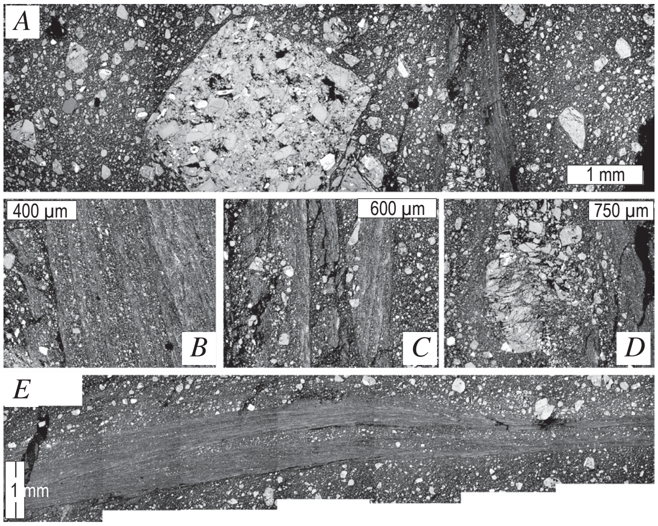

Figure 16. Backscattered electron images showing details of fault gouge sample SH313-1 from spine 4 (see fig. 9*D* for smaller-scale view). *A*, Transect across part of thin section SH313-1C showing a wide range of clast sizes in the gouge and extreme grain-size reduction within the "fault core," right of center. *B*, Detailed image of fine-scale foliated fault gouge showing slight offset in foliation orientation across the image. *C*, Breakage, disruption, and partial rotation of finely pulverized gouge. *D*, Shattered lava fragment adjacent to the fault core. *E*, Composite transect along the fault zone in thin section SH313-1A. Note fine-scale foliation oriented subparallel to the fault zone and anastomosing strands that isolate regions of less extensively pulverized gouge fragments.

Grain-Size Measurements

Sieve data for two powdery gouge samples—SH303-1 collected on November 4, 2004, from spine 3 and SH307-1 collected on February 22, 2005, from a collapsed part of spine 4—confirm the wide range in grain size of the gouge samples (fig. 17*A*). The two samples differ, however, in the extent of comminution. Sample SH307-1 has a bimodal size distribution with peaks at 10 and 350 µm; it has little material <1 µm in size and measurable clasts >5 mm. In contrast, the granulometric analysis for SH303-1 describes a rather broad peak with a poorly defined mode at about 32 µm, a substantial proportion of very fine grains, and no clasts >2.8 mm. This difference is best illustrated in a plot of cumulative volume, which shows the pronounced difference in volumetric contribution of very small particles (fig. 17*B*).

Grain size of fragments can also be estimated by analysis of BSE images. Although measurements of the number of clasts of a given size in area fraction are not directly comparable to measurements of the weight percent of a given sieve size, the image-analysis data provide another view of grain-size characteristics that can be compared directly with data from tectonic faults. Illustrative measurements on images from SH326-2A (figs. 3, 8*A*, 9*C*) show that the number-based data are dominated by the smallest size classes, which are difficult to measure accurately. When viewed as areal abundance, the data show a mode at 500 µm, similar to the volume-based (sieve) data for SH307-1 (fig. 18*A*). These data lack an equivalent peak at 8 µm because this was below our detection limit (~30 µm) for the imaging magnification used.

Quantifying the transition from intact dome lava to powdery gouge is more difficult. We experimented with measuring the reduction in size and abundance of plagioclase phenocrysts in thin section, a measurement that is easy to make using standard image-analysis techniques. The overall abundance of plagioclase, as measured in full thin-section scans (for example, fig. 9), decreases from a maximum of 32 percent in sample SH324-4A to 9.5 percent in consolidated gouge from the same sample (for example, fig. 9*B*; table 1). This range encompasses that of all other samples. Accompanying the decrease in crystal abundance is a decrease in average phenocryst size, which reflects breakage of large crystals to form numerous small crystal fragments. This breakage most severely affects the large phenocrysts, as shown by normalized cumulative plagioclase volume distributions (fig. 19). The median (50th percentile) plagioclase size decreases from about 300 µm in competent dome lava to about half of that in partially comminuted cataclasite sample 324-4A (fig. 19). More striking is the difference in maximum crystal size, which reaches several millimeters in the dome lava but only about 300 µm in SH324-4A cataclasite (table 1). If this analysis were extended to measurement of the finely laminated ultracataclasite zone of sample SH313-1 (fig. 16), the plagioclase size reduction would be even more extreme.

In summary, we have experimented with different ways of quantifying the observed fragmentation of competent dome rocks. Grain-size changes in fault gouge typi-

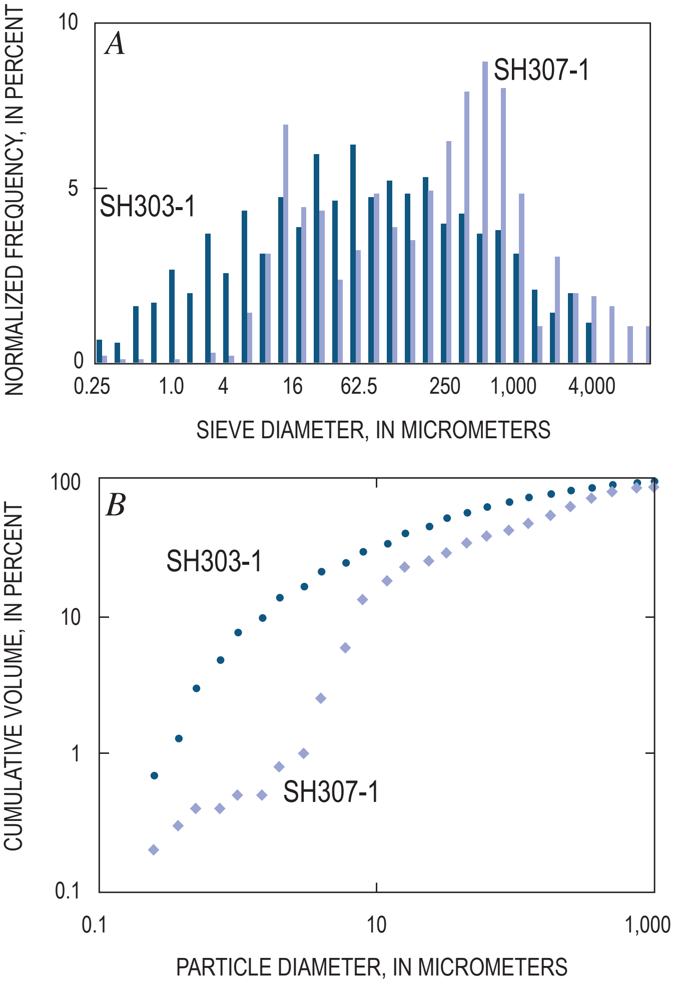

Figure 17. Sieve data for unconsolidated fault gouge samples SH303-1 (spine 3) and SH307-1 (spine 4). *A*, Histograms. *B*, Power-law plots. Note the difference in abundance of very fine particles (<10 µm) in the two samples and the absence of single power-law trend.

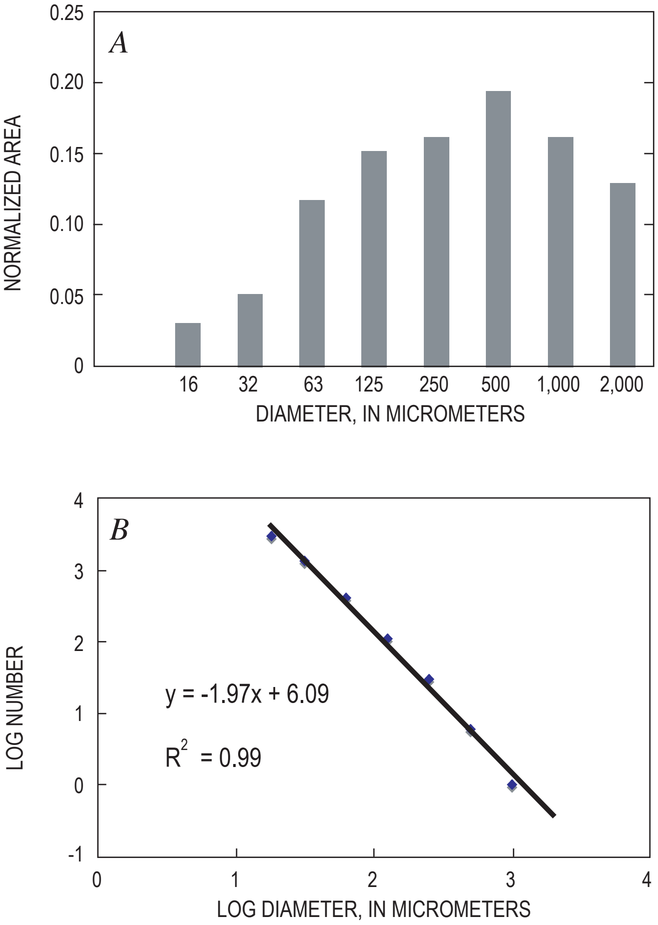

Figure 18. Grain-size data obtained by image analysis of BSE image of SH326-4A from spine 7. *A*, Histogram of data plotted by area (related to but not directly equivalent to volume-based sieve data). *B*, Power-law plot, with y-axis showing cumulative number of fragments greater than a given size. Data fit a power-law distribution over the size range 10–1,000 µm.

Table 1. Plagioclase phenocryst and microphenocryst data obtained from image analysis of whole thin-section scans.

[An example scan is shown in figure 9. Reported are the measured plagioclase area fraction, the total area measured, the total number of plagioclase crystals measured, the average plagioclase number per area, and the maximum and minimum plagioclase diameter. Where abrupt textural changes were preserved within a single thin section (for example, fig. 9*B*), different textural regimes were measured separately (denoted a and b).]

Sample No.	Plagioclase area fraction	Total area (mm^2)	Total number of crystals	Average crystal number	Maximum diameter (mm)	Minimum diameter (mm)
SH315	26.2	355	1,692	4.77	3.32	0.1
SH316(1)	27.9	222.5	2,441	10.97	1.19	0.03
SH316(2)	25.2	219.37	2,389	10.89	0.85	0.03
SH320-1C1(1)	11.7	185.54	2,404	12.96	1.01	0.02
SH320-1C1(2)	12.1	174.67	2,253	12.90	0.624	0.02
SH320-1A2	21.5	250.75	3,068	12.24	1.32	0.02
SH324-4A(1)-a	24	40.58	324	7.98	0.73	0.04
SH324-4A(2)-a	9.5	27.19	289	10.63	0.34	0.04
SH324-4A(1)-b	32	143.83	1,772	12.32	1.43	0.04
SH324-4A(2)-b	19.3	87.41	1,324	15.15	0.608	0.04
SH324-5(1)	25.8	198.9	3,496	17.58	0.91	0.02
SH324-5(2)	24.2	125.37	1,974	15.75	1.22	0.02
SH307-2A1	22.4	479.98	3,330	6.94	2.27	0.05

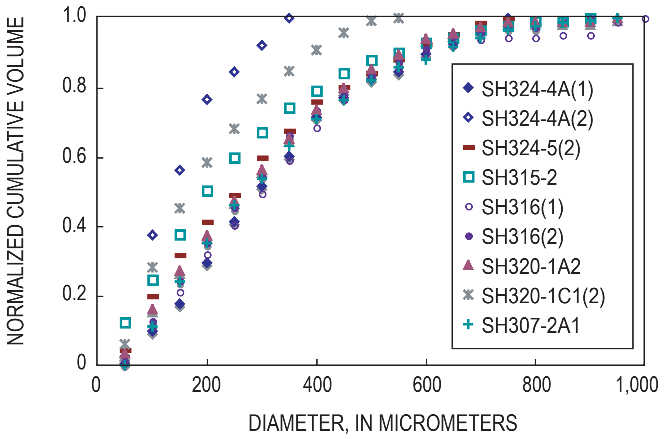

Figure 19. Plagioclase size distributions plotted as normalized cumulative volume for comparison with sieve data. Distributions determined by image analysis of full thin-section images, as shown in figure 9. Minimum size resolution approximately 30 µm (microphenocrysts and phenocrysts). Data show that plagioclase size distributions of undeformed dacite lava change progressively with increasing fragmentation toward smaller median and maximum crystal diameters. This change in size distribution is accompanied by a decrease in overall abundance of macroscopic plagioclase.

cally are measured by sieving, although this is possible only for unconsolidated samples. In cataclasite, clast size distributions may be analyzed using BSE images, although complete sample characterization would require combining multiple images at different magnifications. A simple characterization of progressive cataclasis of dome lava can be made using thin-section measurements of plagioclase phenocryst size and abundance. These data provide evidence of extensive fragmentation and grain-size reduction of dome lava during transport to the surface. Moreover, the common observations of abrupt textural transitions indicate extreme shear localization during transport. When combined with BSE evidence of initial grain shattering (figs. 15*B*, 16*D*) followed by shear, grinding, and wear (figs. 14*B*, 14*C*), these data suggest extensive transport distances (large strains) after initial breakage.

Discussion

The results presented above illustrate the range of processes that contributed to the transformation of dome lava to fault gouge and, in some cases, to ash emitted by small dome explosions (Rowe and others, this volume, chap. 29). In the following sections, we examine those processes in detail, paying particular attention to the role of degassing-induced crystallization and to conditions of fault formation. We generalize these observations by placing them first within the perspective provided by past activity (1980–1986) at Mount St. Helens and then within the context of other spine-forming eruptions.

The Role of Decompression Crystallization

All clasts within both cataclasite and fault gouge are nearly holocrystalline. Thus we infer that fragmentation of dome dacite occurred after most of the groundmass had crystallized. Extensive crystallization is most likely caused by decompression and degassing during the slow ascent of hydrous magma (reviewed above), although we cannot rule out the possibility of minor late-stage cooling along the conduit margin. Extensive crystallization, in turn, changes the rheology of the rising magma, particularly when coupled with changes in melt viscosity resulting from volatile exsolution (for example, Hess and Dingwell, 1996; Melnik and Sparks, 2002, 2005). At Mount St. Helens, these rheological changes transformed the deformation properties of the magma from plastic to brittle, fragmenting the rising magma plug and creating the resultant thick fault gouge. Constraining the depth at which this transformation initiates is important for accurate modeling of dome extrusion (Iverson and others, 2006), as well as for recognizing conditions that might lead to changes in the current eruptive activity.

Interpretation of the crystallization history of 2004–6 Mount St. Helens dacite is complicated by abundant evidence of nonequilibrium crystallization, including (1) rapid late-stage growth of rims on plagioclase phenocryst (fig. 10); (2) spatial heterogeneity of groundmass textures (both vesicles and crystals; fig. 11); (3) the presence of two or, sporadically, three silica phases (fig. 12); and (4) local temperature increases in the groundmass as the result of latent heat released by rapid groundmass crystallization (Blundy and others, this volume, chap. 33; Pallister and others, this volume, chap. 30). Here we briefly review the evidence for each before discussing the likely importance of each process to gouge formation.

Phenocryst textures that suggest rapid late-stage growth include swallowtail-like extensions from the corners of large crystals, irregular growth boundaries, and skeletal overgrowths that either partially or completely trap residual melt (fig. 10). These irregularities preserve glass within the growth protrusions, suggesting entrapment at moderately high pressures (that is, during early phases of groundmass crystallization), perhaps because microlite nucleation was inhibited by local increases in H_2O rejected from the rapidly growing crystal. Therefore it appears that this crystallization, while rapid, was not directly responsible for cataclasis and gouge formation, although it does reflect the overall importance of decompression-induced crystallization during this remarkably steady effusive activity.

More important for determining conditions of marginal fragmentation is the spatial inhomogeneity of groundmass textures found within the early dome lavas. Lavas are heterogeneous in both groundmass crystallinity and vesicularity. Heterogeneity in groundmass crystallinity is particularly evident in the concentration of cotectic quartz-plagioclase intergrowths along euhedral phenocryst margins (fig. 11). However, as most of the groundmass within the cataclasite and gouge samples is holocrystalline, it is unclear what effect, if any, the heterogeneities in groundmass crystallization may have had on brittle deformation of the dome dacite. Heterogeneous vesicle textures are more likely to affect the material properties of the lava when deformed. A feature of many of the holocrystalline clasts within the gouge is the presence of numerous tiny microvesicles that are probably a feature of second boiling during the last stages of crystallization. It is possible that variations in vesicle structure may play a role in clast breakage, although our observations suggest that this, also, does not dominate the failure behavior.

Most important for gouge formation seems to be near-complete solidification of the ascending magma. The depth of this solidification may be estimated using both groundmass phases and crystal textures. Three silica phases occur within the matrix of different gouge clasts: cristobalite, tridymite, and quartz. Cristobalite typically forms large crystals; similar crystals in cryptodome dacite from the 1980 eruption were interpreted by Hoblitt and Harmon (1993) to result from vapor-phase crystallization. Quartz can form discrete groundmass crystals, but it most commonly grows as fine-scale cotectic aggregates with plagioclase and anorthoclase. Tridymite forms discrete acicular grains (fig. 12) that are common in some samples, sparse in others, and completely absent in some dome lava. In their study of Mount St. Helens lava samples from 1980–1986, Blundy and Cashman (2001) found tridymite in a single lava sample erupted during the period of continuous slow effusion in 1983. They used experimental data to argue that equilibrium crystallization of tridymite in H_2O-saturated, anorthite-free melts requires a minimum pressure of 11 MPa and temperature of 885ºC. Addition of anorthite to the melt will increase the temperature of the high quartz-tridymite boundary. Subsequently Cashman and McConnell (2005) found additional examples of tridymite-bearing dacite from pyroclasts stored temporarily at shallow levels prior to explosive eruptions of Mount St. Helens during the summer of 1980. When analyzed for volatile content using FTIR, one such glassy sample preserved ~0.6 weight percent H_2O, suggesting a minimum pressure of 5 MPa (A. Rust, oral commun., 2005). Thus it appears that the presence of tridymite requires shallow (<25 MPa) but not surface (>5–10 MPa) pressures (depths between 200 and 1,000 m for an average magma density of 2,500 kg/m^3). Patterns of silica-phase precipitation thus suggest (1) substantial delays in quartz nucleation to produce the observed high degree of spatial variability; (2) varying *P-T* paths during decompression, as illustrated by differences in the proportions of silica phases among samples; and (3) tridymite crystallization under a limited range of *P-T* conditions.

Experimental data (Hammer and Rutherford, 2002; Couch and others, 2003; Martel and Schmidt, 2003) further suggest that the common groundmass texture of holocrystalline quartz and feldspar intergrowths requires pressures >10 MPa (400 m) and crystallization time scales of weeks. If magma ascends at a constant rate from a storage region at >4 km (Rutherford and Devine, this volume, chap. 31), measured extrusion rates of ~7 m/d allow sufficient time for shallow crystallization (~3 months for ascent from 1,000 to 400 m). Pressures as low as 5 MPa were required to precipitate quartz-alkali feldspar intergrowths in decompression experiments on Pinatubo magma compositions (Hammer and Rutherford, 2002), whereas maximum rates of plagioclase nucleation typically require pressures between 25 and 5 MPa (Hammer and Rutherford, 2002; Couch and others, 2003; Martel and Schmidt, 2003). If gouge forms only after crystallization of the groundmass is nearly complete, these data suggest a shallow origin for the onset of brittle deformation (<400–500 m), consistent with the plug model of Iverson and others (2006). We note, however, that all of these estimates assume only minor cooling of magma during ascent, an assumption that appears reasonable given the high surface temperatures measured by FLIR (Schneider and others, this volume, chap. 17) and high Fe-Ti oxide temperatures from the dacite (Pallister and others, this volume, chap. 30).

Fault Gouge Formation

Extensive research on tectonic fault zones provides a framework for examining gouge formation during the extrusion of the 2004–6 Mount St. Helens spines. Tectonic fault zones commonly are characterized by narrow (millimeter to centimeter) slip planes composed of finely pulverized rock surrounded by broader cataclasite zones (typically meters in scale and locally foliated) mantled outward by a zone of less intensely deformed rock (for example, Chester and Logan, 1986, 1987; Chester and others, 1993; Schulz and Evans, 1998; Storti and others, 2003). These fault-zone characteristics are taken as evidence of strain-weakening behavior, with shear localization into narrow zones that act as the primary slip surfaces (for example, Ben-Zion and Sammis, 2003). Fault initiation in porous material commences with dispersed breakage, porosity reduction, and temporary strain hardening (for example, Mair and others, 2000; Cashman and Cashman, 2000). A change to strain-weakening behavior requires localization of shear through nucleation of interconnected slip surfaces (Biegel and others, 1989; Shipton and Cowie, 2003). Average particle size decreases with increasing strain (Marone and Scholz, 1989; Mair and others, 2000; Hadizadeh and Johnson, 2003) until that strain can be accommodated by rolling (Morgan and Boettcher, 1999), contact creep (Prasher, 1987), or development of new fault strands (if band formation results in local strain hardening; Mair and others, 2000).

In tectonic fault zones, gouge thickness shows a weak dependence on total displacement, a correlation that has been attributed to breakage of increasingly large asperities (Power and others, 1988). Sibson (1986) recognized three different types of natural fault gouge:

1. **Attrition breccia** resulting from wear. This gouge type is rare in tectonic faults, characterized by rolled clasts, and associated only with zones of significant fault slip.
2. **Distributed crush breccia** formed by destruction of local asperities. This gouge type is characterized by pervasive microfractures and jigsaw textures.
3. **Implosion breccia.** This gouge type has textures similar to those of distributed crush breccia.

Gouge within the cores of tectonic faults may contain ultrafine grains (micron to nanometer scale) whose origin has been variously attributed to quasi-static wear and attrition (Sammis and others, 1986; Chester and Chester, 1998), dynamic pulverization resulting from a single rupture event (Reches and Dewers, 2005; Wilson and others, 2005), and large strains (for example, Yund and others, 1990).

Our observations of textural characteristics of cataclasite and gouge samples from Mount St. Helens provide insight into fault gouge formation. Macroscopically, the structure of the fault zone along the conduit margin (for example, fig. 6) is similar to examples described in the fault literature, with an outer breccia that changes to cataclasite and, finally, into either fault gouge containing slickensides or areas of slip localization (figs. 8*C*, 16*A*) at the margin. Microscopically, localized extreme grain-size reduction along slickensides is consistent with experimental generation of ultrafine grains by large shear strains (Yund and others, 1990). Using the correlation for tectonic faults, a gouge thickness of 1–3 m suggests displacements of <1,000 m, in agreement with petrologic assessments of the depth of gouge formation presented above. Moreover, these values suggest total strains (displacement/thickness) less than or about 500. Assuming that all of the slip is concentrated along the conduit margin, observed slip rates of ~8×10^{-5} m/s are orders of magnitude higher than those of creeping faults and orders of magnitude lower than slip events on stick-slip faults. These slip velocities suggest strain rates (velocity/thickness) of 3–8×10^{-5}/s, intermediate to values typical for creeping and stick-slip tectonic faults.

The fault gouge itself appears to represent at least two of Sibson's (1986) types. Extensive grain fragmentation adjacent to the slickenside zones (figs. 15*B*, 16*D*) fits Sibson's description of distributed crush breccia, in that individual pieces of a grain have not been displaced from each other by shear. However, it is clear that these fragments are eventually distributed along the foliation bands by shear displacement after crushing (figs. 15*D*, 16*B*, 16*C*). In contrast, the common rounded fragments in cataclasite and gouge (figs. 14*B*, 14*C*) appear to be attrition breccia, with rounding that results from abrasion and wear during shear transport. The prevalence of these attrition features may reflect not only the large total displacements (shear strain) involved with dome emplacement but also the steadiness of movement. Whereas sporadic movement of tectonic faults allows healing or lithification of fault zones between slip events, steady movement of solidified magma along the conduit margin apparently prevents such healing. Instead, the observed gradual decrease in the percentage of larger clasts apparently allows them to be isolated from each other by the matrix, thus permitting individual clasts to roll and abrade. Continued brittle deformation of fragmented particles results in further grain-size reduction and shear localization along multiple slickensides.

An interesting discussion in the fault zone literature involves the mechanism by which fragmentation occurs. Patterns of grain-size reduction may be characterized by the fractal dimension *D* of particle grain size, where *D* relates cumulative particle frequency $N(S)$ (the number of particles less than *S*, usually measured per volume) to size (*S*):

$$N(S) \approx S^{-D}. \qquad (1)$$

Thus *D* describes the relative proportion of small and large fragments; higher *D* values reflect samples where the grain-size distribution is dominated by smaller particles. Within this framework, the "pillar of strength" model (Allegre and others, 1982) predicts $D = 1.97$, the "plane of fragility" model (Turcotte, 1986) predicts $D = 2.84$, and the constrained comminution model (Sammis and others, 1986; Sammis and others, 1987; Sammis and Biegel, 1989; Turcotte, 1992) predicts $D = 2.6$. The latter model is based on sequential breakage of equal-size particles into a discrete (and relatively small) number of particles. Key to the constrained comminution model is that fragments of similar size are evenly distributed in space. Experimental studies of sheared quartz sand support a model of constrained comminution under conditions of high confining pressure (100 MPa) and particle size range of 10 µm to 1 mm (Biegel and others, 1989; Marone and Scholz, 1989). However, data from natural cataclastic samples are less easily interpreted (for example, Blenkinsop, 1991; An and Sammis, 1994; Storti and others, 2003; Cashman and others, 2007). In many fault zones, *D* values change from low in brecciated damage zones to high in intensely comminuted narrow shear zones (fig. 20). These high *D* values (high degrees of crushing) may result from slip-enhanced surface abrasion during shear transport, as suggested by Hooke and Iverson (1995) for glacially abraded sediment. High degrees of crushing also create the matrix support required to allow rolling and abrasion of remaining larger particles.

The fragmentation schematic shown in figure 20 provides a description of the process of gouge development at Mount St. Helens. Imaging data, which can be used to characterize the larger clast sizes in the cataclasite, yield fractal dimensions ~1.97 for particles from 10 to 1,000 µm in diameter (fig. 18*B*) when measured as number per area; this is equivalent to *D* ~ 2.97 on a volume basis. This high *D* value is identical to that measured by Chester and others (2005) in cataclasite and ultracataclasite of the Punchbowl Fault, a large-displacement fault in the San Andreas Fault system. Sieve data (fig. 17), however, show that grain size data are self similar (fractal) only within limited size ranges. As seen in other fault rocks, fits to straight-line segments suggest that *D* increases with decreasing grain size (for example, Blenkinsop, 1991; An and Sammis, 1994; Storti and others, 2003). High *D* values at very small grain sizes result from extensive comminution of individual clasts, as evidenced by the shattered large crystals and dome fragments that border the slickensides (figs. 15*B*, 16*D*). Thus we interpret the grain-size data to reflect (1) cataclasis and particulate flow over most of the observed gouge thickness and (2) strain localization and intense comminution within the slickensides, which are themselves distributed within the outer gouge zone.

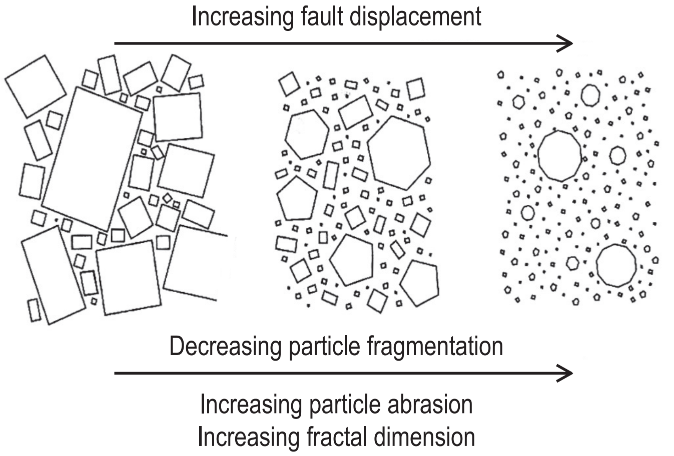

Figure 20. Diagram showing schematic change in size and shape of grains with increasing fault displacement. Although drawn for tectonic faults, this progression from coarse to fine grain sizes and angular to rounded shapes appears appropriate to fault behavior associated with spine emplacement at Mount St. Helens, Washington. Figure from Storti and others (2003).

The frictional properties of 2004–6 Mount St. Helens fault gouge have been investigated by Moore and others (this volume, chap. 20) at room temperature, shear rates of 1.5–5,000×10^{-6} m/s, and low normal stresses (5–195 kPa). They find rate-weakening behavior at shear rates <1×10^{-4} m/s and rate-strengthening behavior at >5×10^{-4} m/s, with stick-slip oscillations observed at the highest normal stress and lowest shear rates. However, although they observe shear localization into a narrow (1 mm) zone, they find no evidence of comminution or crushing of gouge, perhaps because the small cumulative strains and low normal stresses in the experiments were insufficient to produce the grain breakage observed in natural samples.

In summary, the unusually well developed fault gouge that has mantled all of the 2004–6 Mount St. Helens spines provides evidence of profound change in the rheological behavior of dome lava during ascent as a consequence of near-complete crystallization and subsequent brittle breakage and gouge formation. The effect of this extensive brittle deformation on dome extrusion is less clear. Iverson and others (2006) suggest that rate-weakening behavior is required to produce the stick-slip behavior suggested by the repetitive (drumbeat) earthquakes. Alternatively, Mastin and others (this volume, chap. 22) suggest a gouge zone that is, overall, rate strengthening but that fails in a patchwork fashion during extrusion. Field evidence for localized failure includes both observed Reidel shears in the cataclasite and in throughgoing ultracataclasite (slickenside) bands within the gouge.

Comparison with Other Dome Eruptions

The morphology and emplacement conditions of other recent domes and spines of intermediate composition are reviewed above. Here we use observations of the 2004–6 activity at Mount St. Helens to evaluate processes that may have affected extrusive behavior at other volcanoes.

Dome emplacement during the 1980–86 eruption of Mount St. Helens provides the most obvious comparison with current (2004–6) activity. Importantly, although the erupted composition in the 1980s was similar to that of the 2004–6 dacite and average effusion rates were comparable (or slightly lower), the 1980–86 magma had a higher temperature (880–900°C in the early 1980s compared with 840–850°C in 2004–6), and its extrusion was dominantly episodic rather than continuous. Spines were produced on only two occasions: (1) accompanying endogenous growth during continuous effusion in 1983 and (2) following a protracted, 17-day episode of (mostly endogenous) dome-lobe formation in May 1985. Backscattered electron images of a sample from the February 1983 spine look similar to early samples of the 2004 spine (compare fig. 21*A* with fig. 11*C*). In both samples the distribution of groundmass crystals is heterogeneous, as is the distribution of clean glass. In contrast, a marginal sample of the May 1985 spine is holocrystalline (fig. 21*B*), with the characteristic cotectic crystallization fabric seen in the more slowly extruded 2005–6 spine samples.

However, there are two differences between the spine sample from May 1985 and those of the current eruption. First, the extremely fine-scale “myrmekitic” textures occupying interstices between microlites in the May 1985 sample (and not observed in the 2004–6 spine samples) suggest that preeruptive crystallization occurred at shallow levels, most likely within the dome itself. Second, the boundary between the extruded spine and the dome lobe had a different character in 1985. In contrast to the thick gouge zones described above, the spine-dome lobe boundary in 1985 comprised a thin (~10 mm) cataclasite zone that, although showing some of the grain-size reduction characteristics of the recent gouge, was narrower and less

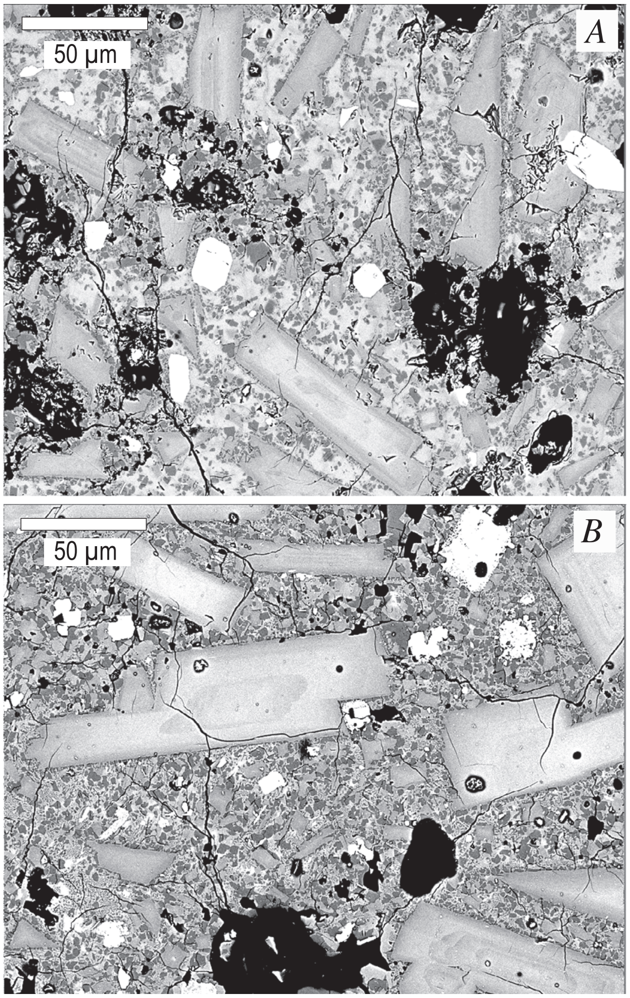

Figure 21. Backscattered electron images showing groundmass textures of 1980s lava spines of Mount St. Helens. Textures are similar to those observed in spines produced during current Mount St. Helens eruptive activity; for example, compare with figures 11*C*, 11*D*, 12*A*, or 12*B*. *A*, February 1983. *B*, May 1985.

comminuted (compare thin-section image of fig. 22 with those of fig. 9). These features suggest that the May 1985 dome was formed by late-stage solidification within the growing dome, with extrusion resulting in only small cumulative displacements (strain), consistent with its small size.

More similar are larger spines produced at Mont Pelée (1903), Unzen (1991–95), and Soufrière Hills (1995–present), which have macroscopic features similar to the 2004–6 spines at Mount St. Helens, including smooth curved forms and pronounced striations parallel to the extrusion direction (reviewed above). Descriptions in the literature suggest that gouge was present on the striated surface of the giant Mont Pelée spine (Jaggar, 1904); gouge and cataclasite also mantle some large dome fragments from Soufrière Hills, Montserrat. Conditions leading to spine formation also appear similar at all of these locations. Most important are estimated ascent rates of $1–3\times10^{-4}$ m/s, rates that are sufficiently slow for the extensive crystallization necessary for both plug and fault gouge formation (see above). The comparison between the 1985 and current spines at Mount St. Helens further suggests that formation of large spines requires that magma solidify well within the conduit. This depth of solidification, in turn, means that solid dome rock must be transported large distances before exiting the vent, with resulting large strains responsible for the development of thick gouge zones.

From Dome to Dust

Brittle deformation is not unique to holocrystalline spines of intermediate composition. Numerous small-scale brittle deformation features have been described along shallow conduit margins and within basal shear zones of glassy obsidian domes, including anastomosing tuffisite veins and fractures, cataclasite zones, and trails of broken phenocrysts (for example, Stasiuk and others, 1996; Tuffen and Dingwell, 2005). Fracture and grain-size reduction in these systems have been explained by shear-strain rates at conduit margins exceeding experimentally determined critical rates for shear-induced fragmentation (for example, Dingwell and Webb, 1989) of high viscosity ($10^{10}–10^{12}$ Pa s) melts at the low strain rates ($10^{-3}–10^{-5}$/s) anticipated for dome extrusion (Gonnermann and Manga, 2003; Tuffen and others, 2003).

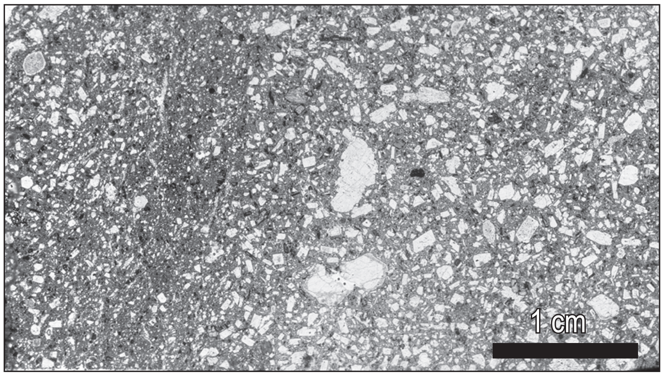

Figure 22. Full thin-section (4.5 cm x 2.5 cm) scan of sample collected across the margin of the May 1985 dome lobe (right) and spine (far left). The darker area of reduced phenocryst size toward the left side of the figure is a thin (<1 cm) cataclasite zone that marks the lava-spine boundary.

Deformation textures in obsidian domes, however, differ dramatically from those described here for the Mount St. Helens gouge zone. First, fracture networks in obsidian are limited to thin (<20 mm) fault and injection veins with limited to no displacement and thicker, irregular “injection voids” (≤80 mm in width; Tuffen and Dingwell, 2005). The largest fault complex observed by Tuffen and Dingwell (2005) is ~5 m in length, with a maximum offset of 0.13 m. Thus these features are substantially smaller than the zones of breccia, cataclasite, and gouge that line the shallow Mount St. Helens conduit, with the possible exception of basal breccia zones in some obsidian flows (Gonnermann and Manga, 2003). Moreover, both tuffisite veins and basal breccias show abundant evidence of annealing and ductile deformation (Gonnermann and Manga, 2003; Tuffen and others, 2003; Tuffen and Dingwell, 2005). In contrast, gouge zones at Mount St. Helens are dominated by brittle fracture and cataclastic flow, with no evidence of re-annealing between fracture events. Finally, fracture zones within obsidian domes appear to lack the distinct zones of breccia, cataclasite, and gouge seen at Mount St. Helens; instead, fragment sizes within the tuffisite veins are very small (much less than 1 mm), with no clasts of intermediate size.

What are the implications of these differences in fragmentation style? Annealing textures preserved within tuffisite veins and basal breccias of obsidian flows result from the strain-dependent rheology of viscous silicate melts; at the same temperature, the melt will flow at low strain rates but will fracture at higher strain rates. For this reason, a model of flow emplacement by repeated fracture and healing *of the same magma* has been suggested for obsidian (Tuffen and others, 2003; Tuffen and Dingwell, 2005). This model has been extended to explain repetitive seismic events accompanying andesitic dome growth at Soufrière Hills, Montserrat (for example, Neuberg and others, 2006). Our observations of fault gouge formation, however, would suggest caution in the direct application of deformation mechanisms in obsidian to the interpretation of seismicity associated with the emplacement of highly crystalline lava. Most importantly, we see no evidence of annealing within the gouge zone between fracture events. Instead, fault gouge forms by fracture and fragmentation of crystals and holocrystalline matrix into successively smaller fragments. For this reason, we suggest that the origin of the repetitive (drumbeat) earthquakes at Mount St. Helens most likely lies in progressive fragmentation of dome dacite rather than by process of repeated fracture and healing. Although definite assignment of individual slip features to specific earthquake characteristics is beyond the scope of this paper, we note that several types of slip zones are apparent at the outcrop to hand-specimen scale, from Reidel shears in the cataclasite (fig. 6) to slickensides in the gouge (fig. 8*C*). If individual drumbeat earthquakes represent slip events of ~5 mm (Iverson and others, 2006), then they may represent the composite effect of fracturing multiple smaller grains (as suggested by the dominance of fine (<10–20 µm) material within the cataclasite and gouge zone. Alternatively, perhaps only the initial fragmentation of larger dome fragments is seismogenic.

This leads to a final point—the role of fragmentation during dome explosions. A common assumption is that dome explosions result from sudden decompression of pressurized dome interiors and resultant brittle fragmentation (for example, Alidibirov and Dingwell, 1996). However, Rowe and others (this volume, chap. 29) demonstrate that ash released during the two substantial dome explosions associated with the current eruption (in January and March of 2005) bears a striking textural resemblance to the fault gouge described here. The implications of this observation are that the explosions themselves transported, but did not generate, much of the ash emitted during each event, an interpretation consistent with the source of the explosions at the junction of the spine and the conduit rather than from within the dome itself. We suspect that gouge formed along conduit margins may commonly supply ash to explosions that accompany spine growth (for example, Jaggar, 1904), a hypothesis that suggests that further studies of the physical properties of volcanic gouge (especially relations between deformation behavior and permeability) could improve our understanding of hazards related to the slow extrusion of lava spines.

Conclusions

We have documented field, hand-sample, and thin-section evidence for cataclasis and gouge formation along the margins of the smooth-surfaced spines extruded from Mount St. Helens from 2004 to present. These observations show brittle breakage and subsequent cataclastic flow to be important in the slow extrusion of intermediate-composition hydrous magma. Detailed textural observations document both crystallization accompanying magma ascent (decompression) and the sequential fragmentation of competent dome rock to produce fine-grained fault gouge. Taken together, these observations provide new constraints on interactions between rates of magma ascent, degassing, crystallization, and brittle fragmentation, interactions that control the dynamics of lava extrusion.

The groundmass of dacite lava samples is variably crystalline, with the extent of groundmass crystallinity apparently increasing with time (decreasing mass eruption rate). Most, if not all, of the crystallization is driven by decompression and degassing rather than cooling; Fe-Ti oxide temperatures suggest that the extensive crystallization may even help to heat the magma (for example, Blundy and others, 2006; Pallister and others, this volume, chap. 30). Within the gouge zone, dome fragments are holocrystalline, indicating solidification along conduit margins prior to brittle fragmentation. Detailed textural observations show that the transformation of competent dacite to fine powder occurred by sequential breakage of rock fragments to form zones of breccia, cataclasite, and gouge. Further concentration of slip along narrow slickenside planes produced thin (1 mm) zones of pulverized and foliated ultracataclasite. Both the extreme grain-size reduction along these slip zones and the shattering of individual grains observed adjacent to narrow slip surfaces are similar to textures observed in near-surface gouge produced by large tectonic faults (for example, Cashman and others, 2007) and suggest large strains. This inference is reasonable given a solidification depth of 400–500 m, above which deformation apparently is concentrated along the conduit margin (for example, Iverson and others, 2006). However, we see no evidence of subsequent annealing, as is commonly observed in tuffisite veins and obsidian flows (for example, Tuffen and others, 2003; Gonnermann and Manga, 2003), suggesting that earthquake-generating mechanisms based on repeated fracturing and healing do not apply to the extrusion of highly crystalline domes. Additionally, the two largest explosions at Mount St. Helens (in January and March of 2005) occurred at the contact between the spine and conduit wall and ejected ash that appears to have originated as fault gouge.

The physical characteristics of dome extrusion at Mount St. Helens from 2004–6 can be generalized to other recent examples of andesite and dacite extrusions. As surmised by Williams (1932), the complete decompression-driven solidification prior to magma extrusion necessary for spine formation requires magma ascent to be slow relative to the kinetics of crystallization and the dynamics of gas loss. Spine formation appears limited to magma ascent rates of $<1–5\times10^{-4}$ m/s, which allows several weeks for magma to transit from ~1,000 m (the point at which crystallinity increases dramatically as a function of decreasing pressure; Blundy and others, 2006) to ~400 m, where extensive cotectic crystallization of quartz and feldspar occurs. Comparison of marginal shear behavior of a small spine produced at Mount St. Helens in 1985 and the large spines produced from 2004 to 2006 also suggest a further point—that formation of large spines requires solidification to occur deep within the conduit, a condition that leads to extensive brittle deformation and gouge formation during transit to the surface.

Acknowledgments

The authors would like to acknowledge all CVO personnel who helped with field observations and sample collection, as well as a host of volunteers who helped to sort and catalogue the samples. We thank reviewers Rob Watts and Nick Beeler for their thoughtful comments on the first draft of the manuscript. Cashman acknowledges support from NSF EAR-0207362 and EAR-0510437.

References Cited

Alidibirov, M., and Dingwell, D.B., 1996, Magma fragmentation by rapid decompression: Nature, v. 380, no. 6570, p. 146–148, doi:10.1038/380146a0.

Allegre, C.J., LeMouel, J.L., and Provost, A., 1982, Scaling rules in rock fracture and possible implications for earthquake predictions: Nature, v. 297, p. 47–49.

An, L.J., and Sammis, C., 1994, Particle size distribution in cataclastic fault materials from Southern California; a 3-D study: Pure and Applied Geophysics, v. 143, p. 203–228.

Ben-Zion, Y., and Sammis, C., 2003, Characterization of fault zones: Pure and Applied Geophysics, v. 160, p. 677–715.

Biegel, R.L., Sammis, C.G., and Dieterich, J.H., 1989, The frictional properties of a simulated fault gouge having a fractal particle distribution: Journal of Structural Geology, v. 11, no. 7, p. 827–846.

Blenkinsop, T.G., 1991, Cataclasis and processes of particle size reduction: Pure and Applied Geophysics, v. 136, p. 59–86.

Blundy, J., and Cashman, K., 2001, Ascent-driven crystallisation of dacite magmas at Mount St. Helens, 1980–1986: Contributions to Mineralogy and Petrology, v. 140, no. 6, p. 631–650, doi:10.1007/s004100000219.

Blundy, J., and Cashman, K., 2005, Rapid decompression-driven crystallization recorded by melt inclusions from Mount St. Helens volcano: Geology, v. 33, no. 10, p. 793–796, doi:10.1130/G21668.1.

Blundy, J., Cashman, K., and Humphreys, M., 2006, Magma heating by decompression-driven crystallization beneath andesite volcanoes: Nature, v. 443, no. 7101, p. 76–80, doi:10.1038/nature05100.

Blundy, J., Cashman, K.V., and Berlo, K., 2008, Evolving magma storage conditions beneath Mount St. Helens inferred from chemical variations in melt inclusions from the 1980–1986 and current (2004–2006) eruptions, chap. 33 *of* Sherrod, D.R., Scott, W.E., and Stauffer, P.H., eds., A volcano rekindled; the renewed eruption of Mount St. Helens, 2004–2006: U.S. Geological Survey Professional Paper 1750 (this volume).

Cashman, K.V., 1992, Groundmass crystallization of Mount St. Helens dacite, 1980–1986; a tool for interpreting shallow magmatic processes: Contributions to Mineralogy and Petrology, v. 109, no. 4, p. 431–449, doi:10.1007/BF00306547.

Cashman, K.V., and Blundy, J., 2000, Degassing and crystallization of ascending andesite and dacite: Philosophical Transactions of the Royal Society of London, v. 358, p. 1487–1513.

Cashman, S.M., and Cashman, K.V., 2000, Cataclasis and deformation-band formation in unconsolidated marine terrace sand, Humboldt County, California: Geology, v. 28, p. 111–114.

Cashman, K.V., and McConnell, S.M., 2005, Multiple levels of magma storage during the 1980 summer eruptions of Mount St. Helens, WA: Bulletin of Volcanology, v. 68, no. 1, p. 57–75, doi:10.1007/s00445-005-0422-x.

Cashman, S.M., Baldwin, J.N., Cashman, K.V., Swanson, K., and Crawford, R., 2007, Microstructures developed by coseismic and aseismic faulting in unconsolidated near-surface sediments, San Andreas fault, California: Geology, v. 35, no. 7, p. 611–614, doi:10.1130/G23545A.1.

Chadwick, W.W., Archuleta, R.J., and Swanson, D.A., 1988, The mechanics of ground deformation precursory to dome-building extrusions at Mount St. Helens 1981–1982: Journal of Geophysical Research, v. 93, no. B5, p. 4351–4366, doi:10.1029/88JB01345.

Chester, F.M., and Logan, J.M., 1986, Implications for mechanical properties of brittle faults from observations of the Punchbowl fault zone, California: Pure and Applied Geophysics, v. 124, p. 79–106.

Chester, F.M., and Logan, J.M., 1987, Composite planar fabric of gouge from the Punchbowl fault, California: Journal of Structural Geology, v. 9, p. 621–634.

Chester, F.M., Evans, J.P., and Beigel, R.L., 1993, Internal structure and weakening mechanics of the San Andreas Fault: Journal of Geophysical Research, v. 98, p. 771–786.

Chester, J.S., Chester, F.M., and Kronenberg, A.K., 2005, Fracture surface energy of the Punchbowl fault, San Andreas system: Nature, v. 437, p. 133–136.

Couch, S., Sparks, R.S.J., and Carroll, M.R., 2003, The kinetics of degassing-induced crystallization at Soufrière Hills Volcano, Montserrat: Journal of Petrology, v. 44, p. 1477–1502.

Devine, J.D., Rutherford, M.J., Norton, G.E., and Young, S.R., 2003, Magma storage region processes inferred from geochemistry of Fe-Ti oxides in andesitic magma, Soufrière Hills volcano, Montserrat, W.I.: Journal of Petrology, v. 44, no. 8, p. 1375–1400, doi:10.1093/petrology/44.8.1375.

Dingwell, D.B., and Webb, S.L., 1989, Structural relaxation in silicate melts and non-Newtonian melt rheology in geological processes: Physics and Chemistry of Minerals, v. 16, p. 508–516.

Donnadieu, D., and Merle, O., 1998, Experiments on the indentation process during cryptodome intrusions; new insights into Mount St. Helens deformation: Geology, v. 26, p. 79–82.

Endo, E.T., Dzurisin, D., and Swanson, D.A., 1990, Geophysical and observational constraints for ascent rates of dacitic magma at Mount St. Helens, *in* Ryan, M.P., ed., Magma transport and storage: New York, John Wiley, p. 317–334.

Fink, J.H., Malin, M.C., and Anderson, S.W., 1990, Intrusive and extrusive growth of the Mount St Helens lava dome: Nature v. 348, p. 435–437.

Gardner, C.A., Cashman, K.V., and Neal, C.A., 1998, Tephrafall deposits from the 1992 eruption of Crater Peak, Alaska; implications of clast textures for eruptive processes: Bulletin of Volcanology, v. 59, p. 537–555.

Geschwind, C.-H., and Rutherford, M.J., 1995, Crystallization of microlites during magma ascent; the fluid mechanics of 1980–1986 eruptions at Mount St. Helens: Bulletin of Volcanology, v. 57, no. 5, p. 356–370.

Gilbert, G.K., 1904, The mechanism of the Mont Pelée spine: Science, v. 19, p. 927–928.

Gonnermann, H.M., and Manga, M., 2003, Explosive volcanism may not be an inevitable consequence of magma fragmentation: Nature, v. 426, p. 432–435.

Hadizadeh, J., and Johnson, W.K., 2003, Estimating local strain due to comminution in experimental cataclastic textures: Journal of Structural Geology, v. 25, p. 1973–1979.

Hammer, J.E., and Rutherford, M.J., 2002, An experimental study of the kinetics of decompression-induced crystallization in silicic melt: Journal of Geophysical Research, v. 107, no. B1, p. ECV 8-1–8-24, doi:10.1029/2001JB000281.

Hammer, J.E., Cashman, K.V., Hoblitt, R., and Newman, S., 1999, Degassing and microlite crystallization during the pre-climactic events of the 1991 eruption of the Mt. Pinatubo, Philippines: Bulletin of Volcanology, v. 60, p. 355–380.

Hammer, J.E., Cashman, K.V., and Voight, B., 2000, Magmatic processes revealed by textural and compositional trends in Merapi dome lavas: Journal of Volcanology and Geothermal Research, v. 100, p. 165–192.

Heliker, C., 1995, Inclusions in the Mount St. Helens dacite erupted from 1980 through 1983: Journal of Volcanology and Geothermal Research, v. 66, nos. 1–3, p. 115–135, doi:10.1016/0377-0273(94)00074-Q.

Hess, K.-U., and Dingwell, D.B., 1996, Viscosities of hydrous leucogranitic melts; a non-Arrhenian model: American Mineralogist, v. 81, p. 1297–1300.

Hoblitt, R.P., and Harmon, R.S., 1993, Bimodal density distribution of cryptodome dacite from the 1980 eruption of Mount St. Helens, Washington: Bulletin of Volcanology, v. 55, no. 6, p. 421–437, 10.1007/BF00302002.

Hooke, R.L., and Iverson, N.R., 1995, Grain-size distribution in deforming subglacial tills; role of grain fracture: Geology, v. 23, p. 57–60.

Iverson, R.M., 2008, Dynamics of seismogenic volcanic extrusion resisted by a solid surface plug, Mount St. Helens, 2004–2005, chap. 21 *of* Sherrod, D.R., Scott, W.E., and Stauffer, P.H., eds., A volcano rekindled; the renewed eruption of Mount St. Helens, 2004–2006: U.S. Geological Survey Professional Paper 1750 (this volume).

Iverson, R.M., Dzurisin, D., Gardner, C.A., Gerlach, T.M., LaHusen, R.G., Lisowski, M., Major, J.J., Malone, S.D., Messerich, J.A., Moran, S.C., Pallister, J.S., Qamar, A.I., Schilling, S.P., and Vallance, J.W., 2006, Dynamics of seismogenic volcanic extrusion at Mount St. Helens in 2004–05: Nature, v. 444, no. 7118, p. 439–443, doi:10.1038/nature05322.

Jaggar, T.A., 1904, The initial stages of the spine on Pelée: American Journal of Science, v. 17, p. 34–40.

Lacroix, A., 1904, La Montagne Pelée et ses éruptions: Paris, Masson et Cie, 662 p.

Mair, K., Main, I., and Elphick, S., 2000, Sequential growth of deformation bands in the laboratory: Journal of Structural Geology, v. 22, p. 25–42.

Marone, C.J., and Scholz, C.H., 1989, Particle-size distribution and microstructures within simulated fault gouge: Journal of Structural Geology, v. 11, p. 799–814.

Martel, C., and Schmidt, B.C., 2003, Decompression experiments as an insight into ascent rates of silicic magmas: Contributions to Mineralogy and Petrology, v. 144, p. 397–415.

Martel, C., Bourdier, J.-L., Pichavant, M., and Traineau, H., 2000, Textures, water content and degassing of silicic andesites from recent plinian and dome-forming eruptions at Mont Pelée volcano (Martinique, Lesser Antilles arc): Journal of Volcanology and Geothermal Research, v. 96, p. 191–206.

Mastin, L.G., Roeloffs, E., Beeler, N.M., and Quick, J.E., 2008, Constraints on the size, overpressure, and volatile content of the Mount St. Helens magma system from geodetic and dome-growth measurements during the 2004–2006+ eruption, chap. 22 *of* Sherrod, D.R., Scott, W.E., and Stauffer, P.H., eds., A volcano rekindled; the renewed eruption of Mount St. Helens, 2004–2006: U.S. Geological Survey Professional Paper 1750 (this volume).

Melnik, O., and Sparks, R.S.J., 2002, Dynamics of magma ascent and lava extrusion at Soufrière Hills Volcano, Montserrat, *in* Druitt, T.H., and Kokelaar, B.P., eds., The eruption of Soufrière Hills Volcano, Montserrat, from 1995 to 1999: Geological Society of London Memoir 21, p. 153–171.

Melnik, O., and Sparks, R.S.J., 2005, Controls on conduit magma flow dynamics during lava dome building eruptions: Journal of Geophysical Research, v. 110, no. B2, B02209, 21 p, doi:10.1029/2004JB003183.

Metrich, N., Bertagnini, A., Landi, P., and Rosi, M., 2001, Crystallization driven by decompression and water loss at Stromboli Volcano (Aeolian Islands, Italy): Journal of Petrology, v. 42, p. 1471–1490.

Moore, P.L., Iverson, N.R., and Iverson, R.M., 2008, Frictional properties of the Mount St. Helens gouge, chap. 20 *of* Sherrod, D.R., Scott, W.E., and Stauffer, P.H., eds., A volcano rekindled; the renewed eruption of Mount St. Helens, 2004–2006: U.S. Geological Survey Professional Paper 1750 (this volume).

Moran, S.C., Malone, S.D., Qamar, A.I., Thelen, W.A., Wright, A.K., and Caplan-Auerbach, J., 2008, Seismicity associated with renewed dome building at Mount St. Helens, 2004–2005, chap. 2 *of* Sherrod, D.R., Scott, W.E., and Stauffer, P.H., eds., A volcano rekindled; the renewed eruption of Mount St. Helens, 2004–2006: U.S. Geological Survey Professional Paper 1750 (this volume).

Morgan, J.K., and Boettcher, M.S., 1999, Numerical simulations of granular shear zones using the distinct element method. 1. Shear zone kinematics and the micromechanics of localization: Journal of Geophysical Research, v. 104, p. 2703–2719.

Nakada, S., and Fujii, T., 1993, Preliminary report on the activity at Unzen Volcano (Japan), November 1990–November 1991; dacite lava domes and pyroclastic flows: Journal of Volcanology and Geothermal Research, v. 54, p. 319–333.

Nakada, S., and Motomura, Y., 1999, Petrology of the 1991–1995 eruption at Unzen—effusion pulsation and groundmass crystallization: Journal of Volcanology and Geothermal Research, v. 89, p. 173–196.

Nakada, S., Miyake, Y., Sato, H., Oshima, O., and Fujinawa, A., 1995a, Endogenous growth of dacite dome at Unzen volcano (Japan), 1993–1994: Geology, v. 23, no. 2, p. 157–160.

Nakada, S., Motomura, Y., and Shimizu, H., 1995b, Manner of magma ascent at Unzen Volcano (Japan): Geophysical Research Letters, v. 22, p. 567–570.

Neuberg, J.W., Tuffen, H., Collier, L., Green, D., Powell, T., and Dingwell, D., 2006, The trigger mechanism of low-frequency earthquakes on Montserrat: Journal of Volcanology and Geothermal Research, v. 153, nos. 1–2, p. 37–50, doi:10.1016/j.jvolgeores.2005.08.008.

Newhall, C.G., and Melson, W.G., 1983, Explosive activity associated with the growth of volcanic domes: Journal of Volcanology and Geothermal Research, v. 17, p. 111–131.

Pabst, A., 1931, Pressure-shadows and the measurement of the orientation of minerals in rocks: American Mineralogist, v. 16, p. 55–70.

Pallister, J.S., Reagan, M., and Cashman, K., 2005, A new eruptive cycle at Mount St. Helens?: Eos (American Geophysical Union Transactions), v. 86, no. 48, p. 499–500, doi:10.1029/2005EO480006.

Pallister, J.S., Thornber, C.R., Cashman, K.V., Clynne, M.A., Lowers, H.A., Mandeville, C.W., Brownfield, I.K., and Meeker, G.P., 2008, Petrology of the 2004–2006 Mount St. Helens lava dome—implications for magmatic plumbing and eruption triggering, chap. 30 *of* Sherrod, D.R., Scott, W.E., and Stauffer, P.H., eds., A volcano rekindled; the renewed eruption of Mount St. Helens, 2004–2006: U.S. Geological Survey Professional Paper 1750 (this volume).

Power, W.L., Tullis, T.E., and Weeks, J.D., 1988, Roughness and wear during brittle faulting: Journal of Geophysical Research, v. 93, no. B12, p. 15268–15278.

Prasher, C.L., 1987, Crushing and grinding process handbook: New York, John Wiley, 482 p.

Reches, Z., and Dewers, T.A., 2005, Gouge formation by dynamic pulverization during earthquake rupture: Earth and Planetary Science Letters, v. 235, p. 361–374.

Rowe, M.C., Thornber, C.R., and Kent, A.J.R., 2008, Identification and evolution of the juvenile component in 2004–2005 Mount St. Helens ash, chap. 29 *of* Sherrod, D.R., Scott, W.E., and Stauffer, P.H., eds., A volcano rekindled; the renewed eruption of Mount St. Helens, 2004–2006: U.S. Geological Survey Professional Paper 1750 (this volume).

Rutherford, M.J., and Devine, J.D., III, 2008, Magmatic conditions and processes in the storage zone of the 2004–2006 Mount St. Helens dacite, chap. 31 *of* Sherrod, D.R., Scott, W.E., and Stauffer, P.H., eds., A volcano rekindled; the renewed eruption of Mount St. Helens, 2004–2006: U.S. Geological Survey Professional Paper 1750 (this volume).

Sammis, C., and Biegel, R., 1989, Fractals, fault gouge and friction: Pure and Applied Geophysics, v. 131, p. 255–271.

Sammis, C., Osborne, R.H., Anderson, J.L., Banerdt, M., and White, P., 1986, Self-similar cataclasis in the formation of fault gouge: Pure and Applied Geophysics, v. 143, p. 54–77.

Sammis, C., King, G., and Biegel, R., 1987, The kinematics of gouge deformation: Pure and Applied Geophysics, v. 125, p. 777–812.

Schilling, S.P., Thompson, R.A., Messerich, J.A., and Iwatsubo, E.Y., 2008, Use of digital aerophotogrammetry to determine rates of lava dome growth, Mount St. Helens, Washington, 2004–2005, chap. 8 *of* Sherrod, D.R., Scott, W.E., and Stauffer, P.H., eds., A volcano rekindled; the renewed eruption of Mount St. Helens, 2004–2006: U.S. Geological Survey Professional Paper 1750 (this volume).

Schneider, D.J., Vallance, J.W., Wessels, R.L., Logan, M., and Ramsey, M.S., 2008, Use of thermal infrared imaging for monitoring renewed dome growth at Mount St. Helens, 2004, chap. 17 *of* Sherrod, D.R., Scott, W.E., and Stauffer, P.H., eds., A volcano rekindled; the renewed eruption of Mount St. Helens, 2004–2006: U.S. Geological Survey Professional Paper 1750 (this volume).

Scholz, C.H., 1990, The mechanics of earthquakes and faulting: New York, Cambridge University Press, 439 p.

Schulz, S.E., and Evans, J.P., 1998, Spatial variability in microscopic deformation and composition of the Punchbowl fault, southern California; implications for mechanism, fluid-rock interaction, and fault morphology: Tectonophysics, v. 295, p. 225–246.

Scott, W.E., Sherrod, D.R., and Gardner, C.A., 2008, Overview of the 2004 to 2006, and continuing, eruption of Mount St. Helens, Washington, chap. 1 *of* Sherrod, D.R., Scott, W.E., and Stauffer, P.H., eds., A volcano rekindled; the renewed eruption of Mount St. Helens, 2004–2006: U.S. Geological Survey Professional Paper 1750 (this volume).

Shepherd, E.S., and Merwin, H.E., 1927, Gases of the Mt. Pelée lavas of 1902: Journal of Geology, v. 35, p. 97–116.

Shipton, Z.K., and Cowie, P.A., 2003, A conceptual model for the origin of fault damage zone structures in high-porosity sandstone: Journal of Structural Geology, v. 25, p. 333–344.

Sibson, R.H., 1977, Fault rock and fault mechanisms: Journal of the Geological Society, London, v. 133, p. 191–213.

Sibson, R.H., 1986, Brecciation processes in fault zones; inferences from earthquake rupturing: Pure and Applied Geophysics, v. 124, p. 159–176.

Snoke, A.W., Tullis, J., and Todd, V.R., 1998, Fault-related rocks—a photographic atlas: Princeton, Princeton University Press, 617 p.

Sparks, R.S.J., Murphy, M.D., Lejeune, A.M., Watts, R.B., Barclay, J., and Young, S.R., 2000, Control on the emplacement of the andesite lava dome of the Soufrière Hills volcano, Montserrat by degassing-induced crystallization: Terra Nova, v. 12, no. 1, p. 14–20.

Stasiuk, M.V., Barclay, J., Carroll, M.R., Jaupart, C., Ratte, J.C., Sparks, R.S.J., and Tait, S.R., 1996, Degassing during magma ascent in the Mule Creek vent (USA): Bulletin of Volcanology, v. 58, p. 117–130.

Storti, F., Billi, A., and Salvini, F., 2003, Particle size distribution in natural carbonate fault rocks—insights for non-self-similar cataclasis: Earth and Planetary Science Letters, v. 206, p. 173–186.

Streck, M.J., Broderick, C.A., Thornber, C.R., Clynne, M.A., and Pallister, J.S., 2008, Plagioclase populations and zoning in dacite of the 2004–2005 Mount St. Helens eruption; constraints for magma origin and dynamics, chap. 34 *of* Sherrod, D.R., Scott, W.E., and Stauffer, P.H., eds., A volcano rekindled; the renewed eruption of Mount St. Helens, 2004–2006: U.S. Geological Survey Professional Paper 1750 (this volume).

Swanson, D.A., and Holcomb, R.T., 1990, Regularities in growth of the Mount St. Helens dacite dome, 1980–1986, *in* Fink, J.H., ed., Lava flows and domes, emplacement mechanisms and hazard implications: Berlin, Springer-Verlag, International Association of Volcanology and Chemistry of the Earth's Interior, Proceedings in Volcanology 2, p. 3–24.

Thornber, C.R., Pallister, J.S., Lowers, H.A., Rowe, M.C., Mandeville, C.W., and Meeker, G.P., 2008a, Chemistry, mineralogy, and petrology of amphibole in Mount St. Helens 2004–2006 dacite, chap. 32 *of* Sherrod, D.R., Scott, W.E., and Stauffer, P.H., eds., A volcano rekindled; the renewed eruption of Mount St. Helens, 2004–2006: U.S. Geological Survey Professional Paper 1750 (this volume).

Thornber, C.R., Pallister, J.S., Rowe, M.C., McConnell, S., Herriott, T.M., Eckberg, A., Stokes, W.C., Johnson Cornelius, D., Conrey, R.M., Hannah, T., Taggart, J.E., Jr., Adams, M., Lamothe, P.J., Budahn, J.R., and Knaack, C.M., 2008b, Catalog of Mount St. Helens 2004–2007 dome samples with major- and trace-element chemistry: U.S. Geological Survey Open-File Report 2008–1130, 9 p., with digital database.

Tuffen, H., and Dingwell, D., 2005, Fault textures in volcanic conduits—evidence for seismic trigger mechanisms during silicic eruptions: Bulletin of Volcanology, v. 67, p. 370–387.

Tuffen, H., Dingwell, D.B., and Pinkerton, H., 2003, Repeated fracture and healing of silicic magma generate flow banding and earthquakes?: Geology, v. 31, p. 1089–1092.

Turcotte, D.L., 1986, Fractals and fragmentation: Journal of Geophysical Research, v. 91, p. 1921–1926.

Turcotte, D.L., 1992, Fractals and chaos in geology and geophysics: Cambridge, Cambridge University Press, 221 p.

Vallance, J.W., Schneider, D.J., and Schilling, S.P., 2008, Growth of the 2004–2006 lava-dome complex at Mount St. Helens, Washington, chap. 9 *of* Sherrod, D.R., Scott, W.E., and Stauffer, P.H., eds., A volcano rekindled; the renewed eruption of Mount St. Helens, 2004–2006: U.S. Geological Survey Professional Paper 1750 (this volume).

Watts, R.B., Herd, R.A., Sparks, R.S.J., and Young, S.R., 2002, Growth patterns and emplacement of the andesitic lava dome at Soufrière Hills Volcano, Montserrat, *in* Druitt, T.H., and Kokelaar, B.P., eds., The eruption of Soufrière Hills Volcano, Montserrat from 1995 to 1999: Geological Society of London Memoir 21, p. 115–152.

Williams, H., 1932, The history and character of volcanic domes: University of California, Bulletin of the Department of Geological Sciences, v. 21, p. 51–146.

Wilson, B., Dewers, T., Reches, Z., and Brune, J., 2005, Particle size and energetics of gouge from earthquake rupture zones: Nature, v. 434, p. 749–752.

Wolf, K.J., and Eichelberger, J.C., 1997, Syneruptive mixing, degassing and crystallization at Redoubt Volcano, eruption of December 1989 to May, 1990: Journal of Volcanology and Geothermal Research, v. 75, p. 19–37.

Wong, T.-f., David, C., and Zhu, W., 1997, The transition from brittle faulting to cataclastic flow in porous sandstones—mechanical deformation: Journal of Geophysical Research, v. 102, no. B2, p. 3009–3025.

Yund, R.A., Blanpied, M.L., Tullis, T.E., and Weeks, J.D., 1990, Amorphous material in high strain experiment fault gouge: Journal of Geophysical Research, v. 95, p. 15589–15602.

A Volcano Rekindled: The Renewed Eruption of Mount St. Helens, 2004–2006
Edited by David R. Sherrod, William E. Scott, and Peter H. Stauffer
U.S. Geological Survey Professional Paper 1750, 2008

Chapter 20

Frictional Properties of the Mount St. Helens Gouge

By Peter L. Moore[1], Neal R. Iverson[1], and Richard M. Iverson[2]

Abstract

Frictional properties of gouge bounding the solid dacite plug that extruded at Mount St. Helens during 2004 and 2005 may have caused stick-slip upward motion of the plug and associated seismicity. Laboratory experiments were performed with a ring-shear device to test the dependence of the peak and steady-state frictional strength of the gouge on shearing rate and hold time. A remolded gouge specimen (~0.012 m^3) was sheared under constant normal stresses ranging from 5 to 200 kPa and at rates ranging from 10^{-6} to 10^{-3} m/s. The gouge exhibited rate-weakening behavior at rates lower than 1×10^{-4} m/s and rate-strengthening at rates above 5×10^{-4} m/s. Peak strengths occurred during the onset of shearing, when displacements were generally less than 0.5 mm. In slide-hold-slide tests, the peak strength of the gouge increased logarithmically as hold times increased from 3 s to almost 10^5 s.

Rate-weakening friction is a requirement for stick-slip behavior that is satisfied by the Mount St. Helens gouge. Indeed, regular stick-slip oscillations were observed in two experiments performed at the highest normal stress and lowest rates of shear. The conditions under which this stick-slip motion occurred indicate that the gouge also satisfies a second criterion for stick-slip behavior of materials exhibiting rate-and-state dependent friction—gouge stiffness exceeds that of the ascending magma that drives upward motion of the plug. The presence of highly compliant magma as a driving element may be crucial for generating stick-slip instabilities at the shallow earthquake focal depths observed during the eruption.

Introduction

Lava dome formation during the 2004–2005 eruption of Mount St. Helens was accompanied by abundant, nearly periodic, shallow-focus earthquakes. These “drumbeat” earthquakes had magnitudes <2, focal depths <1 km, and they typically recurred about every 1–2 minutes. This seismicity is thought to have resulted from incremental uplift of a solid dacite plug driven by magma ascent from below at rates of roughly 1–2 m^3/s (Iverson and others, 2006). Wear along the margin of the plug produced a layer of crushed rock, or gouge, of the same lithology as the extruding rock (fig. 1). Observed at the surface, this gouge formed a coating 0.1–1 m thick on freshly exposed faces of the lava dome. Moreover, these freshly exposed faces were conspicuously striated in directions mostly parallel to the direction of plug motion, indicating that gouge deformation probably accommodated much of the upward displacement of the plug mass. Interpretation of the source of drumbeat seismicity, therefore, requires knowledge of the frictional properties of this gouge.

Gouge is generated by the wear and cataclasis of rock during frictional shear and develops progressively with shear displacement (for example, Engelder, 1974). Although cataclasis may occur episodically in rapidly strained magma near its solidus (for example, Tuffen and Dingwell, 2005), granular gouge dredged from the margin of the new Mount St. Helens lava dome early in 2005 was cool, noncohesive, and bore evidence primarily of mechanical wear and comminution. Therefore, the frictional behavior of the gouge is likely similar to that of low-temperature gouge in shallow crustal faults. Consequently, frictional behavior observed in room-temperature laboratory experiments is relevant to interpreting dome extrusion processes during the 2004–2005 eruption of Mount St. Helens.

Theoretical Background

Rate- and State-Dependent Friction

Gouge behavior closely approximates that of a Coulomb material, such that its shear strength τ is described by $\tau = \mu\sigma'_n + c$, where σ'_n is the effective normal stress, c is cohe-

---

[1] Department of Geological and Atmospheric Sciences, Iowa State University, Ames, IA 50011

[2] U.S. Geological Survey, 1300 SE Cardinal Court, Vancouver, WA 98683

sion and μ is the coefficient of friction. In most granular media at low temperatures, μ can be considered nearly constant, but laboratory experiments have routinely shown that μ is slightly sensitive to both shear rate and the history of deformation. These deviations from a constant coefficient of friction are small but of great interest because under the appropriate conditions they give rise to an instability that may be responsible for earthquakes. In fault mechanics literature, these shear-rate and deformation-history effects are termed "rate" and "state" dependencies, respectively (see Marone, 1998, for a review).

Stemming from the work of Dieterich (1979) and Ruina (1983), the most common expression of the rate- and state-dependence of friction is

$$\mu = \mu_0 + a\ln\left(\frac{V}{V_0}\right) + b\ln\left(\frac{\theta V_0}{D_c}\right), \qquad (1)$$

where μ_0 is a reference coefficient of friction applicable at a reference shear displacement rate V_0, V is shear displacement rate (with dimensions of length/time), θ is a state variable (with dimensions of time), D_c is a characteristic slip distance over which friction adjusts to a steady state in response to a velocity change, and a and b are positive coefficients that are typically of order 10^{-3} to 10^{-2}. Individually, the parameters a and b describe the relative magnitude of the so-called "direct" and "evolution" effects, respectively. The direct effect is a near-instantaneous response of friction to a change in shear rate, whereas the evolution effect is a transient response that takes place over the characteristic length scale D_c. Note that in this paper, we use the term "shear rate" to denote shear displacement rates such as V. Where we wish to distinguish such rates from shear strain rates, which have dimensions of inverse time, we do so explicitly.

The state variable θ in equation 1 describes a time-dependent effect that can be viewed as the length of time that a set of grain contacts persists at a given velocity (Scholz, 2002). According to Dieterich (1979), the evolution of θ with time may be described by

$$\frac{d\theta}{dt} = 1 - \left(\frac{V\theta}{D_c}\right). \qquad (2)$$

Although the characteristic slip distance can be determined from stress-displacement data from experiments with bare rock, it is difficult to determine in experiments with gouge because this displacement depends on the strain distribution in the gouge (Marone and Kilgore, 1993). In a steady state ($d\theta/dt = 0$), $\theta = D_c/V$ and equation 1 reduces to

$$\mu_{ss} = \mu_0 + (a - b)\ln\left(\frac{V}{V_0}\right), \qquad (3)$$

where μ_{ss} is the steady-state friction coefficient. The sensitivity of steady-state frictional strength to shear rate, therefore, is given by the difference between the coefficients a and b for the direct and evolution effects:

$$a - b = \frac{\mu_{ss} - \mu_0}{\ln(V/V_0)}. \qquad (4)$$

If this difference is negative, the material weakens with increasing slip rate, and conversely, if $a - b$ is positive, the material strengthens with increasing slip rate (Scholz, 2002). The coefficients a and b are usually determined experimentally by conducting velocity-stepping triaxial or direct-shear experi-

Figure 1. Photograph of striated gouge near base of extruding spine at Mount St. Helens, July 28, 2005. Field of view approximately 20 m. USGS photo by S.P. Schilling.

ments in which shear rate is varied over a wide range during continuous shear.

Consistent with Dieterich's original reasoning (Dieterich, 1972, 1978, 1979), Beeler and others (1994) demonstrated that the parameter b can also be determined independently by measuring the variation in peak friction as a function of the time that shear is stopped ("hold time"), such that

$$b = \frac{d\mu_{\text{peak}}}{d\ln(t_{\text{hold}})} \; . \qquad (5)$$

Peak shear strength typically increases logarithmically with time as sliding surfaces are held in stationary contact. The mechanisms responsible for this aging effect are thought to be associated with compaction and growth of the area of solid-to-solid grain contact across the shear zone (Losert and others, 2000; Scholz, 2002).

Relation Between Gouge Frictional Behavior and Seismicity

If gouge becomes weaker as shear rate increases ($a - b < 0$), slip instability and stick-slip motion are possible, but according to the rate-and-state dependent friction model, rate weakening alone is not sufficient to induce stick-slip behavior (Rice and Ruina, 1983; Ruina, 1983). The stiffnesses of the gouge and the system that loads the gouge are also important. The decline from peak (static) frictional strength to steady-state (dynamic) strength of the gouge requires a finite displacement that exceeds but is proportional to the characteristic slip distance, D_c. If elastic strain in the materials loading the shear zone is relaxed over a displacement larger than D_c, the applied driving stress momentarily exceeds the resisting stress and slip accelerates until driving and resisting stresses become equal (fig. 2). As defined by Ruina (1983), the "critical stiffness" of the gouge, k_{crit}, is the ratio of shearing-resistance decline to characteristic slip distance upon a change in slip velocity, and k_{crit} has dimensions of stress per unit length. If the loading system requires a slip distance much greater than D_c to reduce the applied stress from the peak to steady-state strength, the loading system's stiffness is smaller than k_c and stick-slip behavior is possible (fig. 2).

According to the arguments summarized above, repetitive stick-slip motion along the subsurface margins of the extruding dacite plug at Mount St. Helens can occur if two conditions are met—(1) the gouge must exhibit rate-weakening behavior at the imposed loading rate, and (2) the most compliant component of the loading system (that is, the magma) must have a stiffness smaller than the critical stiffness of the gouge. The first requirement is readily evaluated with our laboratory experiments. The second requirement is more difficult to address, but our experiments and inferences about the magma-plug system at Mount St. Helens provide some constraints.

Experimental Methods

Gouge was obtained by dredging the surface of the newly extruded spine at Mount St. Helens by helicopter in February 2005. Ring-shear tests were performed at room temperature with dry, remolded specimens. Particles with diameters larger than one-tenth the smallest dimension of the specimen chamber (70 mm) were removed from the gouge, consistent with normal geotechnical testing procedure (Head, 1989). Shearing rates and normal stresses were varied among tests through the ranges permitted by the device (5×10^{-3} to 1.5×10^{-6} m/s and 5 to 195 kPa respectively). These experiments differed from velocity-stepping tests (for example, Blanpied and others, 1987; Biegel and others 1989; Marone and others, 1990) in that shear-rate changes were made only after first stopping shear.

The ring-shear device (detailed in Iverson and others, 1997) has been used to study the mechanical properties of a variety of granular geological materials (for example, Iverson and others, 1998; Iverson and others, 2000; Moore and Iverson, 2002; Scherer and others, 2004). Its large capacity permits inclusion of larger particles that are common in gouge, but the test specimen's large surface area limits the magnitude

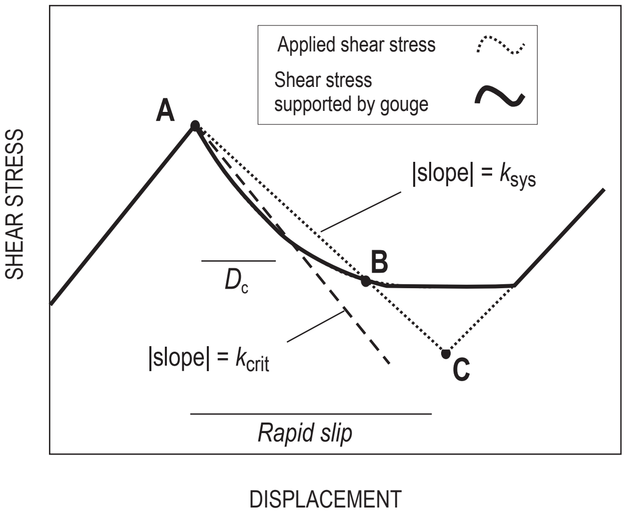

Figure 2. Stress applied by the loading system and shear stress supported by gouge during a stick-slip cycle. When slip commences at A, strength of the gouge initially declines more rapidly than the stress applied by the loading system, and acceleration occurs. When driving and resisting forces are equal again at B, slip begins to decelerate and stops at C. Slope of the decline in applied stress with displacement is the stiffness of the system (k_{sys}). When this stiffness is smaller than the critical stiffness of the gouge k_{crit} as defined by the shear stress decline and the gouge's characteristic slip distance D_c, the system is susceptible to stick-slip. D_c is the characteristic distance of exponential decay of gouge shearing resistance during rapid slip (after Scholz, 2002).

of the normal stress that can be applied. The ~70-mm-thick specimen rests in an annular chamber (annulus OD = 0.600 m, ID = 0.370 m) and is gripped at its base by a toothed platen (fig. 3). This platen is screwed to a base plate, and it and the lower walls bounding the specimen rotate. The toothed lid of the specimen chamber is prevented from rotating with the base by a pair of stationary, horizontally oriented load cells, causing the specimen to shear. The force exerted by the lid on these load cells is approximately the shear force supported by the specimen. Shear is focused in a lens-shaped zone that is 10–30 mm in thickness at the centerline of the specimen and is centered on the sliding interface between the upper and lower walls (fig. 3*B*) (for example, Hooyer and Iverson, 2000). A stress normal to the shearing direction is applied with a lever system that presses downward on the lid (fig. 3*A*). The lid is free to move vertically if the porosity of the specimen changes, and this vertical displacement is measured continuously with three equally spaced linear variable displacement transducers (LVDTs) that press on the perimeter of the lid.

Vertical and circumferential frictional forces between the gouge and the upper walls bounding the specimen are measured independently with a load cell and torque sensor, respectively, which are contained within a suspension called the "yoke" (fig. 3*A*). The yoke holds the upper walls stationary and is not coupled to the lid. The measured forces on the walls are used to correct both the normal stress applied to the shear zone, which is reduced by upward wall drag in a consolidating specimen, and the shear resistance on the lid, which is reduced due to circumferential drag between the specimen and walls. However, owing to extrusion of fine sediment along the interface between the upper and lower walls, a component of the measured circumferential wall force is due to friction between the upper and lower walls rather than between the upper wall and specimen. Thus, when applied normal stress is small, this friction represents an unknown fraction of the wall correction necessary to estimate the total resistance to shear. As a result, in experiments with the smallest applied normal stresses (5–23 kPa), uncertainty in the measured shear stresses and associated friction coefficients is large. Despite the uncertainty, these low-stress measurements are, nevertheless, included to qualitatively illustrate patterns that are available only from the low-stress tests.

Two variable-speed electric motors (1/17 and 1/2 hp) were used to turn the base and thereby shear the gouge specimen. Used in combination with either one or two gearboxes, these motors enabled two ranges of shear rate—1.5×10^{-6} –2.5×10^{-5} m/s and 5.0×10^{-4}–5.0×10^{-3} m/s. The higher-power motor coupled to a single gearbox allowed shearing at the higher range of rates, but this configuration could not deliver sufficient torque to shear the gouge under normal stresses greater than 23 kPa. When the smaller motor was used with both gearboxes normal stresses of as much as 200 kPa could be applied. At higher normal stresses this motor/gearbox configuration was not sufficient to turn the rotating base.

Two groups of experiments were conducted. In one group designed to investigate the rate dependence of gouge friction, shear was driven at a constant rate until shearing resistance became steady, usually after 1–10 mm of total centerline displacement. Shear was then stopped to adjust the motor speed and restarted under the same normal stress, but at a new rate, until shearing resistance again became steady. This process was repeated at multiple shearing rates, and whenever possible tests were repeated in sequences of increasing and decreasing shear rate. In a second group of experiments, periods of shear, which were terminated once shearing resistance became steady, were separated by intervals of hold (no shear) that ranged from 3 seconds to more than one day. In these experiments, shear rate and normal stress were held constant so that the effects of hold time on peak friction could be isolated.

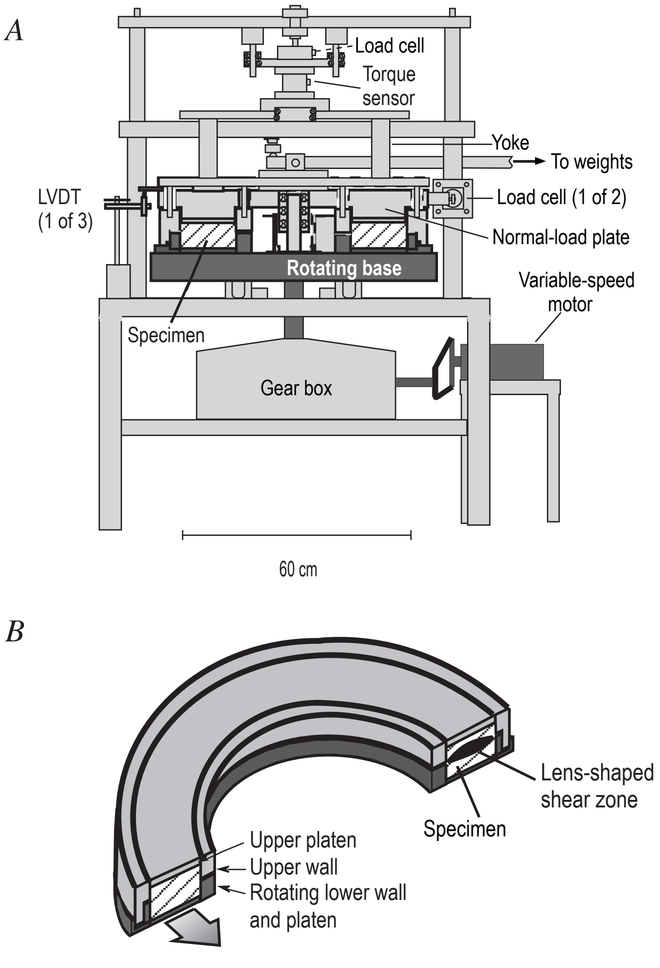

Figure 3. Ring-shear device. Gouge specimen is shown in cross-hachure. *A*, Diagrammatic cross section. Dark-gray parts rotate when motor is on. A second gearbox between motor and large gearbox was used in the experiments conducted at low shear rates (1.5×10^{-6} – 2.5×10^{-5} m/s). LVDT, linear variable displacement transducers. *B*, Oblique sketch of the specimen chamber. Shearing in gouge typically is focused in a lens-shaped zone, shown in black, centered on interface between stationary upper wall and rotating lower wall.

After some of the experiments, the gouge was sieved to measure whether there had been a size reduction of the largest grains; no size reduction could be detected indicating that little comminution or crushing occurred in the experiments.

Results

Data obtained in two typical ring-shear experiments, conducted at different shear rates under an applied normal stress of 159 kPa, are shown in figure 4. Following initial stress peaks related to the "direct effect" of changing shear rate, shear stress became approximately steady after displacements of less than 10 mm. The key feature illustrated by these two data series is that the steady-state shear strength of the gouge was smaller at the faster shear rate. For rates smaller than 10^{-4} m/s, such rate weakening was always observed, except for experiments conducted at a normal stress of 23 kPa in which the shear-rate dependence was neutral or slightly positive, depending on how the data are regressed (fig. 5). In the two sets of experiments conducted at faster shearing rates and low normal stresses, rate strengthening was observed (fig. 5*B*). Unfortunately, because of the torque limitations of our motor/gearbox configurations, the shear rate at which the transition to rate strengthening occurs cannot be pinpointed, but it appears to be on the order of 10^{-4} m/s for the range of stresses considered. As described previously, measurements at the lowest applied normal stresses are uncertain, but the consistently larger apparent friction coefficient at normal stresses of 5 kPa may indicate that the gouge has some cohesion. (Cohesion of about 1 kPa would decrease the apparent friction coefficient at 5 kPa to about 0.4 or 0.5, comparable to values measured at higher normal stresses.) Alternatively, the larger friction coefficient at 5 kPa may reflect steepening of the Coulomb failure envelope that is commonly observed at low normal stresses in various laboratory tests on granular materials (Lambe and Whitman, 1969).

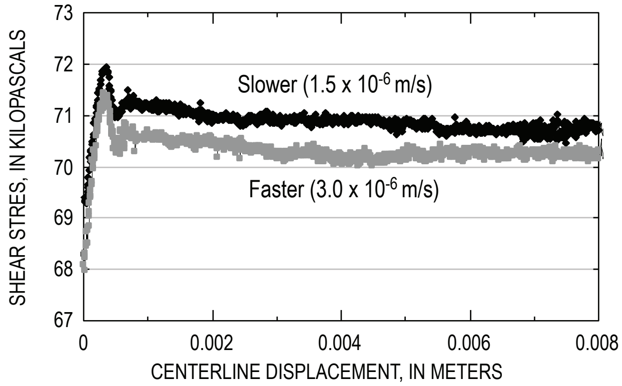

Figure 4. Stress-displacement data comparing two experiments conducted at normal stress of 159 kPa but at different shear rates. Prominent peaks in curves at ~0.5 mm of displacement are peak shear stresses, after which shear stress falls to steady-state value in both experiments.

Values of the rate-dependence parameter *a–b* were estimated for each normal-stress level using equation 4 and a reference shear rate of 1.5×10^{-6} m/s, the smallest shear rate used in the experiments (table 1). Each value of *a–b* was obtained from the slope of the linear regression of the steady-state friction coefficient against $\ln(V/V_0)$. Data from the "slow" (1.5×10^{-6} m/s to 2.5×10^{-5} m/s) and "fast" (5×10^{-4} m/s to 5×10^{-3} m/s) experiments were regressed separately. Values of *a–b* at slow rates and high normal stresses (86–195 kPa) range from −0.0013 to −0.0103, indicating various degrees of rate weakening (fig. 5*A*).

In most of the ring-shear experiments, after a few millimeters of displacement, the shearing resistance of the gouge did not vary systematically, much as in the examples shown in figure 4. However, in the two experiments conducted at the largest normal stress and lowest shear rates, no steady shear stress developed. Instead, shear proceeded by regular stick-slip episodes (fig. 6). Major slip events were accompanied by abrupt consolidation, whereas dilation appeared to occur during "stick" intervals. Apparently the normal stresses and shear rates of these two experiments produced gouge stiffness and rate weakening that met both requirements for stick-slip behavior outlined previously.

In two sets of slide-hold-slide tests at a single shear rate and normal stress, peak strength increased logarithmically with hold time (fig. 7). Fitting these data to equation 5 indicates that $b = 0.0079$ (table 1). Hold time was also recorded during the variable-rate tests and, although these data have more scatter (perhaps due to a dependence of b on shear rate), they indicate a $b = 0.0075$. During hold periods compaction of the gouge was generally not observed, indicating either that growth of contact area between grains may not have been the key aging mechanism or that this effect was too subtle to be measured.

Discussion

Results of our ring-shear tests indicate that the Mount St. Helens gouge exhibits rate weakening at shear rates below about 10^{-4} m/s. At these rates, the magnitude of $a - b$ is comparable to typical published values for fault gouges, which vary from –0.001 to –0.01 (for example, Blanpied and others, 1987; Kilgore and others, 1993). Above 10^{-4} m/s and at the lowest normal stresses of these experiments, $a - b$ is positive, indicating that the gouge is rate strengthening. The apparent transition from negative to positive values of $a - b$ occurs at a shear rate similar to the same transition documented for other rock and gouge shear zones (for example, Shimamoto, 1986; Blanpied and others, 1987; Kilgore and others, 1993).

The transition shear rate in our experiments is only moderately larger than the rate of extrusion estimated for much of the 2004–2005 eruption (3×10^{-5} m/s to 7×10^{-5} m/s), but two observations indicate that gouge shear rates at Mount St. Helens may be well within the rate-weakening regime. Kilgore and others (1993) noted that the transition shear rate increases with increasing normal stress. Because normal stresses in our experiments were probably at least one order of magnitude smaller than those on the margins of the magma plug at depths of 100–500 m at Mount St. Helens (2–10 MPa), rate-weakening behavior at Mount St. Helens would likely be exhibited at higher shear rates than those of the experiments. Secondly, Marone and Kilgore (1993) showed that the characteristic slip distance D_c is more appropriately viewed as a characteristic shear strain (shear displacement divided by the shear-zone thickness) when considering shear within a gouge layer. In ring-shear experiments on the Mount St. Helens gouge in which we placed vertical columns of beads in the gouge to study the shear-strain distribution, more than 90 percent of the strain was distributed over a thickness of 10 mm. At Mount St. Helens, the shear-zone thickness is likely larger, given the ~1 m total thickness of the gouge layer and presence of particles too large to include in the ring-shear experiments. Thus, shear-strain rates in the ring-shear experiments were likely larger at a particular shear rate than those at Mount St. Helens, indicating that the gouge there would likely rate-weaken at higher shear rates than it did in the experiments. Thus, one of the conditions required for stick-slip ascent of the dacite plug—rate weakening of the gouge—appears to be met.

Table 1. Rate-dependence parameters.

[Value *a–b* describes sign and magnitude of rate dependence of gouge friction. The *b* value alone describes magnitude of gouge strengthening as a function of hold time.]

Normal stress (kPa)	Shear-rate range (m/s)	*a–b*	*b*
Fast			
5	$5 \times 10^{-4} - 5\times10^{-3}$	0.0150	
23	$5 \times 10^{-4} - 5\times10^{-3}$	0.0105	
Slow			
5	$1.5 \times 10^{-6} - 2.5\times10^{-5}$	–0.0250	
23	$1.5 \times 10^{-6} - 2.5\times10^{-5}$	0.00099	
86	$1.5 \times 10^{-6} - 2.5\times10^{-5}$	–0.0022	
141	$1.5 \times 10^{-6} - 2.5\times10^{-5}$	–0.0013	
159	$1.5 \times 10^{-6} - 2.5\times10^{-5}$	–0.0024	0.0079
195	$1.5 \times 10^{-6} - 2.5\times10^{-5}$	–0.0103	

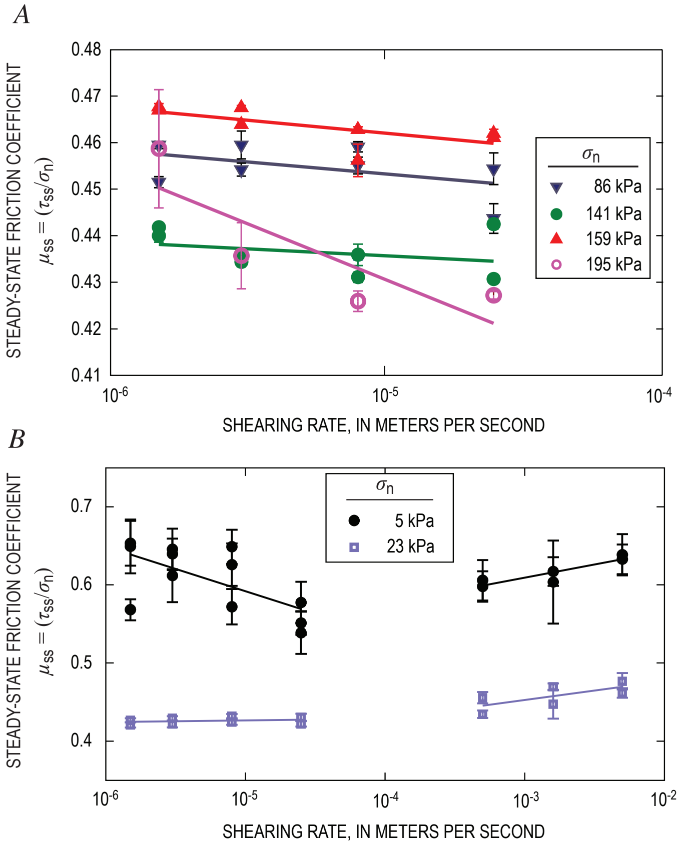

Figure 5. Steady-state friction coefficient as a function of shear rate. Each data point represents results of one experiment. Steady-state friction coefficient is shear stress supported by the gouge divided by corrected normal stress, both averaged over the part of experiment when time-averaged steady state had been attained (see fig. 4). Data are grouped by magnitude of applied normal stress. Error bars represent ±1 standard deviation of observed variability in friction coefficient during the period of the time-averaged steady state. *A*, High applied normal stresses. *B*, Low applied normal stresses.

We now consider the second condition—that the stiffness of the loading system must be smaller than the critical stiffness defined by the evolution behavior of the gouge. Assessment of this condition requires independent estimates of both the in situ critical stiffness k_{crit} of the gouge and the stiffness k_{sys} of the magma that is driving extrusion.

The critical stiffness of the gouge was defined by Ruina (1983) as the post-peak reduction in shear stress divided by the characteristic slip distance over which this reduction occurs:

$$k_{\text{crit}} = \frac{-(a-b)\sigma'_n}{D_c}, \qquad \text{for } (a-b) < 0. \qquad (6)$$

If a lithostatic stress state is assumed at the nucleation depth of the drumbeat earthquakes (~500 m) and pore-water pressure is neglected, such that the total normal stress equals the effective normal stress, then σ'_n ~10 MPa. A reasonable value of *a–b* indicated by our experimental results is –0.003. The characteristic slip distance D_c can be determined from the transition from steady slip to persistent stick-slip behavior that occurred in our experiments with high normal stresses. At this transition the experimental normal stress was 195 kPa (table 1), and k_{crit} equaled the stiffness of the test device. This stiffness is approximately 1.7×10^4 kPa/m (see appendix 1). (Here, again following Ruina (1983), we employ a stiffness having dimensions of stress per unit length (that is, mass/(time^2×length^2))). Substituting this value for k_{crit}, $a-b = -0.003$ and the experimental value of σ'_n (195 kPa) in equation 6 yields $D_c = 34$ µm, which is of the same order as typical laboratory values for gouge (for example, Marone and Kilgore, 1993). Assuming that $D_c = 34$ µm, $a-b = -0.003$, and $\sigma'_n = 10$ MPa are appropri-

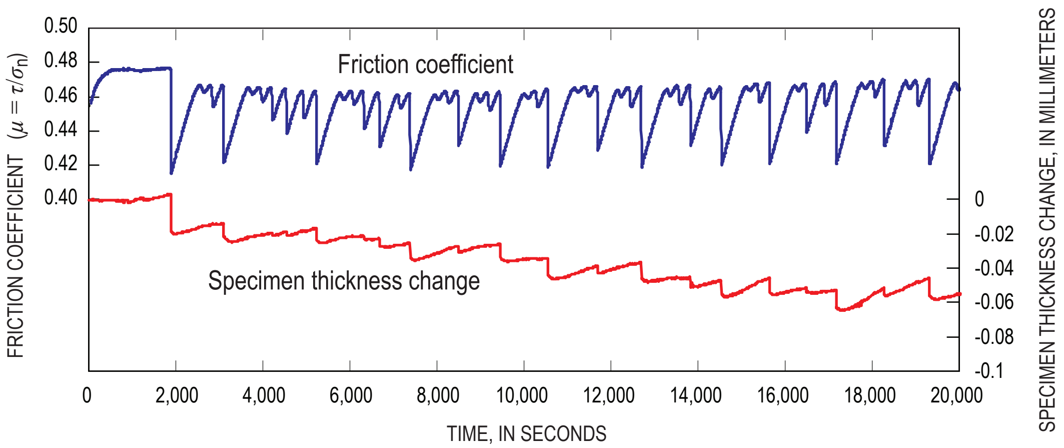

Figure 6. Part of one record of stick slip from experiments conducted at the two lowest shear rates (1.5×10^{-6} and 3.0×10^{-6} m/s) at 195 kPa normal stress. No direct measurement was made of displacement of the rotating base during these tests, so stick-slip displacement was inferred from shear-stress and specimen thickness records.

ate for the in situ gouge at Mount St. Helens, then equation 6 yields an in situ critical gouge stiffness of ~10^6 kPa/m.

To estimate the stiffness of the loading system, we assume that magma underlying the plug drives extrusion (fig. 8), and that the magma contains about 12 percent exsolved gas by volume (T. Gerlach, oral commun., 2005) and has a compressibility $\alpha = 10^{-4}$ per kPa (Iverson, this volume, chap. 21). The pertinent stiffness k is the magmatic "spring force" per unit area of plug-margin slip surface divided by the "spring displacement" associated with magma compression-relaxation cycles (compare with Ruina, 1983). To estimate this k, we approximate the magma body as a right circular column with height $H = 8{,}000$ m and cross sectional area $A=1/4(\pi d^2)$, where d is the mean column diameter, and we approximate the area of the slip surface on the margins of the plug as πdh, where h is the height of the plug in contact with the conduit walls. The spring force associated with magma compression is $(A/\alpha)(\delta/H)$, where δ is the characteristic displacement associated with magma compression or relaxation, and δ/H is the accompanying longitudinal strain of the magma column. Thus, the spring force per unit area of slip surface is $d\delta/(4\alpha hH)$, and dividing this expression by the displacement distance δ yields

$$k = d/(4\alpha hH). \qquad (7)$$

If h is 500 m, and d is 50 m (these values are probably of the correct order of magnitude for the geometry at Mount St. Helens), then inserting these values and the α and H values noted above into equation 7 yields k ~10^{-1} kPa/m, seven orders of magnitude smaller than the critical gouge stiffness k_{crit} ~10^6 kPa/m. Therefore, even if the estimated values of magma compressibility or the geometrical parameters d, h, and H are greatly in error, the gouge is likely much stiffer than the magma column that drives upward movement of the plug. Thus, in addition to rate weakening of the gouge, the second requirement for stick-slip—that the critical stiffness of the gouge exceeds the stiffness of some part of the loading system—is likely satisfied.

The finding that the magma-plug system can exhibit stick-slip behavior at shallow depths contrasts with the common observation that fault slip is aseismic within ~2 km of the surface (Scholz, 2002). The tendency for aseismic tectonic fault slip at shallow depths is commonly attributed either to rate strengthening in unconsolidated gouge or to the dependence of critical stiffness on normal stress, which is low near Earth's surface (Marone and Scholz, 1988; Scholz, 2002). Our results indicate that the Mount St. Helens gouge is rate weakening and the loading-system stiffness is exceptionally small owing to the presence of a large body of highly compressible magma. Therefore, stick-slip behavior should be possible at much smaller depths at Mount St. Helens than would be predicted for tectonically driven crustal faults.

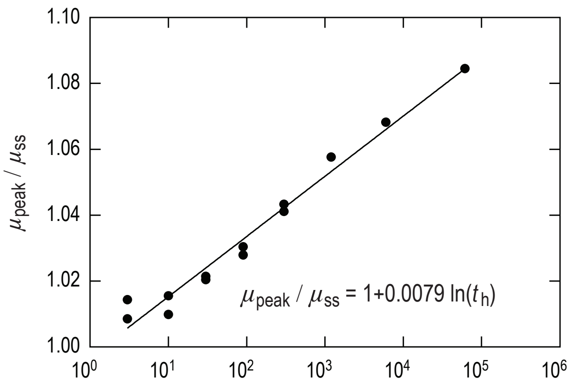

Figure 7. Normalized peak friction coefficient, μ_{peak}, as a function of logarithm of hold time. Standard error of b-value (slope of the regression) is 0.0004. All tests were at a normal stress of 159 kPa and shear rate of 2.5×10^{-5} m/s.

Conclusions

Under normal stresses less than about 200 kPa, gouge sampled from the surface of the newly extruded Mount St. Helens dome in February 2005 exhibits frictional behavior that is described well by the rate- and state-dependent friction model. In our ring-shear device the gouge weakens with increasing steady shear rates up to about 10^{-4} m/s and strengthens at larger shear rates. This transition from weakening to strengthening occurs at an experimental shear rate only moderately larger than the observed time-averaged rate of extrusion at Mount St. Helens, but in situ the transition probably occurs at higher shear rates because in situ normal stresses in the gouge are probably significantly larger than those that could be applied experimentally. Also, the in situ stiffness of the gouge, as estimated using the conditions under which stick-slip occurred in the experiments, is roughly seven orders of magnitude greater than the stiffness of the most compliant component of the system driving uplift of the plug: the underlying magma. The rate weakening and high stiffness of the gouge relative to the magma are requirements for stick-slip behavior when rate-and-state dependent friction is present, so stick-slip behavior provides a viable hypothesis for the source of the observed shallow drumbeat earthquakes at Mount St. Helens. In addition, experiments showed that the peak strength of the gouge increased logarithmically with hold time, indicating that deformation history of the gouge could influence the character of stick-slip behavior and associated seismicity.

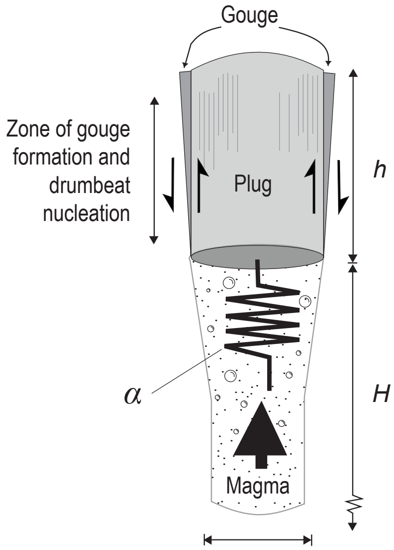

Figure 8. Schematic illustration of hypothesized magma-plug system at Mount St. Helens. Cool, rigid dacite plug is driven upward through upper conduit by ascending compressible magma. Gouge forms by frictional wear at interface between extruding plug and conduit. Because the gouge is stiffer than effective stiffness of the magma that is driving plug uplift, uplift occurs in stick-slip cycles, producing drumbeat earthquakes. Physical and geometrical variables (letters and symbols on figure) are discussed in text.

Acknowledgments

We thank John Pallister for collection of gouge samples from Mount St. Helens. Technical reviews by Nick Beeler and John Power and editorial suggestions by Jim Hendley significantly improved this paper.

References Cited

Beeler, N.M., Tullis, T.E., and Weeks, J.D., 1994, The roles of time and displacement in the evolution effect in rock friction: Geophysical Research Letters, v. 21, no. 18, p. 1987–1990.

Biegel, R.L., Sammis, C.G., and Dieterich, J.H., 1989, The frictional properties of a simulated gouge having a fractal particle distribution: Journal of Structural Geology, v. 11, no 7, p. 827–846.

Blanpied, M.L., Tullis, T.E., and Weeks, J.D., 1987, Frictional behavior of granite at low and high sliding velocities: Geophysical Research Letters, v. 15, no. 5, p. 554–557.

Dieterich, J.H., 1972, Time dependence of rock friction: Journal of Geophysical Research, v. 77, p. 3690–3697.

Dieterich, J.H., 1978, Time dependent friction and the mechanics of stick-slip: Pure and Applied Geophysics, v. 116, p. 790–806.

Dieterich, J.H., 1979, Modeling of rock friction 1—experimental results and constitutive equations: Journal of Geophysical Research, v. 84, no. B5, p. 2161–2168.

Engelder, J.T., 1974, Cataclasis and the generation of fault gouge: Geological Society of America Bulletin, v. 85, p. 1515–1522.

Head, K.H., 1989, Soil technician's handbook: New York, John Wiley, 83 p.

Hooyer, T.S., and Iverson, N.R., 2000, Clast-fabric development in a shearing granular material—implications for subglacial till and fault gouge: Geological Society of America Bulletin, v. 112, no. 5, p. 683–692.

Iverson, R.M., 2008, Dynamics of seismogenic volcanic extrusion resisted by a solid surface plug, Mount St. Helens, 2004–2005, chap. 21 *of* Sherrod, D.R., Scott, W.E., and Stauffer, P.H., eds., A volcano rekindled; the renewed eruption of Mount St. Helens, 2004–2006: U.S. Geological Survey Professional Paper 1750 (this volume).

Iverson, N.R., Baker, R.W., and Hooyer, T.S., 1997, A ring-shear device for the study of till deformation—tests on tills with contrasting clay contents: Quaternary Science Reviews, v. 16, no. 9, p. 1057–1066.

Iverson, N.R., Hooyer, T.S., and Baker, R.W., 1998, Ring-shear studies of till deformation—Coulomb-plastic behavior and distributed strain in glacier beds: Journal of Glaciology, v. 16, p. 1057–1066.

Iverson, R.M., Reid, M.E., Iverson, N.R., LaHusen, R.G., Logan, M., Mann, J.E., and Brien, D.L., 2000, Acute sensitivity of landslide rates to initial porosity: Science, v. 290, p. 513–516.

Iverson, R.M., Dzurisin, D., Gardner, C.A., Gerlach, T.M., LaHusen, R.G., Lisowski, M., Major, J.J., Malone, S.D., Messerich, J.A., Moran, S.C., Pallister, J.S., Qamar, A.I., Schilling, S.P., and Vallance, J.W., 2006, Dynamics of seismogenic volcanic extrusion at Mount St. Helens in 2004–05: Nature, v. 444, no. 7118, p. 439–443, doi:10.1038/nature05322.

Kilgore, B.D., Blanpied, M.L., and Dieterich, J.H., 1993, Velocity dependent friction of granite over a wide range of conditions: Geophysical Research Letters, v. 20, no. 10, p. 903–906.

Lambe, T.W., and Whitman, R.V., 1969, Soil Mechanics: New York, John Wiley, 553 p.

Losert, W., Géminard, J.-C., Nasuno, S., and Gollub, J.P., 2000, Mechanisms for slow strengthening in granular materials: Physical Review E, v. 61, no. 4, p. 4060–4068.

Marone, C., 1998, Laboratory-derived friction laws and their application to seismic faulting: Annual Reviews of Earth and Planetary Science, v. 26, p. 643–696.

Marone, C., and Kilgore, B., 1993, Scaling of the critical slip distance for seismic faulting with shear strain in fault zones: Nature, v. 362, p. 618–620.

Marone, C., and Scholz, C.H., 1988, The depth of seismic faulting and the upper transition from stable to unstable slip regimes: Geophysical Research Letters, v. 15, no. 6, p. 621–624.

Marone, C., Raleigh, C.B., and Scholz, C.H., 1990, Frictional behavior and constitutive modeling of simulated fault gouge: Journal of Geophysical Research, v. 95, no. B5, p. 7007–7025.

Moore, P.L., and Iverson, N.R., 2002, Slow episodic shear of granular materials regulated by dilatant strengthening: Geology, v. 30, p. 843–846.

Rice, J.R., and Ruina, A., 1983, Stability of steady frictional slipping: Journal of Applied Mechanics, v. 50, p. 343–349.

Ruina, A., 1983, Slip instability and state variable friction laws: Journal of Geophysical Research, v. 88, no. B12, p. 10359–10370.

Scherer, R.P., Sjunneskog, C.M., Iverson, N.R., and Hooyer, T.S., 2004, Assessing subglacial processes from diatom fragmentation patterns: Geology, v. 32, p. 557–560.

Scholz, C.H., 2002, Mechanics of earthquakes and faulting (2d ed.): New York, Cambridge University Press, 471 p.

Shimamoto, T., 1986, Transition between frictional slip and ductile flow for halite shear zones at room temperature: Science, v. 231, p. 711–714.

Tuffen, H., and Dingwell, D., 2005, Fault textures in volcanic conduits; evidence for seismic trigger mechanisms during silicic eruptions: Bulletin of Volcanology, v. 67, p. 370–387.

Appendix 1. Stiffness of the Ring-Shear Device

The stiffness of the ring-shear device can be estimated from stress-displacement transients that were common when shearing was initiated in experiments conducted at the highest normal stresses. Particularly after extended hold periods, the start of shear was characterized by sudden stress reductions that accompanied abrupt slip (fig. 9). Abrupt slip displacement was measured with a horizontally oriented LVDT that pressed on an armature extending from the rotating base of the device. This abrupt displacement of the rotating base occurred despite the constant speed of the motor driving the rotation of the base. These events reflect the release of elastic strain energy stored in the drive mechanism of the device, and therefore the ratio of abrupt stress reduction to abrupt slip describes the device stiffness, as applicable to the rate-and-state model of Ruina (1983)—1.7×10^4 kPa/m.

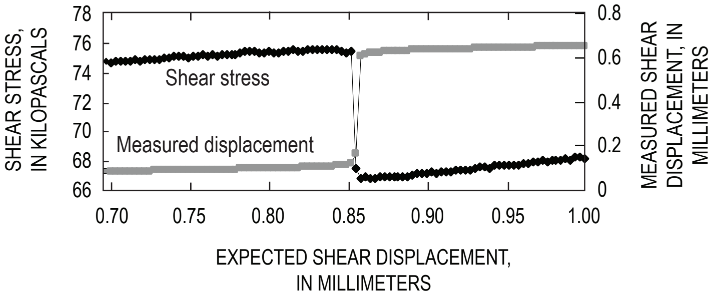

Figure 9. Shear stress and measured shear displacement during initial minutes of a ring-shear test conducted at a normal stress of 159 kPa. Data are plotted as a function of expected shear displacement calculated from rotation rate of motor that drives rotating base (fig. 3). Data begin when motor was actively driving rotation, but no displacement was measured at perimeter of the rotating base. During subsequent abrupt slip, there was a marked reduction in measured shear stress, well below steady-state strength of the gouge. This stress reduction and associated abrupt displacement are interpreted to reflect elastic compliance of the device.

A Volcano Rekindled: The Renewed Eruption of Mount St. Helens, 2004–2006
Edited by David R. Sherrod, William E. Scott, and Peter H. Stauffer
U.S. Geological Survey Professional Paper 1750, 2008

Chapter 21

Dynamics of Seismogenic Volcanic Extrusion Resisted by a Solid Surface Plug, Mount St. Helens, 2004–2005

By Richard M. Iverson[1]

Abstract

The 2004–5 eruption of Mount St. Helens exhibited sustained, near-equilibrium behavior characterized by nearly steady extrusion of a solid dacite plug and nearly periodic occurrence of shallow earthquakes. Diverse data support the hypothesis that these earthquakes resulted from stick-slip motion along the margins of the plug as it was forced incrementally upward by ascending, solidifying, gas-poor magma. I formalize this hypothesis with a mathematical model derived by assuming that magma enters the base of the eruption conduit at a steady rate, invoking conservation of mass and momentum of the magma and plug, and postulating simple constitutive equations that describe magma and conduit compressibilities and friction along the plug margins. Reduction of the model equations reveals a strong mathematical analogy between the dynamics of the magma-plug system and those of a variably damped oscillator. Oscillations in extrusion velocity result from the interaction of plug inertia, a variable upward force due to magma pressure, and a downward force due to the plug weight. Damping of oscillations depends mostly on plug-boundary friction, and oscillations grow unstably if friction exhibits rate weakening similar to that observed in experiments. When growth of oscillations causes the extrusion rate to reach zero, however, gravity causes friction to reverse direction, and this reversal instigates a transition from unstable oscillations to self-regulating stick-slip cycles. The transition occurs irrespective of the details of rate-weakening behavior, and repetitive stick-slip cycles are, therefore, robust features of the system's dynamics. The presence of a highly compressible elastic driving element (that is, magma containing bubbles) appears crucial for enabling seismogenic slip events to occur repeatedly at the shallow earthquake focal depths (<1 km) observed during the 2004–5 eruption. Computations show that fluctuations in magma pressure accompanying such slip events are <3 kPa, indicating that deviations from mechanical equilibrium are slight and that coseismic force drops are $<10^8$ N. These results imply that the system's self-regulating behavior is not susceptible to dramatic change—provided that the rate of magma ascent remains similar to the rate of magma accretion at the base of the plug, that plug surface erosion more or less compensates for mass gain due to basal accretion, and that magma and rock properties do not change significantly. Even if disequilibrium initial conditions are imposed, the dynamics of the magma-plug system are strongly attracted to self-regulating stick-slip cycles, although this self-regulating behavior can be bypassed on the way to runaway behavior if the initial state is too far from equilibrium.

Introduction

The dome-building eruption of Mount St. Helens that began in October 2004 was remarkable in several respects. This paper describes formulation, analysis, and predictions of a mechanistic model that links three key aspects of the eruption. The first and perhaps most striking of these aspects was extrusion of solid rock that emerged from the crater floor as a sequence of spines with conspicuous fault gouge and striations on their freshly exposed bounding surfaces. Second, extrusion proceeded at a nearly constant long-term rate (~1–2 m^3/s) that was sustained from December 2004 through at least December 2005. Third, extrusion was accompanied by more than a million small earthquakes that occurred almost periodically at hypocentral locations <1 km beneath the extruding dome. These eruption characteristics motivate the hypothesis that extrusion was driven by a nearly constant influx of magma at depth and resisted by a plug of solidified magma that slipped incrementally and seismogenically against the wall rock forming the upper parts of the magma conduit. I refer to this hypothesis as SPASM, an acronym for Seismogenic Plug of Ascending, Solidifying Magma.

---

[1] U.S. Geological Survey, 1300 SE Cardinal Court, Vancouver, WA 98683

This paper formalizes the SPASM hypothesis mathematically and tests whether it is consistent quantitatively with behavior observed during the 2004–5 eruption of Mount St. Helens. The mechanistic framework of the SPASM model is simple, reflecting my belief that a relatively simple physical process (that is, one involving few special conditions and contingencies) is most likely responsible for producing persistent, repetitive, natural events—such as nearly periodic earthquakes. Although the SPASM model aims chiefly to explain the origin of these earthquakes, it can also provide insight into conditions under which the eruption style might significantly change, and the potential for such change has large implications for assessment of volcano hazards.

Below, following a brief overview of key features of the 2004–5 eruption of Mount St. Helens, I describe the conceptual basis of the SPASM model. I then present the mathematical formulation of the nonlinear SPASM equations and analytical results obtained from exact solutions of approximate (that is, linearized) versions of these equations. The analytical results demonstrate the plausibility of several broad classes of eruptive behavior, including both stable and unstable behavior. I then use numerical results obtained from approximate solutions of the exact, nonlinear model equations to clarify some consequences of instability. In particular, the numerical results show how stick-slip motion arises as a natural consequence of plug extrusion dynamics. In the final sections of the paper, I discuss implications of these findings for interpreting solid-state volcanic extrusion and accompanying seismicity.

Eruption Overview

Despite Mount St. Helens' famous explosive eruption in 1980, the dome-building activity that began in 2004 is consistent with the volcano's recent geologic history (Mullineaux and Crandell, 1981). Over the past ~4,000 years, Mount St. Helens has extruded rock at a mean rate of about 0.2 m^3/s while constructing a 26-km^3 modern edifice (defined here as the volume above 1,220 m altitude) composed primarily of andesite and dacite lava flows and domes and their detritus. From 1980 to 1986 a dacite dome grew episodically in the crater formed during the 1980 eruption, and its volume ultimately reached 7.4×10^7 m^3 (Swanson and Holcomb, 1990). From 1987 to 2004 Mount St. Helens did not erupt, although at least six phreatic explosions occurred from 1989 to 1991 (Mastin, 1994). Recurrent seismicity at depths of 2–8 km in the late 1980s and 1990s may have been associated with magma recharge but did not lead to eruptions (Moran, 1994).

Renewed eruptive activity began on October 1, 2004, when a small explosion formed a vent through the ~150-m-thick glacier that had grown in the southern part of Mount St. Helens' crater since 1986 (Schilling and others, 2004; Dzurisin and others, 2005; Walder and others, 2005). The explosion was preceded by about 7 days of increasingly intense seismicity at depths <1 km, but deeper seismicity (such as might be indicative of magma-chamber pressurization or depressurization) did not occur then and has not occurred subsequently (Moran and others, this volume, chap. 2). By October 11, explosions had largely ceased, seismic energy release had decreased to a rate about one-tenth that of the preceding two weeks, and extrusion of a solid dacite plug had begun (Dzurisin and others, 2005). By December 2004, extrusion rates had become nearly steady, and by December 15, 2005, the volume of the resulting new lava dome was ~7.3×10^7 m^3 (Schilling and others, this volume, chap. 8). This volume, added to that of the 1980–86 lava dome, implies that the mean extrusion rate at Mount St. Helens from 1980 to 2005 was about 0.2 m^3/s, similar to the mean rate for the past 4,000 years. Thus, the 2004–5 activity of Mount St. Helens was by no means unusual.

The remainder of this section focuses on the quasi-steady eruptive behavior observed at Mount St. Helens from December 2004 through December 2005, because understanding this behavior is the goal of SPASM. Other papers in this volume provide detailed descriptions of the findings briefly summarized below.

Extrusion Rates and Vent Size

After extrusion commenced, it appeared to occur continuously through December 2005, and it produced a sequence of monolithic dacite spines, with some reaching heights >100 m. The fourth of these spines had such a strikingly smooth, symmetrical, elongate form that it resembled a breaching whale and was accordingly dubbed the "whaleback" (fig. 1). Each spine emerged over a period of several weeks to several months and eventually disintegrated as a consequence of fracturing and avalanching of rock from its exposed surfaces. By late 2005, the sequence of spines had formed a composite dome with the appearance of a multicrested pile of rubble, and distinguishing individual spines would in retrospect have been difficult without knowledge of their emplacement history.

Despite the rather complicated details of spine emplacement, photogrammetric analysis showed that the rate of extrusion remained remarkably constant from about December 2004 to December 2005 (fig. 2) and typically ranged from about 1 to 2 m^3/s (Schilling and others, this volume, chap. 8). During the same period, the linear extrusion rate (that is, the speed of spine emergence from the ground) estimated from far-field, ground-based photography typically ranged from about 3×10^{-5} to 7×10^{-5} m/s (3–6 m/day) (Major and others, this volume, chap. 12), and these rates were largely consistent with high-precision data transmitted by short-lived GPS receivers placed intermittently on the extruding spines (LaHusen and others, this volume, chap. 16). Similar linear extrusion rates were inferred from short-duration, short-range photography, which detected centimeter-scale plug emergence over durations as brief as a few minutes (Dzurisin and others, this volume, chap. 14). Thus, all evidence indicates that extrusion rates were essentially constant over time scales longer than the duration of small earthquakes (about 10 s or less) but shorter than the multiyear duration of the eruption as a whole (>10^7 s).

According to the SPASM hypothesis, small, abrupt pulses in plug extrusion were responsible for generating small earthquakes. These pulses would have typically entailed upward plug displacements of ~5 mm (a value obtained by multiplying the typical 5×10^{-5} m/s linear extrusion rate by the typical 100-s interval between earthquakes), but abrupt movements this small were not resolvable by displacement measurements. Moreover, abrupt slip occurring at earthquake hypocentral depths may have been muted at shallower depths owing to inelastic deformation of weak near-surface materials. As a consequence, no direct measurements of coseismic pulses of plug extrusion were made during the eruption. Therefore, the SPASM model addresses the dynamics of stick-slip cycles with properties that have been inferred but not directly measured.

Inference also plays a role in estimating the size of the vent where extruding spines breached the crater floor, because the presence of fragmented glacier ice and accumulated talus, as well as previously extruded rock, partly obscured the vent margins. Moreover, different parts of the vent became visible as successive spines emerged and moved laterally as well as upward. From the standpoint of constraining the SPASM model, the most useful estimates of the effective cross-sectional area of the vent are obtained not from direct observations of spine geometry but from comparison of volumetric and linear extrusion rates measured over extended periods. Division of the typical volumetric rate of 1.5 m^3/s by the typical linear rate of 5×10^{-5} m/s yields an effective vent area of 30,000 m^2, which implies an effective vent diameter of ~200 m if the vent geometry is assumed to be circular. A vent of this size (but not necessarily circular) is assumed for all calculations I present in this paper.

Gouge Properties

Where fresh surfaces of newly extruded spines were exposed, they were coated with granulated, striated dacite interpreted to be fault gouge. The gouge presumably formed as a consequence of mechanical wear during localized shearing along the margins of the dacite plug as it moved upward relative to the adjacent conduit walls (compare Tuffen and Dingwell, 2005). Observations and dredge sampling from hovering helicopters indicated that the gouge thickness was typically about 1 m (J.S. Pallister, U.S. Geological Survey, oral commun., 2005). Striations on the gouge surface were abundant and generally aligned with the direction of extrusion (fig. 3).

Frictional properties of the gouge were measured using a large-scale ring-shear apparatus, in which a remolded, annular specimen (~0.012 m^3) was deformed in simple shear at various imposed rates (Moore and others, this volume, chap. 20). The measurements demonstrated that the gouge typically exhibited peak strength at displacements <0.5 mm, steady-state strength after about 3 mm of displacement, and reduction of steady-state strength with increasing shear rate (for example, fig. 4). At rates $\geq5\times10^{-4}$ m/s (about 43 m/day), this rate-weakening

Figure 1. Oblique aerial photograph of extruding "whaleback" spine 4 at Mount St. Helens, viewed from the northwest, on February 22, 2005. Horizontal length of the smooth whaleback is about 380 m. Arrow shows vent from which the spine emerged. USGS photo by S.P. Schilling.

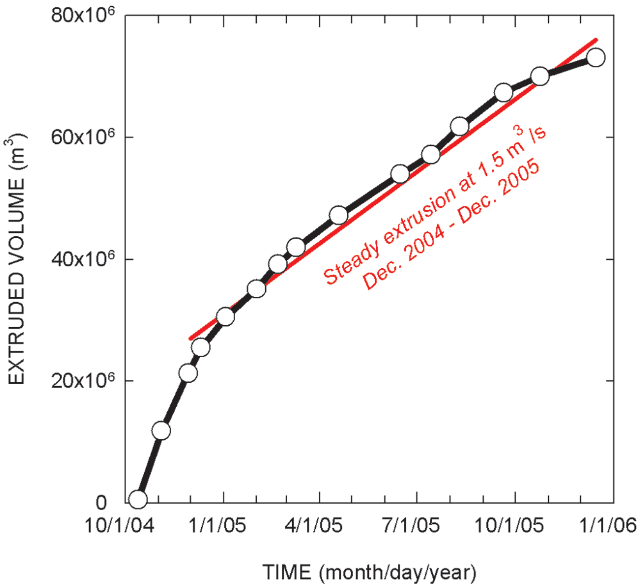

Figure 2. Measured volume of extruded dome rock at Mount St. Helens as a function of time (after Schilling and others, this volume, chap. 8). The red reference line shows growth of dome volume occurring with a constant extrusion rate of 1.5 m^3/s from December 2004 to December 2005.

behavior was supplanted by rate-strengthening behavior, but the relevance of this transition is questionable because the test equipment could shear the specimen at rates $\geq 5\times10^{-4}$ m/s only under very low confining stresses, $\leq$23 kPa (Moore and others, this volume, chap. 20).

Overall, the ring-shear tests of Moore and others (this volume, chap. 20) showed that frictional behavior of the Mount St. Helens gouge was largely consistent with that expected from models of rate- and state-dependent friction (for example, Dieterich, 1979; Ruina, 1983; Marone, 1998). Such models posit that frictional strength varies in proportion to the logarithms of the imposed shear rate and hold time (that is, the time a specimen is held in a static state between successive shear events). In rate-weakening materials, the combined effect of shear rate and hold time causes a reduction of frictional strength as steady shear rates increase. In tests of the Mount St. Helens fault gouge under confining stresses of 86–195 kPa, measured values of steady-state friction coefficients ranged from 0.42 to 0.47, and these values declined logarithmically as the imposed shear rate increased (Moore and others, this volume, chap. 20). Measured peak friction coefficients were 1–9 percent larger than steady-state friction coefficients, and peak values increased logarithmically with hold time. This hold-time effect is typical of rocks and densely packed granular materials (for example, Beeler and others, 1994; Losert and others, 2000).

Testing by Moore and others (this volume, chap. 20) also revealed that the effective in-place shear stiffness of the gouge was probably orders of magnitude larger than the effective stiffness of the magma body that loaded the gouge as it pushed the extruding plug upward. This contrast in stiffness, along with rate-weakening steady-state friction, provides a sufficient condition for stick-slip behavior in materials exhibiting rate- and state-dependent friction (Rice and Ruina, 1983; Ruina, 1983).

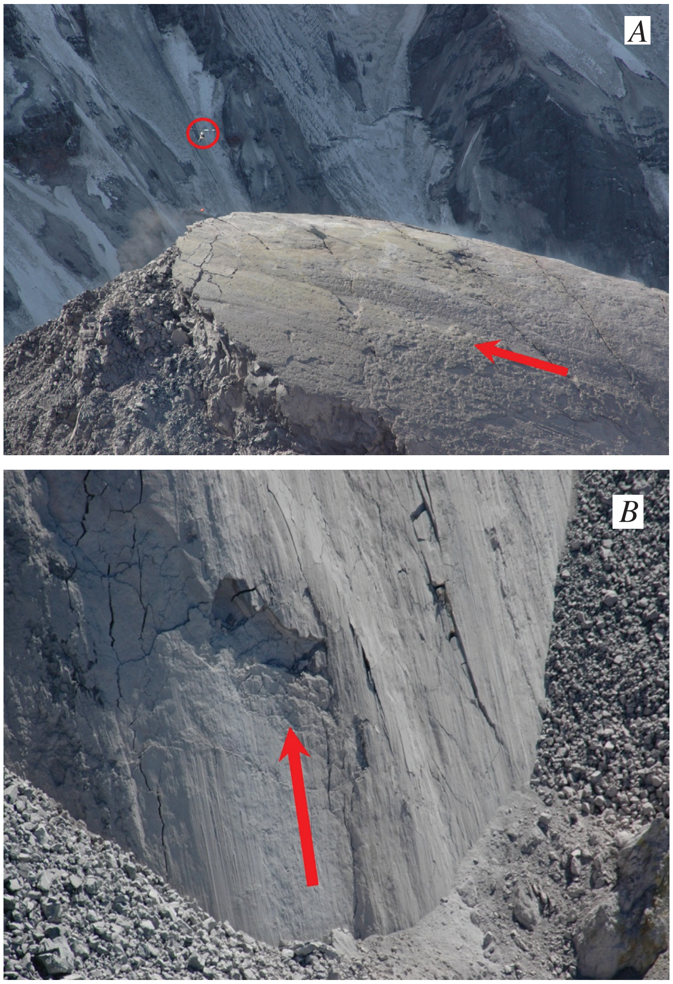

Figure 3. Photographs of striated, gouge-coated surfaces of extruding spines at Mount St. Helens. Arrows show direction of spine motion. *A*, Crest of spine 4 viewed from east on February 22, 2005. Hovering helicopter (circled) provides scale. *B*, Base of spine 5 viewed from north on July 28, 2005. Field of view is roughly 30 m wide. USGS photos by S.P. Schilling.

Drumbeat Earthquakes

An extraordinary feature of the 2004–5 eruption of Mount St. Helens was persistence of small ($M_d \leq 2$), shallow earthquakes that recurred so regularly they were dubbed "drumbeats" (Moran and others, this volume, chap. 2). The period between successive drumbeats shifted slowly with time but was commonly ~100 s (for example, fig. 5) and nearly always in the range 30–300 s. Seismograms showed that

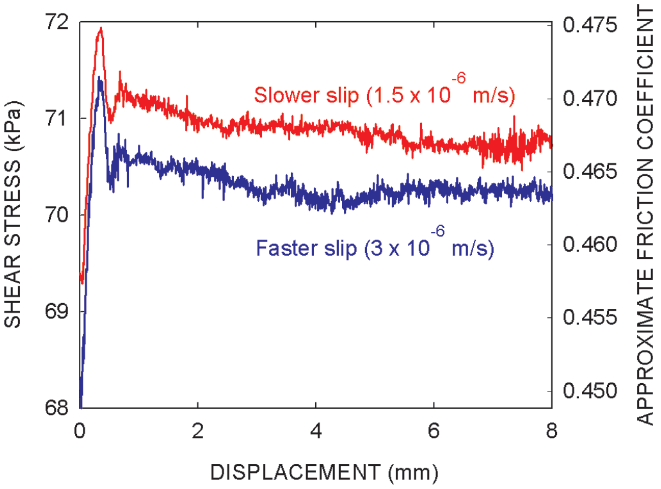

Figure 4. Example of data collected during ring-shear tests of gouge friction by Moore and others (this volume, chap. 20). Measured shear stress as a function of displacement is shown for two steady-state shear rates. Inferred friction coefficients (right-hand axis) represent shear stress divided by a nominally constant normal stress of 159 kPa, but normal stress fluctuated slightly (<1 percent) during the tests, such that friction coefficients are approximate (after Moore and others, this volume, chap. 20).

drumbeat waveforms generally had impulsive, high-frequency onsets and low-frequency codas, similar to waveforms of other hybrid volcanic earthquakes (for example, Lahr and others, 1994; Neuberg, 2000). Over time scales of hours to weeks, drumbeats typically had consistent sizes and did not display a Gutenberg-Richter magnitude-frequency distribution typical of tectonic earthquakes (Moran and others, this volume, chap. 2). Precise location of drumbeat hypocenters was hindered by the geologic and topographic complexity of the Mount St. Helens crater and the low density of crater seismometers, but within resolution limits (~100 m), all drumbeats originated at depths <1 km directly around or beneath the growing dome. Accompanying the drumbeats at irregular intervals were smaller and larger earthquakes (as large as M_d 3.4) with differing seismic signatures, but these earthquakes had little lasting effect on the drumbeats.

The recurrence and character of drumbeat earthquakes implies the existence of a nondestructive seismic source, as has been inferred for other repetitive volcanic earthquakes (Lahr and others, 1994; Goto, 1999; Neuberg, 2000; Neuberg and others, 2006). The most outstanding attribute of the drumbeat earthquakes at Mount St. Helens, however, was their periodicity. This periodicity, together with the presence of striated fault gouge bounding the extruding plug, is the key motivation for the SPASM hypothesis.

Although the SPASM model aims to link plug extrusion and earthquake generation, it does not address resulting seismic radiation. Radiation of seismic waves could result from rapid propagation of rupture that spreads along the fault surface after nucleating in a strong "keystone" patch of fault gouge (see Scholz, 2002). Alternatively, the force drop accompanying frictional slip that occurs uniformly along the plug margins might be so abrupt as to radiate seismic energy (see Marone and Richardson, 2006), and this force drop is calculated by the SPASM model. In relating SPASM mechanics to seismic radiation, however, it must be borne

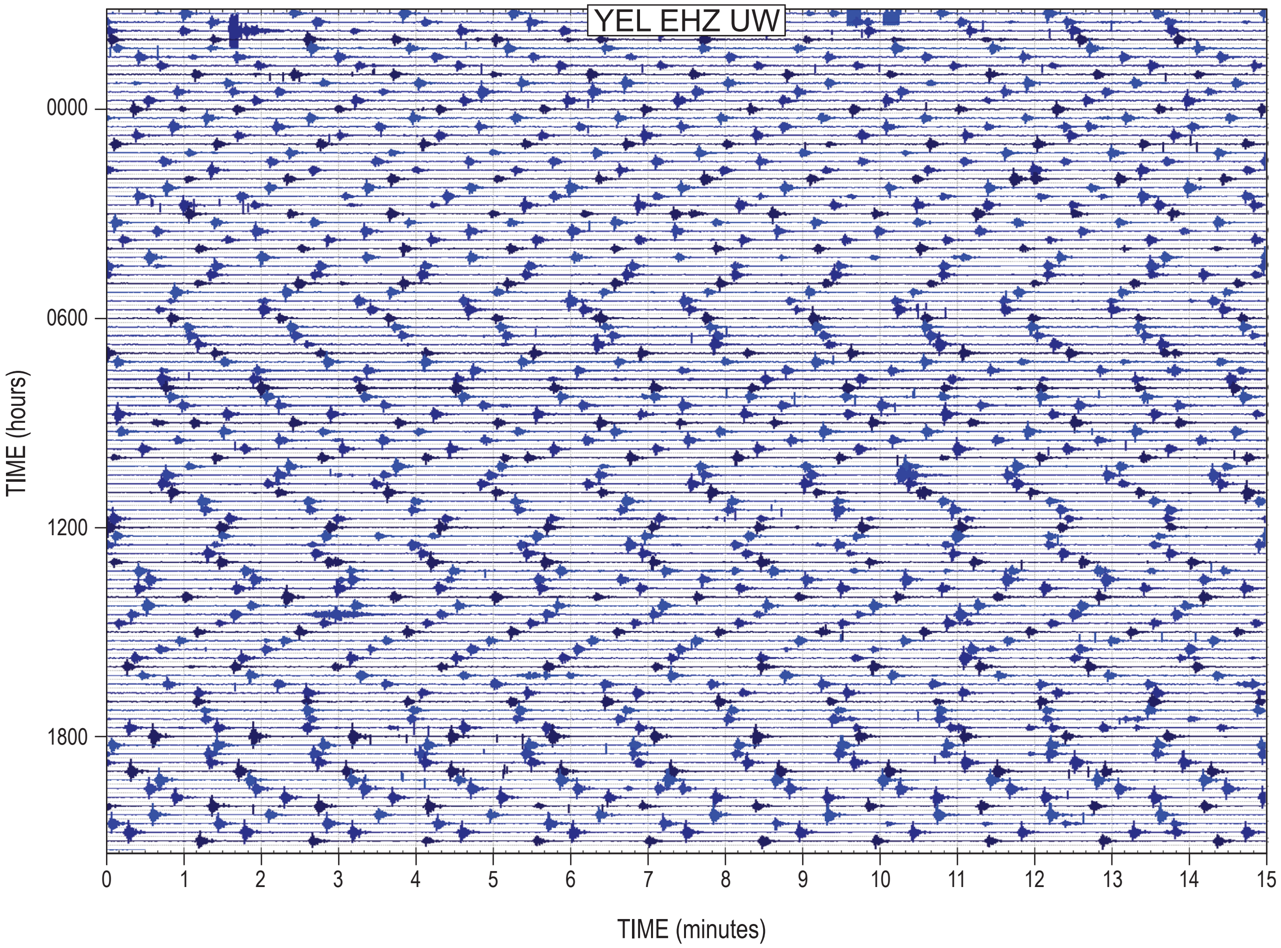

Figure 5. Example of 24-hour seismogram illustrating nearly periodic occurrence of "drumbeat" earthquakes at Mount St. Helens. Graph shows seismicity recorded at station YEL, located 1.5 km north of the 2004–5 vent. Time begins at 21:00 UTC on December 1, 2005, and scrolls from left to right and then top to bottom. Earthquake magnitudes were roughly 0.5–1 during this interval. Data courtesy of Pacific Northwest Seismic Network.

in mind that only a small fraction (<10 percent) of the work done during fault slip typically results in seismic radiation (McGarr, 1999). Generally, more work is done in overcoming friction, and the mechanics of the total work cycle is the primary focus of SPASM.

Magma Solidification and Compressibility

Although genesis of the magma that erupted in 2004–5 remains uncertain, petrologic data indicate that solidification occurred at depths <1 km. This inference derives from the fact that the composition of glass in the newly erupted dacite plots between the 0.1 and 50 MPa cotectics of the modified quartz-albite-orthoclase phase diagram for Mount St. Helens dacites (Blundy and Cashman, 2001) and from the presence of tridymite, which constrains the late stages of solidification to pressures of 10–20 MPa (equivalent to estimated lithostatic pressures at depths ~0.5–1 km) (Pallister and others, 2005, and this volume, chap. 30). These depths are consistent with the maximum hypocentral depths inferred for drumbeat earthquakes (Moran and others, this volume, chap. 2), and they imply that solid-state extrusion and earthquake generation were collocated.

The quantity and composition of volcanic gases emitted during the 2004–5 eruption demonstrate that the magma was gas poor in comparison to the 1980 Mount St. Helens magma but that the 2004–5 magma nonetheless contained sufficient exsolved gas to greatly influence its compressibility. At 8 km depth the gas volume fraction was probably <2 percent, but calculations using methods of Newman and Lowenstern (2002) indicate that the gas volume fraction grew during magma ascent and reached about 50 percent at ~1 km depth, where solidification began (Gerlach and others, this volume, chap. 26). The same calculations indicate that at depths between 8 and 1 km, the gas volume fraction averaged ~12 percent. Allowing for inevitable gas separation from rock during extrusion, these results are consistent with observed vesicle volume fractions of 11–34 percent in samples of the 2004–5 dacite (Gerlach and others, this volume, chap. 26). An exsolved gas volume fraction of 12 percent implies a magma compressibility ~10^{-7} Pa^{-1}, according to the model of Mastin and Ghiorso (2000). Although this value is, of course, inexact, its mechanical significance is clear: the magma was almost certainly much more compressible than solid rock, which generally has compressibilities <10^{-10} Pa^{-1} (Hatheway and Kiersch, 1989). As a consequence, magma compression almost certainly dominated elastic strain as pressure within the magma-conduit-plug system increased.

Geodetic Inferences About Magma Influx

Measured displacements of the volcano flanks and adjacent areas preceding and during the 2004–5 eruption imply that the volume of magma evacuated from depths <10 km was considerably less than the volume of extruded rock (Lisowski and others, this volume, chap. 15). No evidence of systematic preeruption surface displacement was found by global positioning system (GPS) surveys in 2000 and 2003 of a 40-station network centered on the volcano, nor by continuous operation of GPS station JRO1, located 9 km north of the eruption vent. Seismicity that heralded the eruption in late September 2004 was accompanied by only centimeter-scale downward and southward (that is, inward) surface displacements at JRO1 (Lisowski and others, this volume, chap. 15). The displacement pattern measured at all stations corresponds well with that predicted by an elastic half-space model that assumes pressure decrease within a vertically oriented, prolate spheroidal cavity with a mean depth of 8 km and volume loss ~2×10^7 m^3 during the period from October 1, 2004, to November 25, 2005 (Lisowski and others, this volume, chap. 15). This apparent volume loss is less than one-third the volume of rock extruded during the same period, and little of the apparent volume loss occurred after the onset of nearly steady extrusion in December 2004, implying that magma recharge from a deep (>10 km) source accompanied this phase of the eruption.

Conceptual Basis of Mathematical Model

The basic mechanical elements of the SPASM model are shown schematically in figure 6, and table 1 defines all mathematical symbols used in development and analysis of the model. The model assumes that magma flows into the base of a feeder conduit at a steady volumetric rate Q. The conduit is assumed to originate about 8 km beneath the Mount St. Helens crater, a depth inferred from hypocentral locations of pre-2004 earthquakes apparently associated with magma movement (Moran, 1994; Moran and others, this volume, chap. 2). Ascent of magma at the top of the conduit is resisted by force exerted by a near-surface plug of solidified magma, owing to its weight mg and boundary friction F. Seismic and petrologic data collected during the 2004–5 eruption imply that the plug extends to a depth <1 km, and as a baseline value I assume that it extends to a depth ~500 m. The plug mass m can change with time as a consequence of basal accretion of congealing magma at mass rate ρB, where ρ is the magma bulk density, and as a consequence of surface erosion by spalling and avalanching at mass rate $\rho_r E$, where ρ_r is the bulk density of the plug rock. The conduit volume can change with time as a result of motion of the base of the plug and changes in magma pressure that cause elastic deflection of the conduit walls. The magma pressure and density can change in response to the changing balance between the steady magma influx and changing conduit volume. The resulting mathematical model represents the simultaneous evolution of the upward plug velocity u, magma pressure against the base of the plug p, and conduit volume V, which are influenced by concurrent evolution of m and ρ.

Implicit in the SPASM model is a “top-down” perspective of eruption dynamics. The model focuses on observed surface and near-surface phenomena associated with eruptive behavior but does not consider phenomena associated with unobserved changes that might occur in a deep magma reservoir. Instead, in the SPASM model, variations in extrusion rate are postulated to arise naturally as a consequence of the dynamics of the solid plug responding to steady forcing. Unsteady forcing due to unsteady magma influx would complicate behavior exhibited by the SPASM model but would not change its fundamental character.

The SPASM model is one-dimensional and does not explicitly consider the effects of conduit and plug geometry. This simplification poses both an advantage and disadvantage. The advantage derives from the fact that predictions of the SPASM model are independent of geometrical effects and are, in a general sense, applicable to any geometry. The disadvantage is that SPASM yields no insight concerning the effects of geometrical complications such as variations in the shape of the magma conduit, vent, or growing lava dome.

Many previous eruption models have used a one-dimensional approach similar to the one used here, and some models have invoked stick-slip motion as a phenomenon responsible for cyclical eruptive behavior (for example, Denlinger and Hoblitt, 1999; Voight and others, 1999; Ozerov and others, 2003). The SPASM model, however, is the first to demonstrate how stick-slip behavior arises as a natural consequence of system dynamics. Indeed, a key feature of the SPASM model is that forces need not be balanced; therefore, the model can exhibit dynamical behavior not possible in eruption models that assume balanced forces (for example, Mastin and others, this volume, chap. 22).

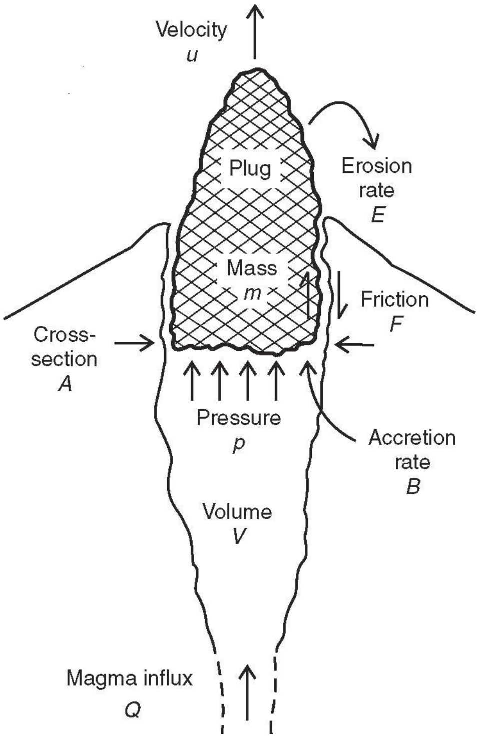

Figure 6. Schematic diagram illustrating the conceptual framework of the SPASM model.

Mathematical Formulation

The most fundamental equations used to derive the SPASM model express conservation of mass and linear momentum of the solid plug and conduit fluid. These conservation laws are supplemented by constitutive equations defining magma compressibility, conduit wall-rock compliance, and the frictional force acting where the plug contacts the conduit walls. In this section the conservation and constitutive equations are presented and reduced to a set of three simultaneous differential equations that describe behavior of the magma-conduit-plug system as a whole.

Conservation of Linear Momentum of Solid Plug

Changes in the upward momentum of the solid plug are described by Newton’s second law of motion, expressed as

$$m\frac{du}{dt}+u\frac{dm}{dt} = p\,A - m\,g - F, \tag{1}$$

where m is the plug mass, u is the vertical (upward) plug velocity, g is the magnitude of gravitational acceleration, and p is the magma pressure against the base of the plug, which has area A in horizontal projection. Upward motion of the plug is driven by the basal magma-pressure force pA and resisted by the plug weight mg and boundary friction force F. Implicit in equation 1 is the understanding that F would change sign (that is, friction would reverse its direction of action) if u were to change sign. A detailed specification of F is provided in the section on “Constitutive Equations,” below.

Conservation of Mass of Solid Plug

Mass change of the solid plug depends on the rate of mass accretion at the base of the plug, ρB, and the rate of mass loss at the surface of plug due to erosion, $\rho_r E$, where B is the volumetric rate of magma conversion to solid rock and E is the volumetric erosion rate of the plug surface. Magma solidification may involve a change in mass density from ρ to ρ_r. Summing these effects yields the mass-conservation equation

$$\frac{dm}{dt} = \rho B - \rho_r E = \kappa, \tag{2}$$

where κ is a convenient shorthand for $\rho B - \rho_r E$. For the sake of simplicity, κ is assumed constant, although this assumption is readily relaxed in numerical analyses if warranted. With constant κ, equation 2 yields the explicit solution

Table 1. Definitions of mathematical symbols.

Symbol	Dimensions	Definition
A	L^2	Horizontal cross-sectional area of base of plug
B	L^3/T	Volumetric rate of magma solidification at base of plug
C	M/T	Dimensional measure of rate dependence of plug friction force
c	none	Dimensionless measure of rate dependence of plug friction force
c_1, c_2	none	Arbitrary constants of integration
D	none	Dimensionless parameter summarizing effects of frictional damping
E	L^3/T	Volumetric rate of erosion of surface of plug
F	ML/T^2	Friction force on margins of plug
F_0	ML/T^2	Value of F at static limiting equilibrium
$F(u_0)$	ML/T^2	Value of F at the steady equilibrium extrusion rate u_0
F^*	none	F/F_0
G	none	Dimensionless parameter summarizing effects of gravity
g	L/T^2	Gravitational acceleration
H_{con}	L	Vertical height of magma-filled conduit
H_{plug}	L	Vertical height of extruding solid plug
K	none	Dimensionless parameter summarizing effects of plug mass change
m	M	Plug mass
m_0	M	Static or steady equilibrium value of m
p	M/LT^2	Magma pressure against base of plug
p_{b}	M/LT^2	Magma pressure at base of conduit
p_{i}	M/LT^2	Value of p at onset of a stick event
p_0	M/LT^2	Value of p at static limiting equilibrium
p_{ref}	M/LT^2	Reference value of p used in magma compression equation
Q	L^3/T	Volumetric rate of magma influx at base of conduit
R	none	Dimensionless parameter equal to $1-\rho/\rho_{\mathrm{r}}$
R_0	none	Value of R when $\rho=\rho_0$
R^*	none	R/R_0
S	none	Dimensionless parameter summarizing rate dependent plug friction
$\hat{S}$	none	Dimensionless parameter summarizing static plug friction
T	T	Oscillation period
t	T	Time
t_0	T	Natural time scale of oscillations, defined in equation 25
t^*	none	t/t_0
u	L/T	Vertical extrusion velocity
u_0	L/T	Value of u at steady equilibrium
u_{ref}	L/T	Reference value of u used in friction equation
u'	L/T	$u-u_0$
u^*	none	u'/u_0
u_{i}^*	none	Initial value of u^*
V	L^3	Volume of magma-filled conduit
V_0	L^3	Static or steady equilibrium value of V
V'	L^3	$V-V_0$
V^*	none	V'/V_0

Table 1. Definitions of mathematical symbols.—Continued

Symbol	Dimensions	Definition
V_i	L^3	Value of V at onset of stick event
W	L^3/T	Parameter defined in equation 53
X	none	Dimensionless parameter defined in equation 44
Y	none	Dimensionless parameter defined in equation 44
Z	none	Dimensionless parameter defined in equation 44
α_1	LT^2/M	Elastic bulk compressibility of magma
α_2	LT^2/M	Elastic compliance of walls of magma-filled conduit
η	M/LT	Magma viscosity
κ	M/T	Rate of change of plug mass
λ	none	Parameter that relates plug weight to boundary normal stress
μ_0	none	Static friction coefficient
ν	none	Dimensionless parameter defined in equation 34
ρ	M/L^3	Bulk density of magma
ρ_0	M/L^3	Value of ρ at static limiting equilibrium
ρ_r	M/L^3	Bulk density of plug rock
ξ	none	Rescaled time variable defined in equation 34

$$m = \kappa t + m_0 \tag{3}$$

where m_0 is the initial value of m.

Conservation of Linear Momentum of Conduit Fluid

Newton's second law for upward motion of magma in the conduit takes a simple form if variations of magma properties and velocity with position are neglected:

$$\rho \frac{dQ}{dt} + Q\frac{d\rho}{dt} = A\left(\frac{p_b - p}{H_{con}} - \rho g - \frac{8\pi\eta}{A^2}Q\right). \tag{4}$$

Here Q is the vertical (upward) volumetric flux of magma, p_b is the magma pressure at the base of the conduit, and η is the magma viscosity. Equation 4 is the fluid-mechanical equivalent of equation 1 and is also equivalent to the Navier-Stokes equation for one-dimensional laminar flow, integrated over the conduit cross-sectional area A and height H_{con}. According to equation 4, upward motion of magma in the conduit is driven by the vertical pressure gradient $(p_b - p)/H_{con}$ and is resisted by the magma unit weight ρg and viscous drag, represented by the last term in the equation. The form of this drag term is inferred from an elementary analysis of Poiseuille flow in a cylindrical conduit, although alternative drag terms (appropriate for other conduit geometries or magma rheologies) could be used without difficulty.

A simplified momentum equation is obtained by assuming that the magma flux Q is independent of time and making the substitution $dQ/dt = 0$ in equation 4. Rearrangement of the resulting equation yields an explicit expression for Q,

$$Q = A\frac{\dfrac{p_b - p}{H_{con}} - \rho g}{\dfrac{d\rho}{dt} + \dfrac{8\pi\eta}{A}}. \tag{5}$$

Equation 5 shows that maintenance of constant Q in the presence of changing H_{con}, p, and ρ (all of which can occur in the context of the SPASM model) can imply that compensating changes occur in p_b and/or η. The model assumes that such compensating changes may indeed occur, but it does not evaluate such changes explicitly. A complete evaluation could be accomplished by using equation 4 together with a mass-conservation equation (see below) to model the dynamics of transient magma flow in the conduit (for example, Melnik and Sparks, 2002). However, such a model also requires specification of a basal boundary condition (for example, magma-chamber pressure) to drive magma inflow. Any such specification involves assumptions that are arbitrary, and the SPASM model minimizes use of arbitrary assumptions by specifying a constant basal magma influx Q.

Conservation of Mass of Conduit Fluid

The mass of the fluid magma in the conduit is ρV, where V is the conduit volume. Changes in ρV depend not only on changes in ρ and V but also on the influx of fluid mass at the base of the conduit ρQ and the loss of fluid mass at the top of the conduit ρB, which results from solidification at the base of the solid plug. These phenomena are summarized by the fluid mass-conservation equation

$$\rho \frac{dV}{dt} + V \frac{d\rho}{dt} = \rho(Q - B). \tag{6}$$

Both Q and B are treated as constants.

Constitutive Equations

Although the conservation equations for Q and m reduce to the explicit forms shown above, the remaining two conservation equations (1 and 6) contain four dependent variables, u, p, V, and ρ and an as-yet-unspecified friction force F. Thus, three constitutive equations must be specified to attain mathematical closure.

Magma Compressibility

The first constitutive equation defines the compressibility of the fluid magma α_1 as

$$\alpha_1 = \frac{1}{\rho}\frac{d\rho}{dp}, \tag{7}$$

and integration of equation 7 yields $\rho = \rho_0 \exp[\alpha_1(p - p_{ref})]$, where ρ_0 is the magma bulk density at a reference pressure p_{ref} . Combination of equation 7 with the chain rule $d\rho/dt = (d\rho/dp)(dp/dt)$ yields an equation that relates magma density change to pressure change:

$$\frac{d\rho}{dt} = \alpha_1 \rho \frac{dp}{dt}. \tag{8}$$

Below, this equation is used to replace density derivatives with pressure derivatives where advantageous.

Conduit Compliance

A second constitutive equation defines the bulk elastic compliance of the conduit walls α_2 as

$$\alpha_2 = \frac{1}{V}\left[\frac{dV}{dp}\right]_0, \tag{9}$$

where the subscript 0 denotes conduit volume change under a condition of zero plug velocity (u=0) and zero plug accretion (B=0). The utility of equation 9 is increased by embedding the equation in a definition of the total rate of conduit volume change that occurs when u and B are nonzero,

$$\frac{dV}{dt} = A\,u - \frac{\rho}{\rho_r}B + \left[\frac{dV}{dt}\right]_0. \tag{10}$$

Here again, the subscript 0 denotes the rate of volume change that would exist if u=0 and B=0, whereas the terms Au and $(\rho/\rho_r)\,B$ describe conduit volume change due to upward plug motion and basal plug accretion, respectively. The factor ρ/ρ_r accounts for the influence of density change from ρ to ρ_r during magma solidification at the volumetric rate B.

To obtain a "systemic" constitutive equation for total conduit volume change, equation 9 is embedded in equation 10 by using the chain rule $[dV/dp]_0 = [dV/dt]_0/(dp/dt)$, yielding

$$\frac{dV}{dt} = A\,u - \frac{\rho}{\rho_r}B + \alpha_2 \frac{dp}{dt}V. \tag{11}$$

The volume change described by equation 11 includes both an irreversible component and a reversible (elastic) component.

Plug Boundary Friction

The final constitutive equation defines the friction force F that acts where the plug contacts the conduit walls. This friction results from shearing of gouge, discussed briefly above in the section on "Gouge Properties" and in detail by Moore and others (this volume, chap. 20). Because friction might potentially exhibit diverse behaviors, and because this diversity has significant ramifications for extrusion dynamics, I represent F with a functional form that is consistent with the key findings of Moore and others (this volume, chap. 20) but that compromises between precision, generality, and simplicity:

$$F \;=\; \operatorname{sgn}(u)\, mg\lambda\mu_0 \left[1 + c\sinh^{-1}\left|\frac{u}{u_{ref}}\right|\right]. \tag{12}$$

Here sgn(u) denotes the sign of u and stipulates that the frictional force always opposes motion; μ_0 is a static friction coefficient applicable when u=0; c is a parameter that describes the sign and magnitude of frictional rate dependence; and u_{ref} is a reference velocity that specifies the extent of nonlinearity of rate dependence (fig. 7). In the simplest case, with c=0, equation 12 specifies that the friction force has a constant value $F = F_0 = \operatorname{sgn}(u)\, mg\lambda\mu_0$. If $c \neq 0$ and $u/u_{ref} << 1$, then equation 12 implies that friction depends almost linearly on slip rate ($F \approx \operatorname{sgn}(u)\, mg\lambda\mu_0[1 + c\left|u/u_{ref}\right|]$), whereas for $u/u_{ref} >> 1$, equation 12 implies that rate dependence of friction is essentially logarithmic ($F \approx \operatorname{sgn}(u)\, mg\lambda\mu_0[1 + c\ln\left|2u/u_{ref}\right|]$) (see Abramowitz and Stegun, 1964, p. 87). This logarithmic dependence mimics behavior observed in the steady sliding experiments of Moore and others (this volume, chap. 20). The fact that nearly logarithmic behavior as well as other styles of frictional behavior may be represented by equation 12 is a significant advantage in analytical studies. Another advantage is that the equation implies that the maximum friction force is finite at u=0 (that is, $F = F_0 = \pm mg\lambda\mu_0$), whereas purely logarithmic friction rules imply that friction is infinite at u=0.

As specified by equation 12, the friction force F is proportional to the effective normal force on the sides of the plug, $mg\lambda$, where λ is a numerical factor that scales this normal force to the plug weight, mg. This definition implies that the maximum plausible value of λ is about 2 (assuming μ_0~0.5, as shown by the data of Moore and others, this volume, chap. 20), in which case sidewall friction suffices to support the entire plug weight. Realistic values of λ are likely to be considerably smaller than 2 and are dependent on the height of the plug in contact with the conduit walls and on the state of effective stress governing the normal traction on the plug margins. Although the effective stress state is unknown at Mount St. Helens, estimates of λ are constrained by the balance of forces implied by the right-hand side of equation 1 for the case of static limiting equilibrium: $F = F_0 = mg\lambda\mu_0 = pA - mg$. Algebraic rearrangement of this balance shows that λ must satisfy $\lambda = (1/\mu_0)[(pA/mg) - 1]$. Therefore, because the magma pressure p is unlikely to deviate much from lithostatic pressure (for if it did, it would cause hydraulic fracturing or conduit collapse), λ is largely determined by the plug geometry, which determines the plug mass m and basal area A, as well as the depth where p operates.

Although friction described by equation 12 represents both the peak-strength effect and shear-rate effect observed in the experiments by Moore and others (this volume, chap. 20), it includes no provision for the hold-time (or "state evolution") effect also observed in those experiments. In the context of equation 12, inclusion of such evolution would entail making μ_0 a time- or state-dependent quantity. This complication would introduce additional constitutive parameters, but it would add little to understanding the mechanism of regularly occurring drumbeat earthquakes at Mount St. Helens. Therefore, I have chosen to exclude state-evolution effects from the SPASM model.

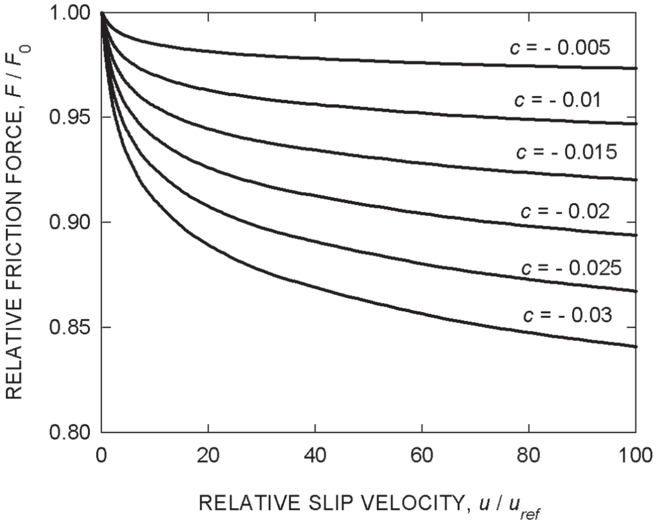

Figure 7. Graph of equation 12, illustrating nonlinear variation of relative friction force as a function of normalized slip rate u/u_{ref} and rate-dependence parameter c. Parameter F_0 is friction force at static, limiting equilibrium, $F_0 = m_0 g\lambda\mu_0$.

Friction represented by equation 12 does include a simple yet fundamental type of state dependence, however. The factor sgn(u) in equation 12 stipulates that the static (zero-velocity) friction force can jump from a positive value $mg\lambda\mu_0$ to a negative value $\geq -mg\lambda\mu_0$ if the extrusion velocity u changes from a positive value to a negative value. If u subsequently becomes positive again, then the friction force again becomes positive. Such jumps ensure that friction opposes motion, and they have great implications for the dynamical behavior of the extruding plug.

Reduced Governing Equations

The equations described above can be reduced to a compact system of three equations governing simultaneous evolution of the dependent variables u, V, and p. In this system the magma density ρ is eliminated as a dependent variable by using equation 8 to replace $d\rho/dt$ in equation 6 with dp/dt and then dividing all terms in the resulting equation by ρ, yielding

$$\frac{dV}{dt} + V\alpha_1\frac{dp}{dt} = Q - B. \tag{13}$$

Equations 11 and 13 are then combined and rearranged algebraically to obtain explicit equations for $d\rho/dt$ and dV/dt. These two equations accompany the equation of motion obtained by combining equations 2 and 12 with equation 1, thereby forming a system of three first-order differential equations,

$$\frac{du}{dt} = -g + \frac{1}{m_0 + \kappa t}\left[pA - \kappa u - F\left(u/u_{ref}\right)\right], \tag{14}$$

$$\frac{dp}{dt} = \frac{-1/V}{\alpha_1 + \alpha_2}\left[Au + RB - Q\right], \quad \text{and} \tag{15}$$

$$\frac{dV}{dt} = \frac{\alpha_1}{\alpha_1 + \alpha_2}\left[Au + RB - Q\right] + Q - B, \tag{16}$$

where R is a nearly constant coefficient defined by

$$R = 1 - \frac{\rho}{\rho_r} = 1 - \frac{\rho_0}{\rho_r}\exp[\alpha_1(p - p_{ref})]. \tag{17}$$

The system of differential equations (14–16) contains four types of nonlinearities: one involving the quotient Au/V in equation 15, one involving the nonlinear dependence of R on p shown in equation 17, one involving the potential for jumps in F described in the section above on "Plug Boundary Friction," and one involving the dependence of F on $\sinh^{-1}\left|u/u_{ref}\right|$ shown in equation 12.

The Forced, Damped Oscillator Equation

The physical implications of the governing equations become clearer when equations 14 and 15 are combined to form a single, second-order equation. Differentiating equation 14 with respect to *t*, employing the chain rule $dF/dt = (dF/du)\,(du/dt)$, and substituting equation 15 into the resulting equation yields

$$(m_0 + \kappa t)\frac{d^2u}{dt^2} + \left(2\kappa + \frac{dF}{du}\right)\frac{du}{dt} + \left(\frac{A^2}{[\alpha_1 + \alpha_2]V}\right)u = -g\,\kappa + \frac{A\,(Q - RB)}{[\alpha_1 + \alpha_2]V}. \qquad (18)$$

This equation has a form like that of equations governing behavior of forced, damped oscillators (Kreyszig, 1979, p. 82 ff.), and it implies that the extrusion velocity *u* has a natural tendency to oscillate about equilibrium. This tendency arises from the interplay of plug inertia, an upward "spring force" due to compression of the magma and conduit, and the downward force due to gravity. Oscillations of *u* are complicated by the presence of a time-dependent mass term $m_0 + \kappa t$, variable damping implicit in dF/du, and variable forcing due to the presence of *R* and *V* in the last term of equation 18, as well as by coupling of equation 18 to equations 16 and 17. Of course, equation 18 is strictly valid only insofar as *F* is a continuously differentiable function of *u*, and this restriction must be borne in mind when interpreting solutions of equation 18.

Linearized Dynamics: Analytical Results

Analytical solutions of equation 18 are important for guiding interpretation and numerical solution of the full equation set, 14–16, despite the fact that analytical solutions can be readily obtained only for various special cases. Analytical results also aid identification of diverse eruptive styles that are represented by the governing equations but are difficult to identify through numerical solutions alone.

Static, Steady-State, and Pseudosteady-State Solutions

The most basic special cases involve assumptions about the extrusion velocity *u*. A very simple special case with great physical importance assumes a condition of static limiting equilibrium, in which $u = 0$ and plug boundary friction just suffices to resist the upward force due to magma pressure. This case also assumes that the plug mass is constant (that is, $\kappa = 0$, $m = m_0$) and that the magma influx rate *Q* and basal accretion rate *B* are zero. These assumptions lead to the static equilibrium solution,

$$u = 0 \qquad p = p_0 = \frac{m_0 g + F_0}{A} \qquad V = V_0, \qquad (19)$$

which satisfies equations 14–16 as well as 18. Here p_0 is the limiting equilibrium magma pressure at the base of the plug, F_0 is the friction force at static limiting equilibrium, $F_0 = m_0 g \lambda \mu_0$, and V_0 is an arbitrary but constant conduit volume.

An equally important special case assumes that the plug mass is constant ($\kappa = 0$, $m = m_0$) but that volumetric rate of basal plug accretion and volumetric rate of magma influx are finite and equal (*B*=*Q*). These conditions lead to an exact steady-state solution satisfying equations 14–16 as well as 18,

$$u = u_0 = \frac{Q - R_0 B}{A} \qquad p = \frac{m_0 g + F(u_0)}{A} \qquad V = V_0 \qquad (20)$$

in which u_0 is the steady-state upward plug velocity, $F(u_0)$ is the steady-state friction force, $F(u_0) = m_0 g \lambda \mu_0\,[1 + c\sinh^{-1}(u_0 / u_{ref})]$, and R_0 is a constant value of *R* that applies when $\rho = \rho_0$ (that is, $R_0 = 1 - (\rho_0 / \rho_r)$). The equation group 20 represents dynamic equilibrium of the steadily ascending magma-plug system, whereas transient states represent departures from this equilibrium. Below, analyses of these departures show that steady states can be stable in some circumstances and unstable in others.

In addition to the exact steady state described by equation group 20, pseudosteady states can exist in which the extrusion velocity *u* remains constant but the magma pressure *p* increases or decreases as the plug mass evolves according to $m = m_0 + \kappa t$. A pseudosteady-state solution that satisfies equations 14–16 and 18 is

$$u = \frac{Q - R_0 B}{A} - \frac{\kappa g(\alpha_1 + \alpha_2)V}{A^2} \qquad p = \frac{m_0 g + F(u)}{A} + \frac{\kappa(gt + u)}{A}$$

$$V = \frac{A(Q - B)}{\kappa g \alpha_1}. \qquad (21)$$

Existence of this pseudosteady state requires that *B*≠*Q* and that *R* changes negligibly as *p* evolves. Despite these restrictions, the state described by equation group 21 has physical significance because it implies that essentially steady extrusion may occur in the presence of evolving plug mass and magma pressure, and it has mathematical significance because it provides a check on numerical results reported later in this paper. Additional pseudosteady states may, of course, exist if values of other parameters (for example, F_0, *A*, α_1, α_2) evolve, but such evolution is not addressed explicitly in this paper.

Linear Approximation of Transient States

Analysis of transient states is facilitated by linearization. As a first step, the dependent variables u and V in equation 18 are decomposed into sums of the steady-state values, defined in equation group 20, and transient deviations from steady state, denoted by primes:

$$u = u_0 + u'(t) \qquad V = V_0 + V'(t). \tag{22}$$

Substitution of equation group 22 into 18 and elimination of terms that sum to zero yields a simplified, but still nonlinear, version of equation 18 that describes the behavior of transient deviations. One linearization of this equation results from the assumption that magma density changes are small in comparison to the steady-state density, which enables R to be approximated by its steady-state value $R_0 = 1-(\rho_0 / \rho_r)$. A second linearization involves the assumption that deviations in the magma-conduit volume are small in comparison to its steady-state volume (that is, $V'/V_0 << 1$). Then neglect of small terms involving V'/V_0 decouples equation 18 from 16 and removes the associated nonlinearity. These two linearizations generally have little effect on model predictions because they involve physical effects that are typically very subtle.

The most significant linearization involves approximation of dF/du in equation 18. If u remains positive, an exact, nonlinear expression for dF/du follows from the definition of F in equation 12 and can be written as (see Abramowitz and Stegun, 1964, p. 88)

$$\frac{dF}{du} = \frac{m_0 g \lambda \mu_0\, c}{u_{ref}} \left[1 + \left(\frac{u}{u_{ref}} \right)^2 \right]^{-1/2}. \tag{23a}$$

Substituting $u = u_0 + u'$ in equation 23a and simplifying the result algebraically yields an approximation of 23a that is valid if velocity deviations from steady state are sufficiently small that $u'/u_0 << 1$ and $u'/u_{ref} << 1$:

$$\frac{dF}{du} \approx \frac{m_0 g \lambda \mu_0\, c}{u_{ref}} \left[1 + \left(\frac{u_0}{u_{ref}} \right)^2 \right]^{-1/2} = C. \tag{23b}$$

Here C is a constant with the same sign as c but with dimensions of mass/time. If friction is rate independent, then C=0, whereas C>0 indicates rate-strengthening friction and C<0 indicates rate-weakening friction.

The linearized form of equation 18 results from making the substitutions shown in equations 21 and 23b and assuming $R = R_0$, $V'/V_0 << 1$, and $u'/u_0 << 1$, which yields

$$\left(1 + \frac{\kappa t}{m_0} \right) \frac{d^2 u'}{dt^2} + \left(\frac{2\kappa + C}{m_0} \right) \frac{du'}{dt} + \left(\frac{A^2}{m_0 V_0 \left[\alpha_1 + \alpha_2 \right]} \right) u' = -\frac{g\kappa}{m_0}. \tag{24}$$

Except for the plug mass-growth factor $\kappa t / m_0$, all coefficients in equation 24 are constant, a property that facilitates analysis.

Natural Period of Oscillations

The form of equation 24 implies that if $\kappa = 0$ (that is, the plug mass is constant), then u' will oscillate freely with constant period $T = 2\pi t_0$, where t_0 is the natural time scale implied by the reciprocal of the coefficient that precedes u' in equation 24:

$$t_0 = \frac{[m_0 V_0 (\alpha_1 + \alpha_2)]^{1/2}}{A}. \tag{25}$$

This result is demonstrated more formally in the section on "Solution for Undamped Free Oscillations" below, but T and the time scale t_0 are introduced here as a basis for normalization of equation 24 and a first comparison of T and the typical interval between repetitive drumbeat earthquakes at Mount St. Helens. To facilitate this comparison, equation 25 is recast in a special form that is appropriate if the magma conduit and plug are approximated as right cylinders (not necessarily circular) with cross-sectional areas A and heights H_{con} and H_{plug}, respectively. In this case the oscillation period $T = 2\pi t_0$ can be expressed as

$$T = 2\pi [(\alpha_1 + \alpha_2) \rho_r H_{con} H_{plug}]^{1/2}. \tag{26}$$

A graph of equation 26 for the values H_{con} = 8 km and ρ_r = 2,000 kg/m^3 is depicted in figure 8. The graph shows how the free oscillation period T varies as a function of the plug height H_{plug} and lumped compressibility α_1+α_2. For reasonable values of H_{plug} and α_1+α_2, the predicted T has values that range from about 10 s to several minutes. The similarity of these values to the observed recurrence period of drumbeat earthquakes during the 2004–5 eruption of Mount St. Helens helps support the hypothesis that the drumbeats were associated with oscillations of the extrusion rate u.

Normalized Oscillator Equation and Dimensionless Parameters

The quantity t_0 defined in equation 25 provides the appropriate time scale for normalization of equation 24, and this normalization leads to identification of the dimensionless parameters that control the linearized dynamics of the magma-plug system. Substitution of the normalized time $t^* = t / t_0$ and normalized velocity deviation $u^* = u' / u_0$ into equation 24 reduces the equation to

$$(1+Kt^*) \frac{d^2 u^*}{dt^{*2}} + (2K+GS) \frac{du^*}{dt^*} + u^* = -KG \tag{27}$$

in which K, S, and G are dimensionless parameters defined as

$$K = \frac{\kappa\, t_0}{m_0}, \tag{28}$$

$$S = \frac{C u_0}{m_0 g}, \quad \text{and} \tag{29}$$

$$G = \frac{g t_0}{u_0}. \tag{30}$$

It is also useful to define a dimensionless damping factor D, which is half the coefficient in the second term of equation 27:

$$D = \frac{1}{2}(2K + GS) = \frac{t_0}{m_0}\left(\kappa + \frac{C}{2}\right) \qquad (31)$$

If K=0, this damping factor plays a role like that of damping factors in textbook examples of linear oscillators, and D=1 constitutes critical damping (for example, Kreyszig, 1979, p. 82 ff.). This interpretation changes only subtly for cases with $K \neq 0$, as shown below.

A complete assessment of the magnitudes of the dimensionless parameters defined above is provided in the section on "Normalized Nonlinear Equations and Control Parameters" below, but for present purposes it suffices to note that typical magnitudes of K, G, and S imply that a satisfactory approximation of equation 27 commonly results from neglecting the plug growth term Kt^* as well as the effect of K on D. An even simpler but still relevant approximation is obtained by setting both K and S equal to 0 in equation 27. On the other hand, because solutions of equation 27 for nonzero values of these parameters imply diverse eruptive behaviors, which can differ qualitatively as well as quantitatively, I analyze the full spectrum of these behaviors before considering numerical solutions of the nonlinear system of equations 14–16.

Solution for Undamped Free Oscillations

For the case in which K=0 and S=0 (implying constant plug mass and constant plug-margin friction), equation 27 reduces to an elementary second–order equation describing undamped, free oscillations of the plug velocity. In this case the simplest nontrivial solution of equation 27 is

$$u^* = u_i^* \cos t^*, \qquad (32)$$

which obeys the initial conditions $u^* = u_i^*$ and $du^*/dt^* = 0$. This solution demonstrates that the natural period of the plug's velocity oscillations is $T = 2\pi t_0$, as inferred in the section on "Natural Period of Free Oscillations" above. According to equation 32, sinusoidal oscillations with period T and amplitude u_i^* continue forever if an initial disturbance with magnitude u_i^* causes them to begin, provided that K=S=0.

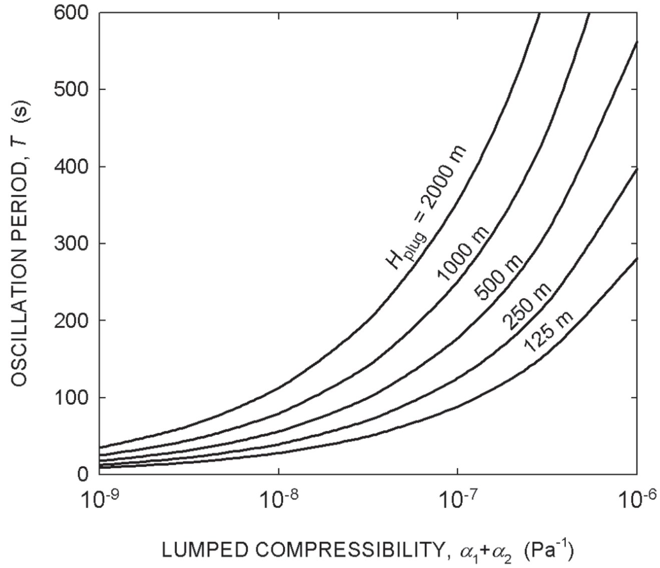

Figure 8. Graph of equation 26, illustrating predictions (from linearized theory) of variation of oscillation period T as a function of lumped compressibility $\alpha_1 + \alpha_2$ and plug height H_{plug}.

Solutions for Damped Free Oscillations—Stability of Quasi-Steady Extrusion

Another class of solutions of equation 27 exists if K=0 but $S \neq 0$. Physically, these conditions imply that the plug mass is constant $S \neq 0$ and that plug-margin friction depends linearly on the extrusion rate. In such cases the behavior of solutions depends on the value of D(= S/2) relative to the transition value D=0 and critical values D=±1, as summarized in table 2. In all cases the solutions imply stable eruptive behavior if D>0 (that is, if rate-strengthening friction exists), because u^* decays with time essentially like e^{-Dt^*}. On the other hand, if D<0 (that is, if rate-weakening friction exists), solutions containing the factor e^{-Dt^*} indicate unstable growth of u^*. The instability can be manifested as either runaway acceleration or oscillations that grow with time, as shown by the solutions listed in table 2.

The solutions listed in table 2 can also be used to infer whether the steady eruptive state represented by equation group 20 is physically accessible from an initial static state that exists before the onset of a volcanic eruption. For all cases with D>0, transient deviations in velocity (u^*) decay toward zero as time proceeds, implying that any transient state will eventually give way to a steady state. On the other hand, for cases in which D<0, dynamic steady states are inaccessible from an initial static state, because any transient motion grows without bound as time proceeds. Of course, this simple picture can change if $K \neq 0$ or if friction is nonlinear, as described in the section on "Nonlinear Dynamics: Numerical Results" below.

Solution for Damped, Forced Oscillations—Effects of Plug Growth on Extrusion Stability

The most complicated solutions of equation 27 apply to cases in which the plug mass changes with time such that $\kappa \neq 0$ and none of the parameters K, S, and G is zero. For such cases, solutions can be obtained by a multistep process that involves a simultaneous change of dependent and independent variables to transform equation 27 into Bessel's differential

Table 2. General solutions of equation 27 for cases with K=0 and D=S/2. All solutions contain arbitrary constants, c_1 and c_2, which are constrained by specifying initial conditions.

$\lvert D\rvert$	General solution of equation 27	Type of behavior
0	$u^* = c_1 \sin t^* + c_2 \cos t^*$	Undamped oscillations with constant amplitude
>0 but <1	$u^* = [c_1 \cos(t^* \sqrt{1-D^2}) + c_2 \sin(t^* \sqrt{1-D^2})]\ e^{-Dt^*}$	Underdamped oscillations; unstable growth if D<0
1	$u^* = (c_1 + c_2 t^*)\, e^{-Dt^*}$	Critically damped oscillation; unstable growth if D<0
>1	$u^* = c_1 e^{(-D+\sqrt{D^2-1})t^*} + c_2 e^{(-D-\sqrt{D^2-1})t^*}$	Overdamped, no oscillations; unstable growth if D<0

equation (appendix 1). Transformation of the well-known Bessel-equation solution back to the original variables u^* and t^* then yields the general solution

$$u^* = -KG + \frac{\xi^{\nu}}{4}\left[c_1 J_{\nu}(\xi) + c_2 Y_{\nu}(\xi)\right], \tag{33}$$

in which

$$\nu = \frac{K-2D}{K} \qquad \xi = 2\sqrt{\frac{1+Kt^*}{K^2}}. \tag{34}$$

Here c_1 and c_2 are arbitrary constants, and J_{ν} and Y_{ν} are Bessel functions of the first and second kind, of order ν (see Abramowitz and Stegun, 1964). Equation 33 describes diverse behaviors, partly analogous to those summarized in table 2. However, oscillations described by equation 33 have periods as well as amplitudes that evolve with time.

The relation between the solution for $K\neq 0$ (equation 33) and the solutions for K=0 (table 2) has important physical implications. The relation is clarified by considering asymptotic approximations of J_{ν} and Y_{ν} that are valid for $\xi >> 1$. (The condition $\xi >> 1$ implies $t^* >> K - 1/K$, a criterion that is typically satisfied as time proceeds if K>0. If K<0, the criterion will not be satisfied as time proceeds, and equation 33 then implies that a singularity develops in which $u^* \to \infty$. Physically, this singularity represents a "catastrophe" in which the plug mass reaches zero, liquid magma reaches the surface, and the governing equations no longer apply.) For $\xi >> 1$ the Bessel function approximations are (Abramowitz and Stegun, 1964, p. 364)

$$J_{\nu}(\xi) \approx \sqrt{\frac{2}{\pi\,\xi}}\ \cos(\xi - \nu\pi/2 - \pi/4), \quad \text{and} \tag{35}$$

$$Y_{\nu}(\xi) \approx \sqrt{\frac{2}{\pi\,\xi}}\ \sin(\xi - \nu\pi/2 - \pi/4). \tag{36}$$

Substituting these approximations into equation 33 and collecting terms containing powers of ξ shows that, over time, u^* decays or grows according to

$$u^* \propto \left(\frac{1+Kt^*}{K^2}\right)^{1/4-D/K}. \tag{37}$$

The exponent $1/4 - D/K$ in equation 37 plays a physical role analogous to that of $-D$ in solutions with K=0 (table 2). The physical meaning of equation 37 becomes clearer if equations 29 and 31 are used to express the exponent in terms of physical parameters, yielding

$$u^* \propto \left(\frac{1+Kt^*}{K^2}\right)^{-\frac{1}{2}\left(\frac{3}{2}+\frac{C}{\kappa}\right)}. \tag{38}$$

The exponent in equation 38 shows that oscillations in u^* will decay or grow depending on whether the criterion

$$\frac{C}{\kappa} > -\frac{3}{2} \tag{39}$$

is satisfied. Several classes of behavior are implied by this result and are summarized in table 3.

The chief physical implication of the results summarized in table 3 is that extrusion stability can depend on a tradeoff involving the rate dependence of the frictional resisting force and the rate of change of plug mass. Stable eruptive behavior can occur in the presence of rate-weakening friction (C<0) if the plug mass increases at a sufficient rate. This behavior contrasts with that of a system with constant plug mass, which necessarily exhibits unstable behavior if C<0 and, therefore, D<0 (table 2). Conversely, unstable behavior can occur in the presence of rate-strengthening friction (C>0) if the plug mass decreases at a sufficient rate.

Although further inferences can be drawn from the analytical results summarized by equations 38 and 39, for present purposes it

Table 3. Summary of behavior of equation 33, which is general solution of equation 27 for cases with changing plug mass $(K\neq 0, \kappa\neq 0)$.

[Behavior for both rate-strengthening friction ($C>0$) and rate-weakening friction ($C<0$) is summarized.]

κ	C	Behavior of equation 33
$\kappa = -(2/3)C$	$C = -(3/2)\kappa$	Undamped, constant-amplitude oscillations
$\kappa > 0$	$C > 0$	Oscillations necessarily decay toward a steady state
$\kappa > 0$	$C < 0$	Oscillations grow if $\kappa < -(2/3)C$ and decay if $\kappa > -(2/3)C$
$\kappa < 0$	$C > 0$	Oscillations grow if $\kappa < -(2/3)C$ and decay if $\kappa > -(2/3)C$
$\kappa < 0$	$C < 0$	Behavior becomes singular

is more useful next to consider numerical solutions of the nonlinear equation set 14–16. Nonlinearities produce important effects that are not revealed by analytical results that strictly apply only when transient disturbances are small (that is, $u'/u_0 << 1$).

Nonlinear Dynamics: Numerical Results

Results of the linear theory point to several questions to be addressed through numerical solution of the nonlinear system of equations 14–16. Do the bounds of stable versus unstable eruptive behavior and character of oscillatory eruptive behavior change when nonlinearities exist? More specifically, can nonlinearities result in stick-slip instabilities like those inferred to produce drumbeat earthquakes at Mount St. Helens? What controls the magnitude and frequency of stick-slip events? Can such events occur repeatedly (that is, forever) until some attribute of the system changes? Can evolution of stick-slip periods and amplitudes yield inferences about evolution of system properties? Do complications such as plug mass change have significant effects? How sensitive are the system's dynamics to disequilibrium initial conditions? (Although the linear theory assumes that departures from equilibrium are always small, nature imposes no such constraint, and volcanic eruptions necessarily begin in disequilibrated states.)

Normalized Nonlinear Equations and Control Parameters

Guidance for investigating the behavior of numerical solutions comes from identification of dimensionless control parameters and their likely magnitudes. Behavior of the nonlinear equations is governed partly by the same dimensionless parameters that govern linearized behavior, but additional parameters also play a role. The additional control parameters are identified by normalizing the nonlinear system of first-order equations 14–16 through use of dimensionless variables defined as $u^* = u/u_0,\ p^* = p/p_0, V^* = V/V_0, t^* = t/t_0$. Substituting these variables into equations 14–16 yields the normalized system

$$\frac{du^*}{dt^*} = -G + \frac{1}{1+Kt^*}\left[G(1+\hat{S})p^* - Ku^* - G\hat{S}F^*\right], \quad (40)$$

$$\frac{dp^*}{dt^*} = \frac{-1/V^*}{G(1+\hat{S})}\left[u^* - 1 + Z(R^* - 1)\right], \quad \text{and} \quad (41)$$

$$\frac{dV^*}{dt^*} = X\left[u^* - 1 + Z(R^* - 1)\right] + Y. \quad (42)$$

Here, G and K are dimensionless parameters defined exactly as in the linear model (that is, in equations 28 and 30). The dimensionless parameter $\hat{S}$ is related to S defined in the linear model (that is, in equation 29), but its definition is somewhat simpler because it involves F_0 rather than the derivative $C = dF/du$:

$$\hat{S} = \frac{F_0}{m_0 g} = \lambda\mu_0. \quad (43)$$

The dimensionless parameters X, Y, and Z have no analog in the linear model and are defined as

$$X = \frac{\alpha_1 m_0 u_0}{A t_0} \qquad Y = \frac{t_0(Q-B)}{V_0} \qquad Z = \frac{R_0 B}{u_0 A}. \quad (44)$$

The variables R^* and F^* in equations 40–42 are normalized versions of the density variable R defined in equation 17 and the friction force F defined in equation 12:

$$R^* = \frac{R}{R_0} = \frac{1 + (R_0 - 1)\exp\left[XG(1+\hat{S})(p^* - 1)\right]}{R_0}, \quad (45)$$

$$F^* = \frac{F}{F_0} = \operatorname{sgn}(u^*)\left(1 + c\sinh^{-1}[u^*(u_0/u_{ref})]\right). \quad (46)$$

In the nonlinear version of the SPASM model, equations 45 and 46 must be satisfied simultaneously with equations 40–42.

Plausible ranges of the values of the dimensionless parameters in equations 40–46 for the 2004–5 eruption of Mount St. Helens are listed in table 4. The tabulated values imply that some of the terms in equations 40–46 will have little influence on numerical results. For example, relevant values of the denominator $G(1+\hat{S})$ on the right-hand side of equation 41 are undoubtedly very much greater than 1, implying that p^* will remain close to its static equilibrium value $p^* = 1$. This inference, together with the inference that $X<<1$ (table 4), implies that the argument of the exponential function in equation 45 will remain close to zero, despite the large probable value of $G(1+\hat{S})$. Therefore, $R^*=1$ is typically a good approximation of equation 45, and this approximation implies that the term $Z(R^*-1)$ in equations 41 and 42 will have only subtle effects. Similarly, the term Y in equation 42 will have subtle effects because $Y<<1$ (table 4). As a basis for prioritizing investigations, then, it is reasonable to assume initially that $Y=Z=0$.

With these simplifications in mind, equation 40 can be differentiated and combined with equation 41 to obtain a second-order equation, which can also be obtained through normalization of the original oscillator equation 18. For the case in which $R^*=1$ is a good approximation, the complete system of normalized nonlinear governing equations thereby reduces to

$$\left(1+Kt^*\right)\frac{d^2u^*}{dt^{*2}} + (2K+GS)\frac{du^*}{dt^*} + \frac{1}{V^*}u^* = \frac{1}{V^*} - K\,G, \quad \text{and} \tag{47}$$

$$\frac{dV^*}{dt} = X(u^*-1). \tag{48}$$

Note that S rather than $\hat{S}$ appears in equation 47, and that the entire set of dimensionless parameters has collapsed to K, G, X, and S in equations 47 and 48. Moreover, the values of K and X are typically much smaller than 1 (table 4), and the effects of terms containing K and X are therefore apt to be modest. On this basis, computational investigations aimed at illuminating the physics represented by the SPASM model can focus principally on the effects of G and S, secondarily on the effects of K, and lastly on the effects of X, Y, and Z.

The strategy of focusing primarily on effects of G and S reduces the need to explore a large, multidimensional parameter space numerically, and it parallels development of the linearized theory, in which D emerged as the key control parameter. Indeed, D defined in the linearized theory applies also to the nonlinear model, provided that D is viewed as a numerical index rather than a constant damping factor. For this purpose it is useful to define the index D as the value applicable when the slip rate equals the steady equilibrium rate ($u = u_0$):

$$D_{u=u_0} = \frac{1}{2}\;(2K + GS) = \tag{49}$$

$$\frac{1}{2}\left(\frac{2\kappa t_0}{m_0} + c\lambda\mu_0\,\frac{gt_0}{u_{ref}}\left[1+\left(\frac{u_0}{u_{ref}}\right)^2\right]^{-1/2}\right).$$

This equation is simply an algebraically expanded version of the definition given in equation 31, and I employ this definition of D to index numerical results.

It is also noteworthy that for cases in which $K=0$ and $u_0/u_{ref} >> 1$, equation 49 reduces to the simplified form

$$D \approx \frac{1}{2}\left(c\lambda\mu_0\,\frac{gt_0}{u_0}\right), \tag{50}$$

which is commonly a satisfactory approximation. In the sparest distillation of the nonlinear SPASM model, then, numerical results can be expected to depend primarily on D as defined in equation 50, which in turn depends only on c, λ, and μ_0 if the equilibrium extrusion rate u_0 and oscillation time scale t_0 are fixed.

Computational Method

Numerical solutions were obtained by using a standard fourth-order Runge-Kutta method described by Press and others (1986). To implement the Runge-Kutta algorithm, a double-precision FORTRAN program was written and executed on a personal computer with a 2.26-GHz processor. Constant time steps were used to generate all solutions and were typically 0.0001 to 0.01 s. Although some exploratory computations required hours of CPU time, no computations reported in this paper required more than several minutes of CPU time when using this constant-time-step approach.

The accuracy of numerical solutions was checked against exact analytical solutions for simple linear cases with constant values of D and K (table 2 and equation 33). For nonlinear cases, some aspects of numerical solutions were checked analytically by exploiting the fact that the governing equations 14–16 yield nearly exact solutions for p and V for the special case in which $u = 0$. These solutions assume that $R = R_0$, and they have the form

$$V = V_i + Wt, \quad \text{and} \tag{51}$$

$$p = p_i + \frac{Q-R_0B}{(\alpha_1+\alpha_2)W}\,\ln\left[1+\frac{W}{V_i}t\right], \tag{52}$$

where

$$W = \frac{\alpha_1}{\alpha_1+\alpha_2}\,\left[R_0B-Q\right]+Q-B. \tag{53}$$

Here V_i and p_i are the values of V and p at the beginning of any "stick" episode with u=0. The duration of stick episodes, T_{stick}, may be calculated by solving equation 52 for t while setting p equal to the static limiting equilibrium pressure p_0 necessary to trigger any slip episode,

$$T_{stick} = \frac{V_i}{W}\left[\exp\left(\frac{(p_0-p_i)(\alpha_1+\alpha_2)W}{Q-R_0B}\right)-1\right]. \tag{54}$$

Table 4. Plausible values of SPASM model parameters applicable to the quasi-steady dome-building eruption of Mount St. Helens, 2004–2005.

[Derived dimensionless parameters determine model behavior and are formed from combinations of physical parameters.]

Parameter	Units	Value(s)	Comments on value(s)
Specified physical parameters			
A	m^2	30,000	Calculated using Q/u_0 and values tabulated here
B	m^3/s	0–10	Cannot differ greatly from Q
c	none	-0.01–0.01	Inferred from results of testing by Moore and others, (this volume, chap. 20)
C	kg/s	$\lvert C \rvert < 5\times10^{13}$	Calculated using equation 23 and values tabulated here
g	m/s^2	9.8	Typical value at Earth's surface
m_0	kg	5×10^{9}–7×10^{10}	Inferred from plug heights 100–1,000 m and A and ρ_r tabulated here
Q	m^3/s	1–2	Inferred from photogrammetric measurements of dome growth
R_0	none	-0.5–0.5	Calculated from typical values of ρ_0 and ρ_r tabulated here
t_0	s	0.4–150	Calculated from equation 25 and other values tabulated here
u_0	m/s	2×10^{-5}–7×10^{-5}	Inferred from measured linear extrusion rate
u_{ref}	m/s	7×10^{-8}–7×10^{-5}	Smaller than u_0 if friction rate-dependence is nonlinear
V_0	m^3	3×10^{6}–3×10^{8}	Inferred from 8 km conduit height and conduit radii 10–100 m
α_1	Pa^{-1}	10^{-8}–10^{-6}	Typical values for silicic magma with 1–50 vol percent bubble content
α_2	Pa^{-1}	$\leq 10^{-9}$	Typical values for fractured rock
κ	kg/s	$\lvert \kappa \rvert < 4{,}000$	Exceptions may occur during dome-collapse events
λ	none	0.1–1	Inferred from plug geometry and plausible effective stress states
μ_0	none	0.4–0.5	Inferred from results of testing by Moore and others, (this volume, chap. 20)
ρ_0	kg/m^3	1,200–2,400	Typical values for silicic magma with 1–50 vol percent bubble content
ρ_r	kg/m^3	1,600–2,400	Inferred from measurements on dome-rock specimens
Derived dimensionless parameters			
D	none	-10^{7}–10^{7}	Influence of D can be very significant
G	none	6×10^{4}–2×10^{7}	Influence of G is very significant
K	none	$\lvert K \rvert \leq 10^{-4}$	Influence of K is subtle except in event of abrupt dome collapse
S	none	-7–7	Influence of S is significant
$\hat{S}$	none	-0.5–0.5	Influence of $\hat{S}$ is significant if multiplied by G
X	none	4×10^{-4}–8×10^{-10}	Influence of X is subtle except perhaps where multiplied by G
Y	none	$\lvert Y \rvert \leq 10^{-4}$	Influence of Y is subtle
Z	none	$\lvert Z \rvert < 0.5$	Influence of Z may be significant, contingent on value of R^*

This equation is useful for checking computational results, and it also has a significant physical implication: the duration of stick episodes increases exponentially with $p_0 - p_i$. From this result it may be inferred that plug displacements during slip events also increase exponentially with $p_0 - p_i$, because the average extrusion velocity is fixed (as given by equation 20), and slip-event magnitude must therefore increase in proportion to stick duration. Although strict validity of equations 52 and 54 rests on the assumption that $R = R_0$, computations that do not employ this assumption show that, nonetheless, equations 52 and 54 generally provide good predictions.

Computational Results

Only a small number of computational solutions are presented here, but hundreds of additional solutions were computed and examined. Results chosen for presentation highlight a range of physical effects that appear particularly important for understanding the origin of drumbeat earthquakes at Mount St. Helens. To a lesser degree, results were also chosen to illustrate the spectrum of behaviors possible within the framework of the SPASM model.

Behavior with *D* Close to Zero

The most basic nonlinear features of solutions appear even when departures from linear behavior are slight. In particular, stick-slip cycles develop in any case in which $D<0$, provided that a jump in F is imposed at $u=0$. Figure 9 illustrates this behavior for a case in which $D=-0.01$, $B=Q$, and F depends linearly on u (that is, $F=\operatorname{sgn}(u)\, m_0 g \lambda \mu_0 [1+c\left|u/u_{ref}\right|]$). The small value of D results from use of an unusually small value of λ, $\lambda=0.01$; physically, this value implies that frictional resistance and the damping it produces are small. The computation also used the initial conditions $u=Q/A$, $V=V_0$, and $p=p_0$, which imposed a slightly perturbed initial magma pressure (because the static equilibrium pressure p_0 slightly exceeds the steady equilibrium pressure) and used the parameter values $K=0$, $Y=0$, $Z=0$, $X=5\times10^{-6}$, $T=10$ s, $\rho_0=\rho_r=2{,}000$ kg/m^3, $m_0=3.6\times10^{10}$ kg, $\mu_0=0.5$, $c=-1.71\times10^{-5}$, and $u_{ref}=0.1(Q/A)=6.66710^{-6}$ m/s. The fact that the value of u_{ref} is significantly smaller than that of the typical extrusion rate (Q/A) implies that effects of rate dependence in the friction rule are important.

Under the conditions described above, the computed extrusion behavior is initially identical to that predicted by the linear analytical theory, and u, p, and V each exhibit exponentially growing sinusoidal oscillations until $u=0$ occurs (at $t\approx$ 27 s in fig. 9). At that time F momentarily changes sign and thereby halts motion of the plug as it starts to descend. This event heralds the end of exponential oscillation growth and the onset of repetitive stick-slip cycles.

In both the sinusoidal and stick-slip cycles shown in figure 9, magma pressure oscillates ¼ cycle out of phase with slip velocity, and conduit volume oscillates ½ cycle out of phase with magma pressure. Although it may seem contradictory that conduit volume decreases as magma pressure increases, this out-of phase response results from conditions at the base of the extruding plug, where solidification and accretion occur continuously at the volumetric rate B, even as plug velocity diminishes to less than the steady-state value $u=Q/A=6.667\times10^{-5}$ m/s. Indeed, as a rough approximation, conduit volume declines whenever the plug extrusion rate is less than the basal accretion rate. The conduit volume also responds elastically to pressure changes, but this effect is typically overshadowed by volume changes associated with plug motion and basal accretion.

Key elements of the solution presented in figure 9 are recast in a phase-plane diagram in figure 10, which shows how pressure deviations from the static equilibrium pressure p_0 vary in concert with velocity deviations from the steady equilibrium velocity Q/A. As portrayed in the phase plane, the initial condition ($u=Q/A$, $p=p_0$, marked I.C. in fig. 10) is unstable. This instability leads to an outwardly diverging clockwise spiral representing simultaneous oscillations of u and p that grow with time. (Note that arrows in phase-plane diagrams throughout this paper point in the direction of advancing time.) When the spiral becomes large enough to encounter the condition $u=0$, divergence ceases and the dynamics become locked in stick-slip limit cycles that repeat endlessly thereafter. If the initial condition is located elsewhere inside the stick-slip limit cycle of figure 10, behavior nonetheless diverges smoothly until locking in the same limit-cycle state. If friction exhibits rate-strengthening rather than

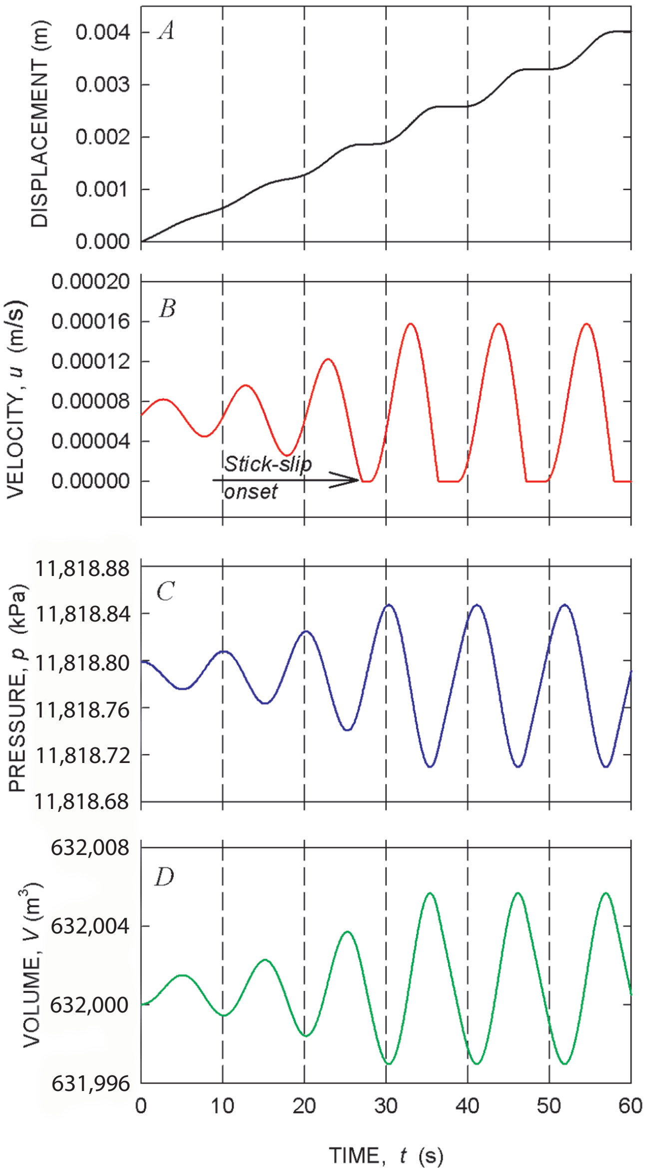

Figure 9. Start-up behavior of solution computed for $D=-0.01$ with linear rate weakening. Initial condition is $u=Q/A$, $p=p_0$, $V=V_0$. Oscillations of slip velocity (u), magma pressure (p) and conduit volume (V) are sinusoidal and match analytical predictions until $u=0$ occurs and stick-slip behavior begins.

rate-weakening behavior (that is, D>0), then behavior converges smoothly to a steady fixed-point equilibrium instead. An analogous fixed-point equilibrium is exhibited by eruption models that assume forces are always balanced (for example, Mastin and others, this volume, chap. 22).

Modification of the behavior depicted in figures 9 and 10 by nonlinearity in the rate-weakening friction rule is illustrated in figures 11 and 12. Initial conditions and parameter values used to generate figures 11 and 12 were the same as those used to generate figures 9 and 10, but the nonlinear friction rule $F = \mathrm{sgn}(u)\, mg\lambda\mu_0 [1 + c\sinh^{-1}|u/u_{ref}|]$ was employed. Comparison of figure 11 with figure 9 demonstrates that the most conspicuous effects of the nonlinearity are to delay the onset of stick-slip behavior and shorten the duration of individual stick events. These effects are unsurprising, because the nonlinearity represented by the $\sinh^{-1}$ function increasingly suppresses rate weakening as the slip rate increases.

Comparison of the phase-plane diagrams shown in figures 10 and 12 demonstrates that the dynamical effects of linear and nonlinear rate weakening also differ in other ways. In both figures 10 and 12 the feature of greatest interest is the outer loop representing stick-slip limit cycles. In the limit cycles shown in both figures, the maximum positive magma pressure deviates by a factor of only 4×10^{-6} from the static equilibrium pressure (~10^7 Pa), and the maximum slip velocity is only slightly more than double the equilibrium slip velocity. The maximum velocity is somewhat larger in the case with linear rate weakening (fig. 10), however, because linear rate weakening enables a larger dynamic overshoot of slip in response to increasing magma pressure. (Here, “dynamic overshoot” means that inertia carries the moving plug upward past an equilibrium point in which forces are balanced.) This larger overshoot produces a commensurately larger decline in magma pressure in response to slip, and the magma pressure deviation at the onset of stick-slip limit cycles is about three times larger in the case with linear rate weakening than with nonlinear weakening (~6×10^{-6} versus 2×10^{-6}). This difference in pressure deviation constitutes the single most important difference between the linear case (fig. 10) and the nonlinear case (fig. 12), because the duration of stick periods (T_{stick}) increases

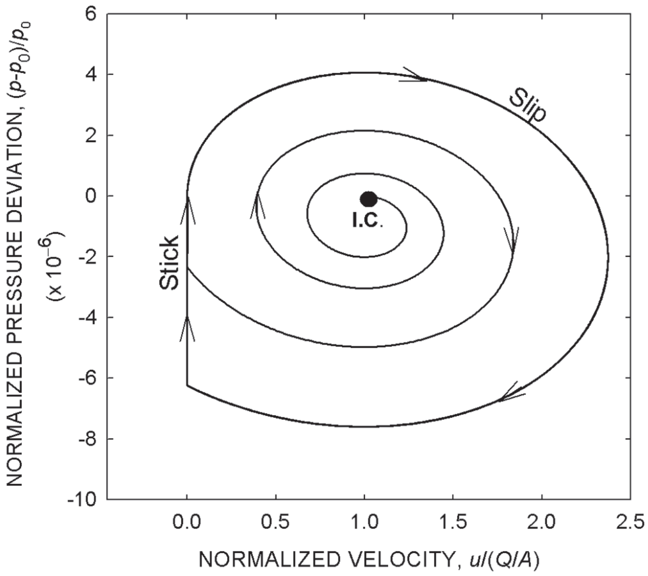

Figure 10. Phase-plane representation of simultaneous evolution of normalized slip velocity and normalized magma pressure computed for D = –0.01 with linear rate weakening. Initial condition (I.C.) is: $u = Q/A$, $p = p_0$, $V = V_0$. Arrows point in direction of advancing time.

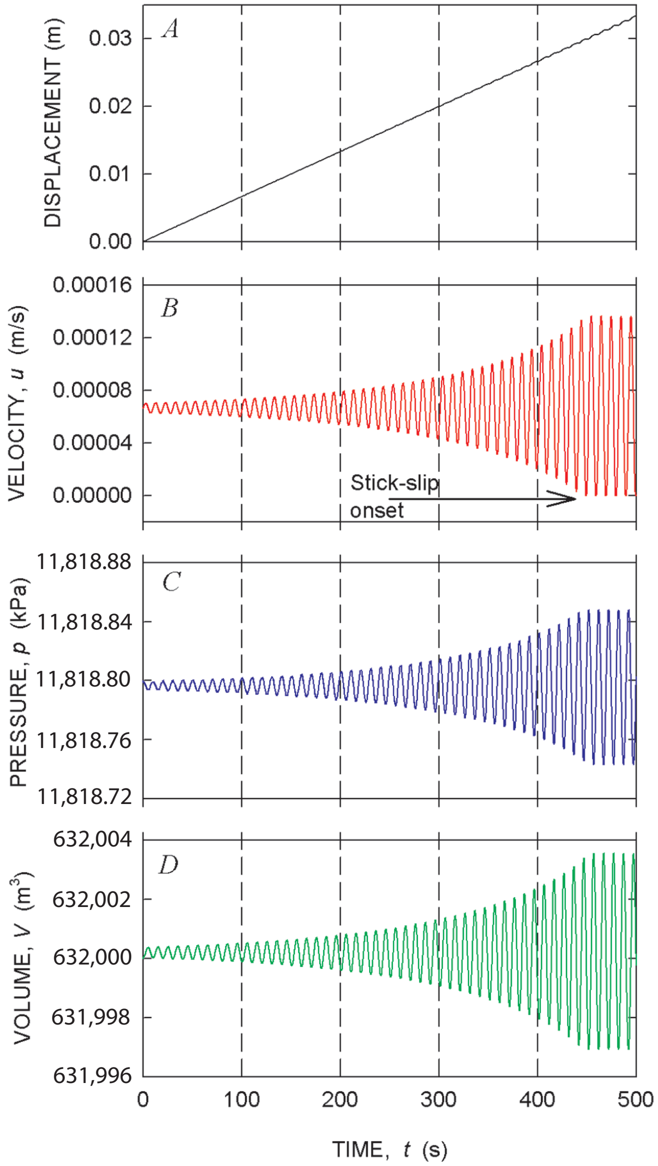

Figure 11. Start-up behavior of oscillatory solutions computed for D = –0.01 with nonlinear rate weakening. Initial condition is $u = Q/A$, $p = p_0$, $V = V_0$. Oscillations of slip velocity (u), magma pressure (p), and conduit volume (V) are sinusoidal until u = 0 occurs and stick-slip behavior begins.

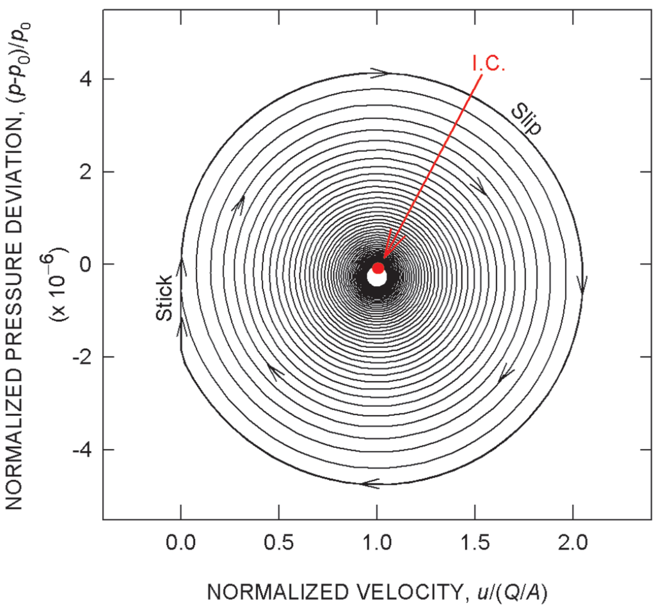

Figure 12. Phase-plane representation of simultaneous evolution of normalized slip velocity and normalized magma pressure computed for $D = -0.01$ with nonlinear rate weakening. Initial condition (I.C.) is $u = Q/A$, $p = p_0$, $V = V_0$. Arrows point in direction of advancing time.

exponentially with this pressure deviation, as indicated by equation 54. Therefore, nonlinearity in the friction rule has a significant effect on predictions of the periods and amplitudes of stick-slip oscillations, and the nonlinear rule was employed to generate all results presented subsequently in this paper.

Effects of the Damping Index *D*

Some of the most important findings of this study are summarized in figure 13, which illustrates computational results obtained by employing the nonlinear friction rule and various values of *D*. Computations that generated these results used the same parameter values used to generate figures 9–12, except that here $\lambda = 0.2$ was used, and varying values of *c* were used to generate *D* values ranging from −0.2 to −4. (The value $\lambda = 0.2$ constitutes a "best-guess" value applicable to Mount St. Helens' plug geometry and state of effective stress, and *c* values ranging from 1.7×10^{-5} to 3.4×10^{-4} were used to simulate subtle rate weakening similar to that observed experimentally by Moore and others, this volume, chap. 20).

Displacement time series shown in figure 13*A* were computed for a family of stick-slip cycles with various values of *D*, and in figure 13*B* the same results are depicted as limit cycles in the velocity-pressure phase plane. Initial conditions used to generate figure 13 assumed a static, limiting equilibrium state (u=0, $p = p_0$, $V = V_0$) rather than the state with $u = u_0$ used to generate figures 9–12. Therefore, no divergent oscillations precede the development of stick-slip limit cycles.

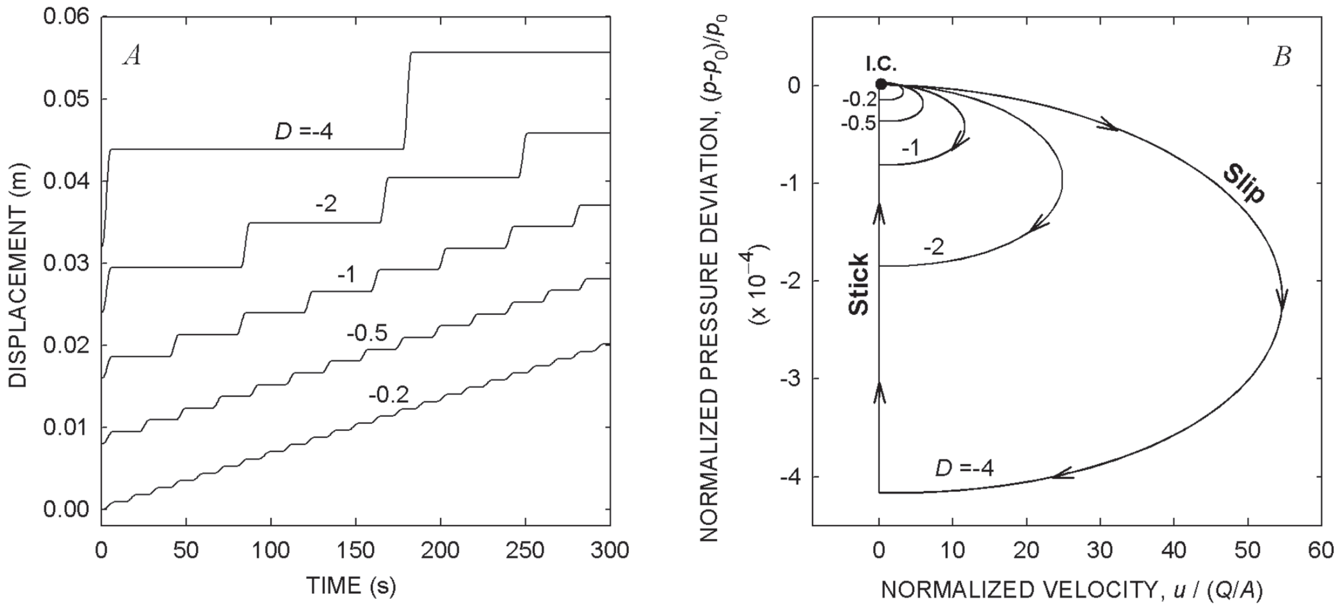

Figure 13. Stick-slip cycles computed for various values of parameter *D* with nonlinear rate weakening. All computations employed baseline parameter values Q=2 m^3/s, B=Q, $R_0 = 0$, K=0, Y=0, Z=0, X=5×10^{-6}, T=10 s, and employed m_0=3.6×10^{10} kg, λ=0.2, μ_0=0.5, and u_{ref}=0.1(Q/A)=6.667×10^{-6} m/s to determine *F*. Varying values of *c* were used to obtain varying values of *D*. *A*, Time series representation of stick-slip displacements. *B*, Phase-plane representation of velocity-pressure limit cycles. Arrows point in direction of advancing time.

The basic dynamics portrayed in figure 13*B* are simple. When basal magma influx produces pressure exceeding the static equilibrium value (p_0), it triggers slip at a rate that may slightly or greatly surpass the steady equilibrium rate (Q/A), depending on the value of D. When a combination of plug inertia and diminishing magma pressure no longer suffices to overcome the effects of gravity and friction, slip terminates and stick begins. Magma pressure then rebuilds until it triggers another slip event. Figure 13*A* shows that periods of stick-slip cycles with $D= -0.2$ differ little from the T=10 s period predicted by linear theory (that is, equation 25), but periods increase as D values range further from 0. For D values sufficiently far from 0, periods increase almost in direct proportion to the magnitude of D, and the amplitudes of slip events increase accordingly. Maximum slip speeds and associated pressure deviations during stick-slip cycles also increase in proportion to the magnitude of D (fig. 13*B*), bolstering the inference that D values encapsulate most of the important controls on system dynamics.

Stick-slip cycles computed with $D= -2$ closely resemble those thought to be responsible for generating drumbeat earthquakes at Mount St. Helens. With $D = -2$, individual slip events entail about 5 mm of displacement in about 5 s and maximum slip rates of ~1.7 mm/s. Attendant fluctuations in magma pressure are <0.02 percent of p_0 (fig. 13*B*), equivalent to only ~2.4 kPa or <0.2 m of static magma pressure head. This result implies that a remarkably delicate shift in the balance of forces distinguishes periods of slip from those with no slip. Multiplied by $A = 30{,}000$ m^2, the ~2.4 kPa pressure change also serves as a proxy for the force drop responsible for generating seismicity (~7×10^7 N).

Details of Baseline Case with D=−2

Deeper exploration of the dynamics computed with $D= -2$ provides further insight to physical phenomena that may be responsible for drumbeat seismicity at Mount St. Helens. Figure 14 illustrates details of repetitive earthquake cycles computed with D=–2. The histories of slip velocity, magma pressure, and conduit volume shown in figure 14 illustrate abrupt decreases in magma pressure and increases in conduit volume during slip events and also illustrate gradual changes of these quantities between slip events. As noted above, magma solidification at the base of the plug causes the volume of the fluid-filled conduit to decline between slip events, despite the fact that magma pressure rises.

Perhaps the most intriguing result illustrated in figure 14 involves the history of shear force along the plug margins. The shear force is large (~3.5×10^{10} N) because it must overcome the effects of both gravity and friction to move the massive plug upward, but the force drop during each slip event is comparatively small (~7×10^7 N) (fig. 14*E*). (This drop in shear force is closely related to the stress drop that occurs in conjunction with tectonic earthquakes, but force drop is, in fact, a more fundamental quantity. The force drop represents the product of the stress drop and the area of the slip surface—a product that appears directly in earthquake energy budgets (for example, Scholz, 2002, p. 184). Shear force might be concentrated in a relatively small patch of gouge bounding the extruding plug at Mount St. Helens, or it might be distributed evenly within the gouge; from the standpoint of force drop, this distinction makes no difference.) Standard estimation methods indicate that such a 7×10^7 N force drop, accompanied by 5 mm of slip (figs. 14*A*, *E*), implies about 2×10^5 J of seismic energy radiation (Scholz, 2002, p. 185), whereas the work done against friction during the slip events depicted in figure 14 is the total shear force times displacement, which yields an estimate of 2×10^8 J. These results are consistent with prior findings that only a small fraction of the work done during fault slip produces seismic radiation (McGarr, 1999).

The temporal pattern of the drop in shear force accompanying slip events also has significant implications. As slip accelerates, the shear force declines smoothly owing to the effects of rate-weakening friction (fig. 14*E*). Similarly, as slip decelerates, the force smoothly rises as friction gradually increases. When slip stops, however, the shear force drops abruptly because it suddenly returns to a static equilibrium value imposed by the plug weight and magma-pressure force, which has declined during slip. Before this reequilibration, the shear force is out of equilibrium with these static forces because rate-weakening friction allows slip to dynamically overshoot the equilibrium point. The net effect is that almost the full force drop (~7×10^7 N) occurs abruptly at the end of the slip cycle, and it thereby provides an impulse capable of radiating high-frequency seismic energy.

Sensitivity of Behavior to Variations of Parameters Within D

Values of D encapsulate the effects of most of the important parameters affecting stick-slip dynamics, but it is nevertheless necessary to examine whether variations in values of these individual parameters have significant effects. Results presented in figures 15 and 16 show that the behavior computed for $D= -2$ is quite insensitive to variations in c, λ, and u_0 / u_{ref} . For example, if values of c and λ range over orders of magnitude, while D is held constant, computed stick-slip limit cycles differ only slightly in a phase-plane diagram depicting coevolution of the normalized pressure deviation and normalized slip velocity (fig. 15*A*). Differences exist exclusively in the magnitude of normalized pressure deviations, reflecting the fact that smaller λ values imply that less magma pressure is needed to satisfy limiting equilibrium and trigger slip. Moreover, if the pressure deviations are "denormalized," as shown in figure 15*B*, such differences disappear entirely, and results for all values of c and λ collapse onto a single curve in the phase plane. This finding demonstrates that values of c and λ individually are unimportant in the system's dynamical behavior, provided that D is constant and the nonlinearity of the friction rule is unchanged.

Results shown in figure 16 illustrate the effects of changing the nonlinearity of the friction rule by allowing the value of u_0/u_{ref} to range over four orders of magnitude while holding $D = -2$. To facilitate comparison with figure 13, figure 16 depicts results as both displacement time series and stick-slip limit cycles. These results show that reducing values of u_{ref} (that is, increasing values of u_0/u_{ref}) produces stick-slip cycles with increased interevent periods, increased slip displacements, increased slip velocities, and increased deviations of magma pressure from its equilibrium value. However, effects of u_0/u_{ref} ranging over four orders of magnitude (fig. 16) are similar to the effects of *D* ranging from about −2 to −4 (fig. 13), reinforcing the view that *D* values encapsulate most of the dynamical controls on system behavior. It is, however, unsurprising that effects of u_0/u_{ref} are not captured entirely by values of *D*, as the effect of u_0/u_{ref} is inherently nonlinear. For values of u_0/u_{ref} smaller than 1, the periods of stick-slip oscillations lengthen, but this behavior is not pursued here because it has little relevance to plug extrusion at Mount St. Helens.

Effects of Plug Mass Change (Nonzero *K*)

Continuous changes in plug mass are represented by nonzero values of *K* (and of κ, its dimensional equivalent). If the condition $B=Q$ is assumed, nonzero values of *K* imply that the rate of mass loss due to surface erosion ($\rho_r E$) does not balance the rate of mass gain due to basal accretion (ρB), and the simplest example of such an imbalance occurs when the erosion rate is zero and the plug mass increases at the rate $\kappa = \rho B$. Figure 17 illustrates time-series behavior computed for this case (that is, κ=4,000 kg/s; $K=1.78\times10^{-7}$) with $D = -2$ and $u_0/u_{ref} = 10$. Comparison of figure 17 with figure 14

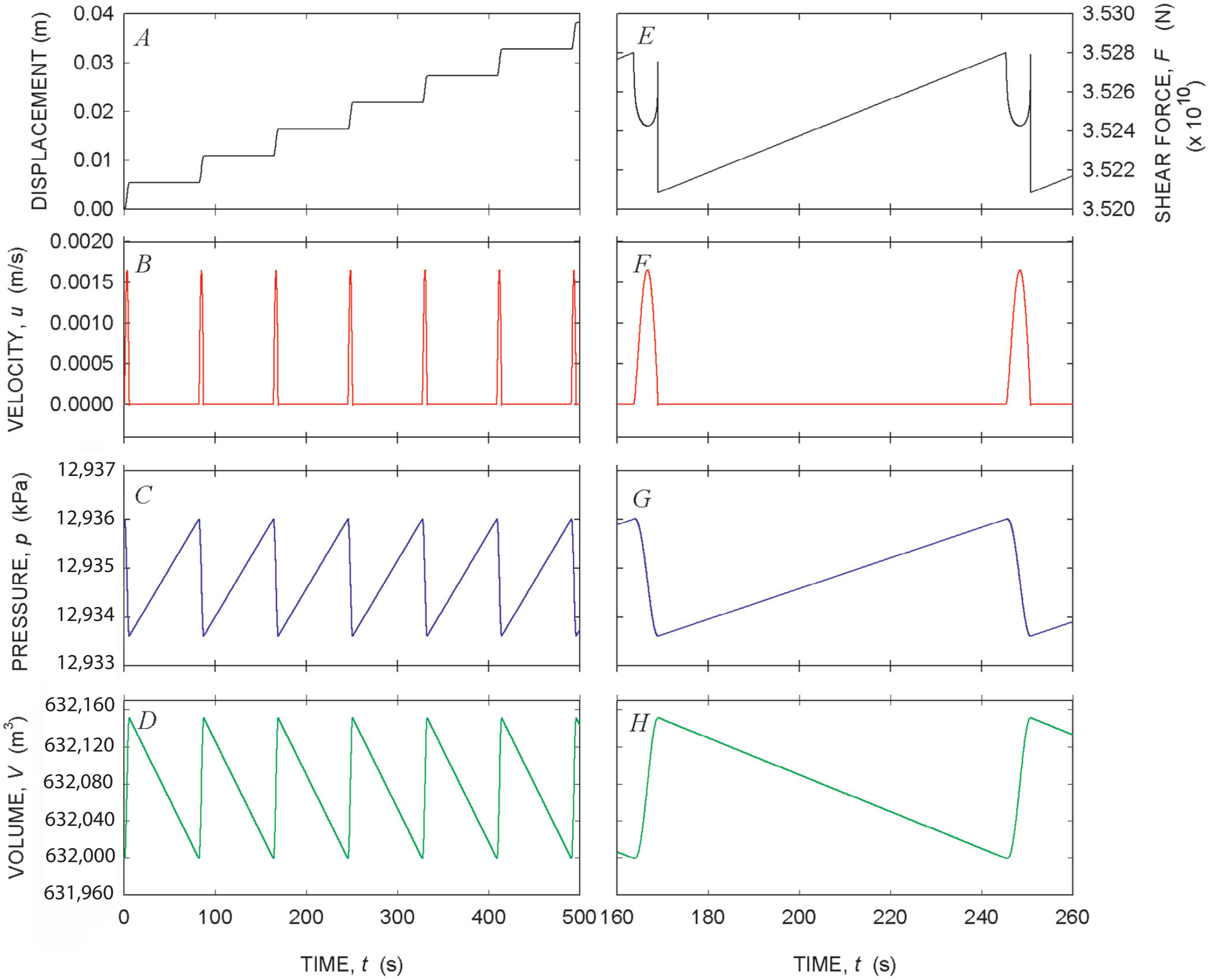

Figure 14. Time series depiction of concurrent changes in plug displacement, slip velocity, magma pressure, and conduit volume during earthquake cycles computed for baseline case with $D = -2$. Parameter values are same as those used to generate figure 13, and $c = -1.71\times10^{-4}$ is used to obtain $D = -2$. Panels *A*–*D* illustrate behavior during seven consecutive slip events, and panels *E*–*H* show details on an expanded time scale. Panel *E* is distinct from other panels because it shows force drops accompanying slip events.

shows that stick-slip cycles computed with $K>0$ have slightly larger periods and amplitudes than those computed with $K=0$, an unsurprising finding in view of analytical results indicating that positive K values will cause growth of oscillation periods (see equation 33). However, in contrast to analytical predictions, periods and amplitudes of stick-slip cycles computed with $K>0$ do not change with time.

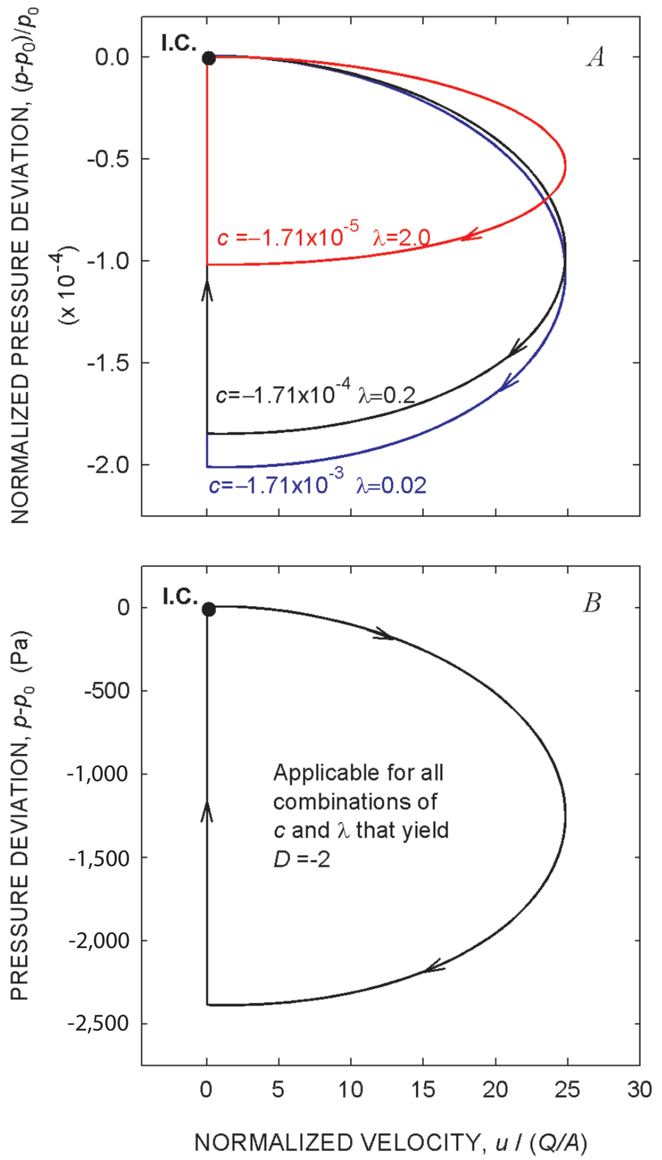

Figure 15. Sensitivity of stick-slip behavior with $D = -2$ to variations in parameters c and λ in the nonlinear rate-weakening friction rule. Other parameter values are same as those used to generate figure 14. Only phase-plane representations are shown, because time series are identical in all cases. Arrows point in direction of advancing time. *A*, Stick-slip cycles represented in terms of normalized pressure deviations. *B*, The same stick-slip cycles represented in terms of physical pressure deviations.

The linear analytical model yields spurious predictions of the effects of positive K values because it neglects explicit coupling between magma-pressure change and conduit-volume change, which is included in the nonlinear computational model. Figure 17 shows that magma pressure rises slightly in each successive stick-slip cycle, because increased pressure is required to drive uplift of the increasingly massive plug. This increasing pressure is accompanied by slightly decreasing conduit volume (fig. 17), because volume change due to compression of the highly compliant magma exceeds volume change due to conduit-wall deflection. Moreover, the percent decrease in conduit volume at the end of each stick-slip cycle is precisely the same as the percent increase in plug mass during the same cycle. Therefore, the effects of changes in conduit volume counterbalance the effects of changes in plug mass, such that the net effect of these changes on the oscillation period is zero. (As shown by equation 25, the time scale for the natural oscillation period, t_0, depends on the product of plug mass and conduit volume.) Numerical results show that the counterbalancing effect of mass changes and volume changes occurs for all positive K values—within reason. As suggested by analytical results, however, very large K or κ values (satisfying the criterion $\kappa > -(2/3)C$) might stabilize extrusion and diminish oscillations. Such large κ values are physically unreasonable, because C scales with the large quantity $m_0 g / u_{ref}$ (equation 23*B*), and mass accretion at a commensurately large rate is not plausible.

The magma pressure build-up depicted in figure 17 is further illustrated by its phase-plane representation in figure 18. As shown in the phase plane, each stick-slip limit cycle is like the preceding cycle, except that each successive slip event begins at a successively larger magma pressure. In this example, use of the maximum plausible rate of mass increase (that is, $\kappa = \rho B = 4{,}000\,\text{kg/s}$) causes magma pressure to double after about 115,000 stick-slip cycles, or about 113 days. To within 1 percent, this result agrees with the pressure doubling time calculated by applying the analytical formula derived for pseudosteady-state extrusion (that is, equation 21) for the case in which $\kappa = 4{,}000$ kg/s. The chief implication of these results is that if the plug mass increases significantly, magma pressure can increase significantly without increasing the extrusion rate. Conversely, changes in extrusion rate need not be linked to changes in magma pressure if the plug mass changes.

Computational results obtained with $K<0$ differ in important ways from results obtained with $K>0$. Figure 19 depicts results computed using a negative K value with the same magnitude as the positive K value used to generate figures 17 and 18 (that is, $K = -1.78\times10^{-7}$), and this value implies that the mass erosion rate, $\rho_r E$, is twice the rate of basal mass accretion, ρB. Comparison of figures 17 and 19 shows that the negative K value produces changes in magma pressure and conduit volume with signs opposite to those for $K>0$ and also produces more frequent slip events (seven as opposed to six in 500 s). Slip events occur more frequently in the presence of diminishing plug mass, because less magma

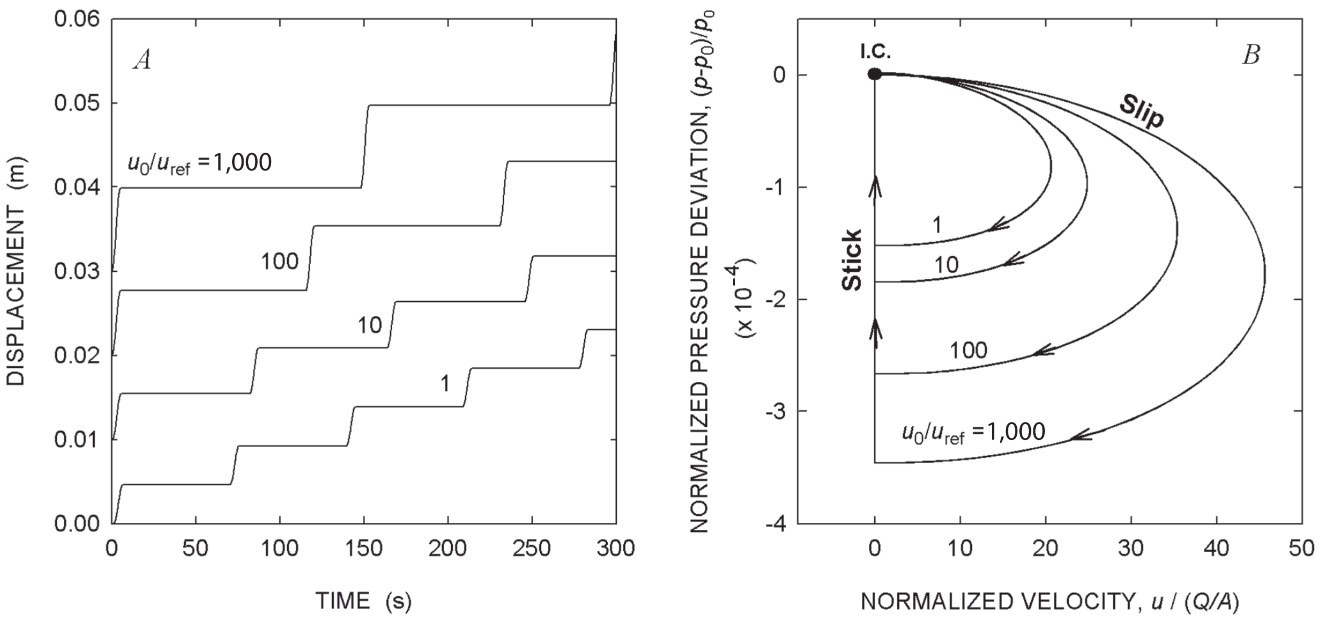

Figure 16. Sensitivity of stick-slip behavior with D = –2 to variations in u_0 / u_{ref} in the nonlinear rate-weakening friction rule. Other parameter values are the same as those used to generate figure 14. *A*, Time-series representation of stick-slip displacements. *B*, Phase-plane representation of velocity-pressure limit cycles corresponding to *A*. Arrows point in direction of advancing time.

pressure is necessary to trigger slip in each successive stick-slip cycle. Importantly, the increased frequency of slip events is accompanied by an increase in the mean extrusion rate (which occurs with a constant magma supply rate, Q=2 m^3/s), and this increase demonstrates the potential for runaway eruptive behavior. Moreover, decreasing plug mass eventually leads to a singularity in which fluid magma reaches the surface and the SPASM equations no longer apply (that is, the case with C<0 and κ<0 identified in table 3).

Runaway behavior is more evident in computational results obtained using negative K values with magnitudes much larger than the value -1.78×10^{-7} used to generate figure 19. Unlike large positive K values, large negative K values are physically plausible, because the plug mass can decrease rapidly if large-scale spalling or avalanching erodes the plug surface. Figure 20 depicts displacement time series computed with negative K values having magnitudes 100, 1,000, and 10,000 times greater than -1.78×10^{-7}. (The value -1.78×10^{-3} corresponds to mass loss at a rate of 4×10^{7} kg/s or a volumetric rate of about 20,000 m^3/s—a rate high enough to remove the entire plug in less than one hour.) The key point illustrated by figure 20 is that, in the presence of significant mass loss, time-averaged displacement rates can be much larger than the steady equilibrium rate $u_0 = Q / A = 6.667\times10^{-5}$ m/s that prevails with K=0, and these high rates would likely lead to a change in eruptive style.

The unstable growth of extrusion rate that occurs with K= -1.78×10^{-3} is represented in the phase-plane diagram depicted in figure 21. The diagram shows that deviations from the equilibrium magma pressure and equilibrium slip rate are exceedingly large during each stick-slip cycle and that maximum slip rates increase during each successive slip cycle—while magma pressure successively declines. In such scenarios, then, extrusion occurs faster and faster until the plug is removed and liquid magma reaches the surface. The accompanying decline in magma pressure could also result in increased vesiculation and explosive potential, although this process is not represented by the SPASM model.

Effects of *X*

The dimensionless parameter X defined in equation 44 mediates the interaction between extrusion rate and conduit volume change, as shown by equations 42 and 48, and it also affects magma pressure change through its influence on R^* (that is, equation 45). The physical meaning of X can be clarified by writing its definition in a simplified, approximate form that is valid if $\alpha_1 >> \alpha_2$, which is almost certainly the case at Mount St. Helens:

$$X \approx u_0 \left(\frac{\alpha_1 m_0}{V_0} \right)^{1/2} . \qquad (55)$$

This definition implies that, for systems in which u_0 and α_1 are constant, variations in X can be viewed as scaled variations in m_0 / V_0. Indeed, because values of m_0 / V_0 can be changed while holding t_0 and D constant, this strategy is used to assess the effects of variations in *X* computationally. The condition *K*=0 is also assumed in this assessment.

Computations in which *X* is increased or decreased by one order of magnitude from its baseline value (5×10^{-6}) show that stick-slip time series and phase-plane diagrams are identical for all values of *X*. However, figure 22 shows that some important details of the earthquake cycle change when *X* is increased by an order of magnitude (to 5×10^{-5}) by simultaneously increasing m_0 and decreasing V_0 by one order of magnitude each from their baseline values, while retaining $D=-2$. Comparison of figure 22 with figure 14 (the baseline case) shows that, although the timing and magnitude of slip events is unchanged when *X* is increased by one order of magnitude, the accompanying magma pressure, pressure change, shear force, and force drop are each increased by one order of magnitude, whereas the conduit volume change is reduced by somewhat less than an order of magnitude. These effects are all logical consequences of the increased plug mass and reduced conduit volume that are imposed by increasing the value of *X*.

The most important fact illustrated by figure 22 is that the predicted magma pressure at the base of the plug (~1.3×10^{8} Pa) is roughly an order of magnitude larger than the expected lithostatic pressure near the plug base (that is, at depths ~500 m). Such a large magma pressure is unrealistic, as it would probably cause hydraulic fracturing and a marked change in eruption style. This result implies that a value $X\approx5\times10^{-5}$ is too large to be realistic. Similarly, if *X* is reduced to 5×10^{-7} while holding t_0 and *D* constant, computed basal magma pressures are an order of magnitude smaller than the likely lithostatic pressure—a result that is also unrealistic. These findings imply that an *X* value similar to the baseline value (5×10^{-6}) is probably appropriate for Mount St. Helens. Therefore, the computed drop in shear force accompanying slip in the baseline case (fig. 14) is also probably appropriate.

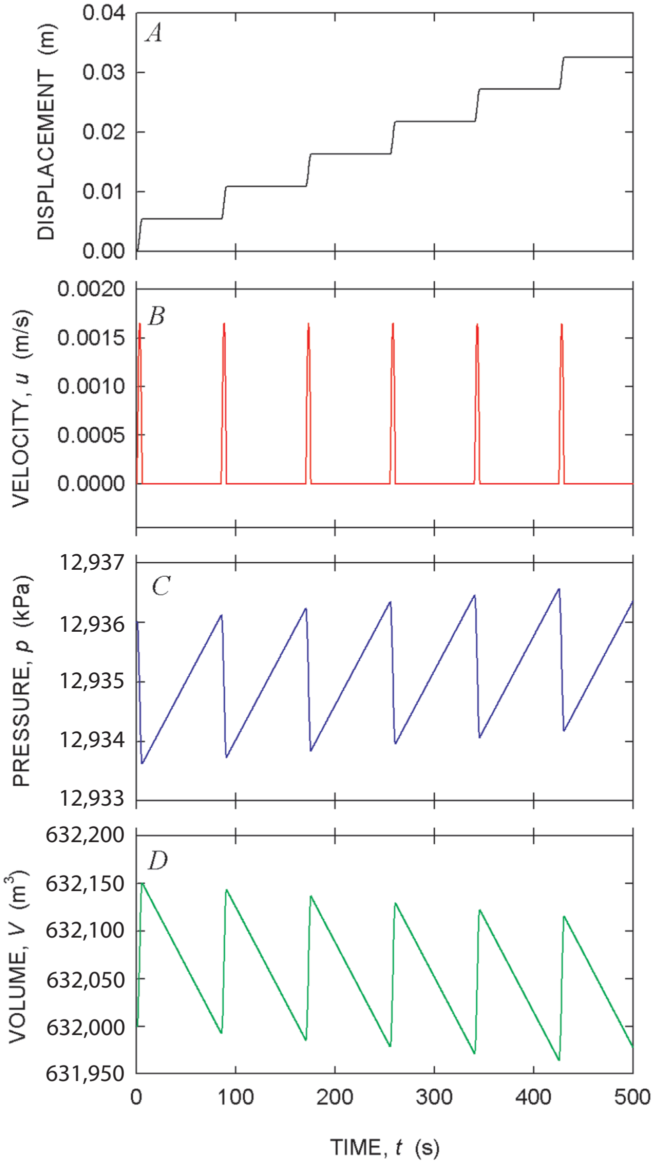

Figure 17. Time-series behavior of solutions computed with $D=-2$, $u_0/u_{ref}=10$, and increasing plug mass specified by $K=1.78\times10^{-7}$ (that is, $\kappa=4{,}000$ kg/s). Other parameter values are same as those used to generate figure 14.

Effects of *Y*

The dimensionless parameter *Y* defined in equation 44 represents the scaled difference between the magma-

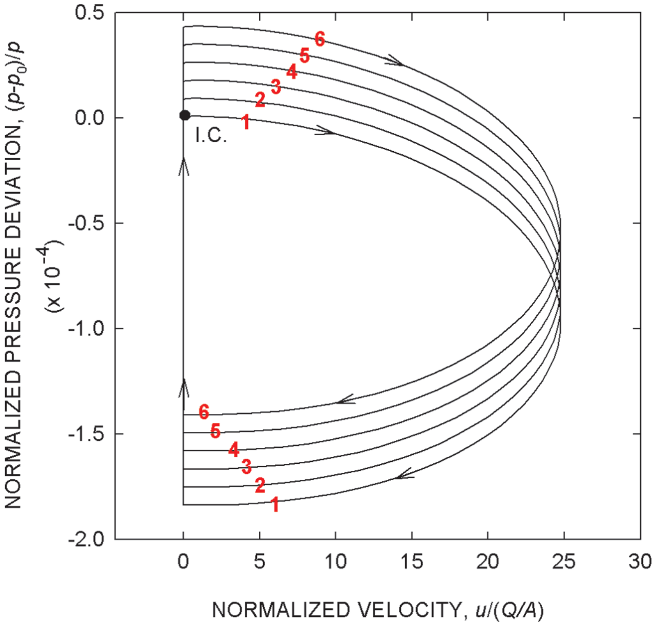

Figure 18. Phase-plane representation of solution depicted in figure 17. Numbers shown in red denote time sequence of successive limit cycles. Arrows point in direction of advancing time.

influx rate Q and magma-solidification rate B. All results presented thus far assume that $B=Q$, which is necessary for the magma-plug system to long remain close to equilibrium. Indeed, if $B \neq Q$ for a sustained period, a transition in eruptive behavior is inevitable. If $B>Q$, for example, the solidification front would propagate downward and the plug mass would increase unless mass loss due to surface erosion balances mass gain due to basal accretion. If such a balance were sustained, the plug would appear to sink progressively, even as extrusion continued, and friction on the plug margins would progressively increase. On the other hand, if $B<Q$, the solidification front would migrate

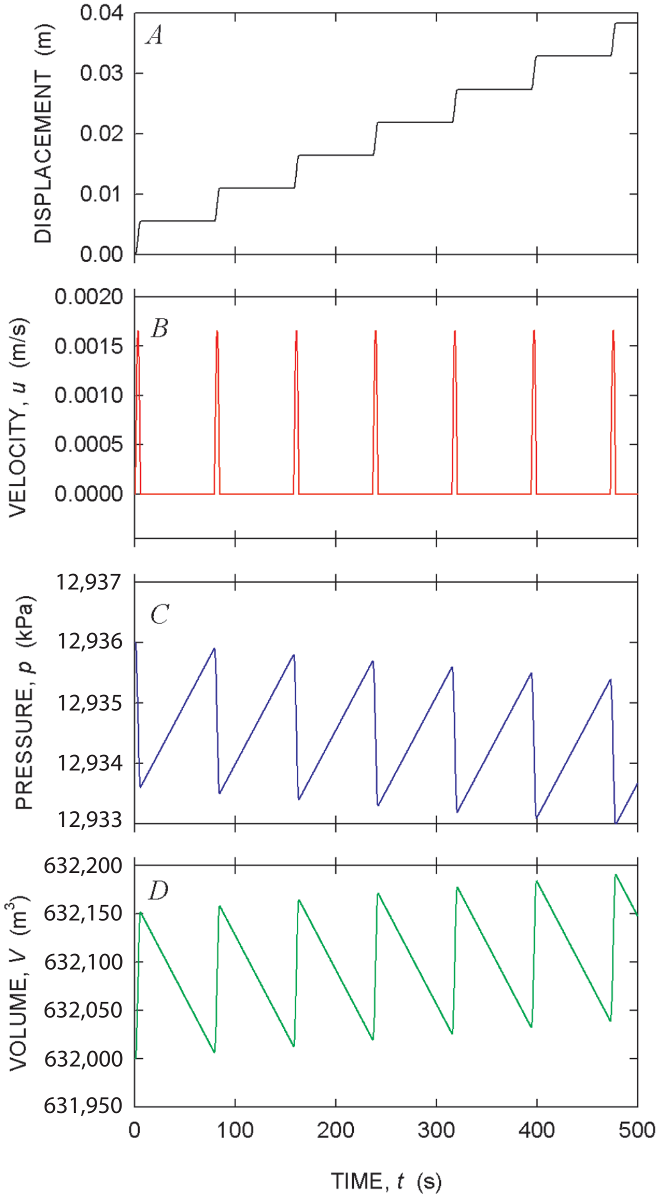

Figure 19. Time-series behavior of solutions computed with $D = -2$, $u_0/u_{ref}=10$, and decreasing plug mass specified by $K = -1.78\times10^{-7}$ (that is, $\kappa = -4{,}000$ kg/s). Other parameter values are same as those used to generate figure 14.

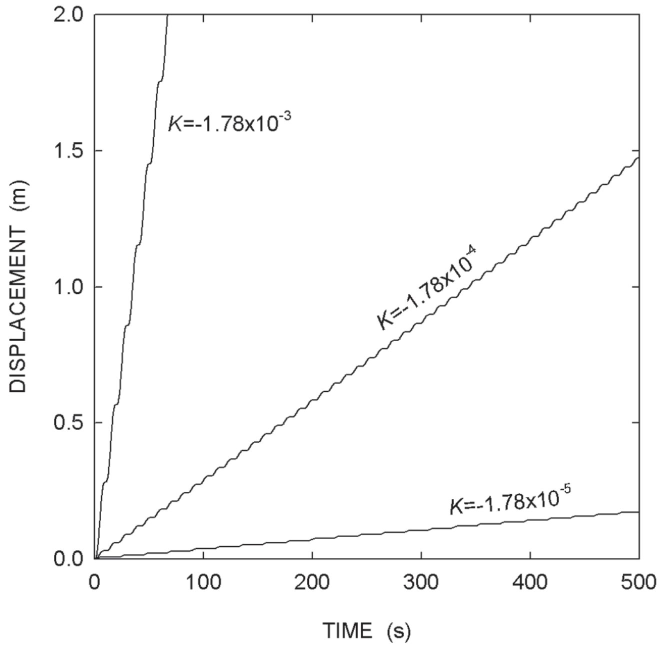

Figure 20. Comparison of displacement time series computed with $D = -2$, $u_0/u_{ref}=10$, and differing rates of decreasing plug mass specified by differing values of K. Other parameter values are same as those used to generate figure 14.

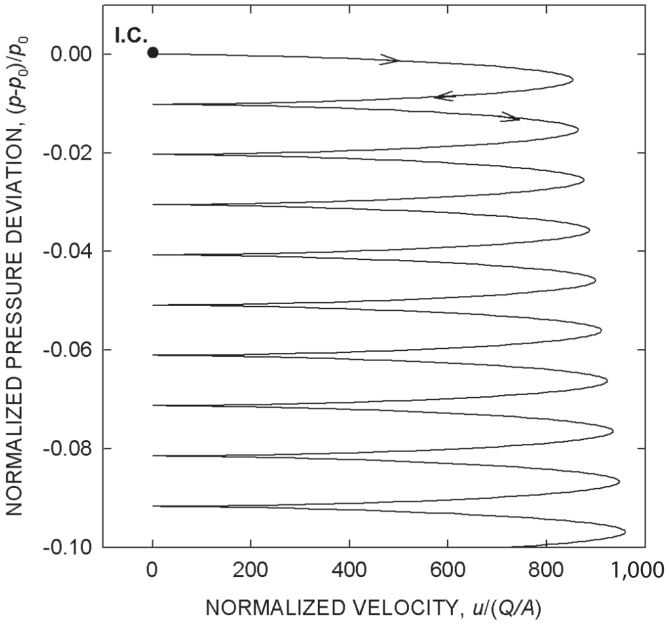

Figure 21. Phase-plane representation of stick-slip limit cycles occurring with $D = -2$, $u_0/u_{ref}=10$, and rapid decrease in plug mass ($K = -1.78\times10^{-3}$; $\kappa = -4\times10^{7}$ kg/s). Other parameter values are same as those used to generate figure 14. Arrows point in direction of advancing time.

upward. In the extreme case of B=0, any changes in plug mass would result exclusively from surface erosion, and the plug would eventually be pushed out the ground as liquid magma reached the surface. This scenario represents singular behavior analogous to that occurring with a negative mass-change rate (K<0). Below, I focus only on short-time behavior for cases with B>Q and B=0.

Behavior computed for a case with B=2Q=4 m^3/s and K=1.78×10^{-7} (that is, κ=4,000 kg/s) is shown in figure 23; this case is exactly like that illustrated in figure 17 except that, here, growth of plug mass occurs as a result of basal accretion in excess of Q. Thus, figure 23 depicts the response to growth of mass exclusively below the surface (with downward migration of the solidification front), whereas figure 17 depicts the response to growth exclusively above the surface (with no downward migration of the solidification front). The results shown in figures 23 and 17 are in most respects identical, except that the conduit volume decreases much more quickly in the case with basal accretion in excess of Q (fig. 23)—an obvious consequence of downward migration of the solidification front. Increasing pressurization of the conduit fluid accompanies this migration, and in the long run this combination of effects is unsustainable because magma pressure eventually would become large enough to fracture surrounding rock.

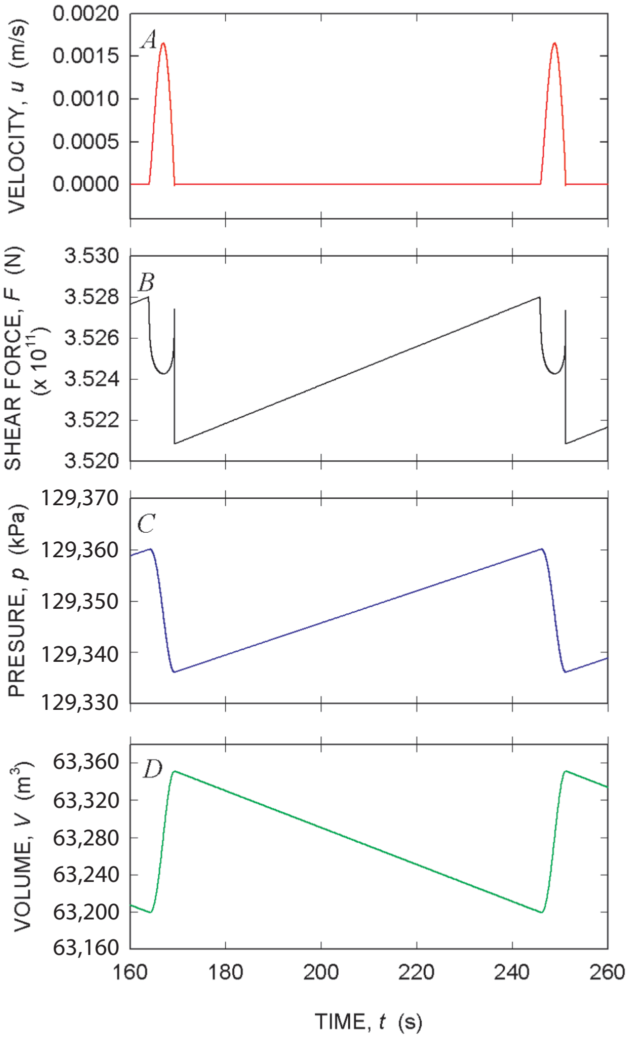

Figure 22. Details of an earthquake cycle computed with $D=-2$, $u_0/u_{ref}=10$, and $X=5\times10^{-5}$ (one order of magnitude larger than the X value used to compute the baseline results shown in figure 14). Other parameter values are same as those used to generate figure 14.

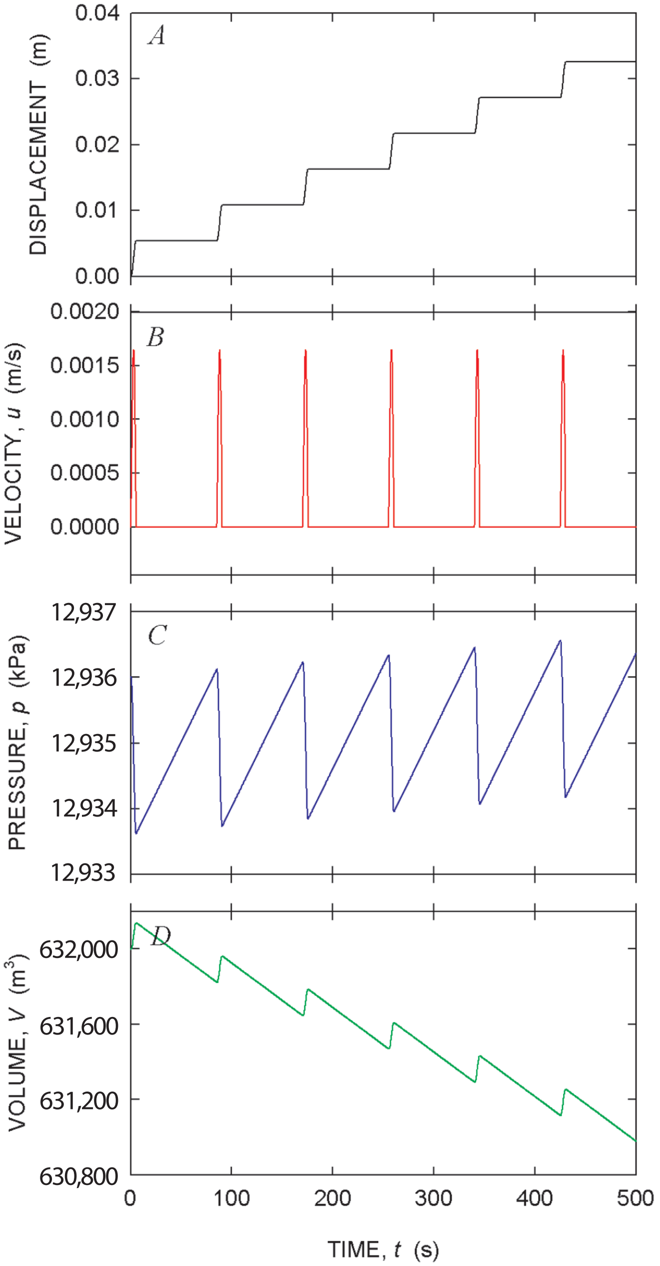

Figure 23. Time series behavior of solution computed with $D=-2$, $u_0/u_{ref}=10$, and excess basal accretion specified by $B=2Q=4$ m^3/s and $K=1.78\times10^{-7}$ (that is, $\kappa=4{,}000$ kg/s). Here $Y=-5\times10^{-6}$. Other parameter values are same as those used to generate figure 14.

The limiting case with small *B* (that is, *B*=0) exhibits behavior almost exactly like that computed for the baseline case with *B*=*Q* and *K*=0. Indeed, with *B*=0, graphs of the behavior for early times are indistinguishable from those shown in figures 13 and 14, except that conduit volume increases with each successive stick-slip cycle (fig. 24). This increase is an obvious consequence of upward migration of the base of the plug, and although this migration affects plug dynamics negligibly in the short term, persistence of this migration eventually must lead to the singularity noted above (that is, magma reaching the surface).

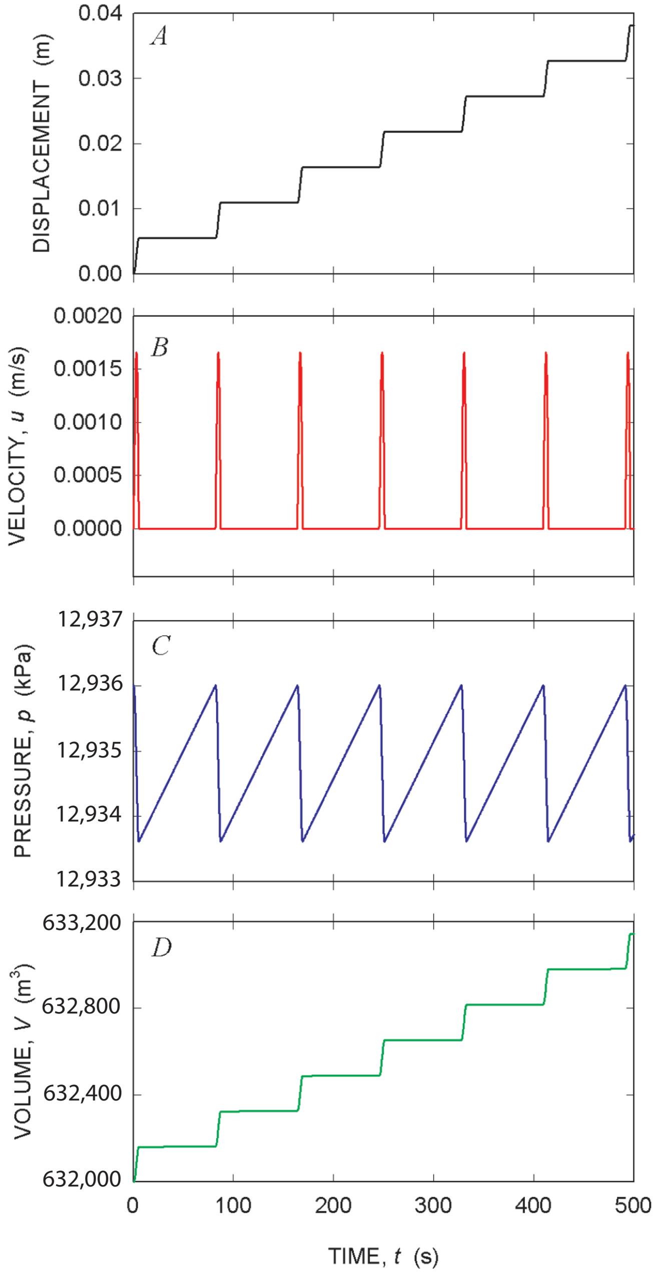

Figure 24. Time series behavior of solution computed with D = −2, u_0/u_{ref}=10, and zero basal accretion (*B* = 0). Here *Y* = 5×10^{-6}. Other parameter values are same as those used to generate figure 14.

Effects of *Z*

The dimensionless parameter *Z* defined in equation 44 may be interpreted as a scaled version of the mass-density ratio difference, $R_0 = 1-(\rho_0/\rho_r)$, which plays its most important role in determining the mean (that is, time-averaged) extrusion rate, $u_0 = (Q - R_0 B)/A$ given by equation 19. The mean extrusion rate is affected by *Z* because R_0 determines the change in density that occurs as magma ascending at rate *Q* solidifies at rate *B*—such that an increase in density during solidification reduces the volumetric extrusion rate of the solid plug. Values of R_0 plausibly range from about −0.5 to 0.5, and for the case with *B*=*Q*, these values yield u_0 values ranging from 0.5(*Q*/*A*) to 1.5(*Q*/*A*). Moreover, with *B*=*Q*, the definition of *Z* also reduces to $Z = R_0/(1-R_0)$, so that *Z* depends exclusively on R_0. Examples of displacement time-series solutions computed for this case, with various values of *Z*, are shown in figure 25.

Interpretation of figure 25 is complicated by the fact that with *A* and *B* held constant, values of *Z* cannot be varied independently of values of *D* and *X* (because *Z*, *X*, and *D* all depend on u_0, which in turn depends on R_0). Therefore, the figure shows results of computations in which *Z*, *X*, and *D* vary simultaneously. Nevertheless, the effect of values of *Z* on the average extrusion rate is clearly evident in figure 25; large departures from the baseline value *Z*=0 yield similarly large departures from the average extrusion rate observed with *Z*=0 (that is, $u_0 = Q/A$). The period of stick-slip cycles remains nearly proportional to the magnitude of *D* (just as in the baseline case illustrated in fig. 13), despite variations in *Z*. Unlike

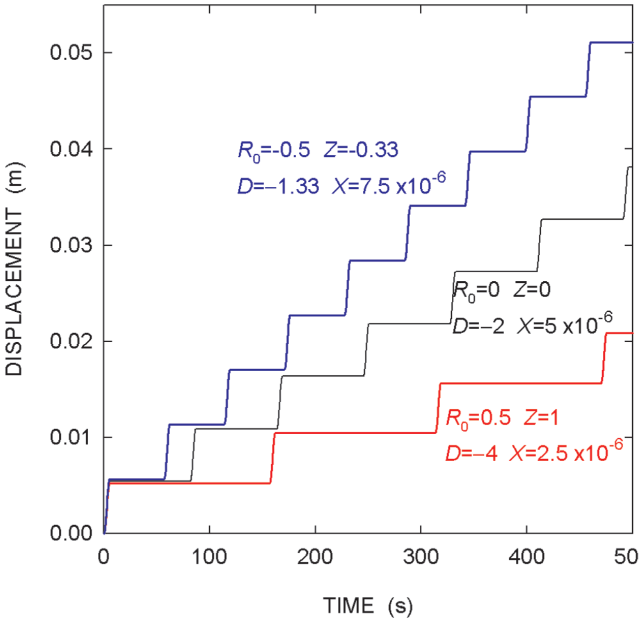

Figure 25. Displacement time series computed with varying values of R_0 and *Z* (with accompanying variation of *D* and *X*). Other parameter values are same as those used to generate figure 14.

the baseline case, however, the time series depicted in figure 25 each involve slip events with about the same magnitude of displacement (~5 mm). This behavior indicates that, while *D* largely controls the system's dynamics, the magnitude of slip events is additionally regulated by *Z*.

Effects of Initial Conditions

The preceding results were computed using initial conditions that assume a state of mechanical equilibrium, but volcanic eruptions presumably begin with an initial disequilibrium state, such as that due to magma pressure in excess of the static limiting equilibrium pressure ($p > p_0$). This section summarizes results of computations that used a disequilibrium initial condition of this type.

All computations with $p > p_0$ predict that an initial pulse of rapid motion occurs until plug momentum is depleted, magma pressure relaxes, and static equilibrium is restored, and this behavior occurs irrespective of the sign or value of *D* (figs. 26, 27). Pressure then rebuilds until it triggers a second stage of motion. For *D*<0 this stage consists of endlessly repetitive stick-slip limit cycles (closed loops in fig. 26) exactly like those produced with equilibrium initial conditions (for example, fig. 13), whereas for *D*>0 the second stage converges to a fixed-point equilibrium representing a state with dynamically balanced forces (fig. 27). It is noteworthy, however, that cases with rate-strengthening friction (*D*>0) and rate-weakening friction (*D*<0) exhibit similar initial pulses if the initial pressure disequilibrium is the same (for example, compare results for *D*=±0.2 in figs. 26*A* and 27).

A key point illustrated in figure 26 is that the maximum speed of the initial extrusion pulse and the magnitude of the associated pressure deviation increase almost linearly with increasing initial magma overpressure. Moreover, this trend is insensitive to the value of *D*, and linear extrapolation can therefore be used to infer the maximum extrusion speed (and pressure deviation) associated with any initial overpressure. With *D*= −2, for example, each increase of 0.005 percent in initial overpressure increases the maximum speed of the initial movement pulse $u_{\max}$ by about $u_{\max}/(Q/A) = 14$ (fig. 26*B*).

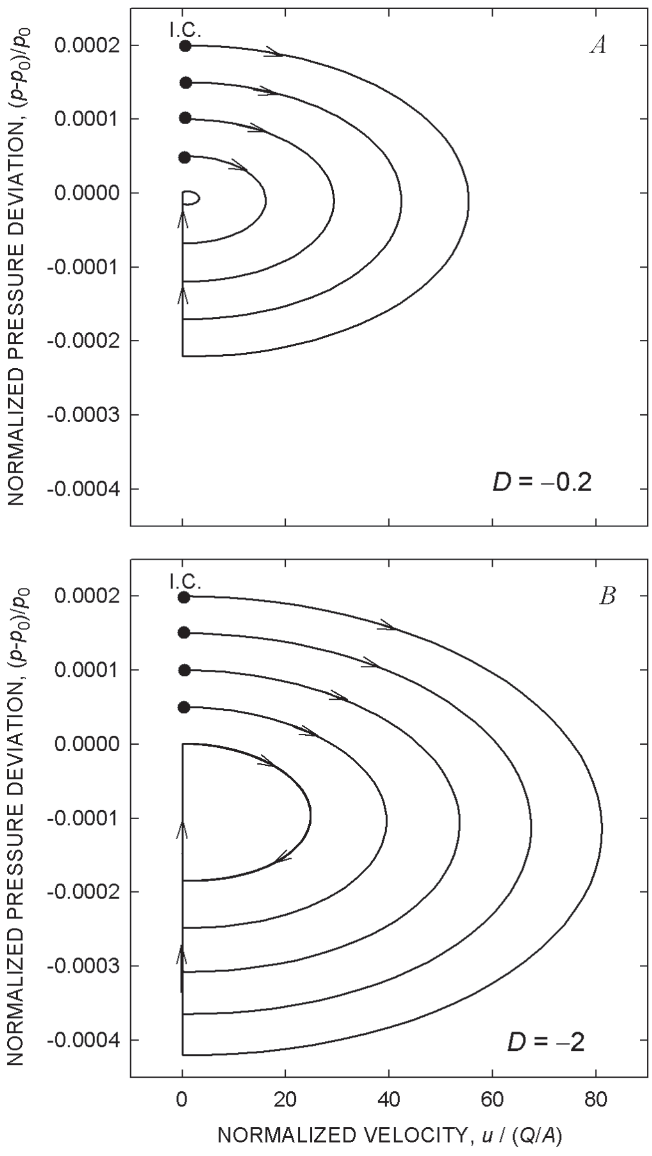

Figure 26. Phase-plane representation of behavior computed with four disequilibrium initial conditions (that is, initial excess magma pressures 0.005 percent, 0.01 percent, 0.015 percent, and 0.02 percent of p_0), for each of two negative values of *D*. Parameter values are same as those used to generate figure 14, except that *c* = −1.71×10^{-5} is used to obtain *D* = −0.2. Arrows point in direction of advancing time. *A*, *D* = −0.2. *B*, *D* = −2.

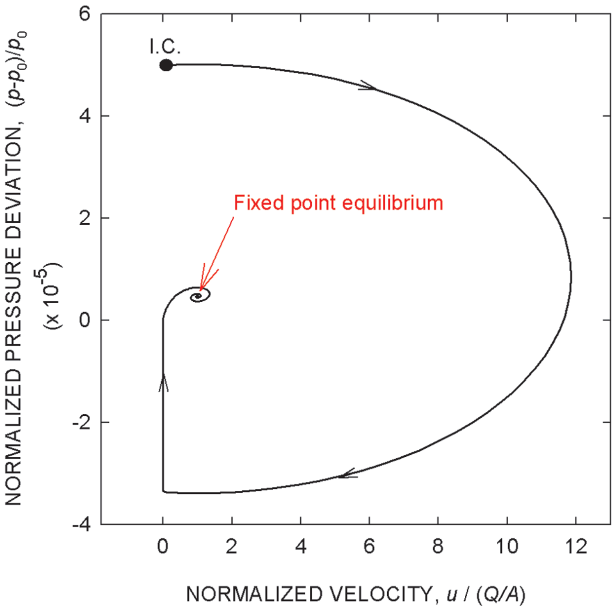

Figure 27. Phase-plane representation of extrusion behavior computed with an initial excess magma pressure (0.005 percent of p_0) and *D* = 0.2. Parameter values are same as those used to generate figure 14, except that *c* = 1.71×10^{-5} is used to obtain *D* = 0.2. Arrows point in direction of advancing time.

In conjunction with the baseline value $Q/A=6.67\times10^{-5}$ m/s for Mount St. Helens, this result implies that a 0.005 percent magma overpressure (relative to the static limiting equilibrium pressure p_0) would produce a maximum extrusion velocity of about 3 mm/s, and that an overpressure of 5 percent would produce a maximum extrusion velocity of ~1 m/s.

Magnitudes of displacements that occur during the initial movement pulses shown in figures 26 and 27 can be estimated from the maximum pressure deviation $p_0 - p$, because the displacement during slip is proportional to the duration of the subsequent "stick time" (as shown by equation 54). By inference from equation 54, then, the displacement during the initial slip event increases like $e^{(\alpha_1+\alpha_2)(p_0-p_i)}$. On this basis, extrapolation from figure 26*B* shows that initial magma overpressures of even a few percent would lead to movement pulses of at least several meters, provided that $D=-2$.

Discussion

The SPASM model was developed to explain the relation between nearly steady solid-state extrusion and nearly periodic drumbeat earthquakes observed during the 2004–5 eruption of Mount St. Helens. Although this relation could result from a complicated interaction of numerous physical and chemical processes, the SPASM model aims for a parsimonious mechanical explanation that employs a minimum of postulates and variables. Some of the parsimony of the SPASM model derives from its central, simplifying assumption: that the volumetric flux of magma into the base of the eruption conduit (Q) is constant. This assumption is consistent with a top-down perspective of eruption dynamics, in which no time-dependent changes in a deep magmatic system are invoked to explain phenomena observed at Earth's surface.

From a mathematical standpoint, the assumption of constant Q enables the SPASM model to be reduced to a nonlinear system of three first-order ordinary differential equations. The relative simplicity of these equations facilitates both analytical and numerical studies of model properties. Indeed, the mathematical behavior of the SPASM model can be understood completely, and understanding of this simple model provides a steppingstone toward understanding behavior of Mount St. Helens during solid-state extrusion in 2004–5.

Analytical study of the SPASM model demonstrates that steady, solid-state extrusion is an equilibrium condition that can be satisfied exactly if the magma influx rate, Q, equals the rate of magma solidification at the base of an extruding plug, B, which in turn is balanced by erosion of the plug surface, E. In addition, pseudosteady states can exist in which the extrusion rate remains constant and changes in plug mass are accompanied by compensating changes in magma pressure. Such pseudosteady states cannot persist indefinitely, however, because changes in plug mass and magma pressure cannot continue without eventually causing a change in eruption style. Therefore, long-term steady-state extrusion at Mount St. Helens in 2004–5 probably involved a near-equilibrium state in which the plug mass effectively remained almost constant and $B \approx Q$ applied.

Analysis of the SPASM model shows that, even when a near-steady eruptive state persists, extrusion velocities have an inherent tendency to exhibit short-term oscillations about the long-term equilibrium rate. These oscillations are an inevitable consequence of the interaction of plug momentum, a variable upward force due to magma compression and pressure, and a downward force due to the plug weight. The oscillations are damped mostly by plug-boundary friction, and if friction exhibits rate-weakening behavior like that observed in experiments with fault gouge obtained from the surface of the Mount St. Helens plug, damping is negative and oscillation amplitudes grow unstably. Oscillation growth is necessarily arrested, however, because friction has the potential to reverse its direction of action when the plug extrusion velocity declines to zero. Growing oscillations are thereby transformed to repetitive stick-slip cycles, and these cycles continue indefinitely (that is, until a change in a parameter such as Q, B, or E occurs). According to the SPASM model, these repetitive stick-slip cycles are responsible for generating nearly periodic "drumbeat" earthquakes observed during solid-state extrusion at Mount St. Helens in 2004–5.

Properties of stick-slip cycles predicted by the SPASM model are controlled by a variety of factors, but both analytical and numerical results support the conclusion that the natural oscillation time scale t_0 and dimensionless damping D exert the most important controls. The oscillation time scale is fixed by conduit and plug properties that affect elastic strain in the system, whereas nonlinearly rate-dependent friction causes damping to vary as a function of the extrusion velocity u. Nevertheless, computational results show that most effects of variable damping are encapsulated by D evaluated at the steady equilibrium extrusion rate, $u = u_0$. These results show that the amplitudes and periods of stick-slip cycles increase almost in proportion to the magnitude of D, provided that t_0 remains constant.

Computations using diverse values of D show that $D=-2$ produces stick-slip cycles most similar to those inferred to generate drumbeat earthquakes at Mount St. Helens throughout much of the 2004–5 eruption, and the dynamics of these cycles are relatively insensitive to variations in values of the physical parameters that constitute D. With $D=-2$, computed interevent periods are about 80 s, the slip distance per event is about 5 mm, maximum slip speeds are about 2 mm/s, and reduction of magma pressure during slip is about 2.4 kPa. This reduction in magma pressure is strikingly small in comparison to the ambient, roughly lithostatic magma pressure (~1.3×10^4 kPa) inferred to exist at the base of the plug, about 500 m beneath the ground surface. The small size of magma-pressure fluctuations indicates that the system deviates little from mechanical equilibrium, even during slip events. Moreover, changes in basal magma pressure during slip events can be multiplied by the inferred basal area of the plug (~30,000 m^2) to provide a proxy for the force drop available to generate seismicity.

A more refined assessment of the force drop during slip events is provided by SPASM output that shows how the shear force due to plug-boundary friction (F) evolves during slip. With $D = -2$, the computed force drop is about 7×10^7 N, and much of the force drop occurs abruptly, despite the fact that slip events have durations of ~5 s. This nearly instantaneous force drop occurs just as the slip velocity, u, decreases from a finite value to zero, and its abruptness results from the interplay of three phenomena: (1) owing to rate-weakening friction during slip, the upward-moving plug gains momentum that causes it to overshoot an equilibrium state in which forces are dynamically balanced; (2) as the upward-moving plug decelerates, a potential for downward motion exists, because basal magma pressure has relaxed to a value smaller than its static equilibrium value; and (3) incipient downward motion of the plug is arrested immediately, however, because friction along the plug margin reverses direction so as to oppose motion. Friction adjusts just enough to stop motion and balance forces, of course, because friction can only oppose motion, not drive it. The abrupt adjustment of the friction force as plug motion ceases produces a sudden force drop that can radiate high-frequency seismic energy.

The mechanics that produce the stick-slip behavior and force drops predicted by the SPASM model are robust because they derive from basic physical principles, but the weakest link in the SPASM formulation involves the nature of friction and its rate dependence. Frictional properties of granulated solids such as fault gouge are poorly understood at a fundamental level, although some degree and type of rate weakening is generally observed in a variety of both idealized and geological granular media (for example, Nasuno and others, 1997; Marone, 1998). Rate-weakening behavior has also been measured in tests of fault gouge collected from the surface of the extruding plug at Mount St. Helens (Moore and others, this volume, chap. 20). In the context of the SPASM model, the most crucial point revealed by these tests is that some degree of rate-weakening occurs as slip velocities increase from zero to a steady equilibrium value u_0. This weakening suffices to generate stick-slip behavior, regardless of subtler nuances of friction. If rate-strengthening friction develops at higher slip rates, for example, it will help arrest slip events but not prevent them. Therefore, the occurrence of stick-slip cycles appears almost inevitable.

Occurrence of stick-slip cycles large enough and abrupt enough to generate drumbeat earthquakes is also contingent on elastic properties of the magma-plug-conduit system. At least one elastic element in the system must be soft enough to strain significantly in response to driving forces that are smaller than those required to shear the fault gouge irreversibly (compare Rice and Ruina, 1983). (The shallow depths of drumbeat earthquakes implies that these driving forces are probably smaller than those causing fault slip at hypocentral depths typical of nonvolcanic earthquakes (that is, >1 km), because confining stress and frictional resistance are relatively small at depths <1 km.) At Mount St. Helens, fluid magma underlying the extruding plug provides an exceptionally soft elastic element, because its estimated 12 percent (by volume) exsolved gas content makes it orders of magnitude more compressible than solid rock. In essence, then, the magma serves as a spongy spring that compresses significantly as it delivers the force to shear the plug-bounding gouge. Strain energy stored during magma compression is released in abrupt slip events that would be smaller and more frequent if the magma were stiffer. Therefore, the earthquake cycle described by the SPASM model differs from a typical tectonic earthquake cycle in two important ways: (1) in SPASM, strain energy is stored principally in a compressed fluid, not in a solid deformed in shear; repeated, nondestructive compression of “soft” fluid enables seismogenic plug slip to occur repeatedly at shallow depths; and (2) in SPASM, after slip has ceased, the plug is reloaded by forces due to gravity and magma influx. This reloading occurs very rapidly in comparison to reloading by tectonic strain accumulation, enabling drumbeat earthquakes to occur much more frequently than tectonic earthquakes.

Gradual evolution of the magnitude and periodicity of drumbeat earthquakes observed during the 2004–5 eruption of Mount St. Helens prompts questions about the cause. Can evolution of drumbeats be a harbinger of changes in eruption rate or style? The SPASM model provides insight to this issue, but it provides no unequivocal answers. According to the model, amplitudes and periods of slip events can change in response to changes in values of any of the parameters that constitute D, even when magma ascent and solidification rates are constant. Because D encompasses the effects of gouge frictional properties and the effective stress state, as well as the natural oscillation time scale t_0, evolution of any of a number of phenomena could be responsible for changing the character of drumbeats. Nonetheless, because field data can to some degree constrain changes in quantities such as plug mass or conduit volume, it is tempting to ascribe changes in drumbeats to unobserved changes in gouge properties or the state of effective stress. Computational results from SPASM indicate that rather subtle changes in these phenomena can alter drumbeat properties significantly. Indeed, it is easy to imagine that the source of drumbeats could migrate around the periphery of the extruding plug as scattered patches of particularly strong gouge form, fail, and reform. A model more elaborate than SPASM would be required to analyze the details of such behavior.

The SPASM model does provide a clear picture of potential changes in eruption style that can occur if conditions far from equilibrium develop. One type of disequilibrium develops if the rate of magma accretion at the base of the extruding plug differs significantly from the rate of plug extrusion. If the accretion rate is less than the extrusion rate, liquid magma eventually will reach the ground surface. Magma pressure will simultaneously decline, and this decline could enhance magma vesiculation and explosive potential. On the other hand, if the plug accretion rate exceeds the extrusion rate, the solidification front will propagate downward and magma pressure will increase, assuming that deep magma influx remains constant.

Increasing pressure could eventually trigger an exceptionally large slip event or fracture surrounding rock, causing a transition in eruption style—or it could suffice to stop magma influx, thereby halting the eruption.

Effects of magma pressure exceeding the static limiting equilibrium pressure can be treated as disequilibrium initial conditions in the SPASM model. If excess pressure exists but is insufficient to fracture rock, a rapid pulse of plug motion occurs until static equilibrium is restored. If magma pressure exceeds the equilibrium pressure by even a few percent, SPASM predicts that this pulse can involve velocities of meters per second and displacements of many meters. Such a pulse could even eject the plug from the volcanic vent and instigate the type of transition in eruption style described above.

The fact that no rapid pulses of extrusion or transitions in eruption style occurred during the 2004–5 eruption of Mount St. Helens implies that the magma-plug system never deviated much from equilibrium, even during the eruption onset. This behavior is, of course, very different from that during the cataclysmic eruption of Mount St. Helens on May 18, 1980. In that case explosive activity was caused by rapid depressurization of a shallow magma body triggered by a massive landslide. Without the landslide trigger, the 1980 eruptions of Mount St. Helens might have been relatively quiescent, much like the eruption of 2004–5.

Conclusion

The central conclusion of this study is that stick-slip oscillations are almost inevitable during an eruption in which steady ascent of compressible magma drives upward extrusion of a solidified plug with margins that exhibit rate-weakening friction. Whether such oscillations are large and abrupt enough to generate repetitive earthquakes like those observed at Mount St. Helens depends on a host of factors, nearly all of which are encompassed within two quantities derived in this paper: the natural oscillation time scale $t_0 = [m_0(\alpha_1 + \alpha_2)V_0]^{1/2} / A$ and the frictional damping index, which can be approximated as $D \approx (1/2)\left(c\,\lambda\,\mu_0\,g\,t_0 / u_0\right)$. Large values of t_0 favor the occurrence of relatively large, infrequent slip events, because they imply that large elastic strains can be accommodated during magma compression. Large negative values of *D* have similar effects because they imply that effects of rate-weakening plug friction are significant, and rate weakening is responsible for “dynamic overshoot” during slip events. As a consequence, negative *D* values far from 0 cause the period between successive slip effects to exceed the period expected on the basis of t_0 alone.

Computations using $D = -2$ predict the occurrence of stick-slip cycles with interevent periods of ~80 s, slip displacements of ~5 mm, and force drops of ~7×10^7 N, and these properties appear consistent with those of events inferred to produce drumbeat earthquakes during the 2004–5 eruption of Mount St. Helens. Although individual modeled slip events last about 5 s, most of the accompanying force drop occurs in a fraction of a second, consistent with requirements for radiation of high-frequency seismic energy.

Persistence of nearly periodic drumbeat earthquakes also requires that slip events are driven by nearly steady forcing. At Mount St. Helens this forcing was provided by nearly steady ascent of magma. Magma solidification at the base of the extruding plug apparently occurred at a rate nearly equal to the rate of magma ascent, enabling the system to remain close to equilibrium. Indeed, model results show that a near-balance between ascent rate and solidification rate is essential for maintaining persistent drumbeats.

The presence of a near-surface body of compressible magma that serves as a driving element may be necessary to generate repetitive, seismogenic stick-slip events at the shallow focal depths (<1 km) observed during the 2004–5 eruption of Mount St. Helens. The strength of gouge at such shallow depths is relatively small (owing to relatively small normal stresses), and the gouge can therefore shear irreversibly before much elastic strain accumulates in a stiff adjacent body such as solid rock. Therefore, in the absence of a soft, near-surface magma body, stick-slip oscillations could still occur, but they would be reduced in size and period, perhaps to a degree that would make them aseismic. Moreover, near-surface fluid magma can undergo repeated elastic compression and decompression without accumulation of irreversible damage that would likely accompany similarly repetitive strain in solid rock.

Lack of large movement pulses during the 2004–5 eruption of Mount St. Helens reinforces the view that the magma-plug system remained close to equilibrium. Indeed, model results indicate that magma pressure exceeding the static equilibrium pressure by even a few percent was probably never present. An implication of this finding is that the dynamic equilibrium state exhibited during the eruption differs little from the static equilibrium state before the eruption onset. Therefore, the eruption trigger was likely very subtle, perhaps involving nothing more than weakening of the conduit cap rock by percolating water derived from late summer rains and glacier melt.

Acknowledgments

Virtually every member of the staffs of the Cascades Volcano Observatory and Pacific Northwest Seismic Network helped make this work possible through their contributions to monitoring the 2004–5 eruption of Mount St. Helens. I am indebted to all of them for their extraordinary efforts, and particularly to Seth Moran for fielding my many questions about volcano seismology. I am also indebted to Nico Gray of the Department of Mathematics, University of Manchester, U.K., who showed me how to obtain the analytical results summarized in equations 33–37 and appendix 1, and to Peter Moore and Neal Iverson, Department of Geological and Atmospheric Sciences, Iowa State University, who performed laboratory tests of the frictional properties of the Mount St. Helens gouge. Roger Denlinger and Joseph Walder provided insightful reviews that helped improve the manuscript.

References Cited

Abramowitz, M.K., and Stegun, I.A., eds., 1964, Handbook of mathematical functions with formulas, graphs, and mathematical tables: Washington, D.C., U.S. Government Printing Office, U.S. National Bureau of Standards Applied Mathematic Series 55, 1046 p.

Beeler, N.M., Tullis, T.E., and Weeks, J.D., 1994, The roles of time and displacement in the evolution effect in rock friction: Geophysical Research Letters, v. 21, no. 18, p. 1987–1990.

Blundy, J., and Cashman, K., 2001, Ascent-driven crystallisation of dacite magmas at Mount St. Helens, 1980–1986: Contributions to Mineralogy and Petrology, v.140, no. 6, p. 631–650, doi:10.1007/s004100000219.

Denlinger, R.P., and Hoblitt, R.P., 1999, Cyclic eruptive behavior of silicic volcanoes: Geology, v. 27, p. 459–462.

Dieterich. J.H., 1979, Modeling of rock friction 1; experimental results and constitutive equations: Journal of Geophysical Research, v. 84, no. B5, p. 2161–2168.

Dzurisin, D., Vallance, J.W., Gerlach, T.M., Moran, S.C., and Malone, S.D., 2005, Mount St. Helens reawakens: Eos (American Geophysical Union Transactions), v. 86, p. 25, 29.

Dzurisin, D., Lisowski, M., Poland, M.P., Sherrod, D.R., and LaHusen, R.G., 2008, Constraints and conundrums resulting from ground-deformation measurements made during the 2004–2005 dome-building eruption of Mount St. Helens, Washington, chap. 14 *of* Sherrod, D.R., Scott, W.E., and Stauffer, P.H., eds., A volcano rekindled; the renewed eruption of Mount St. Helens, 2004–2006: U.S. Geological Survey Professional Paper 1750 (this volume).

Gerlach, T.M., McGee, K.A., and Doukas, M.P., 2008, Emission rates of CO_2, SO_2, and H_2S, scrubbing, and preeruption excess volatiles at Mount St. Helens, 2004–2005, chap. 26 *of* Sherrod, D.R., Scott, W.E., and Stauffer, P.H., eds., A volcano rekindled; the renewed eruption of Mount St. Helens, 2004–2006: U.S. Geological Survey Professional Paper 1750 (this volume).

Goto, A., 1999, A new model for volcanic earthquake at Unzen volcano; melt rupture model: Geophysical Research Letters, v. 26, no. 16, 2541–2544.

Hatheway, A.W., and Kiersch, G.A., 1989, Engineering properties of rock, *in* Carmichael, R.S., ed., Practical handbook of the physical properties of rocks and minerals: Boca Raton, Florida, CRC Press, p. 673–715.

Kreyszig, E., 1979, Advanced engineering mathematics (4th ed.): New York, John Wiley, 939 p.

Lahr, J.C., Chouet, B.A., Stephens, C.D., Power, J.A., and Page, R.A., 1994, Earthquake classification, location, and error analysis in a volcanic environment; implications for the magmatic system of the 1989–1990 eruptions at Redoubt Volcano, Alaska: Journal of Volcanology and Geothermal Research, v. 62, nos. 1–4, p. 137–151, doi:10.1016/0377-0273(94)90031-0.

LaHusen, R.G., Swinford, K.J., Logan, M., and Lisowski, M., 2008, Instrumentation in remote and dangerous settings; examples using data from GPS “spider” deployments during the 2004–2005 eruption of Mount St. Helens, Washington, chap. 16 *of* Sherrod, D.R., Scott, W.E., and Stauffer, P.H., eds., A volcano rekindled; the renewed eruption of Mount St. Helens, 2004–2006: U.S. Geological Survey Professional Paper 1750 (this volume).

Lisowski, M., Dzurisin, D., Denlinger, R.P., and Iwatsubo, E.Y., 2008, Analysis of GPS-measured deformation associated with the 2004–2006 dome-building eruption of Mount St. Helens, Washington, chap. 15 *of* Sherrod, D.R., Scott, W.E., and Stauffer, P.H., eds., A volcano rekindled; the renewed eruption of Mount St. Helens, 2004–2006: U.S. Geological Survey Professional Paper 1750 (this volume).

Losert, W., Géminard, J.C., Nauson, S., and Gollub, J.P., 2000, Mechanisms for slow strengthening of granular materials: Physical Review E, v. 61, p. 4060–4068.

Major, J.J., Kingsbury, C.G., Poland, M.P., and LaHusen, R.G., 2008, Extrusion rate of the Mount St. Helens lava dome estimated from terrestrial imagery, November 2004–December 2005, chap. 12 *of* Sherrod, D.R., Scott, W.E., and Stauffer, P.H., eds., A volcano rekindled; the renewed eruption of Mount St. Helens, 2004–2006: U.S. Geological Survey Professional Paper 1750 (this volume).

Marone, C., 1998, Laboratory-derived friction laws and their application to seismic faulting: Annual Review of Earth and Planetary Sciences, v. 26, p. 643–696.

Marone, C., and Richardson, E., 2006, Do earthquakes rupture piece by piece or all together?: Science, v. 313, p.1748-1749.

Mastin, L.G., 1994, Explosive tephra emissions at Mount St. Helens, 1989–1991; the violent escape of magmatic gas following storms?: Geological Society of America Bulletin, v. 106, no. 2, p. 175–185.

Mastin, L.G., and Ghiorso, M.S., 2000, A numerical program for steady-state flow of magma-gas mixtures through vertical eruptive conduits: U.S. Geological Survey Open-File Report 00–209, 56 p.

Mastin, L.G., Roeloffs, E., Beeler, N.M., and Quick, J.E., 2008, Constraints on the size, overpressure, and volatile content of the Mount St. Helens magma system from geodetic and dome-growth measurements during the 2004–2006+ eruption, chap. 22 *of* Sherrod, D.R., Scott, W.E., and Stauffer, P.H., eds., A volcano rekindled; the renewed eruption of Mount St. Helens, 2004–2006: U.S. Geological Survey Professional Paper 1750 (this volume).

McGarr, A., 1999, On relating apparent stress to the stress causing earthquake slip: Journal of Geophysical Research, v. 104, no. B2, p. 3003–3011.

Melnik, O., and Sparks, R.S.J., 2002, Dynamics of magma ascent and lava extrusion at Soufrière Hills Volcano, Montserrat, *in* Druitt, T.H., and Kokelaar, B.P., eds., The eruption of Soufrière Hills Volcano, Montserrat, from 1995 to 1999: Geological Society of London Memoir 21, p. 153–171.

Moore, P.L., Iverson, N.R., and Iverson, R.M., 2008, Frictional properties of the Mount St. Helens gouge, chap. 20 *of* Sherrod, D.R., Scott, W.E., and Stauffer, P.H., eds., A volcano rekindled; the renewed eruption of Mount St. Helens, 2004–2006: U.S. Geological Survey Professional Paper 1750 (this volume).

Moran, S.C., 1994, Seismicity at Mount St. Helens, 1987–1992; evidence for repressurization of an active magmatic system: Journal of Geophysical Research, v. 99, no. B3, p. 4341–4354, doi:10.1029/93JB02993.

Moran, S.C., Malone, S.D., Qamar, A.I., Thelen, W.A., Wright, A.K., and Caplan-Auerbach, J., 2008, Seismicity associated with renewed dome building at Mount St. Helens, 2004–2005, chap. 2 *of* Sherrod, D.R., Scott, W.E., and Stauffer, P.H., eds., A volcano rekindled; the renewed eruption of Mount St. Helens, 2004–2006: U.S. Geological Survey Professional Paper 1750 (this volume).

Mullineaux, D.R., and Crandell, D.R., 1981, The eruptive history of Mount St. Helens, *in* Lipman, P.W., and Mullineaux, D.R., eds., The 1980 eruptions of Mount St. Helens, Washington: U.S. Geological Survey Professional Paper 1250, p. 3–15.

Nasuno, S., Kudrolli, A., and Gollub, J.P., 1997, Friction in granular layers; hysteresis and precursors: Physical Review Letters, v. 79, p. 949–952.

Neuberg, J.W., 2000, Characteristics and causes of shallow seismicity in andesite volcanoes: Philosophical Transactions Royal Society of London A, v. 358, p. 1533–1546.

Neuberg, J.W., Tuffen, H., Collier, L., Green, D., Powell, T., and Dingwell, D., 2006, The trigger mechanism of low-frequency earthquakes at Montserrat: Journal of Volcanology and Geothermal Research, v. 153, nos. 1–2, p. 37–50, doi:10.1016/j.jvolgeores.2005.08.008.

Newman, S., and Lowenstern, J.B., 2002, VolatileCalc—a silicate melt-H2O-CO2 solution model written in Visual Basic for excel®: Computers and Geosciences, v. 28, no. 5, p. 597–604, doi:10.1016/S0098-3004(01)00081-4.

Ozerov, A., Ispolatov, I., and Lees, J., 2003, Modeling Strombolian eruptions of Karymsky volcano, Kamchatka, Russia: Journal of Volcanology and Geothermal Research, v. 122, p. 265–280.

Pallister, J.S., Reagan, M., and Cashman, K., 2005, A new eruptive cycle at Mount St. Helens?: Eos (American Geophysical Union Transactions), v. 86, p. 499.

Pallister, J.S., Thornber, C.R., Cashman, K.V., Clynne, M.A., Lowers, H.A., Mandeville, C.W., Brownfield, I.K., and Meeker, G.P., 2008, Petrology of the 2004–2006 Mount St. Helens lava dome—implications for magmatic plumbing and eruption triggering, chap. 30 *of* Sherrod, D.R., Scott, W.E., and Stauffer, P.H., eds., A volcano rekindled; the renewed eruption of Mount St. Helens, 2004–2006: U.S. Geological Survey Professional Paper 1750 (this volume).

Press, W.H., Flannery, B.P., Teukolsky, S.A., and Vettering, W.T., 1986, Numerical recipes the art of scientific computing: Cambridge, Cambridge University Press, 818 p.

Rice, J.R., and Ruina, A., 1983, Stability of steady frictional slipping: Journal of Applied Mechanics, v. 50, p. 343–349.

Ruina, A., 1983, Slip instability and state variable friction laws: Journal of Geophysical Research, v. 88, no. B12, p. 10359–10370.

Schilling, S.P., Carrara, P.E., Thompson, R.A., and Iwatsubo, E.Y., 2004, Posteruption glacier development within the crater of Mount St. Helens, Washington, USA: Quaternary Research, v. 61, no. 3, p. 325–329.

Schilling, S.P., Thompson, R.A., Messerich, J.A., and Iwatsubo, E.Y., 2008, Use of digital aerophotogrammetry to determine rates of lava dome growth, Mount St. Helens, Washington, 2004–2005, chap. 8 *of* Sherrod, D.R., Scott, W.E., and Stauffer, P.H., eds., A volcano rekindled; the renewed eruption of Mount St. Helens, 2004–2006: U.S. Geological Survey Professional Paper 1750 (this volume).

Scholz, C.H., 2002, The mechanics of earthquakes and faulting (2d ed.): Cambridge, Cambridge University Press, 471 p.

Swanson, D.A., and Holcomb, R.T., 1990, Regularities in growth of the Mount St. Helens dacite dome, 1980–1986, *in* Fink, J.H., ed., Lava flows and domes, emplacement mechanisms and hazard implications: Berlin, Springer-Verlag, International Association of Volcanology and Chemistry of the Earth's Interior, Proceedings in Volcanology 2, p. 3–24.

Tuffen, H., and Dingwell, D., 2005, Fault textures in volcanic conduits; evidence for seismic trigger mechanisms during silicic eruptions: Bulletin of Volcanology, v. 67, p. 370–387.

Voight, B., and 24 others, 1999, Magma flow instability and cyclic activity at Soufriere Hills Volcano, Montserrat, British West Indies: Science, v. 238, p. 1138–1142.

Walder, J.S., LaHusen, R.G., Vallance, J.W., and Schilling, S.P., 2005, Crater glaciers on active volcanoes; hydrological anomalies: Eos (American Geophysical Union Transactions), v. 86, p. 521, 528.

Appendix 1. Solution of Equation 27 by Transformation to Bessell's Equation

Conversion of the homogenous part of equation 27 into Bessel's equation is accomplished by using a simultaneous change of independent and dependent variables, given by

$$t^* = \frac{1}{K}\left[\left(\frac{K\,z}{2}\right)^2 - 1\right] \qquad u^* = w\left(\frac{z}{2}\right)^{\frac{K-2D}{K}}. \tag{A1}$$

Substitution of equation group A1 into equation 27 converts it into Bessel's differential equation

$$z^2\frac{d^2w}{dz^2} + z\frac{dw}{dz} + (z^2 - \nu^2)\,w = 0, \tag{A2}$$

where

$$\nu = \frac{K-2D}{K}. \tag{A3}$$

The general solution of Bessel's equation is

$$w = c_1 J_\nu(z) + c_2 Y_\nu(z), \tag{A4}$$

where c_1 and c_2 are arbitrary constants and J_ν and Y_ν are Bessel functions of the first and second kind, of order ν (Abramowitz and Stegun, 1964). Equation 33 is obtained by transforming equation A4 back to the original variables t^* and u^* and adding a particular solution of the inhomogeneous version of equation 27, $u^* = -KG$.

A Volcano Rekindled: The Renewed Eruption of Mount St. Helens, 2004–2006
Edited by David R. Sherrod, William E. Scott, and Peter H. Stauffer
U.S. Geological Survey Professional Paper 1750, 2008

Chapter 22

Constraints on the Size, Overpressure, and Volatile Content of the Mount St. Helens Magma System from Geodetic and Dome-Growth Measurements During the 2004–2006+ Eruption

By Larry G. Mastin[1], Evelyn Roeloffs[1], Nick M. Beeler[1], and James E. Quick[2]

Abstract

During the ongoing eruption at Mount St. Helens, Washington, lava has extruded continuously at a rate that decreased from ~7–9 m^3/s in October 2004 to 1–2 m^3/s by December 2005. The volume loss in the magma reservoir estimated from the geodetic data, $1.6–2.7\times10^7$ m^3, is only a few tens of percent of the 7.5×10^7 m^3 volume that had erupted by the end of 2005.

In this paper we use geodetic models to constrain the size and depth of the magma reservoir. We also ask whether the relations between extruded volume and geodetic deflation volume are consistent with drainage of a reservoir of compressible magma within a linearly elastic host rock. Finally, we compare the time histories of extrusion and geodetic deflation with idealized models of such a reservoir. Critical parameters include erupted volume V_e, dome density ρ_e, reservoir volume V_C, initial reservoir overpressure p_0^{ex}, pressure drop during the eruption Δp, reservoir compressibility $\kappa_C \equiv (1/V_C)(dV_C / dp)$, magma density ρ_M, and magma compressibility $\kappa_M \equiv (1/\rho_M)(d\rho_M/dp)$. Seismic velocity and reservoir geometry suggest $\kappa_C \approx 2\times10^{-11}$ Pa^{-1}, but mechanical considerations suggest $\kappa_C = 7–15\times10^{-11}$ Pa^{-1}.

The geodetic data are best fit with an ellipsoidal source whose top is 5±1 km deep and whose base is ~10–20+ km deep. In the absence of recharge, the decrease in magma-reservoir volume dV_C is theoretically related to the erupted volume V_e by $V_e/dV_C = (\rho_M/\rho_e)(1+\kappa_M/\kappa_C)$. For $\kappa_C = $~$7–15\times10^{-11}$ Pa^{-1} and $\rho_M \approx \rho_e$, estimates of V_e and dV_C suggest that $\kappa_M = 1.4–3.0\times10^{-10}$ Pa^{-1}, corresponding to a magmatic gas content in the reservoir of $v_g = 0$ to 1.8 percent by volume.

If we assume that effusion rate is linearly related to reservoir pressure and that the recharge rate into the reservoir is constant, the effusion rate should decrease exponentially with time to a value that equals the recharge rate. Best-fit curves of this form suggest recharge rates of 1.2–1.3 m^3/s over the first 500 days of the eruption. The best-fit constants include the product $V_C p_0^{ex}(\kappa_C + \kappa_M)$, making it possible to constrain reservoir volume using values of κ_C and κ_M constrained from ratios of erupted volume to geodetic deflation volume. If, on the other hand, we assume a logarithmic pressure-effusion rate relation and a constant recharge rate, the dome volume-time curve should follow a modified logarithmic relation, with the total erupted volume at a given time proportional to $V_C\Delta p(\kappa_C + \kappa_M)$. Using $\kappa_C = 7–15\times10^{-11}$ Pa^{-1}, results from log and exponential curves suggest a reservoir volume of at least several cubic kilometers if Δp or p_0^{ex} is less than ~30 MPa. Similar results are obtained from numerical calculations that consider temporal changes in (1) magma compressibility, (2) the weight of the lava dome suppressing effusion, and (3) recharge rate. These results are consistent with the notion that the reservoir volume is at least a few times larger than the largest Holocene eruption of Mount St. Helens (4 km^3 dense-rock-equivalent+volume for the 3.4-ka Yn eruption).

Both the exponential and logarithmic models predict a history of reservoir decompression that imperfectly matches displacement data at GPS station JRO1. Neither model, for example, predicts the rapid radially inward movement at JRO1 during the first month of the eruption. Such movement, followed by long-term linear deflation, suggests that erupted magma has been replaced in increasing proportions by recharge, but that the recharge rate remains somewhat less than the current (early 2006) effusion rate.

---

[1] U.S. Geological Survey, 1300 SE Cardinal Court, Vancouver, WA 98683

[2] U.S. Geological Survey, Reston, VA 20192; now at Southern Methodist University, Office of Research and Graduate Studies, P.O. Box 750240, Dallas, Texas 75275

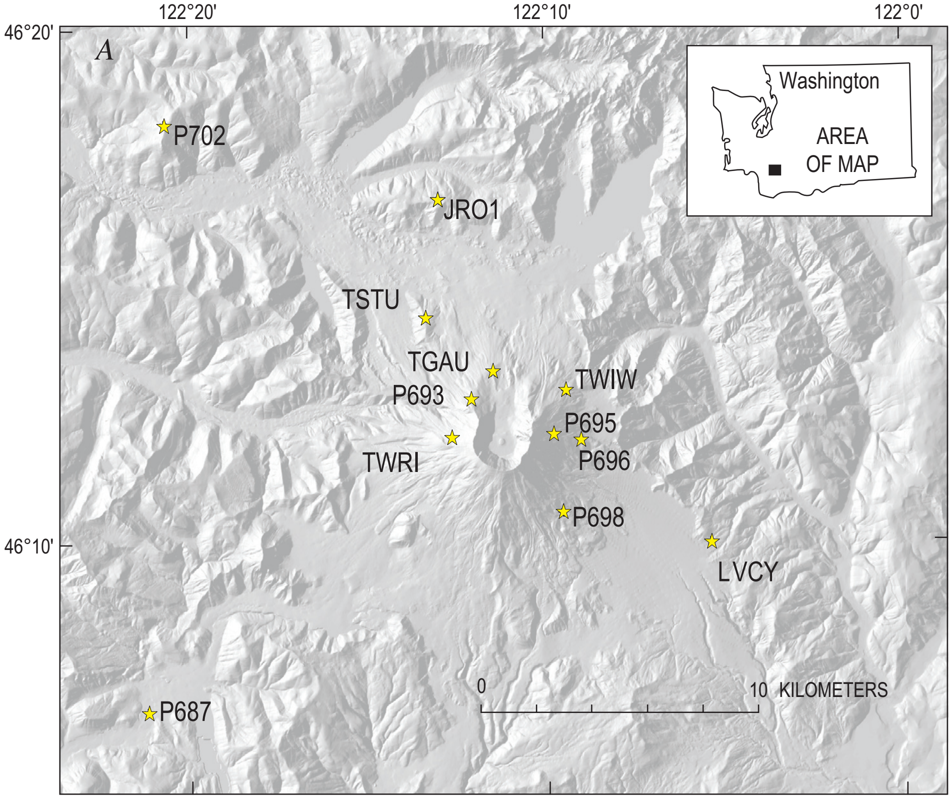

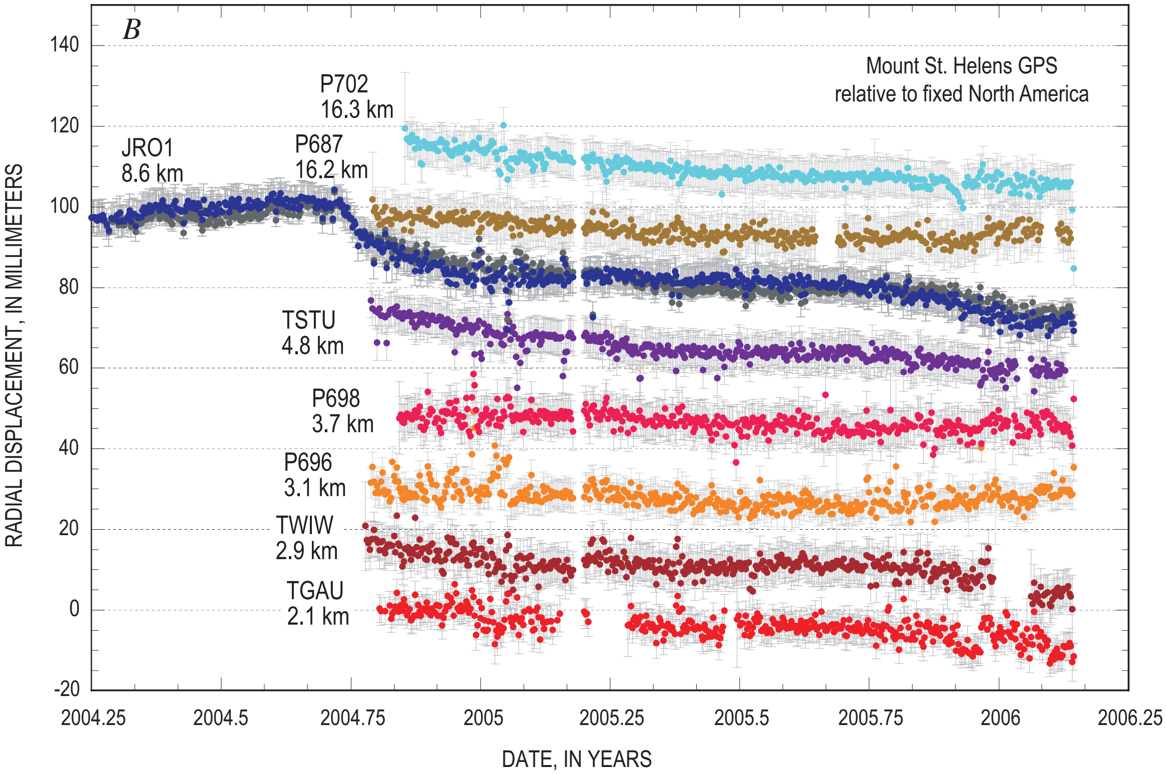

Figure 1. Geodetic stations and results. *A*, Map showing geodetic stations used to model the source of deflation at Mount St. Helens. *B*, Displacement radial to the Mount St. Helens crater versus time at geodetic stations. Outward radial displacements are positive. Error bars represent one standard deviation above and below the data point. Numbers beneath each station label indicate the map distance of each station from the crater center (46.2002° N, 122.1911° W).

Introduction

The current Mount St. Helens eruption extruded about 85 percent as much lava in 14 months (October 2004 to December 2005) as was extruded in 6 years to form the 1980–86 lava dome. At the time of writing (spring 2006), there is no obvious indication of waning growth; indeed, compared with other dome-building eruptions worldwide, the current eruption of Mount St. Helens only slightly exceeds the median duration (540 days) and volume (3.5×10^7 m^3) among historical dome-building eruptions (Newhall and Melson, 1983, and updates, C. Newhall, written commun., 2005). This eruption hardly approaches the duration (>50 years) of the dome building at Bezymianny Volcano, Kamchatka, whose growth followed a sector collapse and lateral blast in 1956 that resembled the 1980 Mount St. Helens sequence.

Dome-building eruptions, like eruptions of mafic lava flows, range in duration from days to decades and in volume from cubic meters to cubic kilometers. Eruption volume and duration are most strongly controlled by reservoir size, exsolved gas content, the amount of recharge into the magma system, and the composition and volatile content of recharging magma (Wadge, 1981; Newhall and Melson, 1983; Huppert and Woods, 2002; Woods and Huppert, 2003). In this study we use geodetic and growth-history data to constrain the volume, overpressure, history of recharge, and exsolved volatile content of the Mount St. Helens magma system.

Key Observations

Over several years prior to September 2004, campaign-style geodetic surveys and measurements at the only continuous global positioning system (CGPS) site at Mount St. Helens (JRO1, fig. 1*A*) showed no discernable inflation signal (Dzurisin and others, this volume, chap. 14; Lisowski and others, this volume, chap. 15). Deflation at JRO1 began with the onset of seismicity on September 23, 2004; uplift on the crater floor was first noticed on about September 26 (Dzurisin and others, this volume, chap. 14) and the first material at magmatic temperature on October 11. Eight new CGPS instruments installed between mid-October and early November 2004 (fig. 1*A*) have recorded more or less radially inward movement toward the crater (fig. 1), suggesting that the source of deflation (the magma reservoir) is roughly spherical or elliptical in shape rather than dike-shaped (Lisowski and others, this volume, chap. 15).

Throughout the eruption, lava has extruded as spines or lobes of more or less solid, nearly holocrystalline lava, their surfaces covered by unconsolidated fault gouge on the order of 1 m thick (fig. 2). The gouge thickness, considering relations between gouge thickness and displacement on tectonic faults (Robertson, 1983; Power and others, 1988), and petrologic information (Cashman and others, this volume, chap. 19) suggest that the faulting may extend from perhaps tens of meters to several hundred meters into the subsurface.

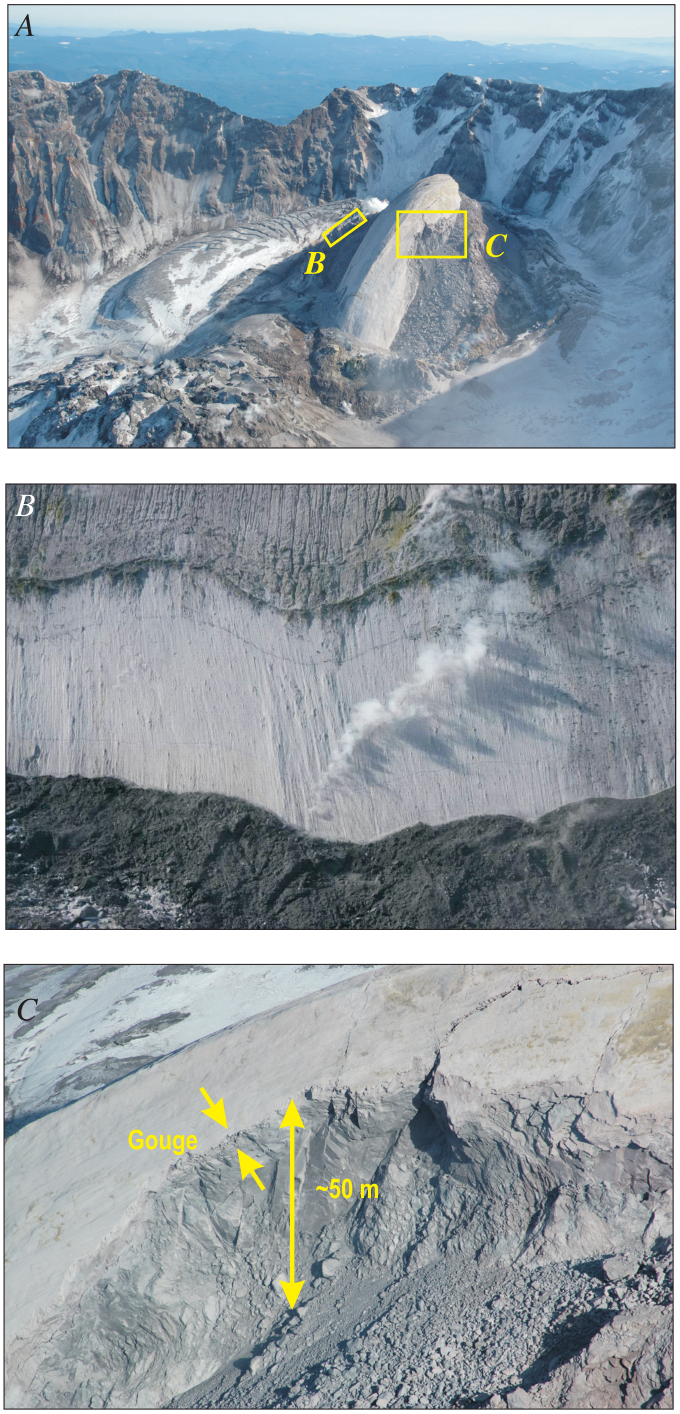

Figure 2. Photos of the growing lava dome of Mount St. Helens. *A*, View of spine 4 from the northwest on February 22, 2005. USGS photo by S.P. Schilling. *B*, Close-up of striated fault gouge covering the exterior of spine 3 as it emerged from the ground on November 11, 2004. Approximate location of that spine on February 22, 2005, shown by box *B* on panel *A*. USGS photo by J.S. Pallister. *C*, Close-up of fresh rockfall scar (~100 m long and 50 m high), revealing gouge thickness in cross section. Approximate location shown by box *C* on panel *A*. USGS photo taken February 22, 2005, by S.P. Schilling.

A series of digital elevation models (DEMs) based on 1:12,000-scale aerial photographs records the growth of the lava dome (Schilling and others, this volume, chap. 8). These DEMs show that in early October 2004 the rate of uplift of cold rock and glacial ice was on the order of 8–9 m^3/s, with nearly 1.1×10^7 m^3 uplifted by the time lava first became visible at the surface on October 11. Lava (“hot rock”) extrusion rates were initially ~6–7 m^3/s in November 2004 but declined to less than 2 m^3/s in March 2005. Since March 2005 (about 150 days into the eruption) the extrusion rate has continued to decline gradually, such that the volume-time curve can be nearly fit with a straight line (fig. 3). Overall, the history of lava-dome volume versus time (fig. 3) has defined a remarkably regular monotonic, concave-downward curve that was noted in early 2005 and could be fit using simple exponential (fig. 3*C*) and logarithmic (fig. 3*A*) curves. In this study we endeavor to find the physical basis for these curve forms.

Geodetic Source Models

Using data from eight continuous GPS stations (fig. 1), we estimate the depth, location, and size of the source of deflation (the magma reservoir) by comparing inward displacements with those predicted for a vertical prolate ellipsoid embedded in a homogeneous, isotropic, linearly elastic half-space, using the equations of Bonaccorso and Davis (1999) (table 1). We evaluate the displacements during two time windows: (1) November 4, 2004, to February 5, 2005, and (2) February 5, 2005, to July 14, 2005. The start and end dates of these windows were chosen to coincide with DEM acquisition dates. We use only two time windows because data quality is insufficient to allow subdivision into shorter time windows. The second time window ends in summer 2005 because displacements since that time have been too small to be accurately modeled.

Measured displacements were adjusted for regional plate movement using the rates 3.461 mm/yr east, 5.91 mm/yr north, 1.46 mm/yr down; and for seasonal changes using sinusoidal adjustments having east, north, and z (vertical) amplitudes of 1.9149, 1.667, and 1.5289 mm and phase angles relative to January 1, 2004, of 51.86, 132.89, and 32.62 degrees, respectively (Lisowski and others, this volume, chap. 15). For the first time window, best-fit models place the top of the reservoir at 3–6 km below the mean altitude of the geodetic stations (which is ~1,300 m above sea level). In plan view the best-fit models lie 1.3–1.6 km east and 5–320 m south of the crater center (figs. 4, 5; table 1). Placing the top deeper than about 6 km tends to underestimate the radial displacement at stations proximal to the crater and overestimate both radial and vertical displacement components in the distal stations. The depth to the bottom of the reservoir is not well constrained but likely lies somewhere below 10 km (fig. 4*A*). Data from the second time period provide significantly poorer constraints (fig. 4*B*).

Geodetic Constraints on Reservoir Size and Pressure Drop

The amplitude of the geodetic signal scales with the product $R^2\Delta p/G$, where R is the horizontal radius of the ellipsoid, Δp is the pressure drop, and G is the host-rock shear modulus. Best-fit values of this product are listed in table 1. Using formulas for ellipsoid volume $V_C=(2/3)\pi R^2 h$ (where h is ellipsoid height) and elastic volume change of the ellipsoid $\Delta V_C=3V_C\Delta p/(4G)$ (McTigue, 1987; Tait and others, 1989; Tiampo and others, 2000), we find that $\Delta V_C=(\pi h/2)[R^2\Delta p/G]$. For the first time window, excluding sources at 4–7 km and 10–14 km depth that clearly do not fit the data, estimates of volume shrinkage of the magma body are $2.1\text{–}3.5\times10^6$ m^3. By comparison, the hot-rock volume (ΔV_e) erupted during this time (Schilling and others, this volume, chap. 8; and fig. 3) was about 2.7×10^7 m^3—eight to twelve times the volume shrinkage of the reservoir. For the second time window, $\Delta V_C=\sim3\text{–}8\times10^6$ m^3 (poorly constrained), whereas the change in dome volume was $\Delta V_e=1.8\times10^7$ m^3. For the entire eruption through late 2005, Lisowski and others (this volume, chap. 15) and Poland and Lu (this volume, chap. 18) estimate $\Delta V_C\sim1.6\text{–}2.7\times10^7$ m^3 from geodetic and InSAR data, whereas hot-rock erupted volume by mid-December 2005 was about 7.3×10^7 m^3 (Schilling and others, this volume, chap. 8). Differences in density of the erupted versus unerupted magma (estimated later) are not great enough to account for these discrepancies.

The reservoir volume and pressure drop can be constrained if the shear modulus G can be estimated. On the basis of estimated seismic P-wave velocity $\upsilon_P=6.7\pm0.2$ km/s at 8–15 km depth (Musumeci and others, 2002, fig. 5), host-rock density $\rho_R=2{,}700\pm200$ kg/m^3 (Williams and others, 1987), an assumed Poisson’s ratio ν of 0.25±0.03, and the formula $G=\rho_R\upsilon_P^2(1-2\nu)/(2(1-\nu))$ (for example, Rubin, 1990), we obtain $G=40\pm4$ GPa. Using this value and $\Delta V_C=2.3\times10^7$ m^3 in the formula $\Delta V_C=3V_C\Delta p/(4G)$, we obtain $V_C\Delta p=1.2\times10^{18}$ $Pa\cdot m^3$. If we further assume that the pressure drop since the start of the eruption is less than a few tens of megapascals, the reservoir volume would have to exceed about 41 km^3—significantly larger than previously hypothesized at Mount St. Helens (>10 km^3 by Scandone and Malone, 1985; 5–7 km^3 by Barker and Malone, 1991). Several factors considered later and in appendix 1 suggest that a lower value of G, and hence smaller reservoir volume, is more appropriate.

An Idealized Magma Reservoir

We idealize the magma system (fig. 5) as an ellipsoidal magma body several kilometers deep within linearly elastic host rock, connected to the surface and to a source of recharge through relatively narrow conduits. The reservoir contains magma of density ρ_M and has a total mass $\rho_M V_C$. As long as the assumption of linear elastic host rock holds and the geometry of the reservoir does not change, the relation between

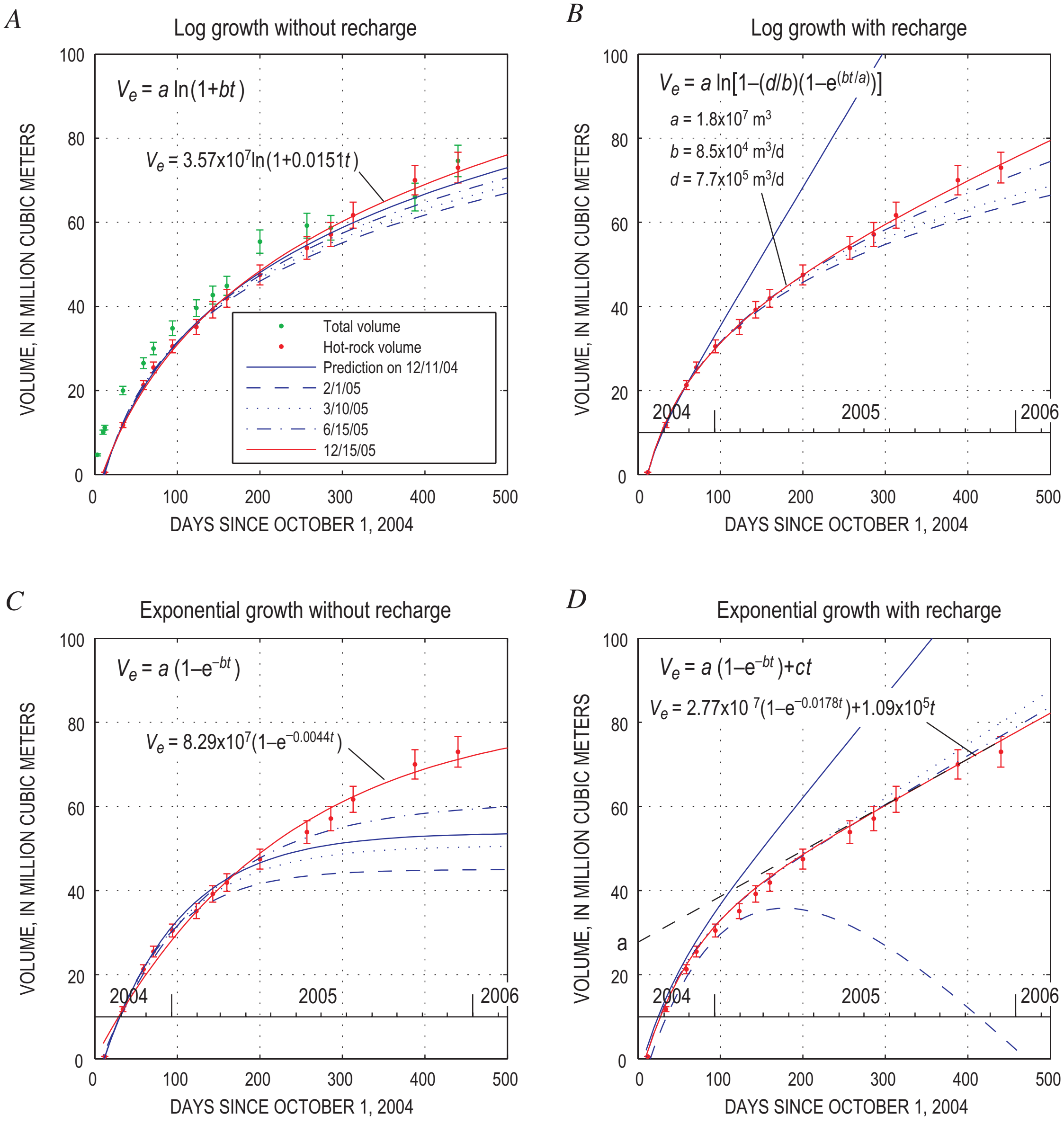

Figure 3. Lava dome volume (red dots) and total surface-deformation volume (green dots) versus time in days since October 1, 2004. Error bars are ±5 percent of the volume. Lines in each plot are fitted to a subset of data as of a certain date and then extrapolated onward as predictions. (Line of 12/11/04 is mostly extrapolation whereas line of 12/15/05 is mostly fitted.) Solid blue line fits volume measurements until about December 11, 2004; dashed blue line, February 1, 2005; dotted blue line, March 10, 2005; dot-dash blue line, June 15, 2005; solid red line, December 15, 2005. Plots *A*, *B*, *C*, and *D* show these best-fit curves using equations of different forms, shown in upper left corner of each plot. Terms *a*, *b*, *c*, and *d* in these equations are fitting coefficients; V_e is total erupted volume, and *t* is time since October 1, 2004.

Table 1. Parameters in geodetic source models plotted in figure 4.

[Parameters in plain type are specified by the user; those italicized are obtained by optimizing the fit between the model and the data.]

Model	Time period	Depth to top (m)	Depth to bottom (m)	Distance east of crater center (m)	Distance north of crater center (m)	Scale factor $\Delta pR^2/G$	$V_c\Delta p$ Pa•m^3 $\times10^{17}$	ΔV_c 10^6 m^3
1	11/4/04–2/5/05	*3,419*	20,000	*1,541*	*-68*	*-135*	-2.18	2.83
2	11/4/04–2/5/05	*3,654*	15,000	*1,511*	*-85*	*-155*	-1.72	3.69
3	11/4/04–2/5/05	*4,294*	10,000	*1,448*	*-100*	*-236*	-1.32	4.68
4	11/4/04–2/5/05	4,000	7,000	*1,492*	*-5*	*-286*	-0.84	1.80
5	11/4/04–2/5/05	6,000	10,000	*1,390*	*-321*	*-459*	-1.79	3.85
6	11/4/04–2/5/05	10,000	14,500	1,600	-500	*-885*	-3.89	8.34
7	2/5/05–7/14/05	3,500	15,500	1,400	-100	*-113*	-1.32	2.83
8	2/5/05–7/14/05	*7,191*	20,000	100	-3000	*-286*	-3.58	7.67

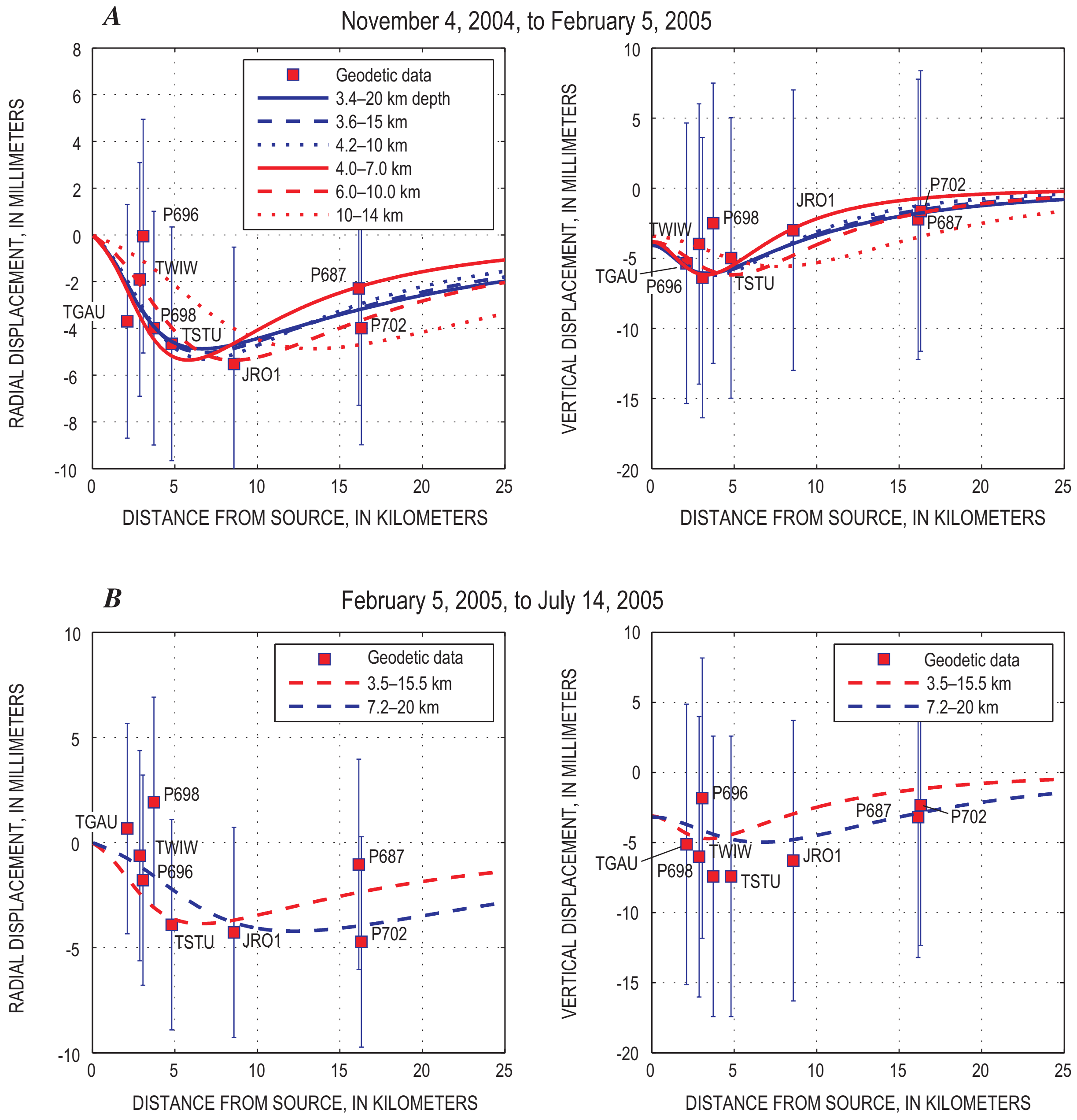

Figure 4 Measured and theoretical geodetic displacements for 252 days of eruption from November 4, 2004, to July 14, 2005. Data points, from continuous global positioning system (CGPS) receivers (fig 1*A*), show radial and vertical displacement; error bars are given as ±5 mm for radial displacement, ±10 mm for vertical displacement. Displacements are positive for outward radial and upward vertical directions. Lines represent theoretical displacements resulting from deflation of a vertical prolate ellipsoid in an elastic half-space. Depths in the explanation indicate, respectively, the depth to top and bottom of the ellipsoid below the mean altitude of the geodetic stations (1,300 m above sea level). *A*, Radial and vertical displacement between November 4, 2004, and February 5, 2005. *B*, Radial and vertical displacement between February 5 and July 14, 2005.

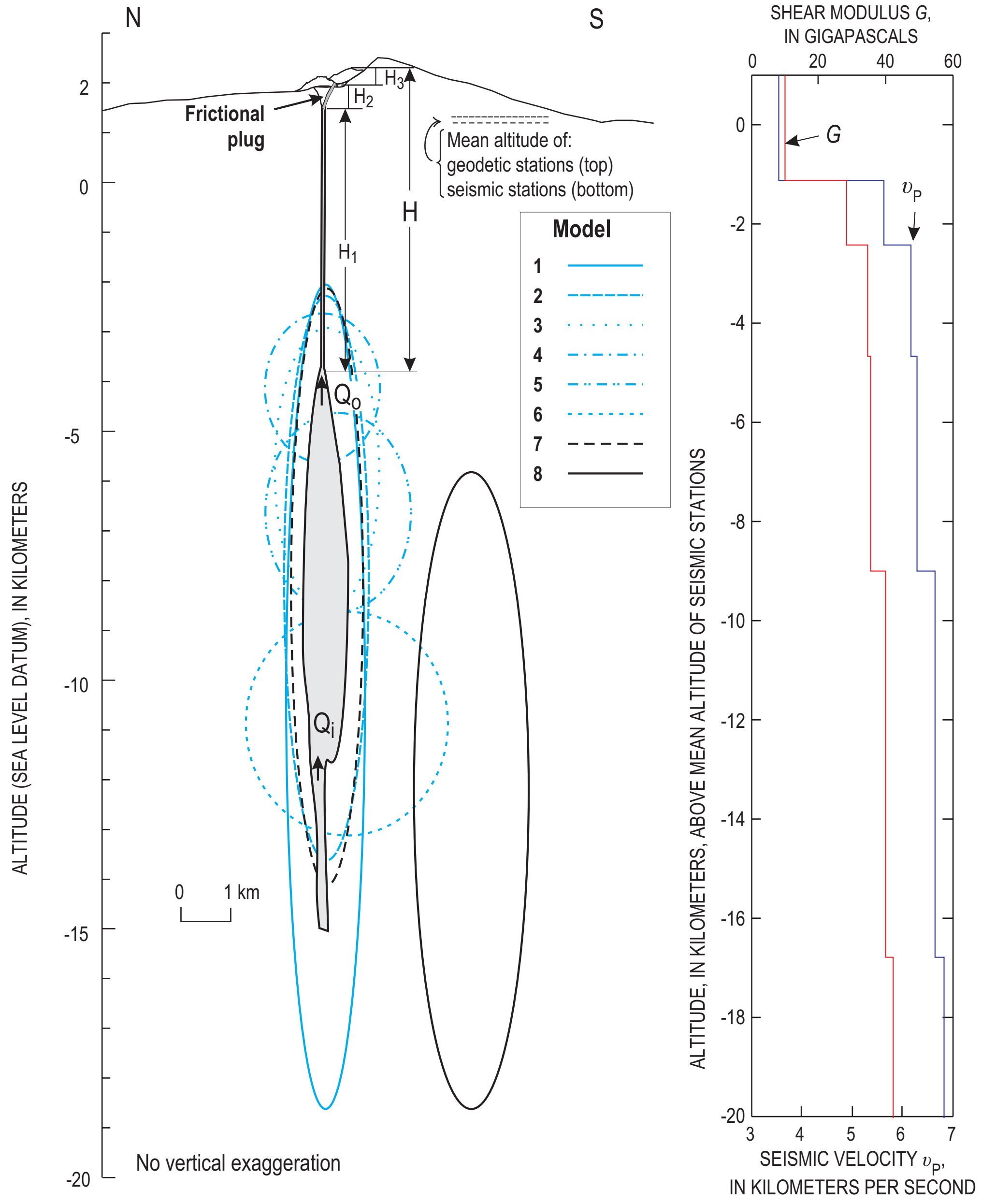

Figure 5. Left, Idealized north-south cross section through Mount St. Helens showing approximate location of the magma body (shaded), as judged from the geodetic modeling and some of the parameters used in this analysis. Blue and black dashed ellipses represent locations of geodetic models 1 through 8 listed in table 1; width of each ellipse represents its radius taken from value of $R^2\Delta p/G$ in table 1, using $\Delta p=10$ MPa and $G=35$ GPa. Right, Profile of seismic velocity (from Musumeci and others, 2002) and shear modulus G (estimated from seismic data and from density data of Williams and others, 1987). Shear modulus was estimated from the formula $G=\rho R v_P^2(1-2\nu)/(2(1-\nu))$, where Poisson's ratio, ν, is taken as 0.25 and ρ is taken as 2,150 kg/m^3 above the seismic datum and 2,700 kg/m^3 below it (Williams and others, 1987, fig. 8). Cross section and seismic profile have same vertical scales, but latter is set to datum of mean altitude of seismic stations.

reservoir pressure p and volume V_C is linear with a proportionality given by the reservoir compressibility κ_C:

$$\kappa_C \equiv \frac{1}{V_C}\frac{\partial V_C}{\partial p} \tag{1}$$

For a sphere or prolate ellipsoid, $\kappa_C = 3/(4G)$ (McTigue, 1987; Tiampo and others, 2000). We also assume that the magma has a finite compressibility (κ_M) given by:

$$\kappa_M \equiv \frac{1}{\rho_M}\frac{\partial \rho_M}{\partial p} \; . \tag{2}$$

Finally, we assume that the change in reservoir mass (dM_C) equals the mass added by recharge ($dM_i = \rho_i dV_i$) minus the mass erupted ($dM_e \approx \rho_e dV_e$), where ρ_i, ρ_e, dV_i, and dV_e are the densities and volumes of injected and erupted magma, respectively. In mathematical terms,

$$\begin{aligned} d\left(\rho_M V_C\right) &= \rho_M dV_C + V_C d\,\rho_M \\ &= -\rho_e dV_e + \rho_i dV_i \end{aligned} \; . \tag{3}$$

Adding terms for κ_C and κ_M into equation 3 and rearranging leads to:

$$dV_C = \frac{\rho_i dV_i - \rho_e dV_e}{\rho_M\left(1 + \dfrac{\kappa_M}{\kappa_C}\right)} \; . \tag{4}$$

In the absence of recharge we have:

$$\frac{dV_e}{dV_C} = -\frac{\rho_M}{\rho_e}\left(1 + \frac{\kappa_M}{\kappa_C}\right) . \tag{5}$$

Equation 5 carries the important implication that the erupted volume should not equal the volume shrinkage in the magma body except in the limiting case where the densities of erupted and unerupted magma are equal and the magma is incompressible ($\kappa_M \rightarrow 0$) (this was also pointed out by Johnson and others, 2000). If compressibility and density do not vary greatly with time during an eruption, equation 5 can be used to give the ratio of erupted volume V_e to the volume change of the magma reservoir ΔV_C. In spherical or ellipsoidal reservoirs, magma compressibility is generally thought to greatly exceed the reservoir compressibility (for example, Huppert and Woods, 2002); hence erupted volume should greatly exceed ΔV_C.

In the absence of recharge, what value of dV_e / dV_C might one expect at Mount St. Helens? The answer requires careful estimation of ρ_M, ρ_e, κ_M, and ρ_C, which we provide in the following several paragraphs.

The density of unerupted, volatile-saturated rhyolitic melt at ~200–250 MPa pressure is about 2,200 kg/m^3 (estimated using the method of Ghiorso and Sack in the program Conflow of Mastin, 2002). Combined with roughly 45 volume percent plagioclase crystals (Pallister and others, this volume, chap. 30) having a density of 2,600 kg/m^3, the bulk density of the magma ρ_M would be about 2,380 kg/m^3. Density measurements of most dome rock samples are about 2,300–2,500 kg/m^3 (K. Russell, written commun., 2006), although pores and voids could reduce the bulk density of the dome, ρ_e, by perhaps 10–20 percent below that of the dome rock. Within the uncertainties, we estimate the ratio ρ_M / ρ_e to be about 1.0 to 1.2. We use a reservoir compressibility of roughly 2×10^{-11} Pa^{-1} based on the formula $\kappa_C = 3/(4G)$ for an ellipsoidal reservoir and the earlier estimate of $G = 40\pm4$ GPa.

Magma Compressibility

Magma compressibility κ_M depends on gas volume fraction, solubility, crystallinity, and rate of loading. When changes in pressure are much more rapid than rates of gas exsolution (for example, the time scale of seismic-wave disturbances), the crystal, melt, and gas phases can be regarded as inert, and the bulk compressibility is simply the sum of the compressibilities of the crystal, melt, and gas phases (κ_x, κ_m, κ_g) multiplied by their respective volume fractions (v_x, v_m, v_g) (for example, Mastin, 2002):

$$\kappa_M = v_m \kappa_m + v_x \kappa_x + v_g \kappa_g \, . \tag{6}$$

If, on the other hand, pressure changes occur over months or years, as in the current eruption, gas exsolution must be considered. Previous investigators (Tait and others, 1989; Huppert and Woods, 2002; Woods and Huppert, 2003) used a simple Henry's solubility law for H_2O and found an abrupt discontinuity in compressibility at the saturation pressure (~240 MPa in fig. 6*C*). Huppert and Woods (2002) and Woods and Huppert (2003) suggested that this discontinuity could have a dramatic, rejuvenating effect on the course of an effusive eruption once the magma reservoir reaches the saturation pressure.

The Mount St. Helens magma contains both H_2O and CO_2, and gas in such a two-component system should exsolve more gradually and over a wider range of pressures than it would if only H_2O were present. We estimate exsolved volatile content and magma compressibility using petrologic constraints from other studies. Phase equilibrium experiments (Rutherford and Devine, this volume, chap. 31) suggest that the currently erupting magma last equilibrated at a temperature of ~850°C, a pressure of ~120 MPa, and a source depth near 5 km. The crystallinity at this depth was 40 to 55 percent (Pallister and others, this volume, chap. 30). The center of deflation, however, is substantially deeper than 5 km, perhaps equal to that of the May 18, 1980, magma at around 8–9 km depth and 220 MPa pressure (Rutherford and Devine, 1988). Following Gerlach and others (this volume, chap. 26), we assume that present-day magma properties at the source resemble those in 1980, with a temperature of about 900°C, pressure of ~220 MPa, 30 percent crystals (Cashman and Taggart, 1983), and

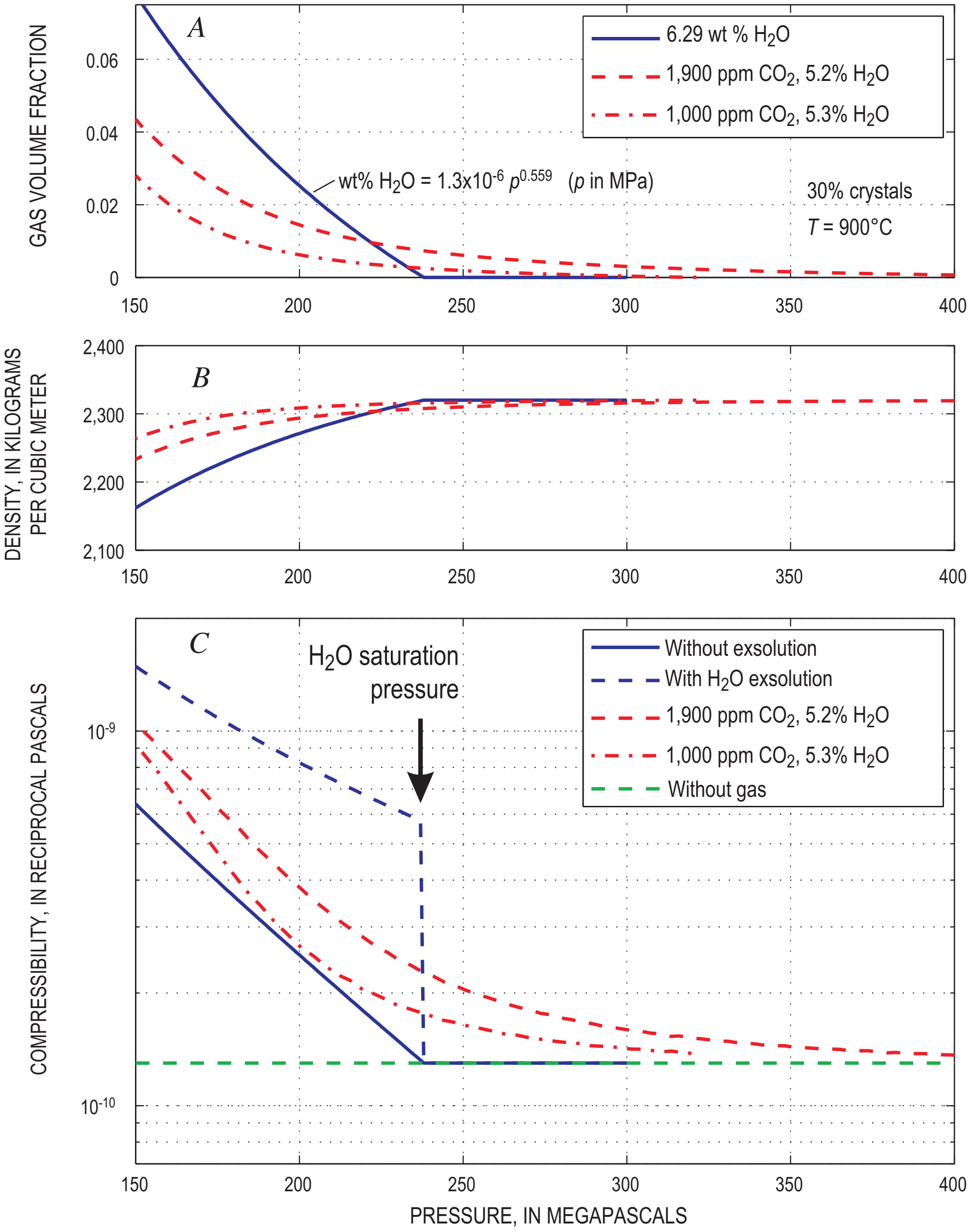

Figure 6. Characteristic features of magma having composition given in text, as function of pressure. Significance of the various lines is explained in text. *A*, Gas fraction by volume. *B*, Density. *C*, Compressibility.

a dissolved water concentration in the melt of about 5 weight percent (Blundy and Cashman, 2001).

Assuming that the CO_2 emitted into the atmosphere during this eruption originated from a mass of magma equal to that of the lava dome, Gerlach and others (this volume, chap. 26) estimate a preeruptive CO_2 concentration in the magma of about 1,100 ppm, or 1,900 ppm normalized to the melt alone (assuming 30 percent crystallinity). At 220 MPa pressure and 900°C temperature, with 5 weight percent dissolved H_2O, such a melt would contain roughly 350 ppm dissolved CO_2; the remaining CO_2 and H_2O would be exsolved in bubbles composing roughly 1.2 volume percent of the magma (Gerlach and others, this volume, chap. 26). The total water content normalized to the melt plus fluid phases would be about 5.2 weight percent.

Using the solubility code VolatileCalc 1.1 (Newman and Lowenstern, 2002), we calculate mass fractions of exsolved H_2O and CO_2 over pressures ranging from 150 to 400 MPa, and we combine these results with ideal gas relations to obtain the volume fraction of exsolved gas (fig. 6*A*). We assume a melt density $\rho_m = 2{,}200$ kg/m^3 and crystal density $\rho_x = 2{,}600$ kg/m^3; the melt density corresponds to a water-saturated melt of 1980 composition (sample SH-084 of Rutherford and others, 1985), calculated by the method of Ghiorso and Sack (1995) using the program Conflow (Mastin, 2002). From these volume fractions and phase densities we calculate the bulk density over the pressure range 150–400 MPa (fig. 6*B*) and then numerically calculate $(1/\rho_M)(\partial\rho_M/\partial p)$ to obtain κ_M (fig. 6*C*). We use a melt compressibility of 2.0×10^{-10} Pa^{-1}, estimated using the method of Ghiorso and Sack (1995) for water-saturated rhyolite at $p=220$ MPa, and a crystal compressibility of 2×10^{-11} Pa^{-1} obtained for albite at $T=900$°C and $p=220$ MPa from the program MELTS using the method of Elkins and Grove (1990).

Our calculations suggest that, over the pressure range of 150–400 MPa, the magma may have a bubble volume fraction of 0.0008 to 0.048 (fig. 6*A*). For comparison, we plot results for $CO_2=1{,}000$ ppm and $H_2O=5.3$ weight percent of the melt+fluid phases and also for a single-component (H_2O) volatile system using the Henry's law solubility illustrated in figure 6*A*, with the H_2O content (6.29 weight percent) set so that the volume fraction of gas at 220 MPa equals that of the two-component system. Both the two-component and the Henry's solubility laws show nearly an order-of-magnitude variation in compressibility over this pressure range, but the two-component systems show little or no discontinuity in κ_M at the saturation pressure. At $p=220$ MPa, the two-component system (1,900 ppm CO_2, 5.2 weight percent H_2O) gives $\kappa_M=2.8\times10^{-10}$ Pa^{-1}. We use this number as a starting point in our calculations. The relation between κ_M and volume fraction of gas for these two-component magma compositions is illustrated in figure 7.

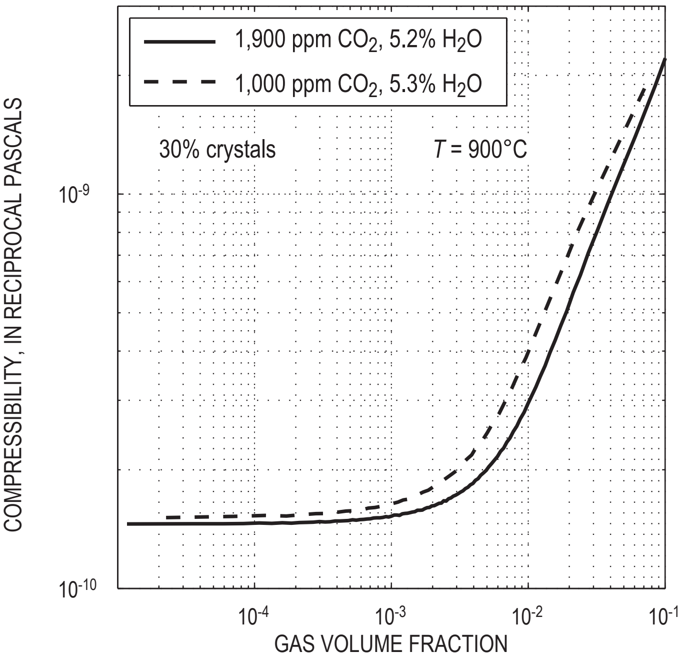

Figure 7. Compressibility versus volume fraction gas for a rhyolitic melt containing 30 percent crystals at 900°C temperature, using two different gas compositions.

Expected Ratio of Erupted Volume to Volume Change in the Reservoir

Using $\rho_M/\rho_e=1$, $\kappa_C=2\times10^{-11}$ Pa^{-1}, and $\kappa_M=2.8\times10^{-10}$ Pa^{-1} (~1.2 percent bubbles), then dV_e/dV_C predicted by equation 5 should be about 16, which is somewhat higher than the ranges of 7.7–12.8 and 2–6 calculated for the first and second time windows, respectively. A temporal increase in κ_M is suggested by the difference in apparent values of dV_e/dV_C between the first and second time windows, though uncertainties in these ratios are too great to make such an inference with confidence. For the overall eruption, the erupted volume by mid-December 2005, 7.3×10^7 m^3, was only about three times the reasonably well-constrained reservoir shrinkage dV_C of ~2.3×10^7 m^3 estimated by Lisowski and others (this volume, chap. 15). A ratio this low suggests a magma compressibility of ~4×10^{-11} Pa^{-1}, which is about one-fourth that of even a bubble-free magma of this crystallinity (fig. 7). If the magma reservoir is in fact bubble free, κ_C must be ~8×10^{-11} Pa^{-1} in order to have $dV_e/dV_C\approx3$; if it contains roughly 1 volume percent bubbles at the source depth, as inferred by Gerlach and others (this volume, chap. 26), κ_C must be ~1.4×10^{-10} Pa^{-1}. In either case, κ_M is only a few to several times greater than κ_C, which we take to indicate that the volume fraction of bubbles in the reservoir is zero or very small, consistent with the findings of Gerlach and others (this volume, chap. 26). If the reservoir was partially recharged during the eruption (a factor we consider later), a still lower ratio of κ_M/κ_C would be implied, suggesting still lower bubble content in the reservoir.

Idealized Models for History of Extrusion and Deflation

Previous studies (Wadge, 1981; Stasiuk and others, 1993; Huppert and Woods, 2002) point out that drainage of an elastic magma reservoir through a Newtonian conduit results in an exponentially decreasing extrusion rate. When combined with constant recharge rate into the magma system, the resulting curve has the form of an exponentially decreasing rate superimposed on a constant rate (fig. 3*D*). If these processes are responsible for determining the dome-growth curve at Mount St. Helens, then some information on the magma reservoir and conduit properties should be embedded in the coefficients to these equations. Information on the magma-reservoir volume and driving pressure are of particular importance.

We know that processes besides Newtonian flow and elastic relaxation may affect the growth history. The highly crystalline magma at Mount St. Helens, for example, probably has a non-Newtonian rheology. The extrusion of lava as a nearly solid plug bounded by frictional faults may also limit the growth rate. Different constitutive laws may predict different growth curves for the lava dome. Some curves fit to the hot-rock data (fig. 3) that have simple analytical forms are:

logarithmic (fig. 3*A*) $V_e = a\ln\left(1+b\left(t-c\right)\right),$ (7)

exponential (fig. 3*C*) $V_e = a\left(1-\mathrm{e}^{-b(t-c)}\right),$ (8)

modified log (fig. 3*B*) $V_e = a\ln\left[1-\frac{d}{b}\left(1-e^{\frac{b(t-c)}{a}}\right)\right],$ (9)

and exponential plus linear (fig. *3D*)

$$V_e = a\left(1-e^{-b(t-c)}\right)+d\left(t-c\right). \tag{10}$$

The terms *a*, *b*, *c,* and *d* are fitting coefficients; their best-fit values are listed in table 2. (Parameter *c*, which represents the day of the eruption start, is used as a variable in these fits, even though its value is roughly known, making the number of truly unknown parameters equal to three.) Curve forms that fit the data best are equations 9 and 10, which, as shown later, assume a constant rate of recharge. The fitting errors are lower using these forms than using equations 7 and 8 (table 2). More importantly, however, curves of equations 9 and 10 have done a better job predicting future growth, as the best-fit coefficients for equations 9 and 10 have changed relatively little since early 2005 (table 2).

Exponential Growth Curve

Exponential curve forms of equations 8 and 10 are derived from two main assumptions. The first is that the magma-reservoir pressure *p* is linearly related to the mass of magma in the reservoir:

$$p = p_0 - \mathrm{C}\left(M_e - M_i\right), \tag{11}$$

where M_e is the mass that leaves the reservoir (assumed to equal the erupted mass), M_i is the mass that enters the reservoir as recharge, p_0 is initial reservoir pressure, and C is a constant that represents the change in pressure with reservoir mass, $\partial p/\partial M_C$. By substituting equations 2 and 1 into equation 3, and rearranging, we find that $\mathrm{C}=[(\kappa_C+\kappa_M)\rho_m V_C]^{-1}$.

The second assumption is that the mass effusion rate $\dot{M}_e$ is linearly related to magma reservoir pressure (*p*):

$$\dot{M}_e = \mathrm{A}p - \mathrm{B}, \tag{12}$$

where A and B are constants. This equation describes, among other possibilities, Newtonian (Poiseuille) flow (fig. 8*A*); Newtonian flow capped by a frictional plug (fig. 8*C*); flow of a solid mass through the conduit separated from the conduit walls by a Newtonian fluid (a “greased plug”; fig. 8*B*); and

Table 2. Fitting coefficients to curves in figure 3.

[Columns labeled $\Sigma(y_i-y)^2$ give the sum of the squares of errors between best-fit predictions and data.]

Date	Days since 10/1/04	Hot-rock volume m³×10⁶	Rate m³/s	Exponential best-fit parameters									Logarithmic best-fit parameters								
				With recharge					Without recharge				With recharge					Without recharge			
				a m³×10⁶	*b* s⁻¹×10⁻⁷	*c* s×10⁵	*d* m³/s	Σ(yᵢ-y)² m³×10¹¹	*a* m³×10⁶	*b* s⁻¹×10⁻⁷	*c* s×10⁵	Σ(yᵢ-y)² m³×10¹¹	*a* m³×10⁶	*b* m³/s	*c* s×10⁵	*d* m³/s	Σ(yᵢ-y)² m³×10¹¹	*a* m³×10⁶	*b* s⁻¹×10⁻⁷	*c* s×10⁵	Σ(yᵢ-y)² m³×10¹¹
10/1/04	0	0																			
10/13/04	12	5.4																			
11/4/04	34	11.8	5.92																		
11/29/04	59	21.3	4.4																		
12/11/04	71	25.5	4.05	14.0	2.94	9.56	2.79	0.31	53.8	1.23	9.49	0.75	8.0	3.81	9.70	8.28	0.21	39.5	1.74	9.55	0.4
1/3/05	94	30.5	2.52	86.7	1.01	9.61	-1.98	1.76	46.7	1.49	9.66	2.27	29.7	$1.47{\times}10^{-7}$	9.71	7.55	2.42	29.5	2.58	9.75	4.8
2/1/05	123	35.1	1.84	94.3	0.96	9.59	-2.26	1.74	45.0	1.58	9.74	2.94	24.2	$2.20{\times}10^{-7}$	9.88	8.34	3.31	24.5	3.40	9.94	13.5
2/21/05	143	39.2	2.37	28.1	2.19	9.76	1.15	10.16	48.2	1.41	9.49	13.24	24.6	$1.40{\times}10^{-7}$	10.00	8.36	11.77	25.3	3.24	9.90	14.4
3/10/05	160	41.9	1.84	23.6	2.55	9.81	1.48	11.81	50.7	1.29	9.22	24.36	25.8	$1.82{\times}10^{-7}$	10.04	8.11	15.17	25.9	3.12	9.86	15.5
4/19/05	200	47.5	1.62	22.9	2.63	9.82	1.52	11.87	55.4	1.10	8.43	57.96	22.2	0.52	9.87	8.28	17.58	26.9	2.92	9.74	18.7
6/15/05	257	53.9	1.3	25.7	2.32	9.72	1.35	14.62	61.1	0.92	7.16	107.49	21.9	0.56	9.87	8.31	17.62	27.8	2.75	9.61	21.8
7/14/05	286	57.1	1.28	26.4	2.25	9.67	1.31	15.41	64.5	0.83	6.31	143.93	21.3	0.63	9.88	8.38	17.93	28.6	2.61	9.47	21.8
8/10/05	313	61.7	1.97	24.9	2.42	9.79	1.39	23.82	69.3	0.73	4.96	253.01	18.1	0.96	9.98	8.92	39.02	30.8	2.29	9.02	77.1
10/24/05	388	70.0	1.28	25.0	2.41	9.77	1.38	23.86	78.3	0.57	1.65	485.74	16.2	1.13	10.06	9.44	51.27	34.4	1.87	7.98	179.4
12/15/05	440	73.0	0.67	27.7	2.06	9.40	1.26	71.01	82.9	0.51	-0.16	551.65	18.0	0.98	9.96	8.89	61.32	35.7	1.75	7.54	195.1

greased-plug flow capped by a frictional plug (fig. 8*D*). We also assume that the linear relations in equations 11 and 12 do not change with time.

If one further assumes that the rate of mass recharge $\left(\dot{M}_i = Q_i\right)$ is constant, equations 11 and 12 can be combined and integrated (appendix 2) to give the erupted mass as a function of time. Noting that the erupted volume (V_e) is equal to M_e/ρ_e, we obtain:

$$V_e = \frac{1}{\rho_e}\frac{\left(\mathrm{A}p_0 - \mathrm{B}\right) - Q_i}{\mathrm{AC}}\left(1 - e^{-ACt}\right) + \frac{Q_i}{\rho_e}t\,. \qquad (13)$$

This equation has the same form as equation 10 with the following coefficients:

$$a = \frac{\left(\mathrm{A}p_0 - \mathrm{B}\right) - Q_i}{\rho_e \mathrm{AC}}\,, \qquad (14)$$

$$b = \mathrm{AC}\,,\ \text{and} \qquad (15)$$

$$d = \frac{Q_i}{\rho_e}\,. \qquad (16)$$

Differentiating equation 13 with respect to time, we find that this curve has an initial volumetric extrusion rate $\dot{V}_e^{t=0} = ab + d = (\mathrm{A}p_0 - \mathrm{B})/\rho_e$ but asymptotically approaches a linear trend having the slope $V_e^{t\to\infty} = d = Q_i/\rho_e$. Best-fit values of *a*, *b*, and *d* for the growth curve (table 2) suggest that $\dot{V}_e^{t=0} = {\sim}7.0$ m^3/s (605,000 m^3/day) and $V_e^{t\to\infty} = {\sim}1.26$ m^3/s (109,000 m^3/day). The latter value (the recharge rate) is several times greater than the long-term magma-supply rate of 0.2 m^3/s at Mount St. Helens, estimated by assuming that most of the volume of the edifice (~25 km^3) was erupted in the past 4,000 years (Iverson and others, 2006). Finally, the volume constant *a*, roughly 2.8×10^7 m^3, is the y-intercept of the long-term growth line in fig. 3*D* (the black dashed line). The y-intercept represents the volume of magma that has erupted and has not been replaced in the reservoir by recharge. The remaining volume, more than 4.5×10^7 m^3, represents recharge.

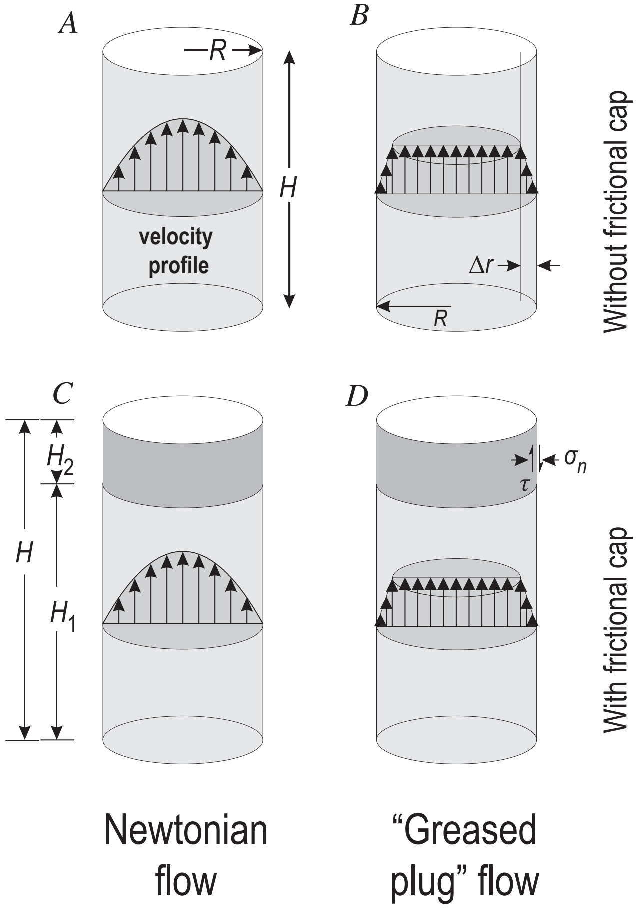

Figure 8. Types of conduit flow that are considered in deriving theoretical lava-dome growth curves. See text for full explanation.

The physical significance of terms in *a* and *b* can be further refined, depending on the type of flow in the conduit. For Poiseuille flow, the mass flow rate is (Mironer, 1979, p. 194):

$$\frac{dM_e}{dt} = \frac{\rho_e \pi R^4}{8\eta H}\left(p - \bar{\rho}gH\right), \qquad (17)$$

where *H* is the conduit length, *η* is the average viscosity, and $\bar{\rho}$ is the average magma density between the magma reservoir and the Earth's surface. This equation assumes that the pressure at the top of the conduit is negligible (an assumption we will evaluate later). For Poiseuille flow, the constants in equation 12 are $\mathrm{A} = \rho_e\pi R^4/(8\eta H)$ and $\mathrm{B} = \rho_e\pi R^4\,\bar{\rho}\,g/(8\eta)$. Inserting these expressions into equation 13, we can recast *a* in the following form:

$$a = \frac{\rho_M}{\rho_e}\left(\frac{\dot{V}_e^{t=0} - \dot{V}_e^{t\to\infty}}{\dot{V}_e^{t=0}}\right)\left(\kappa_C + \kappa_M\right)V_C\left(p_0 - \bar{\rho}gH\right). \qquad (18)$$

Equation (18) can be generalized by noting that $\left(p_0 - \bar{\rho}gH\right)$ is the initial pressure at the base of the conduit in excess of that required to initiate upward flow. Denoting this term as p_0^{ex}, we can rewrite the equations as:

$$a = \frac{\rho_M}{\rho_e}\left(\frac{\dot{V}_e^{t=0} - \dot{V}_e^{t\to\infty}}{\dot{V}_e^{t=0}}\right)\left(\kappa_C + \kappa_M\right)V_C p_0^{ex}, \qquad (19)$$

$$b = AC = \frac{\rho_e}{\rho_M}\frac{\dot{V}_e^{t=0}}{\left(\kappa_C + \kappa_M\right)V_C p_0^{ex}}\,. \qquad (20)$$

It can be shown (appendix 3) that these equations also apply to greased-plug flow (fig. 8*B*) and to flow of either a Newtonian fluid or a greased plug capped by a frictional plug (figs. 8*C*, 8*D*; appendices 4, 5), so long as the plug's geometry and coefficient of friction do not change with time. If a frictional cap is present, p_0^{ex} represents the pressure in the magma reservoir in excess of both the pressure due to the weight of the overlying magma $\left(\bar{\rho} g H\right)$ and the pressure required to overcome frictional resistance of the plug.

Some important relations fall out of the equations above. In the absence of recharge, the final erupted volume is:

$$a = \frac{\rho_M}{\rho_e}\left(\kappa_C + \kappa_M\right) V_C p_0^{ex} \ . \qquad (21)$$

Using $\kappa_C = 8\times10^{-11}$ Pa^{-1}, $\rho_M/\rho_e \approx 1$, $V_C = 10$ km^3, $p_0^{ex} = \sim30$ MPa, and $\kappa_M = 1.6\times10^{-10}$ Pa^{-1} appropriate for a bubble-free magma, the volume a is 7.2×10^7 m^3—roughly equal to the 7.3×10^7 m^3 that has erupted by the end of 2005. The time required for extrusion of 90 percent of this volume is about $3.5/b$, or ~416 days. Using a magma compressibility consistent with 1 percent bubbles ($\kappa_M = 2.8\times10^{-10}$ Pa^{-1}) and $\kappa_C = 1.4\times10^{-10}$ Pa^{-1} (to maintain $dV_e / dV_C \approx 3$ following equation 5), we obtain a theoretical extrusion volume $a = 1.26\times10^8$ m^3 and duration of 2.0 years. These results suggest that the eruption could continue beyond early 2006 without recharge, but only if the exsolved volatile fraction in the reservoir is significantly greater than ~1 percent or if the reservoir is significantly larger than ~10 km^3, or both.

For the case of recharge, taking $\dot{V}_e^{t\to\infty} = 1.26$ m^3/s and $a = 2.8\times10^7$ m^3 (table 2), the product $V_C p_0^{ex}\left(\kappa_M + \kappa_C\right)$ obtained from equation 19 is about 3.4×10^7 Pa·m^3. Constraining the reservoir volume and initial overpressure requires some additional constraint on magma compressibility, which is considered later.

Friction, Faulting, and the Growth Curve

A log-based formula having the form of equations 7 or 9 would be predicted if the growth of the lava dome were controlled by frictional resistance of a solid mass in the upper conduit, with the coefficient of friction increasing with the rate of slip.

Although the coefficient of friction is commonly taken as a constant with a value of ~0.6–1.0 (Byerlee, 1978), it actually varies slightly with sliding rate and with time between sliding events (for example, Scholz, 1998). When μ increases with displacement rate, acceleration is dampened out and stable sliding (or fault creep) results. When μ decreases with displacement rate, sliding can accelerate unstably, leading to earthquakes. In general, rate-strengthening friction is favored when the shear-zone temperature is near the brittle-ductile transition (Chester, 1994), when a thick gouge layer is present (Byerlee and Summers, 1976), and in near-surface conditions when normal stress on the fault plane is low (Marone and Scholz, 1988). These conditions all exist in the shallow conduit at Mount St. Helens.

On the other hand, experimental studies of the Mount St. Helens fault gouge at 25°C (Moore and others, this volume, chap. 20) suggest rate-weakening behavior when displacement rates are less than about 1×10^{-4} m/s and rate-strengthening behavior at rates above 5×10^{-4} m/s. Assuming a 100-m-diameter conduit near the surface, the range of observed volumetric extrusion rates (~1–7 m^3/s) translates into displacement rates of $1\text{–}9\times10^{-4}$ m/s, crossing over the transition between these behavior types. We consider it likely that both rate-strengthening and rate-weakening sliding exist at shallow depth at any given time. Fault patches of rate-weakening gouge will slip abruptly to create small drumbeat earthquakes whereas other parts of the fault surface creep stably under rate-strengthening conditions. If rate-weakening behavior controls conduit flow, the appropriate friction coefficient to use in this model would be a value averaged over many stick-slip cycles. If that average doesn't change with time, the long-term growth curve will be exponential. But if rate-strengthening behavior controls conduit flow, we need to consider the stress-strain rate relations of rate-strengthening fault creep.

The Logarithmic Curve

When the coefficient of friction is rate-dependent, the shear stress that resists slip on a fault plane is commonly expressed as (for example, Scholz, 1998):

$$\tau = \tau_o + A_1 \sigma_n \ln\frac{\dot{\delta}}{\dot{\delta}_o}. \qquad (22)$$

Here σ_n is normal stress at the wall and A_1 is the rate dependence of fault strength. The constant τ_o is an arbitrary reference, the strength of the wall interface when the slip rate is $\dot{\delta}_o$.

In order to derive a growth curve, we assume that the frictional plug of mass M_p and length H_2 occupies a cylindrical conduit of radius R (fig. 8*C*). The frictional force along the plug margin is $2\pi R H_2 \mu \bar{\sigma}_n$, where $\bar{\sigma}_n$ is the mean normal stress on the plug margin. The mass flow rate $\dot{M}_e$ is then related to $\dot{\delta}_o$ by $\dot{M}_e = \rho_e \pi R^2 \dot{\delta}$, and pressure at the plug base (p) is related to mass flow rate as:

$$p = p_o + \alpha \ln\frac{\dot{M}_e}{\dot{M}_o}, \qquad (23)$$

where $\alpha = 2A_1\bar{\sigma}_n H_2 / R$ and $p_0 = 2\tau_0 H_2 / R + Mg / \pi R^2$ are constants.

Rearranging this equation yields:

$$\dot{M}_e = e^{\dot{M}_0} \exp\left[\frac{\left(p - p_o\right)}{\alpha}\right]. \qquad (24)$$

Combining equation 24 with equation 11 (assuming recharge $M_i = 0$) and integrating leads to (appendix 6):

$$V_e = \alpha D \ln\left(1 + \frac{t\dot{M}_0}{\rho_e D \alpha}\right), \qquad (25)$$

where $D = V_M\left(\kappa_C + \kappa_M\right)$ and V_M is the volume of the magma reservoir plus conduit. This equation has the same form as equation 7, with $a = \alpha V_M\left(\kappa_C + \kappa_M\right)$ and $b = \dot{V}_e^{t=0} / a$.

If recharge into the magma reservoir is included, the equation has the form (appendix 6):

$$V_e = \alpha D \ln\left[1 - \frac{\dot{M}_0}{Q_i}\left(1 - e^{\frac{Q_i t}{\rho_e \alpha D}}\right)\right]. \tag{26}$$

This equation has the form of equation 10, with a volume constant $a = \alpha D = 1.47\times10^7$ m^3 (by regression through the most recent data set, table 2), a recharge rate $b = Q_i / \rho_e = 1.0$ m^3/s, and an initial extrusion rate $d = \dot{M}_0 / \rho_e = \dot{V}_e^{t=0} = 8.9$ m^3/s (table 3). The recharge rate is about 30 percent less than the 1.26 m^3/s obtained from the exponential curve. By rearranging equation 23, substituting $\dot{M}_e = \rho_e \dot{V}_e$, $\dot{M}_0 = \rho_e \dot{V}_e^{t=0}$, and $a = \alpha D = \alpha V_M(\kappa_C + \kappa_M)$, we can obtain a formula for the product of volume of the magma system and pressure drop from the beginning of the eruption until the time of the last data point used in this paper (December 15, 2005):

$$V_M \Delta p\left(\kappa_C + \kappa_M\right) = a \ln\left(\dot{V}_e^{t=0} / \dot{V}_e^{last}\right). \tag{27}$$

The parameters Δp and $\dot{V}_e^{last}$ are the pressure change at the base of the frictional plug and the extrusion rate at the end of this time period; the variable a is the numerical value of the fitting coefficient. From the first derivative of equation 9, $\dot{V}_e^{last} = 1.20$ m^3/s as of December 15, 2005 (table 3), giving $V_M \Delta p\left(\kappa_C + \kappa_M\right) = 3.0\times10^7$ m^3. It should be noted that this term contains slightly different parameters from $V_C p_0^{ex}\left(\kappa_C + \kappa_M\right)$ derived for the exponential curve: V_C represents reservoir volume, whereas V_M represents volume of the reservoir plus conduit below the frictional plug, and Δp represents pressure drop at the base of the plug, whereas p_0^{ex} gives the initial overpressure in the magma reservoir. Nevertheless, the values of these terms should be roughly comparable, and they are: $V_M \Delta p(\kappa_C + \kappa_M) = 3.0\times10^7$ m^3 from the log fit (equation 9) versus $V_C p_0^{ex}\left(\kappa_C + \kappa_M\right) = 3.4\times10^7$ m^3 from the exponential fit (equation 10). The fact that these values differ by only 10 to 15 percent suggests that inferences about magma-reservoir size and overpressure do not depend strongly on the assumptions regarding factors that control conduit flow.

Additional Constraints from the Geodetic Time Series

On the basis of their fit to the dome-growth data, neither the logarithmic (equation 9) nor the exponential (equation 10) model can be confidently eliminated. Each, however, predicts a history of reservoir deflation that can be compared with geodetic data. For the case of exponential dome growth, differentiating equation 13 with time under conditions of constant recharge and substituting in equations 4, 14, and 15 gives the following for reservoir deflation with time:

$$\Delta V_C = -\frac{\rho_e}{\rho_M} \frac{a\left(1 - e^{-bt}\right)}{\left(1 + \dfrac{\kappa_M}{\kappa_C}\right)}. \tag{28}$$

The reservoir deflates with the same time constant as the dome-growth curve, implying, for the best-fit value of b with recharge through December 15, 2005 (2.06×10^{-7} s^{-1}), that 90 percent of the geodetic deflation should have occurred after about 200 days, by mid-April 2005, and that by late summer 2005 the deflation should have essentially stopped. This is inconsistent with geodetic data, which show a nearly linear rate of inward displacement through at least the end of 2005. The log curve can theoretically provide a better match to the geodetic data, but the predictions at some point become physically unrealistic. For the case of zero recharge, for

Table 3. Calculations of $V_C\, p_0^{ex}(\kappa_M + \kappa_C)$ or $V_M \Delta p(\kappa_M + \kappa_C)$ obtained from exponential or logarithmic best-fit solutions.

Date	$V_C p_0^{ex}(\kappa_M+\kappa_C)$ exponential		Log with recharge			Log without recharge		
	With recharge m^3×10^6	Without recharge m^3×10^6	$\dot{V}_e^{t=0}$ m^3/s	$\dot{V}_e^{last}$ m^3/s	$V_M \Delta p(\kappa_M+\kappa_C)$ m^3×10^6	$\dot{V}_e^{t=0}$ m^3/s	$\dot{V}_e^{last}$ m^3/s	$V_M \Delta p(\kappa_M+\kappa_C)$ m^3×10^6
12/11/2004	24	54	8.3	3.94	5.9	6.9	3.4	28
1/3/2005	67	47	7.5	2.52	33	7.6	2.5	33
2/1/2005	71	45	8.3	1.82	37	8.3	1.8	37
2/21/2005	33	48	8.4	1.64	40	8.2	1.7	40
3/10/2005	29	51	8.1	1.54	43	8.1	1.5	43
4/19/2005	29	55	8.3	1.40	39	7.8	1.3	48
6/15/2005	31	61	8.3	1.20	42	7.6	1.1	54
7/14/2005	32	64	8.4	1.14	42	7.5	1.0	57
8/10/2005	31	69	8.9	1.23	36	7.1	1.0	61
10/24/2005	31	78	9.4	1.24	33	6.4	0.9	68
12/15/2005	34	83	8.9	1.11	38	6.2	0.8	72

example, combining equations 5 and 25 and substituting $a = a V_C\left(\kappa_C + \kappa_M\right)$ and $b = \dot{V}_e^{t=0}/a$, the volume shrinkage of the magma system should follow the curve:

$$\Delta V_C = -\frac{\rho_e a \ln\left(1+bt\right)}{\rho_M\left(1+\dfrac{\kappa_M}{\kappa_C}\right)}. \qquad (29)$$

In other words, the volume shrinkage of the magma reservoir with time should look like a negative mirror image of the dome growth curve, adjusted by the constant $\rho_e/(\rho_M(1+\kappa_M/\kappa_C))$. This curve leads to the physically unrealistic result that deflation continues indefinitely, even to negative reservoir volumes, at the same time that the lava dome keeps growing. This implication is an outcome of the logarithmic relation between stress and displacement rate (equation 22), which adequately fits experimental data on rate-dependent friction within the range of shear stresses applied during experiments but cannot be realistically extrapolated outside that range.

A More Realistic Model

We are therefore left with the result that neither the exponential curve nor the logarithmic curve can adequately fit both the lava-dome growth curve and the geodetic deflation history. What additional processes might account for the dome growth and deflation histories? Some possibilities include:

- *The effect of the dome's weight in suppressing further extrusion.*—Digital elevation models indicate that the dome rapidly grew to more than 200 m height in the first two months of the eruption, potentially adding several megapascals of increased pressure to the vent at the base of the dome. Our records on dome-height variations with time (fig. 9) can be used to constrain this effect.
- *Changes in magma compressibility with time.*—A decrease in reservoir pressure of 30 MPa can increase magma compressibility several tens of percent (fig. 6*C*), increasing the ability of the magma reservoir to maintain a long-term eruption with time.
- *A nonconstant rate of recharge.*—A more realistic model would have recharge into the reservoir increasing as reservoir pressure decreases.

These effects require a numerical solution to account for changing values with time. We solve the problem using differential equations described below.

To account for the relation between mass eruption rate and reservoir pressure, we assume again that the effusion rate is linearly related to the reservoir overpressure. For Poiseuille or greased-plug flow, the overpressure p^{ex} is simply $p - \bar{\rho} g H$. If a frictional cap is present, the overpressure is $p^{ex} = p - \left(\bar{\rho} g H + F\right)$, where F is the strength of the frictional cap (assumed constant). The growth of the lava dome changes the distance H from the reservoir to the free surface, and in order to account for this, we divide this term into two parts; $\bar{\rho} g H_0$, where H_0 is the distance from the top of the reservoir to the vent at the base of the lava dome, and $\rho_e g H_3$, where H_3 is the height of the lava dome. The relation between pressure and effusion rate is then:

$$\frac{dM_e}{dt} = \mathrm{A}_2\left[\frac{p - \left(\bar{\rho} g H_0 + \rho_e g H_3 + F\right)}{H_0 + H_3}\right]. \qquad (30)$$

The constant A_2 has the value $\rho_e \pi R^4/(8\eta)$ for Poiseuille flow and $\rho_e \pi R^3 \Delta r/(8\eta)$ for greased-plug flow (appendix 4). This

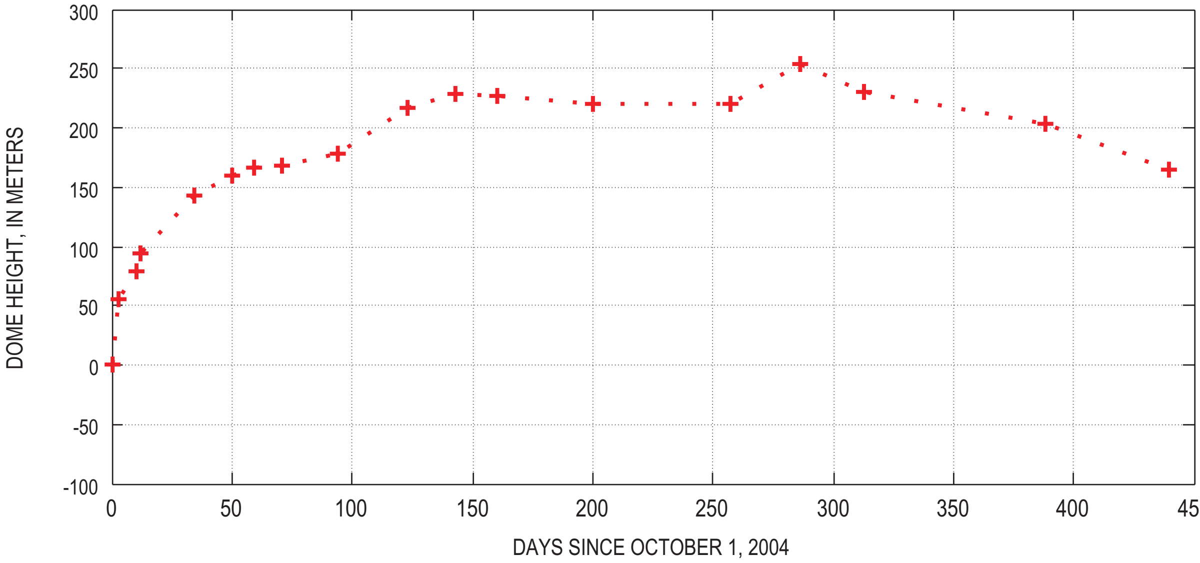

Figure 9. Maximum height of the Mount St. Helens lava dome above the 2003 crater floor (the Crater Glacier surface, approximately 2,115 m above sea level) during the course of the 2004–6 eruption.

equation can be simplified by noting that, at $t=0$, $p^{ex}=p_0^{ex}$ and $dM_e/dt = \dot{V}_e^{t=0}/\rho_e$:

$$\frac{dV_e}{dt} = \dot{V}_e^{t=0}\,\frac{p_0^{ex}+\Delta p-\rho_e g H_3}{p_0^{ex}}\ . \qquad (31)$$

The initial extrusion rate $\dot{V}_e^{t=0}$, the dome height H_3, and the density ρ_e are constrained from measurements; the pressure change in the magma reservoir Δp is calculated by integration (below); and the initial overpressure p_0^{ex} is an adjustable parameter whose value is likely less than a few tens of megapascals.

The rate of pressure change in the reservoir is obtained by differentiating equation 11 with time and substituting $C=[(\kappa_C+\kappa_M)\rho_m V_C]^{-1}$:

$$\frac{dp}{dt} = \frac{\dfrac{dM_i}{dt}-\rho_e\dfrac{dV_e}{dt}}{\rho_M V_C\left(\kappa_C+\kappa_M\right)}\ . \qquad (32)$$

In this calculation, the terms κ_C and ρ_e are considered known; dV_e/dt is obtained from equation 31, and the recharge rate dM_i/dt is calculated from a separate differential equation (below). The magma compressibility κ_M at the beginning of the eruption is an adjustable parameter; during the course of the eruption, it increases with decreasing pressure at a rate that equals the average slope of the curve of κ_M versus p in figure 6*C* (for $CO_2=1{,}900$ ppm, $H_2O=5.2$ weight percent). In each calculation, we use the magma density ρ_M shown in figure 6*B* at the given compressibility. Thus the magma density changes with pressure, though the changes are minor.

In accounting for recharge, we assume that the rate of input into the magma reservoir at the onset of the eruption was negligible but increased as reservoir pressure was depleted. The simplest such relation is linear, using an adjustable proportionality constant Q_{lt}:

$$\frac{dM_i}{dt} = -Q_{lt}\,\frac{\Delta p}{p_0^{ex}}\ . \qquad (33)$$

The parameter Δp is the reservoir-pressure change since the start of the eruption (negative Δp implies a pressure decrease). Like Q_i in equation 13, Q_{lt} in equation 33 largely controls the long-term extrusion rate. The linear assumption implies laminar flow of magma into the reservoir from some deeper source whose pressure remains constant. A more realistic model would consider a finite source whose pressure decreased over time, but we have no constraints on the rate of pressure decrease and hence ignore it under the assumption that the deeper reservoir is much larger than the shallow one that feeds the eruption.

Equations 31, 32, and 33 can be simultaneously integrated to yield both a dome-growth curve and deflation history. The calculations involve four adjustable constants: V_C, p_0^{ex}, an initial value of κ_M, and Q_{lt}. Our solution takes κ_C to be a known quantity, although its value is known only approximately. The above estimates of $V_e/\Delta V_C$ suggest κ_C to be at least a few times greater than our initial estimate of 2×10^{-11} Pa^{-1}, but best-fit values of $V_C p_0^{ex}\left(\kappa_C+\kappa_M\right)$ in table 3 constrain $\left(\kappa_C+\kappa_M\right)$ to be less than about 5×10^{-10} Pa^{-1} for magma-reservoir volumes greater than about 5 km^3 and initial overpressures exceeding about 10 MPa. With these constraints, we run the model using two possible values of 7×10^{-11} and 1.5×10^{-10} Pa^{-1} for κ_C. In theory, the values of Q_{lt} and κ_M can be uniquely determined, as they are the only factors that significantly affect the long-term eruption rate and the ratio $V_e/\Delta V_C$, respectively. The values of V_C and p_0^{ex} are interdependent and nonunique, but ranges of possible combinations can be identified.

In order to compare the deflation history to geodetic measurements, we convert the history of pressure change Δp into a history of magma-chamber shrinkage ΔV_C, using $\Delta V_C = \left(V_C/\kappa_C\right)\Delta p$, and then convert ΔV_C into a theoretical displacement at JRO1 using one of the geodetic models in table 1 (fig. 4). For the first time period (fig. 4*A*), model 5 in table 1 (source depth 6–10 km) matches the JRO1 radial displacements best and predicts a radial displacement of 5.32 mm for a volume loss ΔV_C of 3.85×10^6 m^3, or 1.4×10^{-6} mm displacement per cubic meter volume loss.

Results

Numerical model results are compared with measurement histories of lava-dome volume and radial displacement at JRO1 in figures 10*A* and 10*B*, respectively. The solid black line in fig. 10*A* gives model results that match the hot-rock data for $V_C=17$ km^3, $p_0^{ex}=17$ MPa, and $Q_{lt}/\rho_e = 1.7$ m^3/s. The dashed black line gives analytical results using the exponential curve of equation 10 with $a=2.77\times10^7$ m^3, $b=2.06\times10^{-7}$ s^{-1} and $d=1.26$ m^3/s. These theoretical curves cannot be easily compared with the JRO1 data because deflation at JRO1 began around September 23, 2004, 20 days before the first lava appeared and three days before the first visible surface deformation (Dzurisin and others, this volume, chap. 14). The deflation between September 26 and October 11 was probably associated with extrusion of cold rock ahead of the rising magma. Deflation before September 26 may have been associated with intrusion at shallow depth or gas escape, neither of which can be easily quantified.

In order to simultaneously fit both curves, we add the volume of cold rock extruded before October 11 to the cumulative hot-rock volume (green data points, fig. 10*A*) and use September 27 as the start date (a date determined by a best-fit exponential curve through these new data). We also start with 3 mm of deflation at $t=0$, the approximate amount of deflation measured at JRO1 on September 27.

The blue dashed and solid lines in figure 10*A* represent best-fit analytical (using equation 10) and numerical curves through the modified dataset, respectively. Best-fit coefficients of the analytical curve give $a=3.61\times10^7$ m^3, $b=2.2\times10^{-7}$ s^{-1}, and $d=1.28$ m^3/s. Using $\kappa_C=7\times10^{-11}$ Pa^{-1}, $\kappa_M=1.2\times10^{-10}$ Pa^{-1} (adjusted to match the deflation curve) and equation 28 to calculate magma-reservoir deflation with time, the calculated displacements (dashed blue line, fig. 10*B*) roughly match the measurements during the first few months of the eruption and during the following summer (~250–400 days into the eruption), but they do not predict continued deflation that one would infer from a best-fit line through the JRO1 data after about 150 days.

A numerical solution (solid blue lines) provides a slightly better fit through the data using $V_C = 17$ km^3, $p_0^{ex} = 18$ MPa, $Q_{lt}/\rho_e = 1.7$ m^3/s, and κ_M ranging from an initial value of 1.85×10^{-10} Pa^{-1} to a final value of 1.98×10^{-10} Pa^{-1} (~0.40–0.48 percent bubbles). In this solution, the total volume of erupted magma that has not been replaced by recharge is about 3.9×10^7 m^3. This amount is 1.3×10^7 m^3 less than predicted by the analytical solution (fig. 10*A*). The lower total recharge implies more geodetic deflation; hence the numerical curve can be fit to the geodetic data using a slightly higher average κ_M than required by the analytical solution. Over the time window of the simulation, the magma-reservoir pressure drops by about 11 MPa, so that the excess pressure $\left(p - \bar{\rho} g H_1\right)$ by mid-December 2005 is about 7 MPa, three megapascals greater than the pressure $\rho_e g H_3$ at the vent, owing to the weight of the overlying dome (taking $\rho_e = 2300$ kg/m^3 and $H_3 = 167$ m on December 15, 2005).

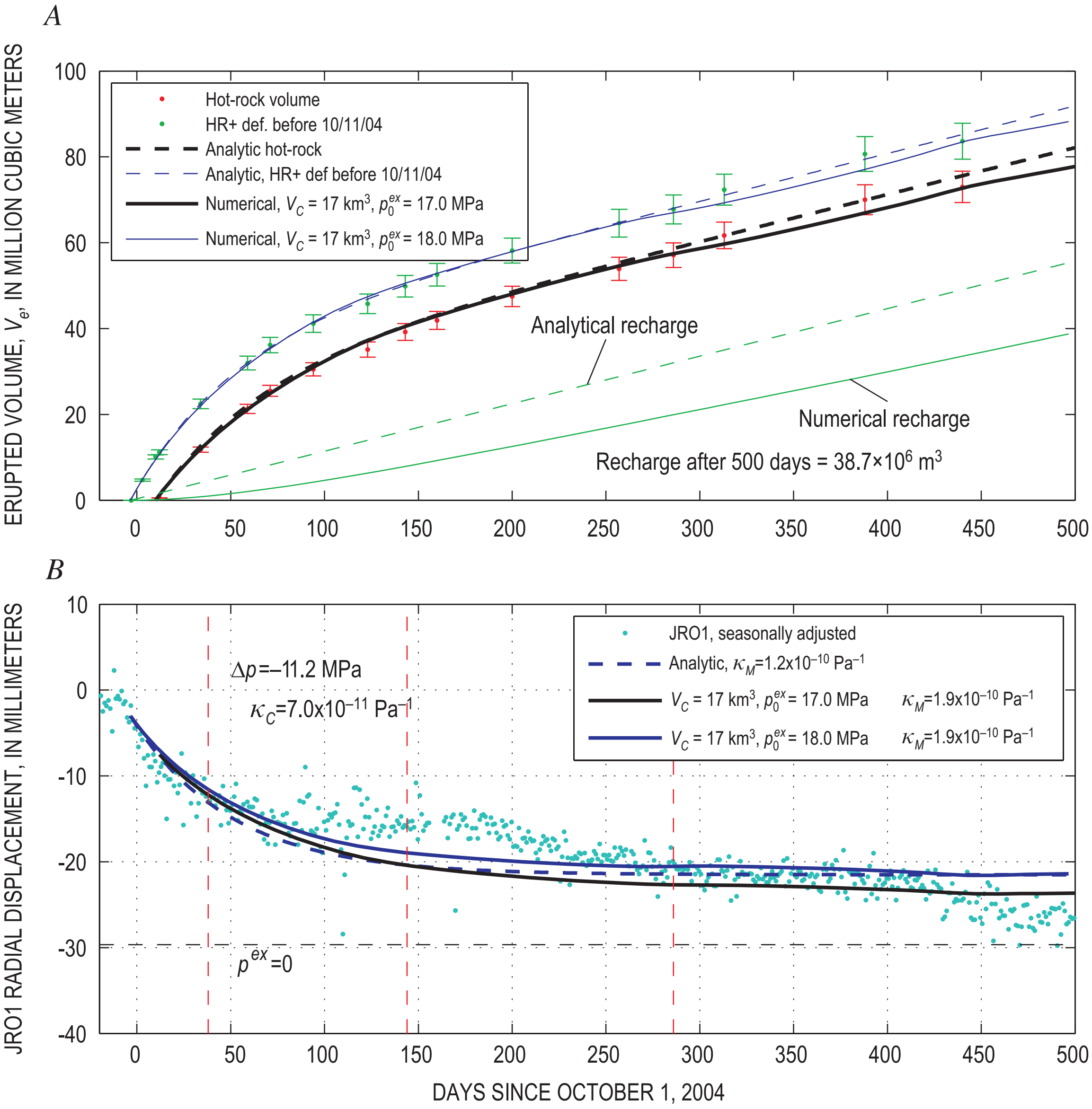

Figure 10. Comparison of theoretical and measured lava-dome volume and magma-reservoir deflation with time at Mount St. Helens. *A*, Erupted volume from digital elevation models. Phrase "HR+def before 10/11/04" refers to data points that represent hot-rock volume of the dome plus volume of uplifted cold crater-floor material that appears before the beginning of lava extrusion on October 11, 2004. Phrase "Analytic, HR+def before 10/11/04" refers to an analytical best-fit line through these data. Details are explained in text. *B*, Radial displacement measured at JRO1 continuous GPS station (fig 1*A*). Negative displacements are radially inward. Red vertical dashed lines in figure 10*B* refer to the start and end dates of time windows used in geodetic analysis (fig. 4 and table 1).

Other combinations of ΔV_C, p_0^{ex}, Q_{lt}, and κ_M that produce reasonable fits by numerical solution are listed in table 4. All combinations require $Q_{lt}/\rho_e = 1.7 \pm 0.1$ m³/s. Runs that use $\kappa_C = 7 \times 10^{-11}$ Pa^{-1} require average values of κ_M around 1.6–1.9×10^{-10} Pa^{-1} (0.18–0.43 volume percent bubbles) and a magma-reservoir volume exceeding ~9 km³ for p_0^{ex}<~30 MPa. Runs that use $\kappa_C = 15 \times 10^{-11}$ Pa^{-1} require $\kappa_M = 4.0$–4.7×10^{-10} Pa^{-1} (1.0–1.8 volume percent bubbles) and a magma-reservoir volume exceeding ~5 km³ for p_0^{ex} less than about 30 MPa. Using a still larger reservoir compressibility ($\kappa_C = 3 \times 10^{-10}$ Pa^{-1}), a magma reservoir larger than 2 km³ (for p_0^{ex} less than about 30 MPa) can still fit the curves using $\kappa_M = 8.9$–9.4×10^{-10} Pa^{-1} (2.8–3.8 percent bubbles). The results that involve $\kappa_C = 7$ to 15×10^{-11} Pa^{-1} correspond to exsolved fluid contents in the source region that match most closely with gas emission data (Gerlach and others, this volume, chap. 26).

The Quandary of Continued Deflation

Like the exponential function, the numerical solution predicts that deflation should have nearly ended several months after the eruption began, which does not agree with the geodetic data. Factors that might keep both the extrusion rate and the deflation rate more or less constant include (1) decreasing magma viscosity or friction coefficient with time; (2) increasing conduit diameter with time; and (or) (3) a nonlinear relation between extrusion rate and friction coefficient, similar to the logarithmic relation.

As of March 2006 there have been no obvious temporal changes in petrology or fault-gouge characteristics that might reflect changes in viscosity or friction coefficient (Pallister and others, this volume, chap. 30). Changes in conduit diameter cannot, however, be dismissed (our field observations are insufficient), nor can the possibility that conduit enlargement alone, in the absence of recharge, is responsible for sustained extrusion rates. Figure 11*B* shows a theoretical deflation curve calculated in the absence of recharge by solving equation 5 for reservoir volume loss dV_C using $(\rho_M/\rho_e) = 1$, $\kappa_M = 3.3 \times 10^{-10}$ Pa^{-1} (adjusted to optimize fit), $\kappa_C = 7 \times 10^{-11}$ Pa^{-1}, and the erupted volume dV_e ($= V_e$) obtained from the best-fit curve, equation 10, through modified hot-rock data (fig. 11*A*). The theoretical curve matches the long-term linear trend quite well but underestimates the deflation in the first few months of the eruption. The rapid early deflation implies that the volume removed from the reservoir per unit erupted volume was initially high but then decreased with time, a characteristic that could be explained by either increasing recharge or by increasing magma compressibility with time. Starting with a slightly lower compressibility (3.2×10^{-10} Pa^{-1}) that increases to 4.1×10^{-10} Pa^{-1} over the course of the eruption (fig. 11*B*, red dashed line) does not appear to reconcile the difference.

Table 4. Combinations of V_C, p_0^{ex}, Q_{lt}, and average value of κ_M that yield reasonable fits to the growth curve and geodetic data by numerical calculation; also given are the pressure drop Δp in the magma reservoir and the recharge volume calculated after 500 days of eruption.

κ_C Pa^{-1}×10^{-11}	V_C km³	p_0^{ex} MPa	avg κ_M Pa^{-1}×10^{-10}	Q_{lt}/ρ_e m³/s	Δp MPa	Recharge m³×10⁶
7	6	41	1.6	1.7	-30.5	48.7
7	8	32	1.6	1.7	-23	46.7
7	10	27	1.8	1.7	-18.7	44.4
7	12	24	1.8	1.7	-16.3	42.9
7	14	21	1.9	1.7	-13.7	40.9
7	17	19	1.9	1.7	-12.0	39.0
7	20	16.5	1.9	1.7	-9.9	37.0
7	24	15	1.9	1.7	-8.6	34.9
7	27	14	1.9	1.7	-7.8	33.4
14	4	34	3.0	1.7	24.7	47.1
14	6	25	3.1	1.7	17.1	43.6
14	8	19	4.0	1.7	-12.0	39.2
14	10	16	4.1	1.7	-9.4	36.4
14	12	14.5	4.2	1.7	-8.2	34.2
14	14	13.3	4.2	1.7	-7.1	32.2
14	17	12	4.3	1.7	-6.0	29.6
14	20	11	4.7	1.7	-5.0	26.7
14	24	10.2	4.7	1.7	-4.3	24.3

The pressure change Δp is related to the volume shrinkage dV_C by $\Delta p = dV_C/(V_C \kappa_C)$. For $V_C = 15$ km³, for example, the deflation in figure 11*B* represents a pressure drop of about 15–16 MPa, requiring an initial overpressure above this value to sustain the eruption for the observed time period. The conduit radius R that could give the instantaneous growth rate in figure 11*A* with the pressure in figure 11*B* can be calculated from equation 17 by substituting $p_0^{ex} + \Delta p - \rho_e g H_3$ for $\left(p - \bar{\rho} g H\right)$, $\dot{V}_e^{t=0}$ for $\left(\pi R_0^4 p_0^{ex} / 8 \eta H\right)$, and $\rho_e \dot{V}_e$ for dM_e/dt:

$$R = R_0 \left[\left(\frac{\dot{V}_e}{\dot{V}_e^{t=0}} \right) \left(\frac{p_0^{ex}}{p_0^{ex} + \Delta p - \rho_e g H_3} \right) \right]^{1/4}. \qquad (34)$$

Here, R_0 is the initial conduit radius. Calculating the change in R with time requires values of V_C and p_0^{ex} to be assumed in advance. For $V_C = 15$ km³ and $p_0^{ex} = 30$ MPa, the observed extrusion history can be produced by a roughly 15-percent decrease in conduit radius in the first few months of the eruption, followed by widening at a slow but accelerating rate (fig. 11*C*). As the overpressure approaches zero, the conduit radius must approach infinity to keep the extrusion rate constant (for example, the line for $p_0^{ex} = 15$ MPa in fig. 11*C*).

These results suggest that the changes in conduit radius required to maintain the observed eruption rate without recharge are less than a few tens of percent and thus probably too small to be easily detected by observed variations in lithic content of the lava or ratios in linear to volumetric extrusion rate. The changes shown in figure 11, however, involve a seemingly unrealistic shrinkage in radius early in the eruption, when effusion rates are high, followed by enlargement at an accelerating rate when effusion rates are low. We cannot dismiss conduit-radius changes in the absence of recharge, but we are inclined to consider them less likely than recharge-driven flow. Future developments may help distinguish these possibilities: If extrusion is sustained by conduit widening without recharge, geodetic deflation will continue and the eruption will eventually wane, then stop. If it is sustained by recharge, geodetic deflation will soon stabilize, but the eruption may continue for years and end gradually as the deeper magma source is depleted.

Finally, one explanation for continued deflation may lie in the results of the numerical models. Model runs using

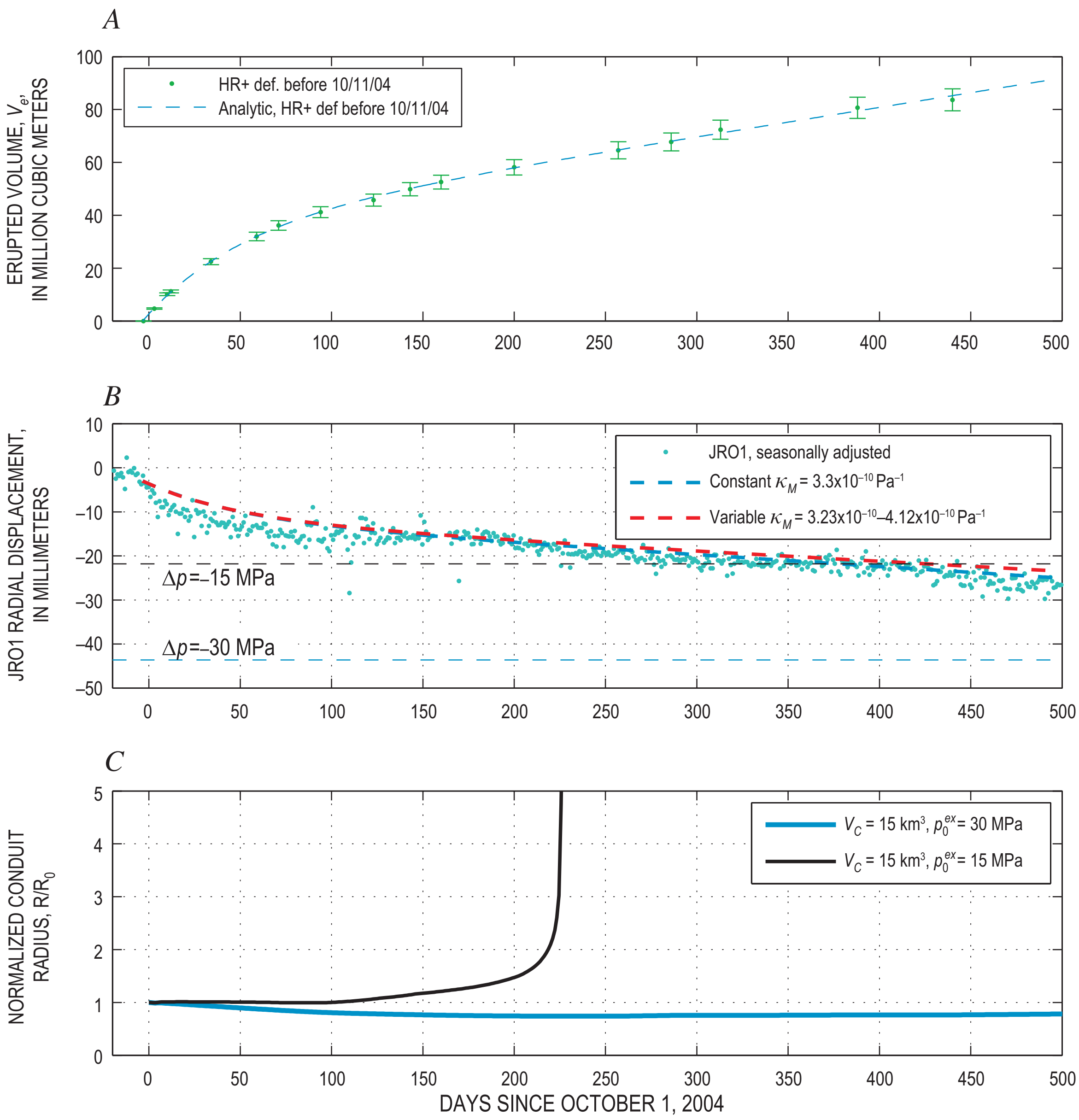

Figure 11. Modeled relation between extruded volume, magma pressure and overpressure, and conduit radius at Mount St. Helens. *A*, Erupted volume, V_e. Data points with error bars represent hot-rock volume of the lava dome plus volume of cold rock uplifted before October 11, 2004 (compare fig. 10*A*). Error bars are ±5 percent as in figures 2 and 10. *B*, Station JRO1 radial displacements (dots) compared with the displacements predicted at this point for deflation of a 15-km^3 ellipsoidal magma body at 6–10 km depth with $\kappa_C = 7\times10^{-11}$ Pa^{-1} and (1) a constant $\kappa_M = 3.3\times10^{-10}$ (blue dashed line) or (2) κ_M increasing from 3.2×10^{-10} to 4.2×10^{-10} as pressure drops by 15 MPa (dashed red line). Negative displacements are radially inward. *C*, Conduit radius, *R*, required to maintain extrusion rate illustrated in figure 11*A*, normalized to the initial conduit radius, R_0. Magma pressure is inferred from deflation curve, assuming an initial overpressure of 30 MPa (blue line) or 15 MPa (black line). Method of calculating pressure change is explained in text.

a small magma body show a rapid deflation curve at JRO1 followed by stabilization as the recharge rate approaches the eruption rate. Runs that involve larger magma bodies show continued long-term deflation but cannot match the rapid deflation seen in the first several weeks of the eruption. The blue solid line in figure 10*B* represents an intermediate reservoir size that shows a little deflation still after 500 days of eruption but not enough to match the data. The steep deflation at short times and the long-term continued deflation at longer times may suggest that decompression initiated within a relatively small body of eruptible magma but expanded with time to a much larger volume that may include cooler or more crystalline, partially solidified material.

Discussion and Conclusions

Within the range of uncertainty, the above results are consistent with the view that the magma reservoir at Mount St. Helens is several to perhaps a few tens of cubic kilometers in size, that the pressure drop in the magma system is several to a few tens of megapascals, and that the reservoir contains less than a few volume percent exsolved gas at the source depth of 8–9 km. Numerous uncertainties prevent us from more accurate estimates of the size, overpressure, volatile content, and degree of recharge of the Mount St. Helens magma reservoir. The greatest limitation is the uncertainty in reservoir compressibility κ_C, which appears to be at least a few times greater over the period of this eruption than during the very brief time scale of seismic wave disturbance. Our conclusion that κ_C is only a few to several times less than magma compressibility contrasts with expectations (for example, Huppert and Woods, 2002) that κ_M would be much greater than κ_C in deep, equant, volatile-saturated magma bodies. The similarity between κ_M and κ_C during this eruption likely reflects both the lower rigidity of the Earth over long time scales and the low exsolved volatile content of the magma.

The observation that geodetic deflation volume dV_C is less than erupted volume V_e is an expected consequence of the finite compressibility of magma, and need not imply recharge. We expect dV_C to be less than V_e during nearly all eruptions. Conversely, in a reservoir that is intruded before an eruption, the injection volume V_i should be significantly greater than the resulting change in reservoir volume dV_C. Deep, stiff reservoirs containing volatile-rich magmas are likely to show the lowest ratios of dV_C/V_i, raising the question of whether preeruptive magma injection into a volatile-rich reservoir might fail to generate a detectable geodetic signal.

Finally, like Huppert and Woods (2002) and Woods and Huppert (2003), we find that the compressibility of magma, which is related to exsolved volatile content, has an overriding influence on the duration and final volume of effusive eruptions. Our study, however, advances those works by showing that, when exsolution of both H_2O and CO_2 is considered, there is little or no discontinuity in compressibility at the saturation pressure, and hence no dramatic change in eruptive style or the rate of decrease in eruptive activity when the saturation pressure is reached in a magma reservoir.

The idealizations in this paper are necessary for developing a simple model. In testing our assumptions, we acknowledge that many such idealizations are unrealistic. Our simple balloon-and-soda-straw cartoon of a magma reservoir may not even approximately resemble the complex of partially molten bodies that could make up the real magma system. Given this complexity, the question of whether the magma body is being recharged may be primarily a question of where one draws boundaries. We nevertheless hope that these simple models offer some insight.

Acknowledgments

Discussion of the form of the growth curve and its relation to physical processes was initiated by Terry Gerlach and Dan Dzurisin, to whom we owe many thanks. Mike Lisowski played a crucial role gathering deformation data used in this study and was offered coauthorship but politely declined. Dan Dzurisin and Peter Cervelli reviewed this manuscript and offered several improvements. Insights into various aspects of this study were provided by John Pallister, Carl Thornber, Richard Iverson, Shaul Hurwitz, Emily Brodsky, and Seth Moran.

References Cited

Barker, S.E., and Malone, S.D., 1991, Magmatic system geometry at Mount St. Helens modeled from the stress field associated with posteruptive earthquakes: Journal of Geophysical Research, v. 96, no. B7, p. 11883–11894, doi:10.1029/91JB00430.

Blackwell, D.D., Steele, J.L., Kelley, S.A., and Korosec, M.A., 1990, Heat flow in the State of Washington and thermal conditions in the Cascade Range: Journal of Geophysical Research, v. 95, no. B12, p. 19495–19516.

Blanpied, M.L., Marone, C.J., Lockner, D.A., Byerlee, J.D., and King, D.P., 1998, Quantitative measure of the variation in fault rheology due to fluid-rock interactions: Journal of Geophysical Research, v. 103, no. B5, p. 9691–9712.

Blundy, J., and Cashman, K., 2001, Ascent-driven crystallisation of dacite magmas at Mount St. Helens, 1980–1986: Contributions to Mineralogy and Petrology, v. 140, no. 6, p. 631–650, doi:10.1007/s004100000219.

Bonaccorso, A., and Davis, P.M., 1999, Models of ground deformation from vertical volcanic conduits with application to eruptions of Mount St. Helens and Mount Etna: Journal of Geophysical Research, v. 104, no. B5, p. 10531–10542.

Brace, W.F., and Kohlstedt, D.L., 1980, Limits on lithospheric stress imposed by laboratory experiments: Journal of Geophysical Research, v. 85, no. B11, p. 6248–6252.

Byerlee, J.D., 1978, Friction of rocks: Pure and Applied Geophysics, v. 116, p. 615–626.

Byerlee, J.D., and Summers, R., 1976, A note on the effect of fault gouge thickness on fault stability [abs.]: International Journal of Rock Mechanics and Mining Sciences and Geomechanics Abstracts, v. 13, p. 35–36.

Cashman, K.V., and Taggart, J.E., 1983, Petrologic monitoring of 1981 and 1982 eruptive products from Mount St. Helens: Science, v. 221, no. 4618, p. 1385–1387.

Cashman, K.V., Thornber, C.R., and Pallister, J.S., 2008, From dome to dust; shallow crystallization and fragmentation of conduit magma during the 2004–2006 dome extrusion of Mount St. Helens, Washington, chap. 19 *of* Sherrod, D.R., Scott, W.E., and Stauffer, P.H., eds., A volcano rekindled; the renewed eruption of Mount St. Helens, 2004–2006: U.S. Geological Survey Professional Paper 1750 (this volume).

Chester, F.M., 1994, Effects of temperature on friction; constitutive equations and experiments with quartz gouge: Journal of Geophysical Research, v. 99, no. B4, p. 7247–7261.

Clauser, C., and Huenges, E., 1995, Thermal conductivity of rocks and minerals, rock physics and phase relations, *in* A handbook of physical constants: Washington D.C., American Geophysical Union, p. 105–126.

Dieterich, J.H., 1979, Modeling of rock friction 1. Experimental results and constitutive equations: Journal of Geophysical Research, v. 84, no. B5, p. 2161–2168.

Dieterich, J.H., and Kilgore, B.D., 1996, Imaging surface contacts; power law contact distributions and contact stresses in quartz, calcite, glass and acrylic plastic: Tectonophysics, v. 256, p. 216–239.

Dzurisin, D., Lisowski, M., Poland, M.P., Sherrod, D.R., and LaHusen, R.G., 2008, Constraints and conundrums resulting from ground-deformation measurements made during the 2004–2005 dome-building eruption of Mount St. Helens, Washington, chap. 14 *of* Sherrod, D.R., Scott, W.E., and Stauffer, P.H., eds., A volcano rekindled; the renewed eruption of Mount St. Helens, 2004–2006: U.S. Geological Survey Professional Paper 1750 (this volume).

Elkins, L.T., and Grove, T.L., 1990, Ternary feldspar experiments and thermodynamic models: American Mineralogist, v. 75, p. 544–559.

Fournier, R.O., 1999, Hydrothermal processes related to movement of fluid from plastic into brittle rock in the magmatic-epithermal environment: Economic Geology, v. 94, no. 8, p. 1193–1211.

Gerlach, T.M., McGee, K.A., and Doukas, M.P., 2008, Emission rates of CO_2, SO_2, and H_2S, scrubbing, and preeruption excess volatiles at Mount St. Helens, 2004–2005, chap. 26 *of* Sherrod, D.R., Scott, W.E., and Stauffer, P.H., eds., A volcano rekindled; the renewed eruption of Mount St. Helens, 2004–2006: U.S. Geological Survey Professional Paper 1750 (this volume).

Ghiorso, M.S., and Sack, R.O., 1995, Chemical mass transfer in magmatic processes IV. A revised and internally consistent thermodynamic model for the interpolation and extrapolation of liquid-solid equilibria in magmatic systems at elevated temperatures and pressures: Contributions to Mineralogy and Petrology, v. 119, p. 197–212.

Heliker, C., 1995, Inclusions in the Mount St. Helens dacite erupted from 1980 through 1983: Journal of Volcanology and Geothermal Research, v. 66, nos. 1–3, p. 115–135, doi:10.1016/0377-0273(94)00074-Q.

Huppert, H.E., and Woods, A.W., 2002, The role of volatiles in magma chamber dynamics: Nature, v. 420, no. 6915, p. 493–495.

Iverson, R.M., Dzurisin, D., Gardner, C.A., Gerlach, T.M., LaHusen, R.G., Lisowski, M., Major, J.J., Malone, S.D., Messerich, J.A., Moran, S.C., Pallister, J.S., Qamar, A.I., Schilling, S.P., and Vallance, J.W., 2006, Dynamics of seismogenic volcanic extrusion at Mount St. Helens in 2004–05: Nature, v. 444, no. 7118, p. 439–443, doi:10.1038/nature05322.

Jaeger, J.C., and Cook, N.G.W., 1979, Fundamentals of rock mechanics (3d ed.): London, Chapman and Hall, 593 p.

Johnson, D.J., Sigmundsson, F., and Delaney, P.T., 2000, Comment on “Volume of magma accumulation or withdrawal estimated from surface uplift or subsidence, with application to the 1960 collapse of Kilauea volcano” by P.T. Delaney and D.F McTigue: Bulletin of Volcanology, v. 61, p. 491–493.

Linker, M.F., and Dieterich, J.H., 1992, Effects of variable normal stress on rock friction; observations and constitutive equations: Journal of Geophysical Research, v. 97, p. 4923–4940.

Lisowski, M., Dzurisin, D., Denlinger, R.P., and Iwatsubo, E.Y., 2008, Analysis of GPS-measured deformation associated with the 2004–2006 dome-building eruption of Mount St. Helens, Washington, chap. 15 *of* Sherrod, D.R., Scott, W.E., and Stauffer, P.H., eds., A volcano rekindled; the renewed eruption of Mount St. Helens, 2004–2006: U.S. Geological Survey Professional Paper 1750 (this volume).

Marone, C., and Scholz, C.H., 1988, The depth of seismic faulting and the upper transition from stable to unstable slip regimes: Geophysical Research Letters, v. 15, no. 6, p. 621–624.

Marone, C., Raleigh, C.B., and Scholz, C.H., 1990, Frictional behavior and constitutive modeling of simulated fault gouge: Journal of Geophysical Research, v. 95, no. B5, p. 7007–7025.

Marone, C.J., Scholz, C.H., and Bilham, R., 1991, On the mechanics of earthquake afterslip: Journal of Geophysical Research, v. 96, p. 8441–8452.

Mastin, L.G., 2002, Insights into volcanic conduit flow from an open-source numerical model: Geochemistry, Geophysics, Geosystems, v. 3, no. 7, 18p., doi:10.1029/2001GC000192.

McTigue, D.F., 1987, Elastic stress and deformation near a finite spherical magma body; resolution of the point source paradox: Journal of Geophysical Research, v. 92, no. B12, p. 12931–12940.

Mironer, A., 1979, Engineering fluid mechanics: New York, McGraw-Hill, 592 p.

Moore, P.L., Iverson, N.R., and Iverson, R.M., 2008, Frictional properties of the Mount St. Helens gouge, chap. 20 *of* Sherrod, D.R., Scott, W.E., and Stauffer, P.H., eds., A volcano rekindled; the renewed eruption of Mount St. Helens, 2004–2006: U.S. Geological Survey Professional Paper 1750 (this volume).

Musumeci, C., Gresta, S., and Malone, S.D., 2002, Magma system recharge of Mount St. Helens from precise relative hypocenter location of microearthquakes: Journal of Geophysical Research, v. 107, no. B10, 2264, p. ESE 16-1–ESE 16-9, doi:10.1029/2001JB000629.

Newhall, C.G., and Melson, W.G., 1983, Explosive activity associated with the growth of volcanic domes: Journal of Volcanology and Geothermal Research, v. 17, p. 111–131.

Newman, A.V., Dixon, T.H., Ofoegbu, G.I., and Dixon, J.E., 2001, Geodetic and seismic constraints on recent activity at Long Valley Caldera, California; evidence for viscoelastic rheology: Journal of Volcanology and Geothermal Research, v. 105, no. 3, p. 183–206.

Newman, A.V., Dixon, T.H., and Gourmelen, N., 2006, A four-dimensional viscoelastic deformation model for Long Valley Caldera, California, between 1995 and 2000: Journal of Volcanology and Geothermal Research, v. 150, nos. 1–3, p. doi:10.1016/j.jvolgeores.2005.1007.1017.

Newman, S., and Lowenstern, J.B., 2002, VolatileCalc; a silicate melt-H_2O-CO_2 solution model written in Visual Basic for Excel®: Computers and Geosciences, v. 28, no. 5, p. 597–604, doi:10.1016/S0098-3004(01)00081-4.

Pallister, J.S., Thornber, C.R., Cashman, K.V., Clynne, M.A., Lowers, H.A., Mandeville, C.W., Brownfield, I.K., and Meeker, G.P., 2008, Petrology of the 2004–2006 Mount St. Helens lava dome—implications for magmatic plumbing and eruption triggering, chap. 30 *of* Sherrod, D.R., Scott, W.E., and Stauffer, P.H., eds., A volcano rekindled; the renewed eruption of Mount St. Helens, 2004–2006: U.S. Geological Survey Professional Paper 1750 (this volume).

Poland, M.P., and Lu, Z., 2008, Radar interferometry observations of surface displacements during pre- and coeruptive periods at Mount St. Helens, Washington, 1992–2005: chap. 18 *of* Sherrod, D.R., Scott, W.E., and Stauffer, P.H., eds., A volcano rekindled; the renewed eruption of Mount St. Helens, 2004–2006: U.S. Geological Survey Professional Paper 1750 (this volume).

Pollard, D.D., and Fletcher, D.F., 2005, Fundamentals of structural geology: Cambridge, Cambridge University Press, 500 p.

Power, W.L., Tullis, T.E., and Weeks, J.D., 1988, Roughness and wear during brittle faulting: Journal of Geophysical Research, v. 93, no. B12, p. 15268–15278.

Reinen, L.A., Weeks, J.D., and Tullis, T.E., 1994, The frictional behavior of lizardite and antigorite serpentinites; experiments, constitutive models, and implications for natural faults: Pure and Applied Geophysics, v. 143, p. 317–358.

Robertson, E.C., 1983, Relationship of fault displacement to gouge and breccia thickness: Mining Engineering, v. 35, p. 1426–1432.

Rubin, A.M., 1990, A comparison of rift-zone tectonics in Iceland and Hawaii: Bulletin of Volcanology, v. 52, p. 302–319.

Ruina, A., 1983, Slip instability and state variable friction laws: Journal of Geophysical Research, v. 88, no. B12, p. 10359–10370.

Rutherford, M.J., and Devine, J.D., 1988, The May 18, 1980, eruption of Mount St. Helens; 3, Stability and chemistry of amphibole in the magma chamber: Journal of Geophysical Research, v. 93, no. B10, p. 11949–11959.

Rutherford, M.J., and Devine, J.D., III, 2008, Magmatic conditions and processes in the storage zone of the 2004–2006 Mount St. Helens dacite, chap. 31 *of* Sherrod, D.R., Scott, W.E., and Stauffer, P.H., eds., A volcano rekindled; the renewed eruption of Mount St. Helens, 2004–2006: U.S. Geological Survey Professional Paper 1750 (this volume).

Rutherford, M.J., Sigurdsson, H., Carey, S., and Davis, A., 1985, The May 18, 1980, eruption of Mount St. Helens; 1, Melt composition and experimental phase equilibria: Journal of Geophysical Research, v. 90, no. B4, p. 2929–2947.

Scandone, R., and Malone, S.D., 1985, Magma supply, magma discharge and readjustment of the feeding system of Mount St. Helens during 1980: Journal of Volcanology and Geothermal Research, v. 23, nos. 3–4, p. 239–262, doi:10.1016/0377-0273(85)90036-8.

Schaff, D.P., Beroza, G., and Shaw, B.E., 1999, Postseismic response of repeating aftershocks: Geophysical Research Letters, v. 25, p. 4559–4552.

Schilling, S.P., Thompson, R.A., Messerich, J.A., and Iwatsubo, E.Y., 2008, Use of digital aerophotogrammetry to determine rates of lava dome growth, Mount St. Helens, Washington, 2004–2005, chap. 8 *of* Sherrod, D.R., Scott, W.E., and Stauffer, P.H., eds., A volcano rekindled; the renewed eruption of Mount St. Helens, 2004–2006: U.S. Geological Survey Professional Paper 1750 (this volume).

Scholz, C.H., 1998, Earthquakes and friction laws: Nature, v. 391, p. 37–42.

Stasiuk, M.V., Jaupart, C., and Sparks, R.S.J., 1993, On the variations of flow rate in non-explosive lava eruptions: Earth and Planetary Science Letters, v. 134, p. 505–516.

Tait, S., Jaupart, C., and Vergniolle, S., 1989, Pressure, gas content and eruption periodicity of a shallow, crystallising magma chamber: Earth and Planetary Science Letters, v. 92, p. 107–123.

Tiampo, K.F., Rundle, J.B., Fernandez, J., and Langbein, J.O., 2000, Spherical and ellipsoidal volcanic sources at Long Valley caldera, California, using a genetic algorithm inversion technique: Journal of Volcanology and Geothermal Research, v. 102, p. 189–206.

Turcotte, D.L., and Schubert, G., 2002, Geodynamics (2d ed.): Cambridge, Cambridge University Press, 456 p.

Wadge, G., 1981, The variation of magma discharge during basaltic eruptions: Journal of Volcanology and Geothermal Research, v. 11, p. 139–168.

Williams, D.L., Abrams, G., Finn, C., Dzurisin, D., Johnson, D.J., and Denlinger, R., 1987, Evidence from gravity data for an intrusive complex beneath Mount St Helens: Journal of Geophysical Research, v. 92, no. B10, p. 10207–10222.

Woods, A.W., and Huppert, H.E., 2003, On magma chamber evolution during slow effusive eruptions: Journal of Geophysical Research, v. 108, no. B8, 2403, p. doi:10.1029/2002JB002019.

Zoback, M.D., and Healy, J.H., 1984, Friction, faulting, and in situ stress: Annalen der Geophysik, v. 2, p. 689–698.

Appendix 1. Processes That Could Affect Reservoir Compressibility

The static shear modulus of large rock masses (kilometers in size) is generally known to be up to an order of magnitude less than that of laboratory-scale specimens (Pollard and Fletcher, 2005, p. 322). The reduction in shear modulus with increasing scale is generally attributed to the presence of fractures that can open or move (Rubin, 1990). In this paper we estimate host-rock shear modulus from the velocities of seismic waves whose wavelength is on the order of a kilometer and does not differ greatly from the dimensions of the rock mass under stress near the magma reservoir. On the other hand, seismic velocities are controlled by stress oscillations that act over a time scale of milliseconds, whereas eruption-associated stress changes evolve over a period of years. Over the longer time scale, subcritical crack growth, poroelasticity, and inelastic creep could deform rock and therefore reduce the shear modulus, G. Because the geodetic signal is measured at the surface, a low shear modulus at shallow depth could perhaps also affect the geodetic signal. These effects are considered below.

Crack growth and poroelasticity.—Crack growth may greatly reduce G at <1–2 km depth (Rubin, 1990), but at 6–12 km depth it is unclear whether cracks of any significant size exist. Near the hot reservoir, cracks are likely to anneal and seal off interstitial fluids (Fournier, 1999). Poroelastic effects theoretically have no effect on shear modulus, though they can decrease Poisson's ratio with time and change estimates of G if such estimates are based on the formula $G=\rho_R \upsilon_P^2(1-2\nu)/(2(1-\nu))$ (for example, Rubin, 1990). Poroelastic effects, however, change G by only a few tens of percent at most; at depths of 6–12 km, interstitial fluids are likely sparse and these effects even smaller.

Elastic inhomogeneity.—Figure 5 shows variations in G with depth estimated from the seismic-velocity profile and density data (explained in the figure caption). In the uppermost 1–2 km the estimated value of G may drop to about 11 GPa; however, at depths below 1–2 km the value of G remains above about 35 GPa. Because the surface displacements are affected by the elastic properties of all materials between the magma reservoir and the surface, the lower elastic moduli of near-surface materials must affect displacements to some degree, but the relation between reservoir stress drop and displacement should be primarily controlled by rock properties near the magma body. For this reason we consider that the effect of less stiff near-surface materials on G is likely to be less than about 20 percent.

High-temperature inelastic deformation near the magma body.—In long-lived magma systems, such as Long Valley in eastern California, viscoelastic creep may reduce by about two-thirds the pressure change required for a given volume change (Newman and others, 2001; Newman and others, 2006). However, the Mount St. Helens magma system is relatively young and surrounded by cooler rock that is gabbroic in composition (Heliker, 1995) and resistant to creep. Regional heat-flow studies suggest that the ambient temperature at 9–10 km depth in this region is about 350°C (Blackwell and others, 1990). If we assume the magma reservoir has existed at its present temperature for about 4,000 to 40,000 years, we can estimate the temperature profile around the magma reservoir by numerically integrating the following one-dimensional transient equation for conductive heat flow:

$$\frac{\partial T}{\partial t}=\frac{k_R}{\rho_R c_R r}\frac{\partial}{\partial r}\left(r\frac{\partial T}{\partial r}\right), \qquad (35)$$

where k_R and c_R are the thermal conductivity and specific heat, respectively, of the host rock, and r is the radial distance of a given point from the center of the magma body. Holding the temperature at the reservoir wall constant at 850°C and using $k_R=2$ W/(m·K) (Clauser and Huenges, 1995) and $c_R=1{,}300$ J/

(kg•K), we obtain the temperature profiles from a 1-km-radius magma body illustrated in figure 12*A*.

If decompression is rapid, the host rock will deform elastically, then relax with time as viscous creep reduces wall stress. The equations for the radial (σ_{rr}) and normal ($\sigma_{\theta\theta}$) stresses near a cylindrical body in an infinite linear elastic medium under plane-strain conditions are (Jaeger and Cook, 1979, p. 251):

$$\sigma_{rr} = \sigma_1\left(1-\frac{R^2}{r^2}\right)+p\left(\frac{R^2}{r^2}\right) \quad , \tag{36}$$

$$\sigma_{\theta\theta} = \sigma_1\left(1+\frac{R^2}{r^2}\right)-p\left(\frac{R^2}{r^2}\right) \quad , \tag{37}$$

where σ_1 is the far-field normal stress (assumed equal in all directions perpendicular to the cylinder axis), p is the internal pressure in the reservoir, and R is the cylinder radius. For $\sigma_1=240$ MPa and $p=210$ MPa, values of σ_{rr} and $\sigma_{\theta\theta}$ are plotted in figure 12*B*. Note that at the reservoir wall, the difference $\sigma_{\theta\theta}-\sigma_{rr}$ is equal to twice (σ_1-p).

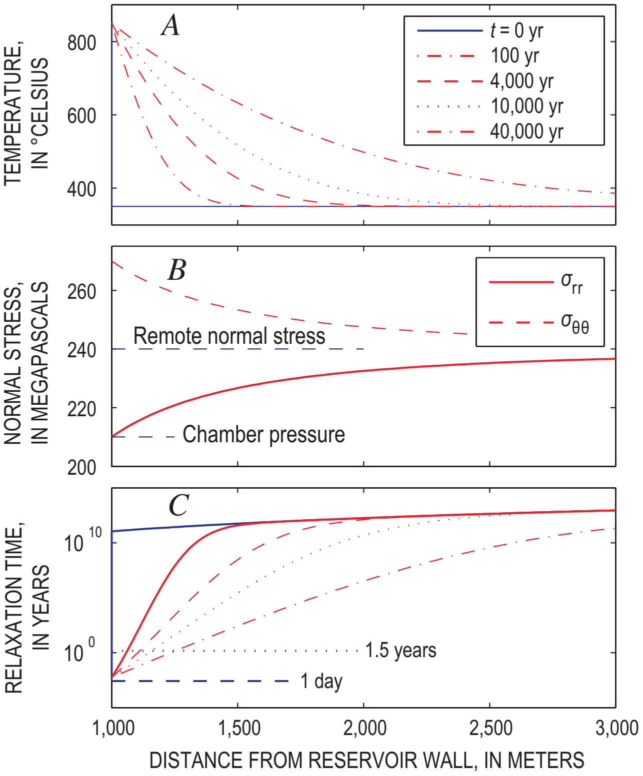

Figure 12. Response of a 1-km-radius magma body through time, as a function of distance from reservoir walls. *A*, Temperature over increasing time periods since emplacement of the magma body. Temperatures were calculated by integrating equation 35 with time. *B*, Circumferential ($\sigma_{\theta\theta}$) and radial (σ_{rr}) normal stresses versus radial distance from the reservoir wall, calculated assuming elastic deformation at short time periods following a rapid pressure change in the magma body. *C*, Viscous relaxation time versus distance for hot rock. The solid blue curve shows relaxation time versus distance assuming the host rock has a uniform temperature of 350°C. Red curves give relaxation time assuming the host-rock temperature varies with distance from the reservoir wall as illustrated by corresponding curves in panel *A*.

The dominant form of stress relaxation is likely to be dislocation creep (Turcotte and Schubert, 2002), which involves a power-law dependence between normal strain rate ($\dot{\varepsilon}_{\theta\theta}$ or $\dot{\varepsilon}_{rr}$) and normal-stress difference ($\sigma_{\theta\theta}-\sigma_{rr}$) (Turcotte and Schubert, 2002, eq. 7-187):

$$\dot{\varepsilon}_{rr} = -\dot{\varepsilon}_{\theta\theta} = C_1\left(\sigma_{\theta\theta}-\sigma_{rr}\right)^n e^{-E_a/R_gT} , \tag{38}$$

where C_1, n, and E_a are fitting parameters, R_g is the gas constant, and T is temperature (in Kelvin). We use $C_1=520$ MPa^{-n}/s, $n=3$, and $E_a=356$ kJ/mol, which are appropriate for diabase (Turcotte and Schubert, 2002, table 7-4). The power-law dependence implies that viscosity is not constant at a given temperature; however, we can estimate a rough average viscosity from the relation:

$$\eta_{eff} \approx \frac{\left(\sigma_{\theta\theta}-\sigma_{rr}\right)}{\dot{\varepsilon}_{rr}} = \frac{e^{-E_a/RT}}{C_1\left(\sigma_{\theta\theta}-\sigma_{rr}\right)^{n-1}} . \tag{39}$$

Using this viscosity and Young's modulus $E=\rho\upsilon_P^2(1-2\nu)(1+\nu)/(1-\nu)=1\times10^{11}$ Pa, (where $\nu=0.25$, $\upsilon_P=6.6$ km/s and $\rho=2{,}700$ kg/m^3), the viscous relaxation time τ_η is:

$$\tau_\eta = \frac{\eta_{eff}}{E} . \tag{40}$$

Rocks having $\eta_{eff}<\sim5\times10^{18}$ Pa·s will relax in less time than the 1.5-year duration of the eruption to date (early 2006). For a magma body that has existed for about 4,000–40,000 years, rocks within ~110–250 m of the reservoir wall will relax within this time period. If these rocks are considered part of the mechanical magma reservoir, its effective volume would be about 20 percent to 50 percent greater than the volume of magma alone. By comparison, no host rock was hot enough to relax during the 24-hour period following the Mount St. Helens eruptions of May and June 1980 (fig. 12*C*). Thus the aseismic body identified by Scandone and Malone (1985) could be as much as a few hundred meters smaller in diameter than the mechanical magma body that is deforming during the current eruption.

Appendix 2. Derivation of the Exponential Equation

Derivation of the exponential relation involves differentiating equation 11:

$$\frac{dp}{dt} = -C\left(\frac{dM_e}{dt}-Q_i\right) \tag{41}$$

and substituting equation 12 into this equation to give:

$$\frac{dp}{dt} = BC + CQ_i - ACp \,. \tag{42}$$

Reversing the denominator in the left-hand term with the right-hand side of the equation and integrating gives:

$$-\frac{1}{AC}\ln\left(BC + CQ_i - ACp\right) + C_2 = t \,, \tag{43}$$

where C_2 is the constant of integration. We find a value for C_2 by noting that, at $t = 0$, $p = p_0$; hence

$$-\frac{1}{AC}\ln\left[\frac{BC + CQ_i - ACp}{BC + CQ_i - ACp_0}\right] =$$

$$-\frac{1}{AC}\ln\left[1 + \frac{AC\left(p_0 - p\right)}{BC + CQ_I - ACp_0}\right] = t \,. \tag{44}$$

Further rearrangement leads to:

$$p = p_0 - \left(p_0 - \frac{B + Q_i}{A}\right)\left(1 - e^{-ACt}\right) \,. \tag{45}$$

This equation can be substituted into equation 12 to give:

$$\begin{aligned}\frac{dM_e}{dt} &= Ap_0 + \left(B + Q_i - Ap_0\right)\left(1 - e^{-ACt}\right) - B \\ &= Q_i - \left(B + Q_i - Ap_0\right)e^{-ACt} \,,\end{aligned} \tag{46}$$

which can be integrated to give:

$$M_e = Qt + \frac{B + Q_i - Ap_0}{AC}e^{-ACt} + C_2 \,, \tag{47}$$

where C_2 is a constant of integration, which can be evaluated by noting that, at $t = 0$, $M_e = 0$. After evaluating C_2, we get:

$$M_e = \frac{\left(Ap_0 - B\right) - Q_i}{AC}\left(1 - e^{-ACt}\right) + Q_i t \,. \tag{48}$$

This equation can be expressed in eruptive volume (V_e) by dividing by lava density ρ_e:

$$V_e = \frac{1}{\rho_e}\frac{\left(Ap_0 - B\right) - Q_i}{AC}\left(1 - e^{-ACt}\right) + \frac{Q_i}{\rho_e}t \,. \tag{49}$$

Appendix 3. The Exponential Equation for "Greased Plug" Flow

The assumption of Newtonian flow implies that the flow profile in the conduit is parabolic. Given the high crystal content of the magma, a more realistic scenario may be that the magma in the center of the conduit moves upward as a solid plug and that shear is concentrated along the conduit margins (fig. 8*B*). If the material in the shear acts in a Newtonian manner, a force balance leads to the following equation:

$$\pi R^2 p - \rho g \pi R^2 H - \frac{2H\eta}{\rho R \Delta r}\frac{dM_e}{dt} = 0 \,, \tag{50}$$

where Δr is the thickness of the shear zone and ρ is the magma density in the conduit. The first term is the upward force at the base of the conduit, the second is the weight of the magma plug, and the third is the viscous force resisting upward flow. The equation can be rearranged as:

$$\frac{dM_e}{dt} = \frac{\rho \pi R^3 \Delta r}{2\eta H}\left(p - \rho g H\right) \,. \tag{51}$$

In this case, the terms A and B in equation 12 have the value $A = \rho\pi R^3 \Delta r/(8\eta H)$ and $B = \pi R^3 \Delta r \rho^2 g/(8\eta)$. Substitution of these terms into equations 14 and 15 leads to expressions for *a* and *b* that are identical to equations 18 and 20; hence the constraints on the product $V_C(p_0 - \rho_m gH)$ are exactly the same for greased-plug flow as for Newtonian flow.

Appendix 4. Exponential Equation for Newtonian Flow Capped by a Frictional Plug with Constant Frictional Properties

The presence of fault gouge along the dome surface at Mount St. Helens suggests that, over some distance near the surface, magma moves upward as a solid plug with frictional sliding along its margins (fig. 8*D*). Assuming that flow below this plug is Newtonian, the equation for mass flux is:

$$\frac{dM_e}{dt} = \frac{\rho \pi R^4}{8\eta H_1}\left(\left(p - p_1\right) - \rho g H_1\right) \,, \tag{52}$$

where H_1 is the length of conduit over which flow is Newtonian and p_1 is the pressure at the base of the frictional plug (fig. 8*C*). That pressure is a function of both plug weight and friction. We assume that the shear stress along the plug margin must exceed the normal stress (σ_n) times a coefficient of friction (μ), which is assumed to be constant:

$$\tau \geq \mu \sigma_n \,. \tag{53}$$

If the plug is cylindrical, vertical, of the same radius (R) as the conduit below, and of length H_2, the pressure (p_1) at the base of an upward-moving plug must exceed the sum of the plug weight and the frictional resistance:

$$p_1 \geq \rho g H_2 + \frac{2\mu \bar{\sigma}_n H_2}{R} \,. \tag{54}$$

In this case, $\bar{\sigma}_n$ represents the mean normal stress on the conduit walls over the length of the plug. In solid rock, the horizontal normal stress could vary greatly even at shallow depth, depending on the state of gas pressure and on geometric factors. On the other hand, at Mount St. Helens, the crater floor is composed primarily of unconsolidated fallback from the 1980 eruptions. If we take this material to be cohesionless, faults of favorable orientation will form when the ratio of effective normal to shear stress on any potential fault plane exceeds that allowed by the coefficient of friction of the material (μ_h). Thus the ratio of most compressive (σ_1) to least compressive (σ_3) normal principal stress at any depth is limited to (Brace and Kohlstedt, 1980; Zoback and Healy, 1984):

$$\frac{\sigma_1 - p_p}{\sigma_3 - p_p} \le \left[\mu_h + \left(\mu_h^2 + 1\right)^{1/2}\right]^2 \ , \tag{55}$$

where p_p is the pore pressure in the host rock. For $\mu_h = 0.6$ and p_p ranging from 0 to σ_3, σ_1/σ_3 ranges from 1 to ~3. For this reason, we consider the normal stress on the conduit wall to be one-third to three times the vertical stress, and express the normal stress as the vertical stress times a constant γ of order 1. If the frictional plug extends from the surface to a depth H_2, the mean normal stress on the plug wall is $\bar{\sigma}_n = \gamma \bar{\rho} g H_2 / 2$. We also assume that $\mu \cong 0.5$; these simplifications allow us to rewrite equation 54 as:

$$p_1 \approx \rho g H_2 \left(1 + \gamma \frac{H_2}{R}\right) . \tag{56}$$

Inserting this value into equation 52 and noting that $H_1 + H_2 = H$, we have:

$$\frac{dV_e}{dt} = \frac{1}{\rho_e} \frac{\rho \pi R^4}{8 \eta H_1} \left(p - \bar{\rho} g \left(H + \gamma \frac{H_2}{R}\right)\right). \tag{57}$$

Hence $A = \rho_e \pi R^4 / (8 \eta H_1)$ and $B = \pi R^4 \rho_e^2 g (H + \gamma H_2 / R) / (8 \eta H_1)$. These terms lead to the following values of a and b:

$$a = \frac{\left(dV_e/dt\right)_{t=0} - \left(dV_e/dt\right)_{t\to\infty}}{\frac{\rho_M}{\rho_e}\left(\frac{dV_e}{dt}\right)_{t=0} \frac{K_M}{V_C\left(p_0 - \bar{\rho} g \left(H + \gamma \frac{H_2}{R}\right)\right)}}$$

$$\approx 0.8 \frac{V_C\left(p_0 - \bar{\rho} g \left(H + \gamma \frac{H_2}{R}\right)\right)}{K_M} \ , \tag{58}$$

$$b = AC = \frac{\rho_e}{\rho_M}\left(\frac{dV_e}{dt}\right)_{t=0} \frac{K_M}{V_C\left(p_0 - \bar{\rho} g \left(H + \gamma \frac{H_2}{R}\right)\right)} . \tag{59}$$

Appendix 5. Exponential Equation for "Greased Plug" Flow Capped by a Frictional Plug with Constant Frictional Properties

As with the case above (appendix 4), this case involves modifying the greased plug equation to include a term for the pressure at the base of the frictional plug:

$$\frac{dM_e}{dt} = \frac{\rho \pi R^3 \Delta r}{2 \eta H_1}\left(\left(p - p_1\right) - \rho g H_1\right) . \tag{60}$$

Inserting the expression for p_1 in equation 56, we have:

$$\frac{dM_e}{dt} = \frac{\rho \pi R^3 \Delta r}{2 \eta H_1}\left[p - \rho g \left(H + \gamma \frac{H_2}{R}\right)\right] . \tag{61}$$

Hence $A = \rho \pi R^3 \Delta r / (2 \eta H_1)$ and $B = \pi R^3 \Delta r \rho^2 g (H + \gamma H_2 / R) / (2 \eta H_1)$.

Appendix 6. Derivation of Logarithmic Growth Curve

We envision a one-dimensional system consisting of a magma-filled reservoir and conduit system applying a pressure p to the base of an extruding solid rock plug of mass M_p and displacement rate $\dot{\delta}$ against gravity and frictional resistance to slip between the plug and the conduit wall. The rate of extrusion is controlled entirely by frictional resistance. That is, in this end-member model the magma below the plug has negligible viscosity.

Plug force balance.—Consider a "quasi-static" force balance for motion of a cylindrical plug (force resulting from acceleration is assumed to be negligible, $M \, d\dot{\delta}/dt \approx 0$). This quasi-static assumption is well justified by results of simulations in which inertia is considered; these "dynamic" simulations are not discussed in this appendix or elsewhere in this paper. The plug mass is assumed to be constant ($dM_p/dt \approx 0$), resulting from a balance between the rate of surface erosion of the plug and an equivalent subsurface accretion rate (for example, Iverson and others, 2006). The force balance per unit cross-sectional area in the conduit is:

$$p = \frac{M_p g}{\pi R^2} + \frac{2 \tau H_2}{R} \ , \tag{62}$$

where p is the fluid pressure of the magma applied to the base of the plug, R is plug radius, H_2 is plug height, g is the acceleration due to gravity, and τ is the shear resistance of the interface between the plug and the conduit wall. Because the mass is assumed constant, R and H_2 are also constant.

Faults have a well-known second-order dependence of shear strength on slip rate $\dot{\delta}$ (Dieterich, 1979; Ruina, 1983) and related, somewhat complicated dependencies on accumulated slip and time of contact ("state" effects in rate and state friction) (for example, Linker and Dieterich, 1992). However, fault strength can be assumed to be purely slip-rate dependent when subject to sustained sliding if the ratio of asperity contact size to slip rate is small relative to the duration of sustained slip. Daily extrusion rates at Mount St. Helens from October 2004 to October 2005, converted to boundary slip rates, are in the range 70 to 7,000 μm/s, assuming that the plug has radius in the range of 25 to 75 m. Taking asperity contact size to be no more than 20 μm, as laboratory data on rock friction suggest (for example, Dieterich and Kilgore, 1996), its ratio to slip rate is 0.29 to 0.0029 seconds, meaning that time-dependent and slip-dependent changes and friction can be ignored for sustained slip durations longer than 0.5 to 1.0 seconds. Data on extruded volume are collected over intervals of a few weeks to a month. Therefore, we ignore complicated “state” effects on fault shear strength, and represent it by a simple slip-rate-dependent relation,

$$\tau = \tau_o + A_1 \sigma_n \ln \frac{\dot{\delta}}{\dot{\delta}_o} \ . \tag{63}$$

Here σ_n is normal stress at the wall and A_1 is the rate dependence of fault strength. The constant τ_o is an arbitrary reference, the strength of the wall interface when the interface slip rate is $\dot{\delta}_o$.

For shear of thick fault-gouge layers (for example, Byerlee and Summers, 1976; Marone and others, 1990), for shear near the brittle-ductile transition (for example, Blanpied and others, 1998), and for near-surface faulting (Marone and Scholz, 1988), fault strength increases with slip rate (velocity strengthening, rate strengthening). Because all of these conditions are present at the plug wall at Mount St. Helens, we expect that fault slip is predominantly rate strengthening, and thus A_1 in equation 63 is a small positive constant, typically between 0.001 and 0.03 (Marone and Scholz, 1988; Blanpied and others, 1998).

The volume of extruded material V_e is the product of the conduit cross-sectional area and the slip at the wall, and the extruded mass M_e is proportional to the extruded volume, so equation 63 is equivalently

$$\tau = \tau_o + A_1 \sigma_n \ln \frac{\dot{M}_e}{\dot{M}_o} \ , \tag{64}$$

where notation for the mass rate of extrusion $dM_e/dt = \dot{M}_e$ is used. Combining equations 62 and 64 leads to a relation between magma pressure and the rate of plug extrusion

$$p = p_o + \alpha \ln \frac{\dot{M}_e}{\dot{M}_o} \ , \tag{65}$$

where $\alpha = 2A_1\sigma_n H_2/R$ and $p_0 = 2\tau_0 H_2/R + Mg/\pi R^2$ are constants.

Magma mass balance.—During plug extrusion, the volume and driving pressure of the magma will change. To characterize these changes we consider, in turn, mass and volume balances for the magma. We define the magma mass $M_M = \rho_M V_M$ as the mass of magma in the magma reservoir and in the conduit below the frictional plug. The rate of change of mass can be expressed as

$$\frac{dM_M}{dt} = \rho_M \frac{dV_M}{dt} + V_M \frac{d\rho_M}{dt} \ , \tag{66}$$

where ρ_M and V_M are magma density and volume, respectively. The mass change rate is also equivalent to the difference between the rate of mass input to the system Q_i and the rate out of the system Q_o, or

$$\frac{dM_M}{dt} = Q_i - Q_o \ . \tag{67}$$

Because magma is not being extruded at the surface, Q_o represents the magma-volume loss due to magma freezing onto the plug (Iverson and others, 2006). Combining and rearranging so that fluid volume is the dependent variable yields

$$\frac{dV_M}{dt} = -\frac{V_M}{\rho_M}\frac{d\rho_M}{dt} + \frac{Q_i}{\rho_M} - \frac{Q_o}{\rho_M} \ . \tag{68}$$

Reference to the magma density and its time derivative can be replaced by the pressure dependence through expanding the density derivative in equation 68:

$$\frac{d\rho_M}{dt} = \frac{\partial \rho_M}{\partial p}\frac{dp}{dt} \tag{69}$$

and using the definition of the elastic compressibility of the magma $\kappa_M \equiv (1/\rho_M)(\partial\rho_M/\partial p)$. Making these substitutions into equation 68 leads to

$$\frac{dp}{dt} = -\frac{1}{V_M \kappa_M}\left(\frac{dV_M}{dt} + \frac{Q_o}{\rho_M} - \frac{Q_i}{\rho_M}\right). \tag{70}$$

Magma volume balance.—The volume of the magma system increases as the solid plug is extruded at a rate dV_e/dt, and decreases as magma freezes to the plug at the rate $-Q_o/\rho_M$. We also allow the walls of the magma system (reservoir and conduit) to respond elastically to changes in magma pressure using a representative reservoir and conduit compressibility κ_c so that the rate of elastic change of magma volume is $\kappa_c V_M \, dp/dt$. The combined rate of magma volume change is then

$$\frac{dV_M}{dt} = \frac{dV_e}{dt} - \frac{Q_o}{\rho_M} + \kappa_c V_M \frac{dp}{dt} \ . \tag{71}$$

Combining equations 70 and 71 yields the relation between the mass rate of extrusion and the rate of change of the driving pressure

$$\frac{dp}{dt} = -\frac{\dot{M}_e/\rho_e - Q_i/\rho_M}{V_M\left(\kappa_C + \kappa_M\right)} \ , \tag{72}$$

where the extruded mass is $M_e = V_e \rho_e$.

Solutions

Solutions for extrusion rate with time can be found by taking the time derivative of equation 65

$$\frac{dp}{dt} = \frac{\alpha}{\dot{M}_e}\frac{d\dot{M}_e}{dt} \tag{73}$$

and equating to equation 71, resulting in the single differential equation

$$\frac{d\dot{M}_e}{dt} = -\frac{1}{\alpha V_M\left(\kappa_c + \kappa_M\right)}\left(\frac{\dot{M}_e^{\,2}}{\rho_e} - \frac{\dot{M}_e Q_i}{\rho_M}\right). \tag{74}$$

If the magma volume is large relative to the extruded volume, then V_M can be treated as a constant and equation 74 is separable. In the solution that follows we assume negligible density contrast between the magma and plug, $\rho_e = \rho_M$, as justified elsewhere in this paper.

No Recharge.—When $Q_\mathrm{i}=0$ the extrusion rate is:

$$\dot{M}_e = \frac{D\alpha\dot{M}_0}{t\dot{M}_0 / \rho_e + \alpha D} \, , \tag{75}$$

where $\dot{M}_0$ is the extrusion rate at $t=0$, and $D = V_M\left(\kappa_C + \kappa_M\right)$. The cumulative mass of extruded material goes as

$$M_e = \rho_e \alpha D \ln\left(1 + \frac{t\dot{M}_0}{\rho_e D \alpha}\right). \tag{76}$$

This is the logarithmic form that well characterizes stress relaxation due to fault slip in some laboratory experiments (Reinen and others, 1994) and during earthquake afterslip (for example, Marone and others, 1991; Schaff and others, 1999).

With recharge.—If $Q_i>0$ the extrusion rate is

$$\dot{M}_e = \frac{Q_i}{1 - \left(1 - \dfrac{Q_i}{\dot{M}_0}\right) e^{\frac{-Q_i t}{\rho_e \alpha D}}} \, . \tag{77}$$

Note that equation 77 is for $Q_i>0$ and does not easily reduce to equation 75 for $Q_i=0$.

Cumulative extruded mass goes as

$$M_e = \rho_e \alpha D \ln\left[1 - \frac{\dot{M}_0}{Q_i}\left(1 - e^{\frac{Q_i t}{\rho_e \alpha D}}\right)\right] \, . \tag{78}$$

This expression can be converted to erupted volume V_e by dividing by ρ_e.